University of Sussex

Magnetic Aspects of the Cryo-nEDM experiment

Aikaterini G. Katsika

Submitted for the degree of Doctor of Philosophy

University of Sussex

September 2011

Declaration

I hereby declare that this thesis describes my own original work, except where explicitly stated. No part of this work has previously been submitted either in the same or different form, to this or any other University in connection with a higher degree or qualification.

Signature:

Aikaterini George Katsika

UNIVERSITY OF SUSSEX

Aikaterini G. Katsika, Doctor of Philosophy

Magnetic Aspects of the Cryo-nEDM experiment

Abstract

The provision of a temporally stable and spatially uniform magnetic field is a precondition for the Cryo-nEDM experiment to conduct a successful measurement. These two aspects and some further data analysis are largely the subjects of my thesis.

I propose a technique to improve the current dynamic magnetic shielding of the existing apparatus by more than 2 orders of magnitude without distorting the homogeneity of the magnetic field more than the limitations set on the proposal. By testing a 12.5 th scale model of the apparatus I have shown that the placement of a 1m long superconducting shield inside the solenoid can improve the magnetic shielding by at least a factor of 500.

Magnetostatic simulations have been carried out for the full model of the experimental apparatus to investigate the effect of various parts to the magnetic field configuration over the neutron guides and the storage bottles. This model can be considered as a basis on which further additions can be made if needed.

The actual response of the 21 compensation coils has been measured experimentally. This information was used to develop a systematic method to calculate the optimum currents for these coils to smooth the magnetic field inhomogeneities in the area of the storage cells of neutrons. Applying this method to the existing apparatus, it has been estimated that we can increase the T_2 relaxation time from 2 seconds to more than 20 seconds.

Finally, I have analysed the data taken over winter 2010 run in terms of neutrons polarisation. As a result, very useful information was extracted for the issues that have to be resolved and taken into account in future runs to improve the polarisation of neutrons and therefore the sensitivity of the experiment.

Acknowledgements

First, I would like to thank my supervisors Mike Hardiman and Philip Harris. Their support and consistent guidance were vital for me to complete this thesis. They have acted in a complementary manner to help me get along with this mission. They are both great physicists and great teachers. I have learnt a lot from them and I was improved as a physicist and as a person.

Mike Pendlebury, the "father"of this experiment as I call him, is the person who always surprised me not only with the vast variety of the knowledge he possesses and his brightness, but mainly with his modesty. I am simply honoured that I have met a man and a physicist like him in my life.

Ian Wardell, has taught me how to approach physics problems starting with the simple question: "OK, firstly, how does this work?"He is one of the smartest people I have met and the personification of the word simplicity on the way we have to think.

As with everybody who has worked in the cryogenics lab, I have been benefited greatly from the help of all the technicians at Sussex. In the first years, Dave Shiers spent a lot of his time explaining to me the details of the technical designs and answering many of my naive questions about the experiment. The Legend, or for the rest of the world John Knight, was always present with a smile on his face when I and my student colleges needed him. I could write a whole thesis again only for his personality! He, Bob Woodhouse and Keith Nie were the people to trust when we needed a technician expert, showing a lot of understanding for the time restrictions that a PhD student has.

Melissa A. George joined her forces with mine to find the exit to the labyrinth of the polarisation data. I think and I hope we did our best.

Markus Vogt worked with me as part of his final year project and I have to confess that I learnt lots of things from him especially about electronics. He was always up with a solution to the problems occurring in a typical cryogenics lab; from a fancy screwdriver to a lorry jack.. Just Markus! Debbie Hill also worked with me as part of her summer project. She was one of the people who helped me adjust myself to the lab, Sussex and the UK.. Her working in the lab has to be attributed as a smart decision of Mike Hardiman. It

was great-great fun working with these people. The contribution of both of these students has been significant to the progress of my experimental work and I am grateful for that.

Maurits van der Grinten, Andrei Khazov and Sergei Ivanov were the people I have worked closely with at ILL. It was a precious experience working at ILL when the experiment was running and these were mainly the people, along with the Oxford collaborators as well, to discuss the emerging problems.

Sussex fellow students have been left to last but not least.

I owe a big thank you to Ippocratis Saltas who helped me the most during my first year at Sussex. We spend many hours together till the morning solving Quantum Field Theory exercises and discussing about physics in general.

Matt Raso-Barnett had the "luck"to work at ILL at the same time with me. Physics combined with dancing music in difficult early morning times, discussions about the last technological achievements on phones and other less important things as life in general, were mainly the ways we spent the time together. I am grateful to him for his help over our time at ILL and here at Sussex. He is a great and very easy going person to work with.

Andrew J. Davidson (or just AD) is the student mate that I started and finished my PhD studies with. We worked in the same lab for something less than 4 years and he was the first person to ask for a help or an opinion. We have memories of leaving the lab at 7 am but yet, we were happy for having made some progress. We had never pretended that we knew something if we didn't, so we explored the mysteries of physics together from the same start. My cooperation with him has been just perfect without personal friction, an achievement for people working together for years.

Finally, I want to dedicate all of my work and the result of it as presented here, to my mother Olympia.

Τελος, $\theta\epsilon\lambda\omega$ $\nu\alpha$ $\alpha\phi\iota\epsilon\rho\omega\sigma\omega$ ολη $\mu\sigma\upsilon$ $\tau\eta\nu$ $\epsilon\rho\gamma\alpha\sigma\iota\alpha$ $\kappa\alpha\iota$ το $\alpha\pi\sigma\tau\epsilon\lambda\epsilon\sigma\mu\alpha$ $\alpha\upsilon\tau\eta$ς ως $\pi\alpha\rho\sigma\upsilon\sigma\iota\alpha\zeta\epsilon\tau\alpha\iota$ $\epsilon\delta\omega$, $\sigma\tau\eta$ $\mu\eta\tau\epsilon\rho\alpha$ $\mu\sigma\upsilon$ Ολυμπια.

Contents

Abbreviations

6WS: Six Way Section

BC: Background Counts

BCR: Background Count Rate

CDSF: Cryogenic Dynamic Shielding Factor

CP: Charge Conjugation and Parity Symmetry

CPT: Charge Conjugation, Parity and Time Reversal Symmetry

Cryo-nEDM: the Cryogenic Neutron Electric Dipole Moment Experiment

DVM: Digital Volt-Meter EDM: Electric Dipole Moment

FWHM: Full Width at Half Maximum

He-I: Normal state of liquid helium

He-II: Superfluid state of liquid helium

HS: Horizontal Shields

HV: High Voltage

ILL: Institut Laue-Langevin (at Grenoble / France)

LHe: Liquid Helium

LN2: Liquid Nitrogen

NMR: Nuclear Magnetic Resonance

OVC: Outer Vacuum Containment

RC: Ramsey Cells

SC: Superconducting

SCV: Supefluid Containment Vessel

SM: Standard Model

SQUID: Superconducting QUantum Interference Device

SS: Stainless Steel

Tc: Critical (or Superconducting Transition) Temperature

TDSF: Total Dynamic Shielding Factor

UCN: Ultra Cold Neutrons

YS: Yoshiki Shields

List of Tables

List of Figures

Introduction

The predominance of matter over antimatter in the Universe is one of the most fundamental cosmological questions that is yet to be resolved. In 1957, the Russian physicist Andrei Sakharov postulated three requirements for baryon asymmetry to occur. The second of these was that the physical laws which are responsible for the observed asymmetry have to violate the combined action of the parity and charge conjugation otherwise the production rate of baryons and antibaryons would be equal.

The Standard Model accommodates CP violation phenomenologically via the non-zero complex phase in the CKM matrix, but it can not explain the observed matter-antimatter asymmetry. Understanding the extent and the actual mechanisms of CP violation is vital for developing theories that will explain both baryon asymmetry and CP-violating processes in particle physics mainly in meson decaying systems.

A non-zero electric dipole moment (EDM) of any elementary particle violates time invariance symmetry and, via the CPT theorem, CP as well. Over the last 60 years, many experiments have tried to measure the magnitude of the neutron EDM but have not succeeded. Their sensitivity has proven insufficient and they have only set upper limits. The last one was released by the Sussex/RAL collaboration Room Temperature nEDM experiment and is equal to $\mid d \mid < 2.9 \cdot 10^{-28}\ e \cdot cm$.

Significant progress has been made in understanding the physics of the neutron itself due to the availability of so-called Ultra Cold Neutrons (UCN). These have energies up to few hundred of neV corresponding to velocities in the 5-7 m/s range. As a consequence, they can be easily confined in physical bottles of appropriately chosen materials.

The Cryo-nEDM experiment is designed to measure the neutron EDM by applying the NMR technique to bottled ultra cold neutrons (UCN), and is aiming to improve the current upper limit by two orders of magnitude. The sensitivity of the experiment depends largely on the magnetic environment experienced by neutrons; it has to be strong enough and uniform in space to retain their polarisation state, and finally constant in time so that a false EDM signal is not generated.

The experimental work on this thesis falls mainly into these two areas; the spatial uniformity and the temporal stability of the magnetic field. Both experimental studies and magnetostatic simulations and calculations were performed to solve issues related to these subjects. The last part of this thesis presents a detailed analysis of the data taken during winter 2010 run at ILL,in order to determine accurately the neutron polarisation.

As last part of my thesis, I analysed the data taken during winter 2010 run at ILL from polarisation point of view.

The first chapter summarises the theory of CP violation and its relation to electric dipole moments of elementary particles such as the neutron. It is pointed out that any theory that will successfully explain the matter-antimatter asymmetry in the Universe has also to predict the correct value for the magnitude of the neutron electric dipole moment.

The second chapter gives an overview of the Cryo-nEDM experiment. The physical principles of the Ramsey technique applied to stored UCN is the heart of this experiment. A detailed description of the apparatus and its parts in order to understand some of the technical aspects is given as well. The cooling process, the polarisation of the cold neutrons before they reach the entrance of the cryostat, the deceleration of the cold to ultra cold neutrons, the way we transfer and manipulate them to conduct the experiment and finally the detection of neutrons of some defined spin state are also explained in this chapter.

The next three chapters detail the contribution of the author to this experiment. The third chapter deals with a current problem with the apparatus which provides a dynamic magnetic shielding three orders of magnitude less than that required to reach the desired sensitivity. The problem stems from the relative positions of some superconducting (SC) parts of the apparatus. The solution tested was to place an inner superconducting shield around the neutron storage cells. A 12.5th scale model of the SC parts of the real apparatus was built, and previous magnetic shielding data (at Sussex in 2004/05) were reproduced. It is shown that applying by the proposed solution, we can improve the shielding factor to the required level.

Chapter 4 deals with issues related to the polarisation holding field between the exit of the cold neutron polariser and the cells where neutrons are stored. Both magnetostatic simulations and analytical calculations have been done to estimate the effects of various parts of the apparatus on the polarisation of neutrons as these are guided to the cells. A model of the full experimental apparatus was designed in OPERA simulation package and is now the basis of further work in the future. The effect of the SQUID magnetometers around the neutron guides to the field homogeneity and depolarisation time has been

examined particularly.

Chapter 5 considers the magnetic field seen by neutrons while resonance is carried out. Due to intrinsic magnetic inhomogeneities in the vessel that accommodates the neutron storage cells, a full magnetic scan was performed over the summer of 2010 to obtain a detailed map of the field over this region. Additionally, we measured the response of the 21 compensation coils within the existing high permeability shields around the apparatus, as this is not expected to be trivially the same as their response in free space. Having these two pieces of information, we proposed a systematic method to find the optimum correction coils currents of the to improve the axial and azimuthial uniformity of the magnetic field to the level necessary to conduct a successful EDM measurement.

Chapter 6 includes the polarisation analysis on the data taken during winter 2010 run. The aim of that run was to observe a Rabi resonance and extract information about the polarisation and number density of neutrons. However, this analysis showed that the UCN were highly depolarised and this was the primary reason for a failure to detect a resonance. The analysis revealed many problems related to data recording. We extracted very useful information about detectors and how to set up a successful run.

Finally, Chapter 7, summarises the work presented in this thesis and includes suggestions for further work in the future.

Chapter 1

Theory of the neutron Electric Dipole Moment

1.1 Introduction

The importance of the neutron electric dipole moment (nEDM) measurement can only be understood within the frame of three invariance principles in nature and their combinations; the charge conjugation (**C**), the space inversion (**P**) and the time reversal (**T**) symmetries. It is well established that the individual symmetries are violated in weak interactions while the combined product of **CPT** seems to remain an exact symmetry in nature.

A non-zero electric dipole moment of any fundamental particle (such as neutron) violates the **CP** (or equivalently **T**) symmetry, as do the physical processes during the early stages of Universe responsible for the matter over antimatter excess. Phenomenologically, the Standard Model (SM) of particle physics can accommodate **CP** violation but it fails to explain the observed baryon-antibaryon asymmetry.

The measurement of the neutron EDM is of particularly significant importance as it would be the first observation of **CP** violation apart from meson (Kaons and B-mesons) decay systems. To date, the upper limits released from various experimental groups over the last six decades for the value of the nEDM have set severe constraints on many theories beyond the SM that attempt to predict successfully **CP**-violating mechanisms (see Figure 1.1).

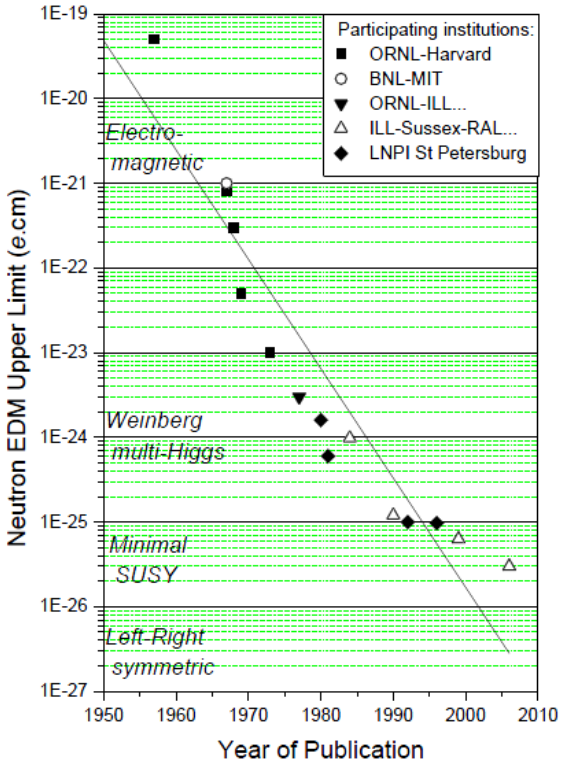

Figure 1.1: Improvement of the nEDM upper limit with time. Some theoretical models predicting the magnitude of nEDM are also shown on the left of the graph.

1.2 C, P and T symmetries

The charge conjugation (**C**) operation transforms a particle to its counterpart antiparticle whilst keeping the dynamic variables the same. Invariance under this operation means that the physical processes that involve particles and the same processes that involve their antiparticles both occur in nature and that they do so with the same probability. In the late 1950's [7] it was known that even though strong and electromagnetic interactions are invariant under C operation, weak interactions are not; free neutrinos (antineutrinos) were observed to have their spin antiparallel (parallel) to their momentum. Hence, applying the charge conjugation operator, the left-handed neutrino should be transformed to a left-handed antineutrino (as the spin is unchanged under **C**). The latter particle though has never been observed and it is believed that does not exist in nature.

Parity (**P**) operation is equivalent to a coordinate inversion ($\vec{r} \rightarrow -\vec{r}$). Invariance under parity means that a physical process and its mirror-reflected process occur in nature with the same probability. Lee and Yang [8] were the first to suggest that parity might not be conserved either in weak interactions. This theory was first confirmed experimentally by Wu [9] by measuring the angular distribution of the electrons emitted by polarised ^{60}Co

nuclei. [10] led to the same conclusion too.

Landau in 1957 [11] [12] proposed that it is the combination of charge conjugation and mirror reflection that is actually preserved in physical processes including weak interactions (**CP** invariance). This was indeed the common belief until 1964 when Christenson et al [13] observed the **CP** violating decay of the long lived Kaons $K_L^o \rightarrow \pi^+\pi^-$ in a K^o beam. Their experimental result was confirmed many times afterwards and finally a direct **CP** violation was observed in CERN in 1988 [14]. **CP** violation was also observed in B^o mesons by the BELLE experiment for first time in 2001 by finding decay rate differences between B^o and $\bar{B}^o$ [15] [16].

Based on the equality of particle-antiparticle masses and lifetimes, Löders and Pauli [17] [18] [19] claimed that a Lorentz invariant Hamiltonian is not necessarily invariant under the discrete transformations of **C**, **P** or **T** but that it must be so under the combined operation of all three of these symmetries. An important consequence of this **CPT** theorem is that if any individual or pair of symmetries is violated then a compensating violation in the other operator(s) must occur so that the **CPT** invariance for all known forces in nature is upheld. Thus the **CP** violation predicted by the SM and confirmed in the meson systems must be accompanied by a **T** symmetry violation as well.

1.3 Baryon asymmetry in the Universe

The fact that the (visible) Universe is matter dominated is a long standing cosmological problem that has yet to be resolved. The birth and evolution of Cosmos can be described quite successfully by the Hot Big Bang model but this theory predicts a matter-antimatter asymmetry about 10 orders of magnitude less than the value found experimentally.

By detecting cosmic rays, radioastronomers have measured the baryon asymmetry (η) given by the ratio of baryon (η_B) over photon (η_γ) number density:

$$\eta = \frac{\eta_B}{\eta_\gamma} = 6 \cdot 10^{-10} \tag{1.1}$$

In a baryon-symmetric Universe this ratio is expected to be zero, but its measured value indicates that for about every billion particle-antiparticle pairs there was one extra particle created.

In 1967, Andrei Sakharov [20] pointed out that in order to have a transition from a baryon-symmetric to an asymmetric Universe, the reactions responsible for this must meet three requirement; firstly, they must not conserve the baryonic number so that the initial state (B=0) of the vacuum changes (to B$\neq$0). Secondly, they must also violate **C** and **CP**

symmetries. If charge conjugation which interchanges quark and antiquark was a valid symmetry, such interactions, even if they did not conserve the baryon number, would leave $N_q = N_{\bar{q}}$ over long periods of time. Additionally, **CP** needs to be violated so that the rate of production of baryons exceeds that of antibaryons. Finally, the interactions responsible for baryogenesis must have been out of thermal equilibrium at some early stage of the formation of the Universe. In the equilibrium state, the interactions are time reversal invariant so having no sense of time direction would lead to equal numbers of baryons and antibaryons. After the process of baryogenesis had been complete however, the Universe had settled in thermal equilibrium and the generated asymmetry was irreversible.

1.4 Neutron EDM

1.4.1 Classical Description

Classically, two discrete charges (±q) separated by a distance $\vec{x}$ constitute a dipole whose moment is given by the product:

$$\vec{d} = q \cdot \vec{x} \tag{1.2}$$

In the case of a charge distribution $\rho(\vec{r})$ the above polar vector becomes:

$$\vec{d} = \int \rho(\vec{r})\vec{r}dV \tag{1.3}$$

The neutron is not a point-like particle and although electrically neutral, it consists of charged components whose distribution is such as the positive and negative centres of charge do not coincide but may be slightly offset from one another (see Figure 1.2). The alignment of this electric dipole must be along the spin axis of neutron, the only intrinsic vector quantity allowed in spin-1/2 particles. Its units are the units of charge × length and in particle physics it is common to use the electron charge (e) × cm.

If it contains electrically charged constituents, any particle can exhibit a non-zero electric dipole moment when subject to external electric field. When we refer to the neutron EDM, we mean the permanent electric dipole due to its internal charge distribution in zero electric field.

1.4.2 nEDM as evidence for CP violation

The neutron is a Dirac particle and it has been known since 1930 [21] [22] [23] that it possesses a non-zero magnetic dipole moment ($\mu = -1.913\mu_N$ where μ_N is the nuclear

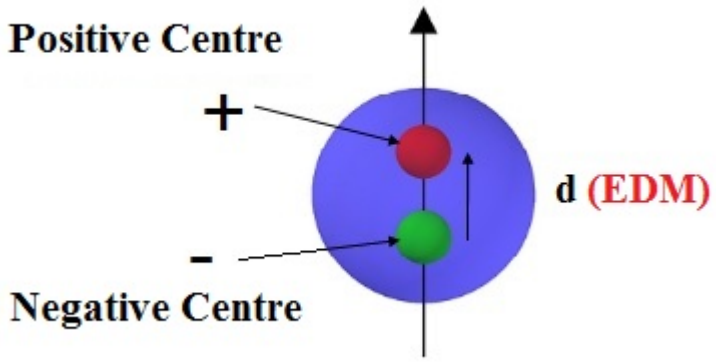

Figure 1.2: A schematic representation of the offset of the two oppositely charged areas inside the neutron.

magneton) due to the virtual mesons cloud around it. The existence of an additional finite permanent electric dipole moment in the neutron (and in any particle whose state is described by a non-degenerate wavefunction) would constitute a direct P- and T- violation but is yet to be measured.

Neutrons are very convenient particles to use for EDM measurements, as they are electrically neutral and can be trapped in bottles for sufficiently long times using ultra-cold beams. In addition the value for the neutron EDM is expected to be many orders of magnitude bigger than that of point-like particles such as the electron and hence requires less sensitive experiments for its detection.

Quantity	**C action**	**P action**	**T (CP) action**
Charge Density (n)	-n	n	n
Current ($\vec{J}$)	- $\vec{J}$	- $\vec{J}$	- $\vec{J}$
Spin ($\vec{s}$)	$\vec{s}$	$\vec{s}$	-$\vec{s}$
Electric Field ($\vec{E}$)	-$\vec{E}$	-$\vec{E}$	$\vec{E}$
Magnetic Field ($\vec{B}$)	-$\vec{B}$	$\vec{B}$	-$\vec{B}$

Table 1.1: **C**, **P** and **T** transformation of various physical quantities.

Consider a neutron inside an electric ($\vec{E}$) and magnetic ($\vec{B}$) field. The interaction Hamiltonian is given by:

$$H = -d\vec{\sigma} \cdot \vec{E} - \mu\vec{\sigma} \cdot \vec{B} \tag{1.4}$$

where the electric (d) and magnetic (μ) moments are proportional to the Pauli spin vectors

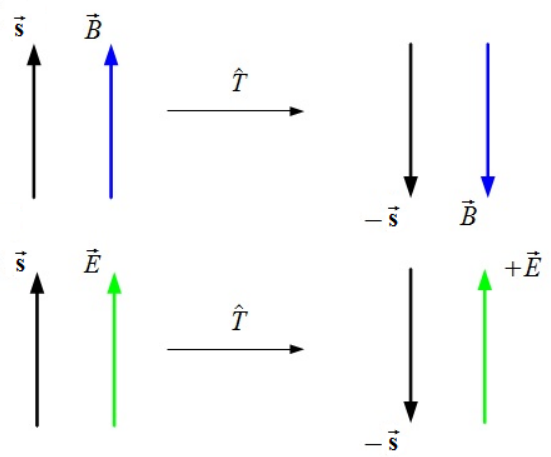

Figure 1.3: The result of time operator (**T**), equivalent to a **CP** action, on the spin vector ($\vec{s} = s \cdot \vec{\sigma}$), the magnetic ($\vec{B}$) and electric ($\vec{E}$) fields.

$\vec{\sigma}$. Under parity reversal (**P**) the axial spin ($\vec{\sigma}$) and magnetic field ($\vec{B}$) vectors remain unchanged while the polar vector of the electric field ($\vec{E}$) is reversed (see Table 1.1):

$$\widehat{P}\widehat{H} = -d\vec{\sigma} \cdot (-\vec{E}) - \mu\vec{\sigma} \cdot \vec{B} = +d\vec{\sigma} \cdot \vec{E} - \mu\vec{\sigma} \cdot \vec{B} \neq \widehat{H} \tag{1.5}$$

On the other hand, under time inversion **T** (or equivalently, via the **CPT** theorem, under **CP** action) the $\vec{\sigma}$ and $\vec{B}$ change sign and $\vec{E}$ remains unchanged:

$$\widehat{T}\widehat{H} = -d(-\vec{\sigma}) \cdot \vec{E} - \mu(-\vec{\sigma}) \cdot (-\vec{B}) = +d\vec{\sigma} \cdot \vec{E} - \mu\vec{\sigma} \cdot \vec{B} \neq \widehat{H} \tag{1.6}$$

In both cases, the part of the Hamiltonian that describes the magnetic interaction is even, but the term that gives the coupling of the electric dipole moment with the applied electric field is P- and T- odd.

Hence measuring a non-zero electric dipole moment in neutron would be direct evidence of both **P** and **T** (or **CP**) violation. This is not the case for more complicated particles such as atoms or molecules; for example a finite EDM of the ammonia molecule does not lead to parity violation as this molecule is described by a degenerate wavefunction that is symmetric under space reversal.

1.5 CP Violation in the Standard Model

There are two sources of CP violation within the Standard Model; the first comes from the electroweak and the second from the strong sector. Eventhough both contributions

have been calculated in the framework of the SM, there are always present regardless any extension of the SM considered.

1.5.1 Electroweak Interactions

The time reverseal operator is defined as $\hat{T} = \hat{U} \cdot \hat{K}$, where $\hat{U}$ transforms $t \rightarrow -t$ and $\hat{K}$ carries out complex conjugation on anything that lies on the right of it. The matrix elements for the transition from $|\psi_i\rangle \rightarrow |\psi_f\rangle$ are given by:

$$\langle \psi_f | \hat{H} | \psi_i \rangle \tag{1.7}$$

Under $\hat{T}$ operation we take:

$$\langle T\psi_f | T^{-1} \hat{H} T | T\psi_i \rangle \tag{1.8}$$

Equations 1.7 and 1.8 are equal if the transition $|\psi_i\rangle \rightarrow |\psi_f\rangle$ is T-invariant, or in other words if the Hamiltonian, or equivalently the Langrangian ($\mathcal{L}$), is real. If $\hat{H}$ (or $\mathcal{L}$) is complex, 1.7 and 1.8 are different and the transition from the initial to the final state violates T, and via the CPT theorem, the CP-symmetry.

In the electroweak sector, a Lagrangian can have real all the coupling and mass terms only in the case of two quark generations. This is achievable as any complex number in the Cabibbo rotation matrix [24] can be eliminated by redefining the quark phases. When a third generation of quarks is added, however, the quark mass mixing (CKM) matrix [25] can be written as a function of three real angles and one complex phase:

$$V_{CKM} = \begin{pmatrix} c_{12}c_{13} & s_{12}c_{13} & s_{13}e^{-i\delta} \\ -s_{12}c_{23} - c_{12}s_{23}s_{13}e^{i\delta} & c_{12}c_{23} - s_{12}s_{23}s_{13}e^{i\delta} & s_{23}c_{13} \\ s_{12}s_{23} - c_{12}c_{23}s_{13}e^{i\delta} & -c_{12}s_{23} - s_{12}c_{23}s_{13}e^{i\delta} & c_{23}c_{13} \end{pmatrix} \tag{1.9}$$

where $0 \leq \theta_i \leq \frac{\pi}{2}$ are the three Cabbibo-like mixing angles, $i = 1, 2, 3$ are the three generation labels, $c_{ij} = cos\theta_{ij}$ and $s_{ij} = sin\theta_{ij}$. Finally the complex phase $0 \leq \delta \leq 2\pi$ is the parameter due to which CP-violation can be accommodated in the SM, provided that it is not zero and that there is mixing between all three generation. The end result of any nEDM (d_n) calculation in the electroweak sector will be proportional to this phase angle [26]:

$$d_n \approx (10^{-29} - 10^{-28}) s_{12}s_{13}sin\delta \; e \cdot cm \tag{1.10}$$

where [27] [28]:

$$2 \times 10^{-4} \leq s_{12}s_{13}sin\delta \leq 2 \times 10^{-3} \tag{1.11}$$

Therefore, the contribution of δ to nEDM is found to be:

$$d_n \approx (10^{-33} - 2 \times 10^{-31})\ e \cdot cm \tag{1.12}$$

1.5.2 Strong interactions

It is G. 't Hooft [29] who first suggested that the Langrangian density in quantum chromodynamics (QCD) must consist of two parts:

$$\mathcal{L} = \mathcal{L}_o + \mathcal{L}_\theta \tag{1.13}$$

where $\mathcal{L}_o$ describes the colour triplets of quarks, the colour octets of gluons and their interactions. The second term ($\mathcal{L}_\theta$) can be written as:

$$\mathcal{L}_\theta = -\theta_{QCD}\frac{g^2}{32\pi^2}G_{\mu\nu}\tilde{G}^{\mu\nu} \tag{1.14}$$

where $0 \leq \theta \leq 2\pi$ is an angle parameter, g is the strong coupling constant, and $G_{\mu\nu}$, $\tilde{G}^{\mu\nu}$ the two gluon field strength tensors, with $G_{\mu\nu}\tilde{G}^{\mu\nu} = \epsilon^{\mu\nu\alpha\beta}G_{\alpha\beta}$.

$\mathcal{L}_\theta$ is C-even (because it has even number of gluon field tensors) and P-odd (due to the anti-symmetric $\epsilon^{\mu\nu\alpha\beta}$). Therefore, contrary to $\mathcal{L}_o$, $\mathcal{L}_\theta$ violates CP and it is the source of non-zero EDMs within the strong sector of the SM. The contribution this term makes to the nEDM (d_n) has been calculated in several models [30], [31], [32] and lies between:

$$2 \times 10^{-6} < \left|\frac{d_n}{\theta_{QCD}\ e \cdot cm}\right| < 5 \times 10^{-6} \tag{1.15}$$

The current experimental limit of nEDM [33], $d_n < 2.9 \times 10^{-26}\ e \cdot cm$, places a constraint for θ_{QCD}:

$$|\theta_{QCD}| < 10^{-10} \text{ rad} \tag{1.16}$$

This extremely small value for the -in principle arbitrary- angle θ_{QCD}, is known as the "Strong CP problem". By complex renormalisation of the quark mass matrix at the two-loop level, θ_{QCD} has been estimated to be [34]:

$$\theta_{QCD} \approx 10^{-16}\ rad \tag{1.17}$$

and hence:

$$d_n \approx 10^{-32}\ e \cdot cm \tag{1.18}$$

which is comparable to the δ-phase contribution in the electroweak sector. Nonetheless, there are other models [35] [36], where θ_{QCD} is actually zero. In one of these, the Peccei-Quinn model [37], the existance of the axions (particles that are not yet observed) is required to explain the required CP-violation for the baryon asymmetry.

1.6 CP Violation Beyond the Standard Model and Supersymmetry

The CP-violation within the Standard Model is related to the highly suppressed flavour changing processes. This is largely the reason why the observed baryon asymmetry of the Universe is many orders of magnitude less than what the SM predicts. Most theories beyond the SM have new imaginary phases and allow first order contributions to CP violation and therefore they predict larger nEDM.

In a generic supersymmetric (SUSY) extension of the SM for example (one of the most promising theories of new physics where each SM particle has a superpartner whose spin differs by $\frac{1}{2}$) the extra particles are associated with extra CP violating parameters which are introduced by the additional terms in the effective Lagrangian:

$$\mathcal{L} = \mathcal{L}_{SUSY} + \mathcal{L}_{soft} \tag{1.19}$$

The supersymmetric term depends, in addition to the three gauge couplings of the SM, on the superpotential W:

$$W = \sum_{ij} (Y^u_{ij} h_u \tilde{q}_{Li} \tilde{u}_{Rj} + Y^d_{ij} h_d \tilde{q}_{Li} \tilde{d}_{Rj} + Y^l_{ij} h_d \tilde{L}_{Li} \tilde{l}_{Rj}) + \mu h_u h_d \tag{1.20}$$

where h_u, h_d, q_{Li}, L_{Li}, $\tilde{u}_{Rj}$, $\tilde{d}_{Rj}$, $\tilde{l}_{Rj}$ are the chiral superfields. The three 3×3 Yukawa matrices $Y^{u,d,l}_{ij}$ that give mass to the quarks and leptons -and their superpartners - are functions of 27 real and 27 imaginary parameters.

As none of the spartners have yet been discovered, SUSY must be considered as a broken symmetry in the vacuum state. If supersymmetry were unbroken, then there would have been superparticles with masses exactly equal to their SM partners and therefore been detected. It is the second part of the Lagrangian (in equation 1.19) that violates supersymmetry. It is denoted as soft as it is related to positive mass dimension of scale

$\mathcal{O}$(1 TeV) to cancel quadratic divergences. This part of the Lagrangian contributes to the interactions of some particles but not to their superpartners, clearly breaking SYSU and leading to sparticles that can not be observed at low energies.

$$\mathcal{L}_{soft} = (\alpha^u_{ij} h_u \tilde{q}_{Li} \tilde{u}_{Rj} + \alpha^d_{ij} h_d \tilde{q}_{Li} \tilde{d}_{Rj} + \alpha^l_{ij} h_d \tilde{L}_{Li} \tilde{l}_{Rj} + b h_u h_d + h.c.)$$

$$- \sum_{all\ scalars} m^{S2}_{ij} A_i \bar{A}_j - \frac{1}{2} \sum_{(\alpha)=1}^{3} (\tilde{m}_{(\alpha)})(\lambda\lambda)_{(\alpha)} + h.c. \tag{1.21}$$

The soft supersymmetry breaking terms (in equation 1.21) are the gaugino mass terms $(\tilde{m}_{(\alpha)}(\lambda\lambda)_{(\alpha)})$, the hermitian 3×3 mass-squared matrices for sfermions ($m^{S2}_{ij} A_i \bar{A}_j$ where A are the scalar fields) and the $\alpha^{u,d,l}$ matrices (which are equivalent to the Yukawa couplings matrices of the superpotential in equation 1.20). The three $\alpha^{u,d,l}$ matrices depend again on 27 real and 27 imaginary parameters, while the five m^{S2}_{ij} are a function of 30 real parameters and 15 imaginary phases. Finally, the gauge and Higgs sectors depend on another 11 real and 5 imaginary parameters.

Summing over all sectors and taking into account the global symmetries that remove 15 of the real and 30 of the imaginary parameters, we are left with 80 real and 44 imaginary physical parameters. So, apart from the CKM δ phase, there are in principle 43 new potential CP-violating phases.

The experimental findings from both the neutral mesons and the nuclear and atomic electric dipole moments can impose severe constraints on these parameters. Some of the proposed theories have already been excluded as they predict too large nEDM values. The Minimal Supersymmetry for instance [38] [39], where there are no additional flavour mixings predicts nEDM value of $d_n \approx 10^{-25}\ e \cdot cm$. The Weinberg multi-Higgs model [40] [41] on the other hand, where the new CP-violation sources stem from the mixing of CP-odd and CP-even neutral scalars, a complex mixing matrix for charged scalars and the (CP-odd) Yukawa couplings in the quark mass basis, predicts $d_n \approx 10^{-24}\ e \cdot cm$. Both of these values are greater than the current experimental upper limit.

The theories that can be considered the next ones under test by experimental results are the Left-Right (LR) models [42] [43]. These were originally proposed to explain parity violation but have been also used to extend the minimal supersymmetry model, introducing several additional phases. In LR models, new gauge and Higgs fields appear with masses below the GUT scale, and the new sources of CP violation are the phases in two generalised Kobayashi-Maskawa matrices and four Majorana phases. The predicted first-order contribution to the nEDM is $d_n \geq 1.9 \times 10^{-27}\ e \cdot cm$, which is within the next

generation nEDM experiments sensitivity.

Useful reviews of the nEDM theories beyond the Standard Model can be found in [38] and [39].

Chapter 2

The Cryo-nEDM Experiment

2.1 Physical Principles of the Experiment

Since a neutron is not an elementary particle but is made of charged constituents, it possesses a magnetic dipole moment $\vec{\mu}_n$ and potentially a non-zero electric one $\vec{d}_n$. Both of these vector quantities are aligned with the spin vector of the neutron $\vec{s}$, the only intrinsic alignment of this particle. When, therefore, the neutron is placed in a magnetic field, its magnetic moment will precesses about the field orientation at the Larmor frequency. This frequency also defines the energy separation of the two possible states of the spin-1/2 neutron, corresponding to the two projections (parallel and anti-parallel) of the magnetic moment along the spin axis (see Figure 2.1). The relationships are:

$$\Delta E_o = 2\vec{\mu}_n \cdot \vec{B} \Rightarrow \hbar\omega = h\nu = 2\vec{\mu}_n \cdot \vec{B} \Rightarrow \nu = 2\mu_n \vec{s} \cdot \vec{B}/h \tag{2.1}$$

where $\hbar$ is the reduced Planck constant. The equation above can be written in terms of the angular velocity of precession $\vec{\omega} = \gamma\vec{B}$ where γ is the neutron gyromagnetic ratio:

$$\gamma = \frac{2\mu_n}{\hbar} = 1.8\ 10^8\ Hz/T \tag{2.2}$$

Quantitativly, the neutron in a magnetic field $\vec{B}$ precesses with frequency ν equal to:

$$\frac{\nu}{B} = \frac{\omega/2\pi}{B} = \frac{\gamma}{2\pi} = 29.165\ MHz/T \tag{2.3}$$

In the case of the neutron possessing a non-zero electric dipole moment, the application of an additional electric field will change the precession frequency since the total interaction Hamiltonian now becomes:

$$H = h\nu = 2\mu_n \vec{s} \cdot \vec{B} \pm 2d_n \vec{s} \cdot \vec{E} \tag{2.4}$$

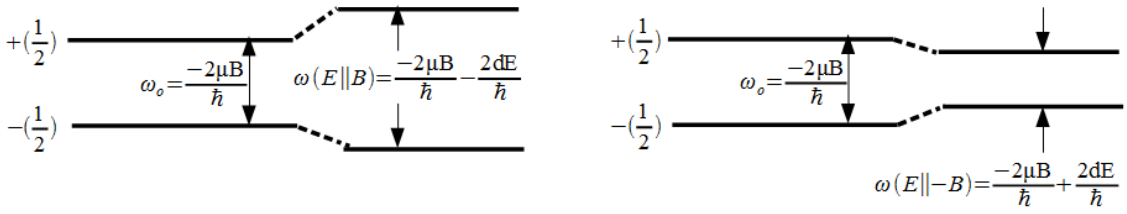

Figure 2.1: Energy states of neutron in parallel (left) and antiparallel (right) magnetic and electric field.

where the negative (positive) sign before the second term corresponds to parallel (antiparallel) electric and magnetic fields.

To maximise the sensitivity of such an experiment we need to enhance as much as possible the shift in precession frequency due to the edm coupling with the electric field. By changing the polarity of the latter, we can gain easily a factor of two in this interaction term, as the precession frequency changes by:

$$\delta\nu_o = -\frac{4d_n E}{h} \tag{2.5}$$

Hence, the underlying principle of the Cryo-nEDM, and most of the current neutron edm experiments, is the measurement of the shift in precession frequency that occurs between the two relative alignments of the electric and magnetic fields. The basic precondition for this method is full temporal and spatial control of the magnetic field experienced by neutrons while the electric field is applied and reversed. This is necessary in order to eliminate any potential frequency shifts due to magnetic field variations. Practically, the aim is to limit any magnetic contributions be at least one order of magnitude less than that coming from the edm coupling term as defined by the proposed sensitivity of the particular experiment.

2.1.1 Ramsey Method of Separated Oscillating Fields

We consider polarised neutrons entering a storage volume with their spin aligned along a magnetic field $\vec{B}_z$ (spin-up state). Even though classically we can think of the spin angular momentum as accurately known (being exactly parallel with another vector), in terms of quantum mechanics we do not refer to the actual spin vector but to its projection on the z-axis and the probability of finding it in one direction or the other. The spin vector itself precesses about $\vec{B}_z$ with frequency $\omega_z = \gamma B_z$.

Using a pair of AC coils, we introduce an additional oscillating magnetic field $\vec{B}_{xy}$ perpendicular to B_z. This linear field can be regarded as two fields both rotating at ω_{rot}

but in opposite directions. One of this fields will then rotate in the same sense as the neutron and will have an arbitrary phase difference with respect to the neutron spin (ϕ_o). The spin vector now also precesses about $\vec{B}_{xy}$ with frequency $\omega_{xy} = \gamma B_{xy}$. The resultant motion of the neutron spin, due to the two precessions, is a spiral, departing from the z-axis and approaching the xy plane. In the Cryo-nEDM experiment, the precession about $\vec{B}_{xy}$ is far slower than that about $\vec{B}_z$ with $\omega_{xy} \approx 5rad/s << \omega_z \approx 942rad/s$.

The oscillating field is applied for a period such that the spin vector is tipped from the z-axis by an angle $\delta\theta = \pi/2$ such that it is lying on the xy plane after a time Δt_1, where:

$$\omega_{xy} = \gamma B_{xy} \Rightarrow \frac{\Delta\theta}{\Delta t} = \gamma B_{xy} \Rightarrow \Delta t_1 = \frac{\pi/2}{\gamma B_{xy}} \tag{2.6}$$

In the Cryo-nEDM experiment, Δt_1 is typically $\approx$2 sec. At the end of this period, the neutrons are left to precess at ω_z for a relatively long time, $T_s \approx 300$ sec, with the AC coils turned off but keeping the AC source running in the background. If $\omega_{rot} = \omega_z$, i.e. if the AC frequency is the same as that of the neutron precession, the initial phase difference, ϕ_o, will remain exactly the same over T_s. Energising the AC coils again for a time $\Delta t_2 = \Delta t_1$, the second oscillating field pulse, which will still be coherent with the first one, will rotate the neutron's spin for another angle of $\pi/2$ downwards, so the neutrons end up in the spin-down state. Application of the above sequence of AC pulses at the resonance frequency, $\omega_{rot} = \omega_z$, results in a final state with the minimum number of neutrons in the initial spin-up state.

If on the other hand $\omega_{rot} \neq \omega_z$, then an additional phase difference is accumulated over the storage time given by:

$$\phi = \phi_o + (\omega_{rot} - \omega_z)T_s \tag{2.7}$$

For such frequencies, the final state of the z-component of the spin vector ($\vec{s}$) depends strongly on the phase difference between $\vec{s}$ and the oscillating field B_{xy}. This is because when the relative angle between $\vec{s}$ and $\vec{B}_{xy}$ exceeds π, the second pulse rotates the spin back towards its initial direction (upwards). When it exceeds the value of 2π, the spin is rotated downwards, then for over 3π upwards and so on. The pattern we get for the number of neutrons in their initial spin state (spin-up in our case) is shown in Figure 2.2 where we can see their periodic dependance on the applied field frequency ν_{rot}. In the actual experiment, the number of neutrons in each spin state is counted at the end of the pulse sequence.

Near the resonance frequency, ν_o, the number of neutrons at either of the spin ori-

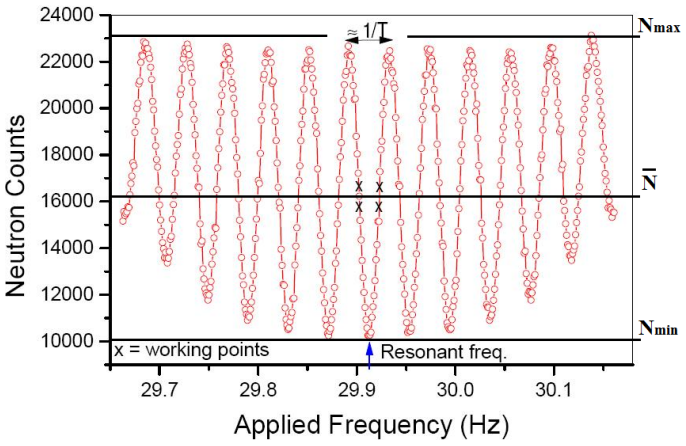

Figure 2.2: Neutron counts in the initial spin state as a function of the frequency ν_{rot} of the oscilating field B_{xy} (Ramsey resonance curve). This plot corresponds to a $B_z \approx 1\mu T$ and a resonance frequency close to 30 Hz. In the Cryo-nEDM experiment $B_z \approx 5$ μT and we expect the central fringe to be around 145 Hz. The maximum, the minimum and the average values of neutron counts are also highlighted.

entations (up ($N_\uparrow$) and down ($N_\downarrow$)) as a function of the applied frequency ν_{rot} is given by:

$$\bar{N}_{\uparrow\downarrow}(\nu_{xy}) = \bar{N}_{\uparrow\downarrow} \mp \alpha_{\uparrow\downarrow}\bar{N}_{\uparrow\downarrow}cos(\frac{\pi(\nu_{rot} - \nu_o)}{\Delta\nu_{rot}}) \tag{2.8}$$

where $\bar{N}_{\uparrow\downarrow}$ is the average number of neutrons at given spin state:

$$\bar{N}_{\uparrow\downarrow} = \frac{N_{\uparrow\downarrow\ Max} - N_{\uparrow\downarrow\ Min}}{2} \tag{2.9}$$

α represents the "visibility coefficient"of the fringes and is the product of the neutron polarisation and the analysing power of the polarisation detection scheme:

$$\alpha_{\uparrow\downarrow} = \frac{N_{\uparrow\downarrow\ Max} - N_{\uparrow\downarrow\ Min}}{N_{\uparrow\downarrow\ Max} + N_{\uparrow\downarrow\ Min}} \tag{2.10}$$

and $\Delta\nu_{rot}$ is the width of the central fringe at half height and depends on both the time for which the oscillating field is applied ($\Delta t = \Delta t_1 = \Delta t_2$) and the free precession time T_s:

$$\Delta\nu_{rot} = \frac{1}{2(T_s + 4\Delta t/\pi)} \approx \frac{1}{2T_s} \tag{2.11}$$

given that Δt and therefore $4\Delta t/\pi << T_s$.

Finally, for later use in this thesis, we have to refer to some of the usual magnetic resonance convention; this is to denote the characteristic time for decay of the any out-

of equilibrium component of the longitudinal magnetisation by spin-flips as T_1 and the corresponding time for the transverse component by T_2. Hence, T_1 describes the rate of energy loss by the spin system and T_2 the rate at which the individual spins dephase from one another. Hence, they also referred to as the spin-flip and spin-spin relaxation times [44].

2.1.2 Calculating d_n and Limitations imposed by the Uncertainty Principle

The separated-field resonance technique described above was developed by Norman Ramsey in 1949 [45] and is actually a modification of the original ideas of Isaac Rabi [46]. The Cryo-nEDM experiment utilises this technique to search for a shift in the neutron's precession frequency when an electric field is applied parallel (or anti-parallel) to a pre-existing $\vec{B}_z$ field. This should cause the Ramsey fringes to be shifted to higher or lower frequencies, depending on the polarity of the applied E-field. A measurement of this shift, together with the value of the applied electric field enables d_n to be found, at least in principle. In practice, the parameter that is actually measured is the neutron counts, N, from a given spin state. The formula used to calculate d_n is then:

$$\mid d_n \mid = \frac{[(N_{\uparrow\Uparrow} - N_{\downarrow\Uparrow}) - (N_{\uparrow\Downarrow} - N_{\downarrow\Downarrow})]\hbar}{2\alpha E T_s N_{total}} \tag{2.12}$$

where the single arrows indicate the spin state, the double arrows $\Uparrow$ and $\Downarrow$ represent the parallel and anti-parallel alignment of the $\vec{E}$ and $\vec{B}_z$ fields respectively, and N_{total} is the total number of neutrons over the two directions of the electric field. The "working points"of the Ramsey resonance curve are those where the largest change in neutron counts occurs when varying the frequency of the rotating field ν_{rot}. They are shown as the four points in Figure 2.2 in the middle of the central fringe. Counts are taken at only these four frequencies for both $\vec{E}$ orientations and a fitting procedure is used to determine the resonance frequency, ν_o.

Ignoring for the moment any systematic effects, the theoretical limits on the determination of the neutron edm is imposed by the Heisenberg Uncertainty Principle. We know that for only 1 neutron:

$$\Delta E \geq \frac{\hbar}{t} \tag{2.13}$$

while for N neutrons over a number of cycles, the uncertainty in energy is reduced such that:

$$\Delta E \geq \frac{\hbar}{t\sqrt{N}} \tag{2.14}$$

Given that $\Delta E \propto \vec{d_n} \cdot \vec{E}$ and setting $t \equiv T_s$ we obtain:

$$d_n \geq \frac{\hbar}{ET_s\sqrt{N_{total}}} \tag{2.15}$$

The experimental uncertainty, σ_n, in the determination of d_n is slightly different [47] [3] as it depends also on the visbility coefficient α:

$$\sigma_n \geq \frac{\hbar}{2\alpha ET_s\sqrt{N_{total}}} \tag{2.16}$$

The equation shows that in order to maximise the statistical sensitivity we need to maximise the elctric field $\vec{E}$, the storage (free precession) time T_s, the number density N_{total} and finally the visibility coefficient.

2.1.3 Systematic Uncertainties

Apart from the ultimate constraint on EDM sensitivity due to the Heisenberg principle, many systematic effects have to be taken into account in order to exclude the possibility of detecting a false EDM. The basic principles of some of these systematics are given in this section. A more detailed description and the analytical derivations and calculations can be found in [48] [49].

$\vec{v} \times \vec{E}$ Effect

Undoubtedly, the dominant systematic uncertainties come from this effect. While the neutrons are undergoing the Ramsey sequence, they move around within the storage cells and experience both electric and magnetic fields. The underlying physical principle of the so-called $\vec{v} \times \vec{E}$ effect has to do with the fact that the total magnetic field ($\vec{B'}$) seen by a moving particle within a background $\vec{B}$ and $\vec{E}$ fields is given by the Lorentz transformation of these two fields to the particle's reference frame:

$$\vec{B'} = \gamma(\frac{\vec{B} - \vec{v} \times \vec{E}}{c^2}) - \frac{\gamma^2}{c^2(\gamma + 1)}\vec{v} \cdot (\vec{v} \cdot \vec{B}) \tag{2.17}$$

For the case of slowly moving particles such as UCN, $\gamma = 1/\sqrt{1 - v^2/c^2} \approx 1$ and the first term dominates the result:

$$\vec{B'} = \vec{B} - \frac{\vec{v} \times \vec{E}}{c^2} \Rightarrow \delta B' = \frac{\vec{v} \times \vec{E}}{c^2} \tag{2.18}$$

The extra contribution to the B-field seen by the neutrons will result in a frequency shift ($\delta\nu \propto \delta B^{'}$) directly proportional to the applied electric field (since $\delta B^{'} \propto E$) and thus appear as a false edm signal.

1. First order $\vec{v} \times \vec{E}$ effect

   If the electric and magnetic fields are not perfectly aligned, then the cross product of $\vec{v} \times \vec{E}$ will produce a magnetic field with a non-zero component along the z-axis. This component will change the neutron's precession frequency and therefore induce a spurious EDM signal d_n^{sp}. The magnitude of this is given by:

$$\mid d_n^{sp} \mid = \frac{\mu_n}{c^2} v_\perp \epsilon E \tag{2.19}$$

   where ϵ is the fraction of $\vec{E}$ perpendicular to $\vec{B}$ and $v_\perp$ is the component of the neutrons' centre of mass (CoM) velocity (v_{CoM}) which is perpendicular to both $\vec{E}$ and $\vec{B}$. The first order effect occurs for both translation and rotation of the neutrons'CoM. The areas in the Cryo-nEDM experiment where the electric field is not exactly parallel to the magnetic field $\vec{B}_z$ are essentially close to the edge of the metal electrodes and near the insulating walls of the cylindrical resonance "Ramsey cells".

   One of the advantages of using UCN compared with other EDM experiments using beams of faster particles, is that the velocity of neutrons' CoM. is relatively small and their orbits are random minimising the first order $\vec{v} \times \vec{E}$ effect. Nevertheless, it is not negligible and can lead to a false EDM signal of about $(0.2 - 0.3) \cdot 10^{-28}\ e \cdot cm$ false signal.

2. Second Order $\vec{v} \times \vec{E}$ and Geometric Phase effects

   The combination of the $\vec{v} \times \vec{E}$ effect and of a non-zero axial gradient in the background field $\vec{B}_z$ can result in a rotating magnetic field in the neutron's reference frame. Writting Maxwell's second law ($\vec{\nabla} \cdot \vec{B} = 0$) in cylindrical coordinates we have:

$$\frac{1}{r}\frac{\partial (r B_r)}{\partial r} + \frac{1}{r}\frac{\partial B_\theta}{\partial \theta} + \frac{\partial B_z}{\partial z} = 0 \tag{2.20}$$

   If azimuthial symmetry holds, the second term vanishes and B_r can be written as:

$$B_r = (a\ r)\hat{r} \tag{2.21}$$

After a little maths, equation 2.20 leads to:

$$\vec{B}_r = -\frac{r}{2}\frac{\partial B_z}{\partial z}\hat{r} \tag{2.22}$$

Thus, a finite axial gradient in B_z creates a radial component B_r which always points to the centre of the cells. There are two extreme cases of neutron paths: The "straight path orbit "in which neutrons bounce and the so-called "garland orbit "where neutrons follow a polygonal path bouncing at very large angles of incidence. In most cases, however, the neutrons follow a path between the two extremes. Such a realistic orbit has been chosen in Figure 2.3 to explain the geometric phase effect.

We consider only those neutrons that move in the xy plane as the velocity component that is parallel to $\vec{E}$ does not contribute to this effect. Hence these neutrons "feel" the magnetic field from the cross product of $\vec{v} \times \vec{E}$ (denoted as B_v in the Figure) and the radial component, B_r, due to $\frac{\partial B_z}{\partial z} \neq 0$, both drawn in grey. The radial vector, $\vec{B}_r$, always points to the centre of the cell and its value is increasing as the neutrons move away from $r = 0$. Therefore, the total magnetic fields that neutrons finally experience in their rest frame are B_z along the z-axis and now two rotating fields in the xy plane: the one that we apply (B_{xy} with frequency ω_{xy}) and the vector sum of $\vec{B}_v$ and $\vec{B}_r$.

This effect clearly alters the acculmulated phase shift of the neutrons and during a Ramsey sequence can lead to a false EDM signal d_n^f. This has been calculated by Pendlebury et al [50] to be equal to:

$$\mid d_n^f \mid = -\frac{s\hbar}{2}\frac{\partial B_z}{\partial z}\frac{{v^2}_{xy}}{B_z c^2(1-(\omega_{cells}-\omega_z)^2)} \tag{2.23}$$

where s=1/2 is neutron spin quantum number and ω_{cells} is the weighted average of the angular velocity by which neutrons orbit the storage cells. It is quite clear that in order to minimise this spurious signal we have to keep the axial gradient as small as possible and have a relatively high B_z. For the Cryo-nEDM experiment, the aim is to keep this signal to about $1.7 \times 10^{-28}\ e \cdot cm$.

Leakage currents

These are currents flowing on the surface or through the material of the storage cells as a result of the applied large $\vec{E}$ field. We can distinguish between the cases of axial and azimuthial currents: Axial currents do not contribute to the background field along the

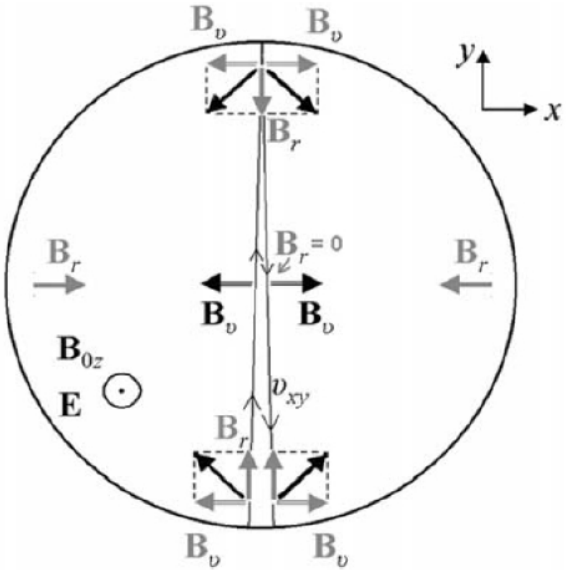

Figure 2.3: Geometric phase effect: the total magnetic field that neutrons experience on the xy plane is the Pythagoras sum of the radial field B_r (induced by the axial gradient $\frac{\partial B_z}{\partial z}$) and B_υ (induced by the $\vec{v} \times \vec{E}$ effect. This field rotates in neutron's reference frame changing its precession frequency and thus leading to a spurious EDM signal.

z-axis and therefore they do not lead to a spurious EDM signal. Azimuthial currents, on the other hand, can create a magnetic field component parallel $\vec{B}_z$ and therefore give a false EDM signal, d_n^{fz}, by changing neutron's precession frequency. The magnitude of this signal is:

$$\mid d_n^{fz} \mid \propto \frac{If}{rE} \tag{2.24}$$

where I is the current, f the fraction of the circumference of the storage bottle over which this current travels, r the radius of the bottle and E the magnitude of the electric field applied.

2.2 Overview of the experiment

The Cryo-nEDM experiment is situated at the Institute Laue-Langevin (ILL) in Grenoble, France, taking advantage of the most intense neutron beam in the world which provides 1.5×10^{15} neutrons per second per cm^2, at thermal power of 58.3 MW.

Figure 2.4 shows the overall layout of the experiment. "Cold" neutrons from the reactor, with energies between 0.1 meV < E < 10 meV, corresponding to wavelengths between 0.29 nm $< \lambda <$ 29 nm, are polarised just before entering the apparatus. These pass into the "Superthermal UCN Source" which is filled with superfluid ^{4}He at $\approx$ 0.5 K and they are

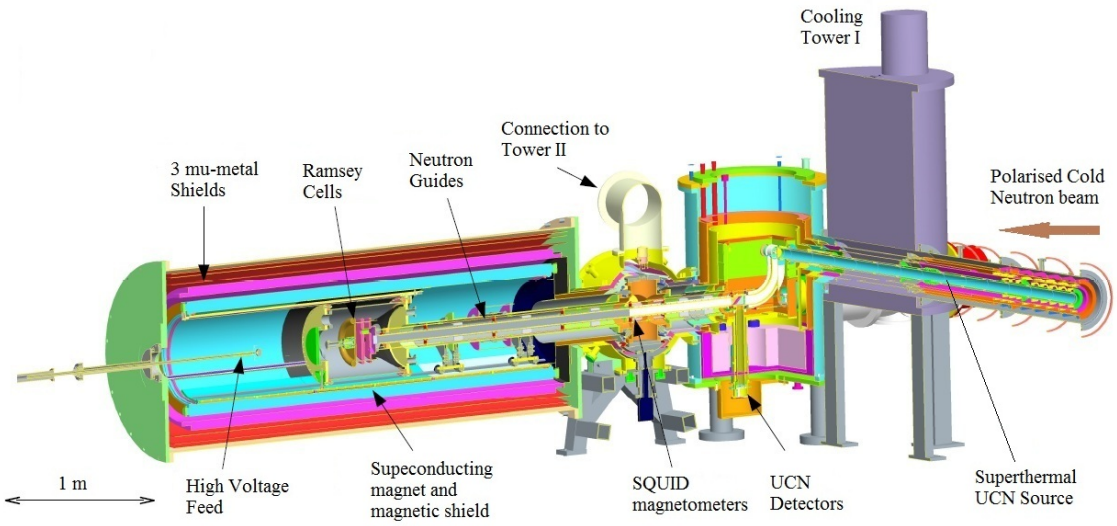

Figure 2.4: The main parts of the Cryo-nEDM experiment.

downscattered to UCN with energies E < 1 μeV (typically ≈ 100 neV) and wavelengths λ > 28.6 nm (typically $\lambda \approx 90$ nm), retaining their spin state. The UCN then move through the apparatus towards the Ramsey cell whilst always remaining in superfluid ^{4}He. Once in the Ramsey cell, they are stored and the magnetic resonance is performed. The stable and homogeneous B-field required for this is provided by the superconducting solenoid and magnetic shielding. The electric field in the Ramsey cell is provided via a high voltage feed from a power supply at room temperature. After the resonance has been carried out the Ramsey cell is open and the neutrons allowed to reach the spin-sensitive UCN detectors.

The cryogenic requirements are delivered through two cooling towers. Tower 1 contains a ^{3}He evaporator which cools the ^{4}He in which the UCN are produced and then remain until find detection. Tower 2 cools the magnet and the superconducting shields. A more detailed account how each of the different parts of the experiment functions is given in the sections below.

2.3 Cryoegenic Requirements

2.3.1 The Superfluid Volume

In order to produce and contain UCN in the apparatus we need to fill all the volumes in which the neutrons move, with superfluid ^{4}He below 0.7 K. The UCN remain within the source tube, several guide sections and the Ramsey Cell. These components are in turn inside various superfluid containment tubes and the large Superfluid Containment Vessel (SCV) which surrounds the Ramsey Cell. The whole superfluid volume is surrounded first

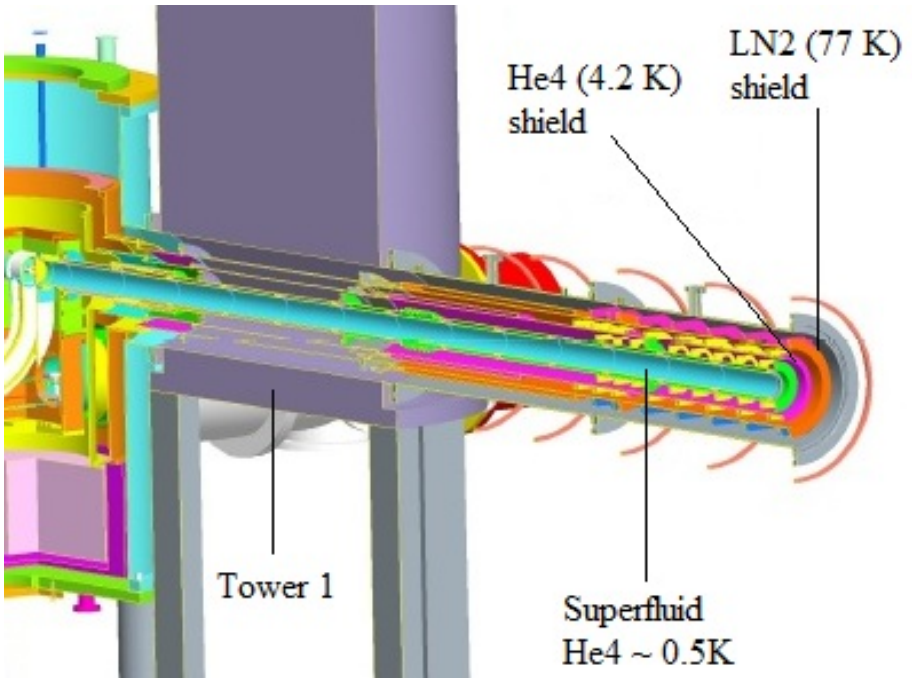

Figure 2.5: The Superthermal UCN Source Tube. The 0.5 K ^{4}He/He-II volume is shielded thermally by the 4.2 K Helium and the 77 K Liquid Nitrogen jackets.

by a ^{4}He tank or a shield at 4.2 K and then by a liquid nitrogen-cooled shield at 77 K. The arrangment around the source tube is shown in Figure 2.5.

The superfluid volume is initially evacuated and then left to cool radiatively. It is vital that the superfluid ^{4}He in which the UCN move is isotopically pure to a very high degree. ^{4}He is an ideal environment for polarised UCN having zero neutron absorption cross section and zero magnetic moment (as it has even number of protons and neutrons and its nuclear shells are full).

On the other hand, the ^{3}He nucleus, with one unpaired neutron in its shells, interacts strongly with neutrons either by absorption interactions or by coupling with their magnetic moment. Therefore, ^{3}He is a highly undesirable component to have and has to be removed. Commercial liquid helium contains the natural abundance of ^{3}He of about 1 part to 10^6 – 10^7 [51] and a purification process is needed.

In this experiment, this is done by using superleaks [52], a technique that takes advantage of the fact that the lambda point (i.e. the temperature where a liquid passes from fluid to superfluid phase) for ^{4}He is higher than that of ^{3}He. The superleaks are made from a very weakly porous material through which superfluid components can nevertheless pass relatively easily. They are situated on the bottom of a small container of ^{4}He (the 1K pot) inside the Tower 1, which is held at 1K by evaporative cooling. This temperature

is below lambda point of ^{4}He (λ = 2.17 K) and above the lambda point of ^{3}He (λ = 2.5 mK). The 1K pot is filled from the main Tower 1 ^{4}He bath containing commercial helium. In operation, superfluid ^{4}He passes from the 1K pot through the superleaks into the UCN-containing superfluid volumes, while the ^{3}He, on the other hand, together with all other impurities is blocked.

Removing all of impurities from the liquid helium is essential for the experiment. The presence of these will reduce the number density of neutrons with time, mainly through absorption and upscattering. Additionally, it is expected that any impurities in the ^{4}He will reduce the maximum electric field achievable in the Ramsey cell. There are many suggestions of mechanisms for how impurities actually initiate a breakdown in superfluid ^{4}He. A detailed review of these theories can be found in [53].

Once the whole superfluid volume is full of isotopically pure ^{4}He, its temperature is reduced to below $\sim$ 0.7 K. For this purpose, there is a copper ^{3}He container in thermal contact with the UCN tubes. The ^{3}He in this container is cooled by evaporative cooling.

2.3.2 Superconducting magnet and shield

Tower 2 is used to cool the Ni-Ti solenoid magnet and the Pb shield around the Ramsey Cells below their superconducting transition temperatures (T_s) of $\sim$9.1 K and $\sim$7.2 K, respectively. Both of these items are situated inside a 4.2 K liquid helium tank which in turn is shielded by super-insulation and a 77 K liquid nitrogen tank. The latter is also wrapped with super-insulation layer, see Figures 2.6 and 2.7.

2.4 Producing Polarised UCN

2.4.1 From Fast Fission Neutrons to Cold Neutrons

Neutrons produced in the ILL reactor, both prompt and delayed neutrons, are emitted with energies in the range of MeV. Such fast neutrons are travelling with velocities of $\sim$14,000 km/s per 1 MeV. These are thermalised by inelastic scattering via strong nuclear force with deuterium in heavy water (D_2O acts as both the moderator and the coolant for the ILL nuclear reactor at about 35 ^oC). These thermal neutrons have a most probable kinetic energy of 25 meV, corresponding to a velocity of 2.2 km/m and a Maxwell-Boltzmann (M-B) energy distribution given by the temperature of the moderator. Finally, the thermal neutrons encounter a polycrystalline beryllium block which removes neutrons above 4meV ($\lambda < 4.5$, v $>$ 880 m/s) for use in other experiments.

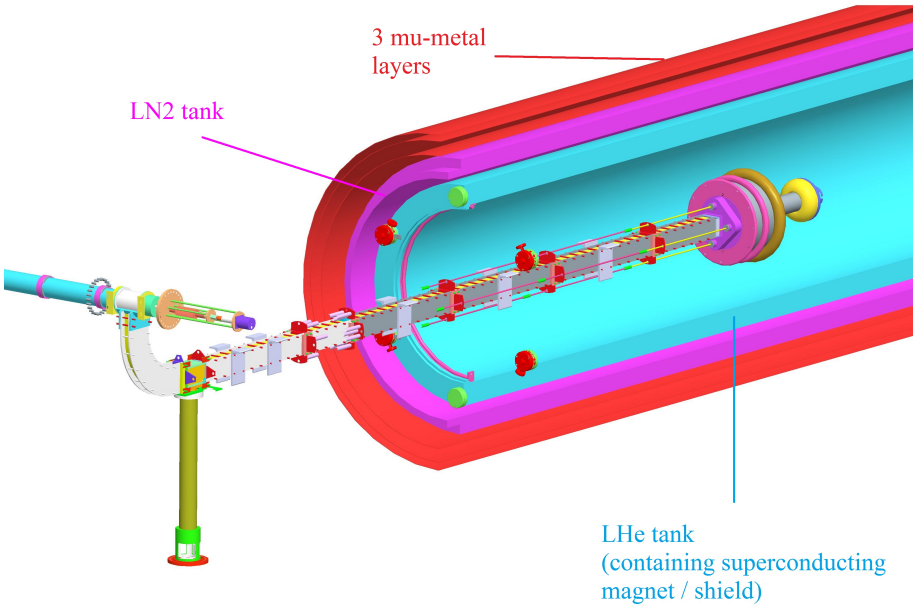

Figure 2.6: Model drawing of the thermal and magnetic shields positions.

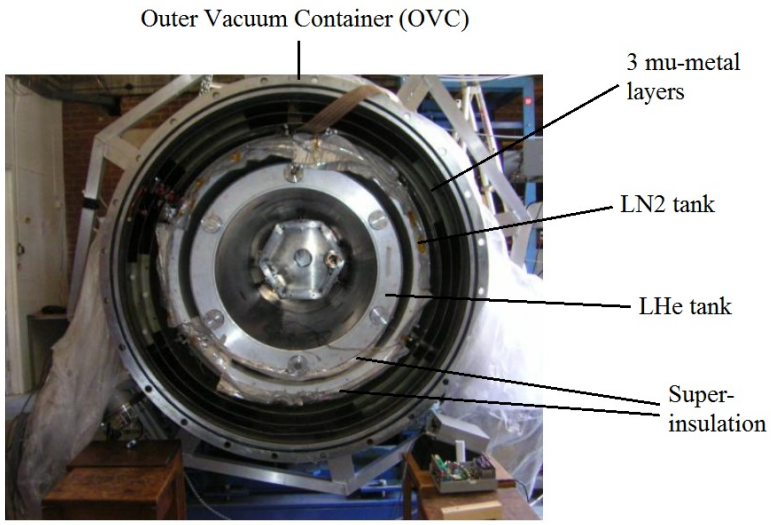

Figure 2.7: Picture showing the liquid Nitrogen, liquid Helium tanks and the 3 mu-metal cylinders all placed inside the Outer Vacuum Container (OVC). The gaps between the two tanks and the OVC are filled with super-insulation. The picture is taken from the high voltage end of the apparatus.

This leaves us with a cold neutron beam with energies below 4 meV. The low energy tail of this beam does contain some UCN, with energies up to a few hundred neV (and velocities up to $\sim$ 7 m/s) but their number density is too low for our purposes. Instead, we take advantage of the more abundant cold neutrons, polarise these and then convert them to UCN. The methods used to do these two things are described in the following sections.

2.4.2 Polarisation of Cold Neutrons

The spin dependence of the strong nuclear interaction is the key point in neutron polarising techniques. As will be explained in more detail in section 2.5.1, the potential barrier seen by a neutron that hits the surface of a magnetised material is given by:

$$V = \frac{2\pi\hbar^2}{m}\sum_i (N_i\alpha_i) - \vec{\mu}_n \cdot \vec{B} \tag{2.25}$$

where m is the mass of neutron, N_i is the number density of nuclei of the material which are associated with coherent scattering lengths α_i, μ_n is the magnetic moment of neutron and B the local magnetic field. The first term (known as the Fermi potential) describes the strong short range nuclear interaction of the neutrons with the individual nuclei of the material while the second one gives the magnetic interaction of the neutron magnetic moment with the local magnetic field B. The spin dependence of this potential barrier enters not only into the magnetic interaction term, but also into the first term as the coherent scattering length depends on the relative orientation of spins between the incident neutron and the "target" nucleus.

Hence, using a magnetisable material in a very strong magnetic field, the two spin states of neutron will see a significantly different potential barrier; a very high one for the spin direction antiparallel to the field and a very low one for the other alignment. In other words, cold neutrons with one polarisation direction are reflected and guided to the superthermal source, while those with the opposite spin alignment escape.

To explain this in a bit more detail, the neutrons' kinetic energy associated with the component of the velocity normal to the surface must be less than the potential energy V:

$$E_\perp = \frac{1}{2}m(v\ sin\vartheta)^2 < V \tag{2.26}$$

in order to be reflected by a material surface. Therefore for a given energy (or wavelength) range, their angle of incidence θ must be smaller than a critical value (θ_c) equal to:

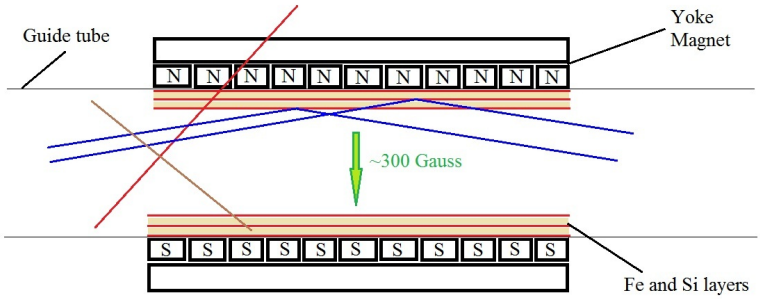

Figure 2.8: The polariser: only cold neutrons of one spin direction relative to the magnetisation of the Fe layers and with an angle of incidence smaller than the critical angle θ_c (blue lines) are reflected and guided to the superfluid source tube. Neutrons with the undesired spin direction or too large an angle of incidence will either escape (red line) or be absorbed (brown line) in the polariser.

$$sin\vartheta \leq \lambda(\frac{Na}{\pi} \pm \frac{m}{2\pi\hbar^2}\mu_n B)^{\frac{1}{2}} = sin\vartheta_c \tag{2.27}$$

where λ is the neutron wavelength.

The polariser of the Cryo-nEDM experiment (see Figure 2.8) is about 3 m long and made of successive layers of iron and silicon. The Fe layers are supposed to be magnetically saturated but in practice this might not be the case, limiting the polarisation efficiency of a single layer to about 90%. This leads to the need to have more Fe layers so that the neutrons will have more chances to be reflected. The Si layers between the Fe represent a potential well so essentially most of the neutrons just pass through (while some of them are absorbed). With this technique, the theoretical value of neutron polarisation at the exit of the polariser rises to about 95%.

2.4.3 Producing UCN in the Superthermal Source

Naively, a possible way to slow neutrons down to the desired level would be to put them in thermal equilibrium with a moderator sufficiently cold such that their M-B energy distribution would yield neutrons of low enough energies. There are many problems though with this idea; the moderator has to be placed near the reactor core so the heat input is large (directly or via gamma rays) requiring a high cooling power to achieve low enough temperatures. Additionally, the material used for this purpose has to be quite robust in terms of radiation damage from the reactor and also to have very small (ideally zero) neutron absorption cross section and a Fermi potential lower than of the walls enclosing

the moderator.

In the room temperature EDM experiment, the thermal (v $\sim$ 2.2 Km/s) neutrons leaving the moderator entered a vertical tube whose height was such that neutrons exited it with velocities of about only 50 m/sec, having converted kinetic into potential energy. Finally, these neutrons were decelerated down to the UCN energy range by collision with a neutron turbine whose, the blades of which receding at $\sim$25 m/s.

In 1975, Golub and Pendlebury [54], [2] proposed a technique for obtaining UCN densities higher by at least one order of magnitude than those achieved from neutrons at thermal equilibrium with a moderator. For this reason this method is known as "Superthermal UCN production". Their idea involves the down-scattering of cold neutrons with wavelength of λ=8.9 A by superfluid ^{4}He nuclei at 0.5 K to convert them to UCN [55].

This concept is linked to how a particle loses energy when it enters the superfluid; at low energies phonons are created while at higher values the local excitations are rotons [56] [57] [58]. This leads to the Feynman-Landau phonon-roton dispersion curve (energy of excitations versus the momentum of the liquid) shown in Figure 2.9. The linear part of this corresponds to phonon and the higher-**k** region to rotons. The dispersion relation for free neutron is shown on the same plot and this crosses the linear part of the superfluid curve at k=0.7 A^{-1}. Thus, neutrons with wavelength of $\lambda = 8.9$ ($\equiv k = 0.7A^{-1}$ or v $\sim$ 440 m/s) can interact with the superfluid ^{4}He by single phonon emission and be downscattered to become UCN.

Golub and Pendlebury noted three further features of ^{4}He which make it ideal as a medium for UCN; it has zero neutron absorption cross section; its critical energy for total reflection is about 10 times smaller than that of most of the common wall materials; Finally, since ^{4}He is a boson with zero magnetic moment, neutrons are scattered by it in a purely coherent manner and their initial polarisation is preserved

The single phonon process is the dominant one down-scattering cold neutrons to UCN but if any multi-phonon processes occur, they will only contribute positively to the UCN production rate.

The probability of having the inverse process – a single phonon from the superfluid ^{4}He to up-scatter UCN to higher energies – is proportional to the Boltzmann factor (–exp[-ΔE/T]) and in this case is highly suppressed as the excitation energy ΔE is much bigger than the temperature of the medium T; the excitation energy is the difference between the energies of the initial (UCN corresponding temperature $\sim$ mK) and final (12 K) energy

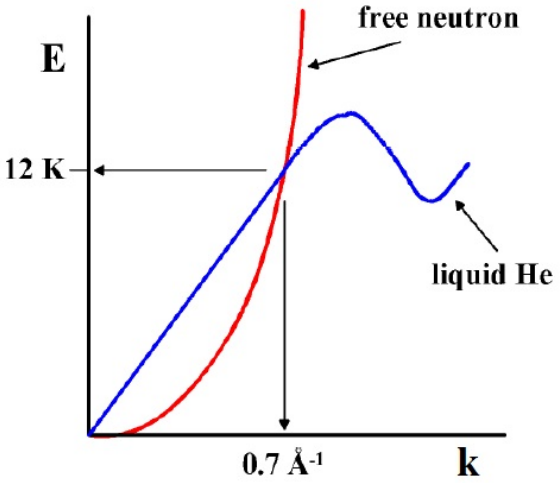

Figure 2.9: Dispersion curves for supefluid ^{4}He and free neutrons ($E = h^2k^2/2m$). Cold neutrons with $k = 0.7\ A^{-1}$ ($\lambda = 8.9\ A$, v$\sim 440m/s$) can be down-scattered to generate a single 12K phonon (figure from [2]).

states at which neutron has to be, so $\Delta E = (12 - 10^{-3})K \sim 12K$, while the He-II/$^4He$ temperature is $\sim$ 0.5 K. In other words, there are almost no 12 K phonons in the 0.5 K superfluid ^{4}He to transfer their momentum to UCNs and upscatter them to cold neutrons. The upscattering process begins to be noticeable when the superfluid ^{4}He is at about 0.7 K, therefore we have to make sure that we keep it below this temperature. A multi phonon inverse process is also proportional to the Boltzmann factor and its contribution is negligible too.

The wall material used for the Superthermal source tube is Beryllium coated copper. The low atomic number of ^{4}Be allows the more energetic (cold) neutrons to pass through while it traps the UCN. This is known as Be window. Finally, the free mean path of cold neutrons into the superfluid ^{4}He before they are down-scattered to UCN is about 10m. The length of the Superthermal source in the Cryo-nEDM experiment is about 3m, so about 70% of the incoming cold neutrons are lost from the downstream end of the source tube. At this point, there is a 90^o elbow so the cold neutrons leave the guides and absorbed by a lead brick shield provided for this reason.

2.5 UCN storage and transfer

The sensitivity of the Cryo-nEDM experiment is inversely proportional to the free precession time and to the number of neutrons. Both of these factors depend directly on the probability of neutron loss during storage and transport. In addition, the polarisation of

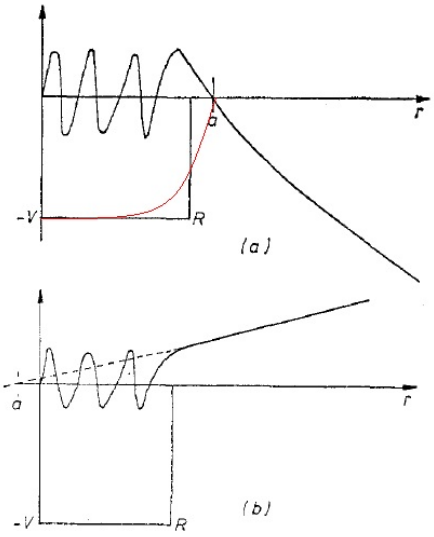

Figure 2.10: A strong nuclear potential square well and one with rounded corners (Fermi's approach) marked with red line. The neutron wavefunction is oscillating inside the well and for most of the cases it goes to zero for positive α (2.10 a). Figure 2.10 b shows the quite rare case for negative α.

neutrons should only change while undergoing the Ramsey resonance in the storage cells and not while they are moving in the guide tubes towards the cells or the detectors.

Essentially, for a given polarised UCN production rate, we are interested in preserving the number and polarisation of neutrons for as long as possible.

2.5.1 Neutron interaction with matter

The neutrons are expected to interact mainly with nuclei in and on the wall of the neutron guides, the cells etc, and with impurities within the liquid ^{4}He. Neutrons can be scattered or captured by the strong, short range, interaction or inelastically scattered by the thermal motion of these nuclei.

Neutron strong interactions

For the case of strong interactions, when a neutron approaches a nucleus, it sees a potential well at range of about R $\sim 10^{-15}$ m from which is scattered (see Figure 2.10).

Having a single scattering nucleus at the origin ($r_n = 0$), the total wavefunction (ψ) outside the well ($r > R$) is the incident wave ($e^{i\vec{k}\vec{r}}$) plus the scattered wave:

$$\psi = e^{i\vec{k}\vec{r}} + f(\theta)\frac{e^{i\vec{k}\vec{r}}}{r} \tag{2.28}$$

where f(θ) is the scattering amplitude, k the wavenumber of the neutron and r the distance from the scattering nucleus.

For ultra cold neutrons, the wavelength λ is much larger than the range of the nuclear force and hence they are only weakly scattered as s-waves. Thus, f(θ) has a constant value which was first set by [59] as:

$$f(\theta) = -\alpha \tag{2.29}$$

For kr << 1 (as holds for UCN):

$$\psi \simeq 1 - \frac{\alpha}{r} \tag{2.30}$$

Hence, α is the distance from the scattering nucleus where the total neutron wavefunction goes to zero and is termed the 'scattering length'. The value of α for a single nucleus is given by:

$$\alpha = R - \frac{tanKR}{K} \tag{2.31}$$

with:

$$K = \sqrt{\frac{2m \cdot (E + V_o)}{\hbar^2}} \tag{2.32}$$

where E is the neutron energy and V_o the depth of the potential well. As we can see from equation 2.31, α can take both positive and negative values. A more detailed approach of this can be found on [47] and [60]. The physical meaning of α is that its square is equal to the differential cross section per unit solid angle:

$$\frac{d\sigma}{d\Omega} = \alpha^2 \tag{2.33}$$

Fermi Potential

Because of the strength of the nuclear interaction, the resulting neutron wavefunction is very different from that in the absence of the attractive potential and perturbation theory cannot be used to describe it. Fermi [61] noticed that by introducing a pseudo potential for each of the scattering nuclei equal to:

$$V(\vec{r}_\iota) = \frac{2\pi}{m}\hbar^2 \alpha_\iota \delta^2(\vec{r}_\iota) \tag{2.34}$$

where m is the neutron mass, he could successfully describe the scattered wavefunction using the first order Born approximation. Equation 2.34 is known as the "Fermi potential" and by taking the volume average of it we find the effective potential that can be introduced into the Schrdinger equation:

$$V_{eff}(\vec{r}) = \frac{2\pi\hbar^2}{m}\sum_i N_i\alpha_i \tag{2.35}$$

Finally, by averaging the spin-dependant α_i over all theta (for the case that wall material is not magnetised) we get the "coherent scattering length α" and the effective potential becomes:

$$V_{eff} = \frac{2\pi\hbar^2}{m}N\alpha \tag{2.36}$$

where N is the scattering nuclei number density.

This potential presents an energy barrier to neutrons when they hit the surface of a material. Classically, if the neutron kinetic energy associated with its velocity component ($v_\perp$) perpendicular to the surface is $E_\perp < V_{eff}$, then the neutron will be reflected, while if $E_\perp > V_{eff}$ it will pass through. It is this potential barrier that we take advantage of to store or guide neutrons. The highest values of V_{eff} are around few hundred neV and thus cold neutrons, with energies between 50 μeV and 25 meV, will only be reflected at grazing incidence. UCN, on the other hand, can have energies comparable or less than the Fermi potential of selected materials. This means that they will be reflected at any angle of incidence and can thus be "bottled". Beryllium, with Fermi potential of 250 neV (corresponding to $v_{\perp(max)} \approx 6.89$ m/s), is a material of choice for this purpose. The UCN guides in the Cryo-nEDM experiment are Be-coated electrically polished copper.

Quantum mechanically, even for $E_\perp < V_{eff}$, there is an exponentially decaying wave that penetrates the classically forbidden potential barrier. The penetration length takes values between infinity for $E = V_{eff}$ to $\lambda_c/2\pi$ for $E = 0$, where λ_c is neutron wavelength with $E_\perp = V_{eff}$. The neutrons thus travel within some distance inside the wall material and can interact with the nuclei in two ways:

1. Absorption; a neutron is captured by a nucleus emitting a γ-photon. The cross-section for this interaction is inversely proportional to neutrons velocity: $\sigma_{abs} \propto 1/v$.

2. Inelastic scattering; Neutrons can, in principle, either lose or gain energy by hitting a (thermally) vibrating nucleus. For UCN however, whose energy is much lower than the wall temperature (0.5 K >> $\sim$ 2 mK), this process almost always leads to energy

gain (upscattering) by neutrons. In other words, the neutron gas tends to equilibrium at the wall temperature for which: $k_B T_{wall} >> V_{eff}$. Therefore, neutrons ultimately have total kinetic energy that exceeds the Fermi effective potential barrier and (at least for some angles of incident) penetrate the wall and are lost. The cross section for this interaction is again inverse proportional to neutron velocity: $\sigma_{inel.scatter} \propto 1/v$.

These two interactions are the main wall loss mechanisms for UCN. The effective potential that incorporates them is different from that given by equation 2.36 and becomes:

$$V'_{eff} = V_{eff} - iW = \frac{2\pi\hbar^2}{m} N(\alpha - i\alpha_{loss}) \tag{2.37}$$

where the imaginary effective potential W describes the loss mechanisms and $\alpha_{loss} = \frac{\sigma_{loss} k}{4\pi}$ with $\sigma_{loss} = \sigma_{abs} + \sigma_{inel.scater}$ to be the total cross section. The imaginary potential $W \propto \sigma_{loss} v$ is velocity independent as $\sigma_{loss} \propto 1/v$.

Practically, we are interested in knowing the wall loss probability which depends on the neutron energy (E) and the incident angle (θ):

$$\mu(E, \theta) = 2f \left(\frac{E\cos^2\theta}{V_{eff} - E\cos^2\theta} \right)^{1/2} \tag{2.38}$$

where f (the amplitude of the scattered neutron wave) is given by the ratio $f = \frac{W}{V_{eff}}$.

2.5.2 Neutron storage time and density

The combined effect of all the possible loss mechanisms leads to a storage time (τ) of neutrons in a container:

$$\frac{1}{\tau} = \frac{1}{\tau_{loss}} + \frac{1}{\tau_\beta} + \frac{1}{\tau_{leak}} + \frac{1}{\tau_{^3He\_abs}} + \frac{1}{\tau_{phon\_up}} \tag{2.39}$$

The contributing terms are:

1. $1/\tau_{loss}$ which is the rate of UCN loss on the wall material, including both absorption and inelastic (up) scattering. The first contribution can be minimised by limiting the hydrogen contamination, for example in the form of water molecules, as this element is one of the rare ones that have negative scattering length (α = - 3.7423 fm) plus it has a large neutron capture cross section. There is essentially nothing that can be done about the second contribution to the wall losses, as it is physically impossible to cool the apparatus down the UCN energy range ($\sim$ 2mK).

2. The $1/\tau_\beta$ term arises form the electroweak β-decay:

$$n \rightarrow p + \bar{e} + \bar{\nu}_e + 782\ keV$$

with half-life $\tau_\beta = 878.5 \pm 0.7(stat) \pm 0.3$ (syst) s. This lifetime of a free neutron defines the ultimate neutrons storage time limitation in any kind or size of container.

3. $1/\tau_{leak}$ describes the rate at which UCN can escape through holes and gaps in the guide tubes and the storage cells.

4. The UCN absorption in the superfluid ^{4}He due to ^{3}He contamination is included in the $1/\tau_{^3He\_abs}$ term. The UCN capture cross section by ^{3}He nuclei is $\sigma = 5 \cdot 10^6\ b$ when the spin vectors of the neutron and the ^{3}He nucleus are antiparallel (and $\sigma = 0$ for the case of aligned spins). Theoretically, the superleak technique used in the Cryo-nEDM experiment should keep the ^{3}He contamination down to 1 part to 10^{12}. This is two orders of magnitude less than the ^{3}He concentration that would make the neutron storage time comparable with the β-decay lifetime.

5. At 0.5 K the inverse process of UCN upscattering by a single or multiple phonons to cold neutrons is negligible. It becomes significant at temperatures of about 0.7 K and this is incorporated in the last term $1/\tau_{phon\_up}$.

The one term that has not been included above is that from neutron-neutron (n-n) interactions. These are very rare though, with the collision relaxation time to be about $\tau \sim 10^{19}$ s. Thus neutrons are considered to be moving like an ideal gas with no energy gains or losses due to n-n collisions (for which the cross section is about $\sigma \sim 34$ b).

The storage time (τ) of neutrons in a container of volume (V) yields the UCN density (ρ_{ucn}) for a given UCN production rate (Q_{ucn}) [54]:

$$\rho_{ucn} = \frac{\tau\ Q_{ucn}}{V} \tag{2.40}$$

where:

$$Q_{ucn} = V \int \varphi(E_{cold})\ \sum(E_{cold} \rightarrow E_{ucn})\ dE_{cold} \tag{2.41}$$

with $\varphi(E_{cold})$ the incoming flux of cold neutrons (of energy E_{cold}) and $\Sigma(E_{cold} \rightarrow E_{ucn})$ the macroscopic differential down-scattering cross section of cold neutrons to UCN.

2.5.3 Preserving Neutron Polarisation

The polarisation of neutrons after they exit the polariser must be preserved along their way to and from the storage cells until they reach the detectors. Their spin state should

only change while they undergo the Ramsey resonance and nowhere else, otherwise any alteration to the resonance frequency will be attributed to an electric dipole moment contribution leading to a false EDM signal.

In the absence of magnetic shielding, the magnetic field (B) seen by neutrons between the polariser and the entrance of the mu-metal shields (see Figure 2.4) should be relatively strong and not vary with time faster than the Larmor precession frequency (ω_L) in the local field. This leads to the adiabatic condition to be satisfied as:

$$\frac{1}{\tau} = |\frac{\partial B}{\partial t}|\frac{1}{B} << \gamma B = \omega_L \tag{2.42}$$

When the above expression holds, the transition probability for a spin-flip is $\approx 1/(\omega_L \tau)^2$. The time change of the magnetic field experienced by the neutrons depends on their velocity and the gradient of the field along their path (z):

$$|\frac{\partial B}{\partial t}| = |\frac{\partial B}{\partial z}\frac{\partial z}{\partial t}| = |\frac{\partial B}{\partial z}|\ v_{ucn} \tag{2.43}$$

Hence, for the cold neutrons (between the polariser and the superthermal source) we need a higher and smoother magnetic field than for UCN. To provide the required field configuration, a set of eight guide field coils is used spaced at intervals along the guides (see Figure 2.11, Table 2.1). The first four small coils, C1 to C4, and the last four bigger coils, C5 to C8, are in series. About 6 A for C1-C4 and about 20 A for C5-C8 provide an axial magnetic field component of about 8 Gauss on the central axis at the position of the coils. More on this on section 4.1.2.

Coil	Diameter [m]
c1, c2, c3, c4	$\varphi = 0.5$
c5	$\varphi = 0.6$
c6	$\varphi = 1$
c7, c8	$\varphi = 0.92$

Table 2.1: The diameter of the 8 guide field coils.

2.6 UCN manipulation in Ramsey Cells

The penultimate stage of the experimental sequence is the storage of the polarised UCNs in two cells for $T_s \approx 300$ sec to carry out the Ramsey resonance. The parts of the apparatus

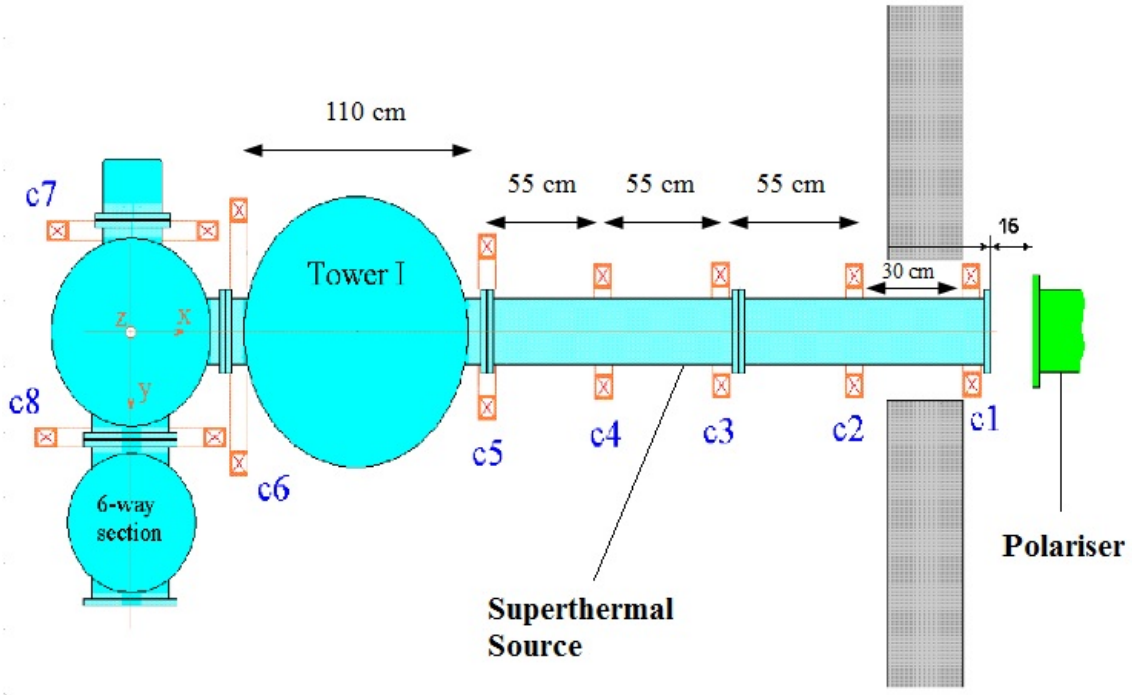

Figure 2.11: Guide field coil configuration.

related to this stage (see Figure 2.12) are called collectively the "Horizontal shields" or the "Yoshiki shields" because, apart from the removable parts (SCV/cells/high voltage supply), they were designed and constructed in Kure University in Japan by Professor H. Yoshiki. A more detailed description of these parts is given in the following sections.

2.6.1 The Ramsey Cells

The UCN are held in two Ramsey cells (Figure 2.13) that are formed by three beryllium electrodes separated by two beryllium oxide tubes. The electrode on the far end of the apparatus can be connected to a high voltage feed coming from a Spellman supply which can deliver up to 400 kV. The other two electrodes are grounded ($V = 0$). The two compartments are isolated by means of valves (see Figure 2.14). The cells sit at the centre of the Superfluid Containment Vessel (SCV).

2.6.2 The Main Static and the AC Magnetic Fields for Resonance

The Main Static Field

Ideally, as will be explained in more detail in Chapters 3 and 4, for the region of the Ramsey cells we require a spatially homogeneous and temporally stable magnetic field parallel to the symmetry axis (z) of the apparatus (B_z) with no radial (B_r) or azimuthial, (B_θ), components. The stored UCN will sample all parts of the Ramsey cells and hence,

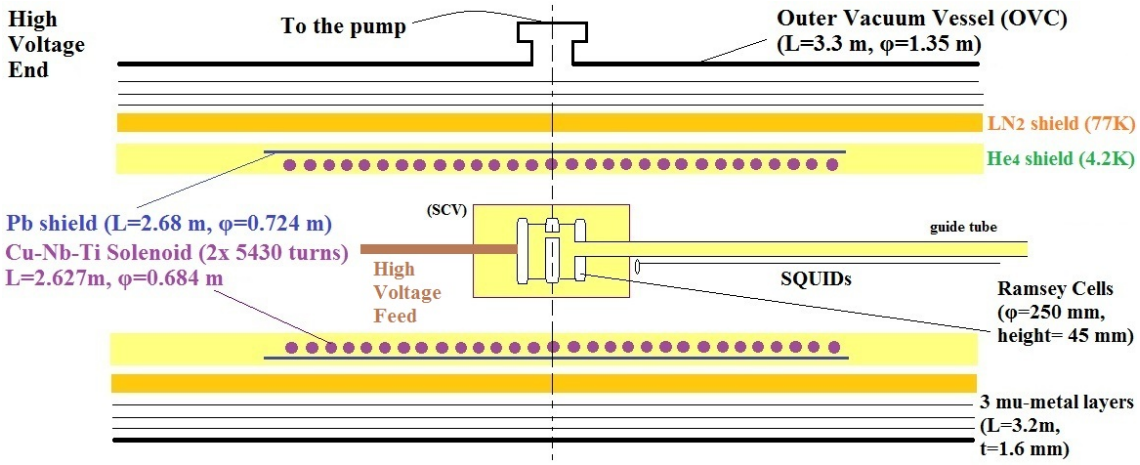

Figure 2.12: A depiction of the storage Ramsey cells at the end of the guide tube and the surrounding parts providing the necessary thermal, electric and magnetic environment to perform magnetic resonance on the trapped UCNs.

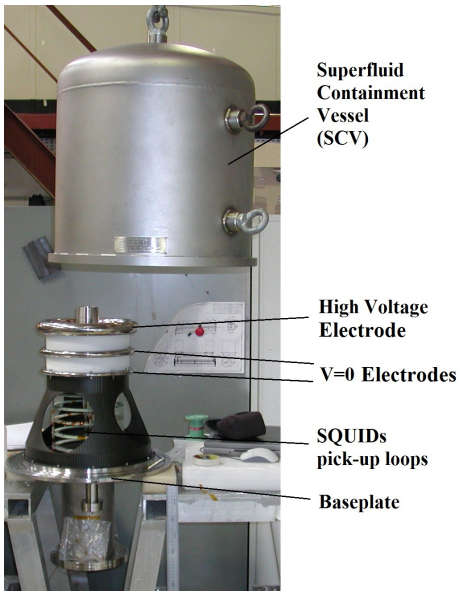

Figure 2.13: The Ramsey cells and the SCV; the top electrode is electrically connected to a high voltage feed while the other two are grounded. The cells are mounted on a carbon fibre former which, in turn, is connected to the baseplate. The whole set is here mounted vertically during assembly.

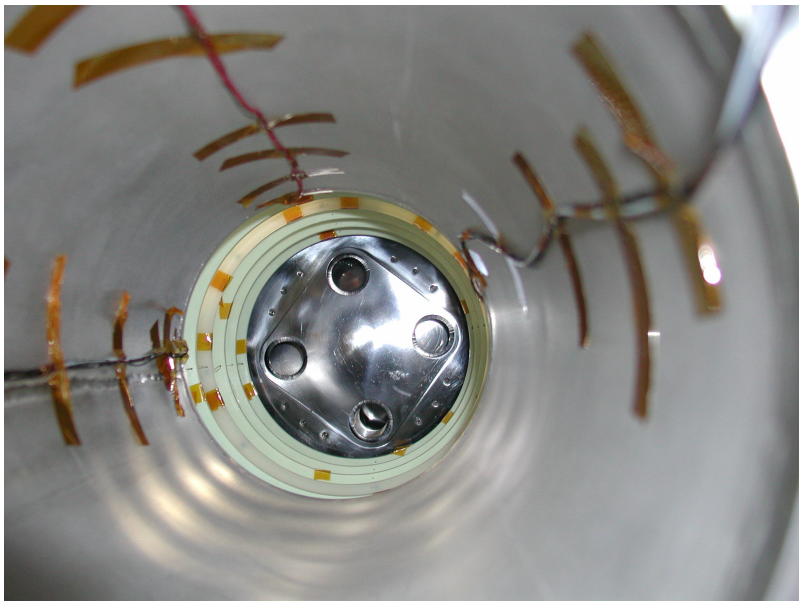

Figure 2.14: Picture of the valves on the first ground electrode.

any spatial inhomogeneities will result in different precession frequencies in different parts of the cells. This in turn leads to a dephasing of the neutrons during the free precession part of the Ramsey cycle, characterised by the transverse relaxation time, T_2. To maximise the sensitivity, we need, at the very least for $T_2 > T_s$, the achievable neutron storage time in the cells. In the cryoEDM experiment, with a design $T_s \approx 300$ s, and a 5 μT static field, the requirement is that $|\frac{\partial B_z}{\partial z}| \leq 0.83$ nT/m.

This requirement is met in several stages in our experiment. As shown in Figure 2.12, the basic field is provided by a horizontal 2.627 m superconducting solenoid of diameter 0.684 m and with 10,800 turns of 0.48 mm Nb-Ti wire wound uniformly in two equal layers. The solenoid has $T_c \approx 9.2$K, sits in an annular 4.2 K helium tank and is operated in the persistent mode at about 0.971 mA.

Unfortunately, the solenoid field alone does not meet the homogeneity requirement; the gradient at the extremes of the 2-compartment Ramsey cells and on axis is easily calculable ([3], p.63) to be equal to $|\frac{\partial B_z}{\partial z}| = 0.31$ nT/m. This number is even bigger for the case of 4-compartment cells and at points off the central axis. The first stage correction to the field is made by two "End Correction Coils" at the ends of the solenoid / LHe tank. These are made of 0.5 mm copper wire, are mounted on the inside surface of the tank and each is powered by separate power supply (see Table 2.2 for their details). Calculations by [3], p. 70 indicate that use of these should achieve the required homogeneity.

Measurements of the field profile made at Sussex in December 2004-January 2005 indicated a further departure from cylindrical symmetry, which was tentatively attributed

Trim Coil	N	z [m]	R [m]
6 Way-Section End	283 ± 3	1.43	0.305
High Voltage End	274 ± 3	1.40	0.305

Table 2.2: Characteristics of the two trim coils at the ends of the solenoid; We denote with N: the umber of turns, z: the distance from the centre of the OVC and R: the radius.

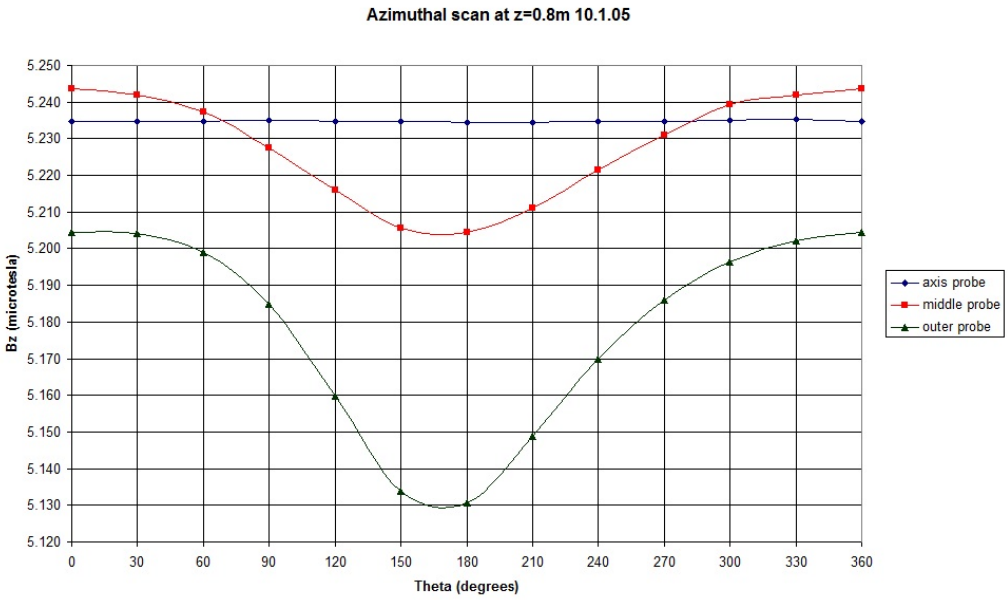

Figure 2.15: The azimuthial asymmetry (the so-called "gulls wing" anomaly) recorded during the magnetic scans held in Sussex was maximum at z=0.8 m from the centre of the OVC towards the HV end.

to a local variation in the number of turns per meter (see Figure 2.15).

To compensate for this second level inhomogeneity, a second set of nineteen "Compensation Coils" were added. These are mounted on a carbon fibre former (see Figure 2.16) which fits between the SCV and the inside of the YS LHe tank. Seven of these are dedicated for smoothing the axial gradient of the magnetic field (the "axial" coils), while the other twelve trim the azimuthial asymmetry of the field (the "azimuthial" coils). Each coil can be powered separately. More details about these coils are given on Chapter 5 while a full explanation of their construction and the fields produced at room temperature by this arrangement are given in [3].

Again as shown in Figure 2.12, the solenoid is closely surrounded by a multi-layer lead shield wrapped on the same former within the 4.2 K tank. The purpose of this shield, which has a Tc of 7.2 K is to provide dynamic shielding against external field

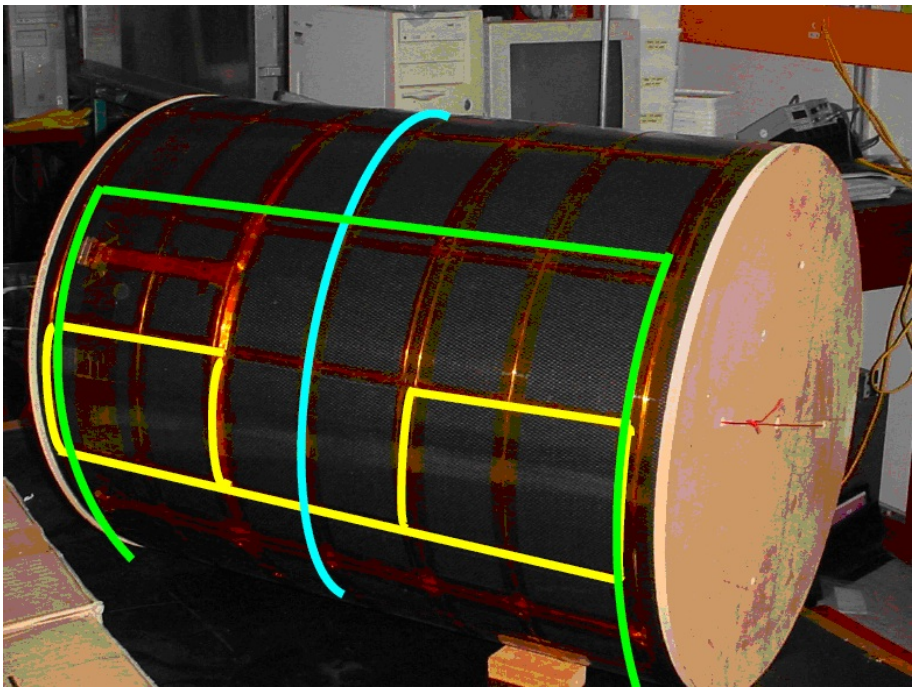

Figure 2.16: The 19 correction coils (7 axial coils, here only the middle one is shown by the blue line, and 12 azimuthial coils one of which shown by the yellow lines) and the 4 AC coils are wound on the carbon fibre former (one shown by the green line).

perturbations. The December 2004 measurements at Sussex also showed clearly that the degree of homogeneity achieved is affected strongly by the manner in which the shield / solenoid arrangement is cooled through the superconducting transition of the lead shield (see Figure 2.17). By first ensuring that the whole Pb shield and solenoid system is isothermal at ∼8K, with the solenoid fully persistent, and then cooling slowly through the Pb shield transition at 7K results in the best obtainable homogeneity.

Continuing problems with obtaining a superfluid-tight composite (and hence totally non-magnetic) SCV forced the Autumn 2010 cooldown to be carried out using a stainless steel SCV. This was known to have significant magnetic fields associated with it but nevertheless an attempt was made to mitigate against these by use of the 19 Compensation Coils. Although these were then being used to produce compensating gradient fields at least an order of magnitude greater than their design specification, this attempt was moderately successful. Full details of this are given in Chapter 4.

AC Field

The AC field is produced by two pairs of coils attached on the carbon fibre former as shown in Figure 2.16 and in more detail in Figure 2.18. For a 5 μT main static field, the resonance frequency is around 145 Hz. The strength of the oscillating field and the time

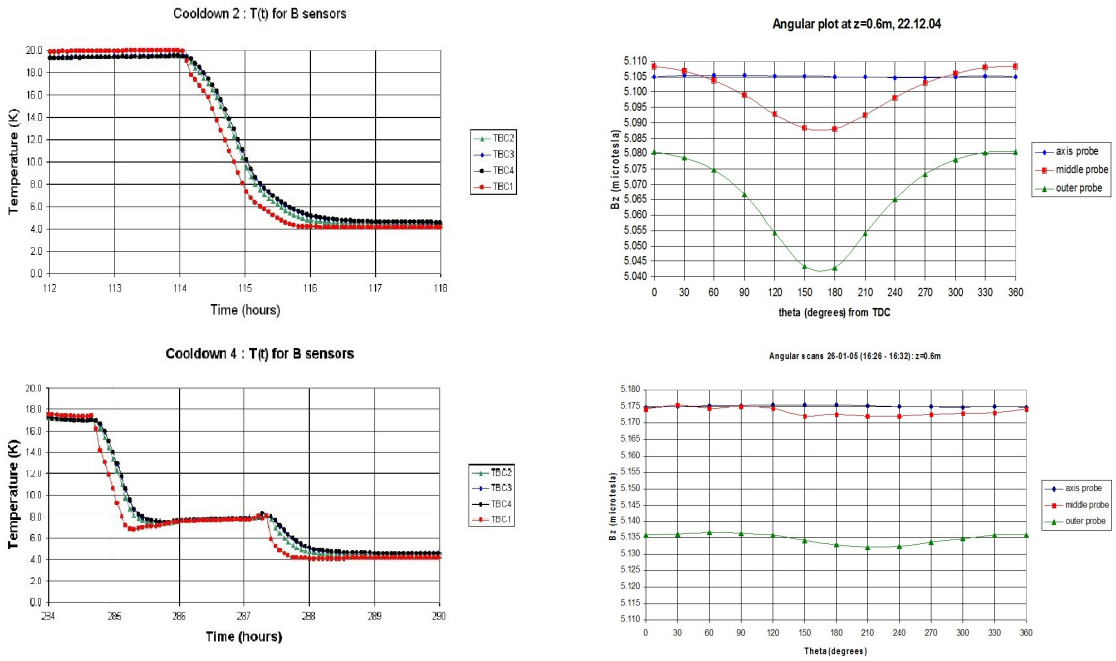

Figure 2.17: The effect of the cooling procedure on the magnetic field homogeneity. When slower, the cooling of the superconducting items is spatially uniform and results in the reduction of the "gulls wing" anomaly.

for which it must be applied to rotate the neutron spin by $\pi/2$ is given by:

$$B = \frac{\pi}{|\gamma|\ \tau} \tag{2.44}$$

Hence, for a $\tau = 2$ s pulse, the magnitude of the field must be B = 8.6 nT. Further details about the construction of these coils are given in [3], Chapter 7.

2.6.3 Temporal Stability of the Magnetic field and Dynamic Shielding

Any magnetic fluctuations during the free precession of neutrons in the cells will also result in some change in precession frequency. The aim is to keep these fluctuations down to a level that this shift is smaller than the expected shift due to the electric field coupling to an electric dipole moment. If the nEDM is of the order of 10^{-27} e·cm, the resonance frequency shift due to an electric field of, say, E = 400 kV across the electrodes will be about $\delta\nu \approx 86$ nHz. On the other hand, a variation of the magnetic field of δB = 0.1 pT in the Ramsey Cells, will lead to a frequency shift of $\delta\nu \approx 2.6$ μHz. Nontheless, the contribution of the random fluctuations of the ambient magnetic field during the data taking process, can be reduced by averaging over thousands of run cycles. Over 10^4 batch cycles, the frequency shift due the magnetic changes can be suppressed by a factor of 100.

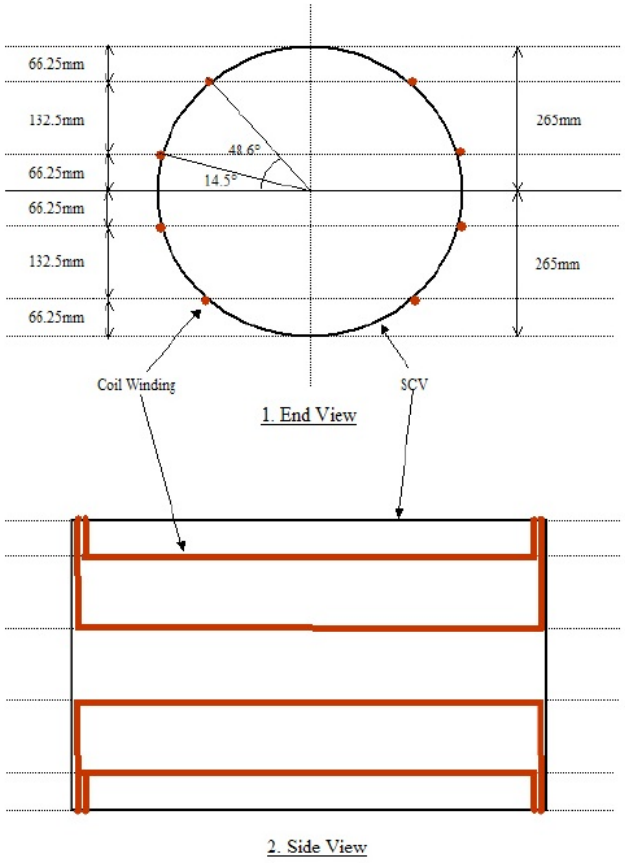

Figure 2.18: Geometric features of the AC field coils ([3], Figure 7.3).

Therefore, the variation of δB = 0.1 pT will change the resonance frequency by only 26 nHz, about a third of that due to the nEDM coupling with the applied electric field, and can be considered as the maximum variation we can tolerate within the Ramsey Cells.

The typical ambient magnetic field fluctuations in the ILL experimental area are of the order of 0.1-0.3 μT (mainly due to the IN15 experiment magnet, upstream in the neutron beam and about 50 m away). Hence, the Total Dynamic magnetic Shielding Factor (TDSF) we require is of the order of 10^6. Analytical calculations about this, can be found in the next Chapter.

Currently, the magnetic shielding provided by three mu-metal layers and a superconducting shield (see Figure 2.12) is some two orders of magnitude less due to their relative position. The reasons for this are discussed in Chapter 3. The resolution of this problem has been largely the experimental part of this thesis. A 12th scale model of the superconducting items of the apparatus has been built and tested in the lab to reproduce the existing DMSF. The idea of adding an extra superconducting shield ($\approx$1 m long) within the solenoid has been shown to work in order to restore the total SF back to the needed value of 10^6 and is discussed in detail again in Chapter 3.

Monitoring the magnetic environment is crucial. We need to know the approximate static field to know where to search for the resonance experimentally. For this purpose, there is a fluxgate (a Bartington Mag-01H / low temperature single axis magnetometer) on the baseplate of the SCV on the upstream side. The temporal stability of the magnetic environment is measured by the use of SQUID (Superconducting Quantum Interference Device) magnetometers, the most sensitive devices to date for detecting small (tens of fT) magnetic field fluctuations. Their pick-up loops (their detecting areas) are placed inside the SCV and just before the Ramsey cells on the upstream side.

2.7 The Detectors

2.7.1 Detectors setup

Over the Autumn 2010 run, there were six ORTEC detectors attached to the apparatus. These are solid-state silicon detectors with a 600 μg/cm^2 thick lithium fluoride (^{6}LiF) converter deposited on an aluminium layer on their top surface. Two of these, named the Tower 1 (T1) and Source Valve (SV) Monitor Detectors, due to their locations, were of $\sim$ 1 cm^2 surface area. These detected both cold and ultra cold neutrons coming through a 3mm diameter hole in the bottom of the Source Volume. The other four detectors, named

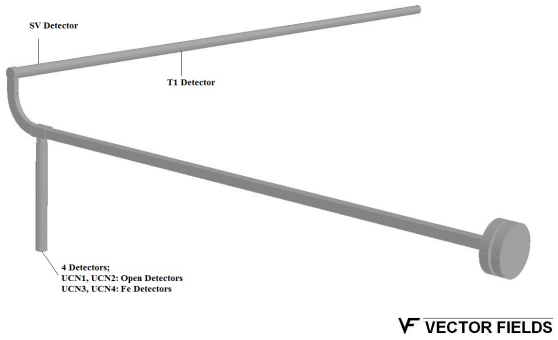

Figure 2.19: Detector positions along the neutron guides in the Autumn 2010 run. Tower 1 (T1) and Source Valve (SV) monitor detectors were attached on the UCN Source Volume looking at both Cold and Ultra Cold neutrons. The detectors UCN1-4 were mounted below the transfer section and looked solely at UCN. The first two of these, UCN1 and UCN2 (named Open Detectors), could detect neutrons of both spin states while the latter two, UCN3 and UCN4 (named Iron Detectors) could only detect the spin down neutrons (the incoming neutrons are considered as spin-up).

UCN 1 to 4, were of $\sim$35 cm^2 surface area and were placed on the bottom of a vertical tube mounted at the point where the 90^o Transfer Section connects to the Guide Tube (see Figures 2.19 and 2.20). The first two of these (UCN1 and UCN2) were intended to see UCN of both spin states while the latter two (UCN3 and UCN4) had a 1500 Å iron foil on top of the ^{6}LiF film. This was magnetised by a yoke magnet to allow the passage of only one spin direction neutrons (the one opposite to the initial spin state of the neutrons after they exit the polariser).

2.7.2 The Detection Chain

Alpha and triton particles are produced by neutron capture from ^{6}Li according to the following reaction:

$$n + {}^{6}_{3}Li \rightarrow \alpha\ (2.05\ MeV) + T\ (2.73\ MeV) \tag{2.45}$$

These pass into the detectors and produce voltage pulses whose amplitude is proportional to the energy that the particles deposit in the detectors. The pulses are fed to an amplifier and then sent along two parallel paths (see Figure 2.21);

a) Through an Analog to Digital Converter (ADC) to a Pulse Height (or Multi-Channel) Analyser (MCA); The MCA records the number of pulses between energy values that correspond to 0-10 Volts of the ADC output and sorts them by their height into 512

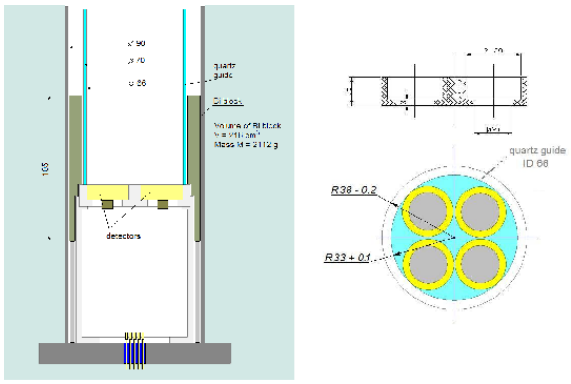

Figure 2.20: Drawing of UCN1-4 detectors (Balashov [4]), showing the dimensions of the detectors and the tube in which they are mounted. They are flush with a Teflon base and are surrounded by an inner quartz tube.

bins. The MCAs were activated over some period of time defined by the timer box which was controlled by the DAQ PC.

b) To a Multi-Channel Scaler (MCS); The MCS records the counts of pulses between the discriminator settings as a function of time and stores them into 1000 time intervals. The discriminator Lower (LL) and Upper Levels (UL) were established by visual inspection of the area of the triton peak for the different detectors.

It should be mentioned here that the amplification of all amplifiers was set manually (by turning a knob) at the same value in order to have the freedom to swap them between the different detectors.

Both MCA and MCS outputs were sent to and displayed on the DAQ PC. Finally, these are eventually securely stored on the minostux server at Sussex.

2.7.3 Ideal Pulse Height Spectrum

In Figure 2.22, after Baker et al. [5], the measured pulse height spectrum of the ORTEC detectors are shown for different thicknesses of ^{6}LiF converter. As the thickness of ^{6}LiF increases, the peaks become wider and move to lower energies. This is explained by the fact that the reaction products have to penetrate deeper layer and thus lose more energy before they are detected. In all cases, both peaks are well separated and above any background.

For the 600 $\mu g/cm^2$ case (Figure 2.22(b)), the alpha peak occurs at about half the energy of the triton peak. Furthermore, the resolution for the alpha peak is worse than that of triton. This is because the interaction length for α particles (1.5 $\mu g/cm^2$) is shorter than that of tritons (7.8 $\mu g/cm^2$) in ^{6}LiF, and they therefore interact and diffuse more before they reach the silicon of the detector. Ideally, this is the type of spectra we expect

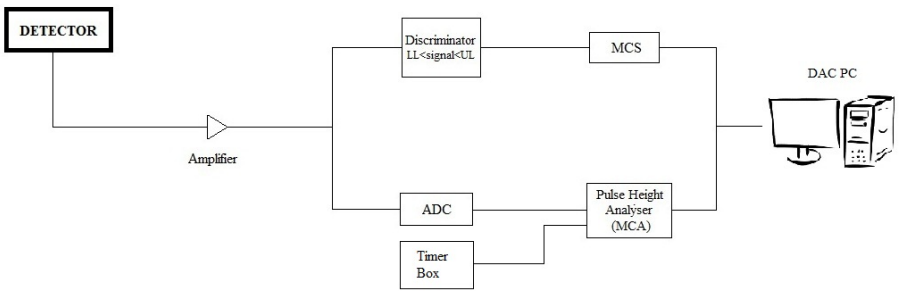

Figure 2.21: The detection chain; the voltage pulses from the detector were sent to an amplifier and then guided to a Multi-Channel (Pulse Height) Analyser (MCA) and a Multi-Channel Scaler (MCS). A timer box defines the period during which the MCA is activated and the discriminator settings defines the voltage (energy) range over which the MCS records the count rate. Finally, the DAQ PC collects the two outputs and stores them into the secure server provided.

from the detectors in the Cryo-nEDM experiment. The actual, rather different, spectra that were finally observed on the run # 160 in Autumn 2010 are given on Chapter 6 along with the polarisation analysis.

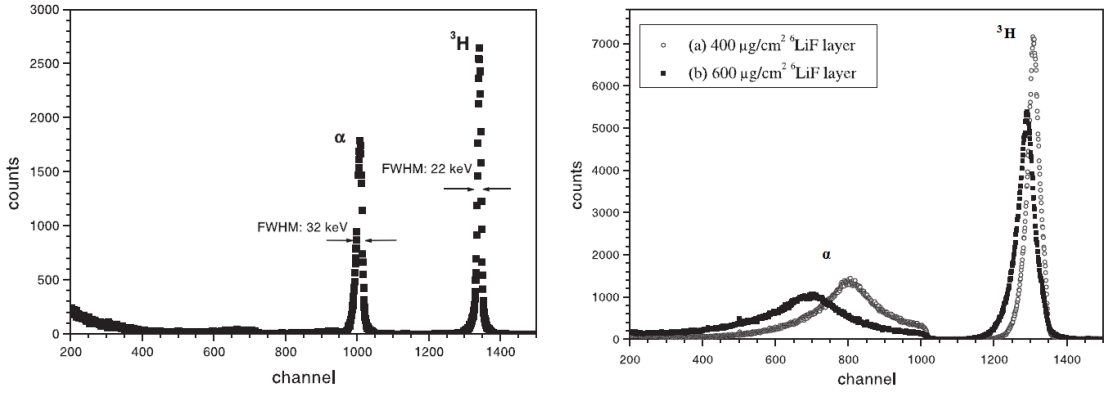

(a) 10 $\mu g/cm^2$ ^{6}LiF converter (b) 400 and 600 $\mu g/cm^2$ ^{6}LiF converter

Figure 2.22: Neutron-generated pulse height spectra from ORTEC silicon detectors with ^{6}LiF converter of different thicknesses [5]. The detectors used in Cryo-nEDM experiment have a 600 μg/cm^2 thick ^{6}LiF converter.

2.8 A Typical Operation Sequence of the Cryo-nEDM experiment

A typical experimental run consists of four steps;

1st. Fill the UCN Source Volume: The valve at the antrance of the Source Volume (termed as V1) opens to allow cold neutrons from the reactor to enter into the 2m long tube of 0.5 K He II where they are down-scattered to ultra cold neutrons as described in detail in section 2.4.3. The UCN are accumulated in the Source Volume whilst keeping the Source Valve (SV) closed at the end of the tube while the beryllium window is transparent only to higher energy neutrons. During this process, the valve placed after the SV and above the detector tube to control the neutron flux to the guides and the detectors (termed as Flap Valve, FV), can be either open or closed.

2nd. Fill the guide tube and the cells: SV and FV are open to release UCN from the Source Volume and let them diffuse to the guide tube and the cells. The detector volume is blocked by the FV which is set at its fully open (i.e. horizontal) position.

3rd. Store UCN in the cells and empty the guide tube: Cells valves are closed and the Ramsey technique is applied to the trapped neutrons. At the same time, the FV is closed (positioned vertically) in order to empty the guide tube by exposing the detectors tube to neutrons of this area.

4th. Detect UCN that exit the cells: We detect the UCN first from the zero E-field Cell, then from the High Voltage Cell. Keeping the FV vertical, we open the two cell valves at different times, so neutrons from each of them are consecutively dispersed to all the available volume up to the detectors where they are finally captured.

During a run, many valve operation sequencies are followed to extract different information such as neutron storage time on different sections of the apparatus, neutron total lifetime, depolarisation time etc. All the various combinations used on run #160 are given on Chapter 6. The above sequence, can be consider as the one for carrying a final EDM run.

Chapter 3

Temporal Stability of the Magnetic Field over the Ramsey Cells region

3.1 Introduction

According to the Hamiltonian for a neutron in a constant electric field E and a varying magnetic field ΔB:

$$h\delta\nu = 2\mu\Delta B \pm 2dE \tag{3.1}$$

the measurement of a genuine nEDM signal requires that the magnetic interaction term is smaller than the EDM term. Otherwise, any shift observed in the resonance curve will not be due to the EDM interaction with the applied electric field but primarily due to the interaction of the magnetic dipole moment with any magnetic fluctuations within the Ramsey cells during the storage time of neutrons.

In the present configuration of the Cryo-EDM apparatus, the attenuation of changes in the ambient magnetic field has been found to be about ≈ 500 less than that optimally required to achieve an experimental sensitivity of 10^{-27} e·cm. This (initially unexpected) reduction is due to the particular configuration of the superconducting shield and solenoid contained within the Horizontal Shields (HS). The reasons for this behaviour are given later in this chapter, together with a description of the measures taken up until now to mitigate the problem. A longer term solution to recover the shielding factor has been proposed which involves adding a further superconducting (SC) shield to the apparatus.

This chapter contains a detailed account of the construction and testing of a $1/12.5^{th}$

scale model of the SC parts of the HS to which an additional inner superconducting shield (ISS) was added. With this model we were first able to reproduce the previously measured shielding factors and then to show that incorporation of the ISS leads to an increase in shielding by a factor of at least 500.

We also present here calculations and simulations of the theoretically expected shielding factor and of the effects an ISS may have on the field homogeneity at the Ramsey Cells position. These confirm the measured increase in Shielding Factor (SF) and show that practically achievable implementations of a full-size ISS should meet our design criteria for the field homogeneity.

3.2 Dynamic Magnetic Shielding and Experimental Sensitivity

Assuming that we might have nEDM of the order of 10^{-27} e·cm and are able to apply 400kV across the 4.5 cm separated electrodes of the high voltage (HV) cell, the expected precession frequency shift is given by:

$$|\delta\nu|_{el} = \frac{4dE}{h} = \frac{4\ 10^{-27}(1.6\ 10^{-19}\ C)(0.01\ m)(400\ 10^3/0.045\ (V/m))}{6.62607\ 10^{-34}} = 0.086\ \mu Hz \quad (3.2)$$

Hence, the maximum magnetic field fluctuation we can tolerate can be found by equating the electric ($|\delta\nu|_{el}$) and magnetic ($|\delta\nu|_{mag}$) contributions to the frequency shift:

$$|\delta\nu|_{el} = |\delta\nu|_{mag} = \frac{2|\mu|\Delta B_{max}}{h} \Rightarrow \Delta B_{max} = \frac{|\delta\nu|_{el}\ h}{2\ |\mu|} =$$

$$= \frac{0.086\ 10^{-6}\ (Hz)\ 6.62607\ 10^{-34}\ (J\ s)}{2\ 9.66\ 10^{-27}\ (J/T)} = 3.3\ 10^{-15}\ T \Rightarrow$$

$$\Rightarrow \Delta B_{max} = 3.3\ fT \quad (3.3)$$

The typical change of the laboratory magnetic field in the experimental area at ILL is of the order of 0.03 μT. Nevertheless, there are two source of magnetic field disturbance above this level: the spin-echo spectrometer IN15 [62] that lies about 30 meters diagonally away from the horizontal shields and the movement of the crane above them. When the Cryo-nEDM experiment was designed, the IN15 field was not anticipated to be present. When the IN15 magnet is energised, the field changes between $\approx 0.1 - 0.35$ μT (Figure 3.1 shows a typical performance). The magnetic perturbation coming from the this magnet

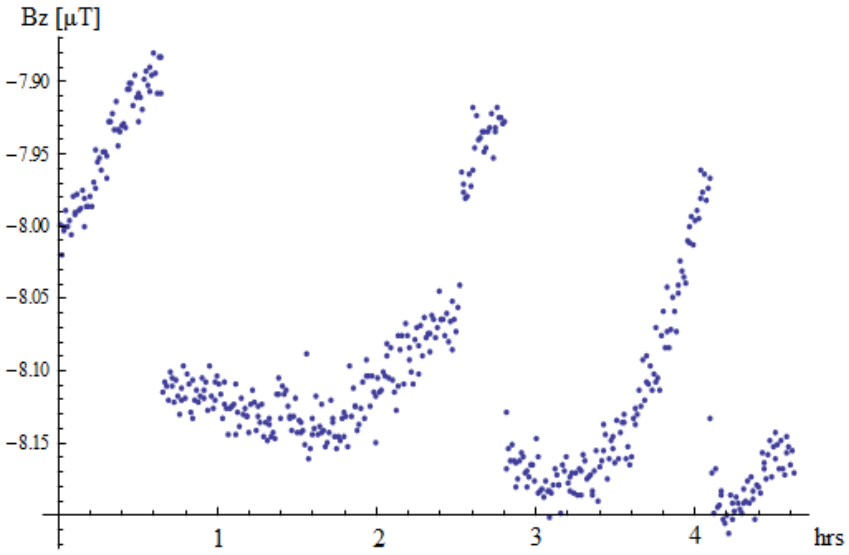

Figure 3.1: The horizontal component (from the 6WS towards the HV end) of the IN15 magnetic field change with time, as this was recorded from the fluxgate positioned ≈ 2 m above the OVC on 07/03/2010.

does not follow a normal distribution, therefore it can not be eliminated in a systematic way during the data analysis.

The data files when the IN15 is in operation should be excluded from our analysis. The same holds for the files when the crane is moving as the corresponding field change has been measured to be of the order of 0.2 μT. If this requirement is fulfilled, we need to reduce the magnetic noise by a factor of R_{MN} equal to:

$$R_{MN} \approx \frac{0.03\ \mu T}{3.3\ fT} \approx 10^7 \tag{3.4}$$

If we assume that any variation in the ambient B-field is effectively randomized by averaging over 10,000 batch cycles of (reversed E-field) EDM measurement we gain a factor of 100. The other five orders of magnitude for each batch cycle need to come from an adequate magnetic shielding of the Ramsey Cells against external magnetic fluctuations:

$$TDSF = \frac{\Delta B_{ext}}{\Delta B_{RC}} \approx 10^5 \tag{3.5}$$

The above ratio is defined as the Total Dynamic magnetic Shielding Factor (TDSF) with ΔB_{ext} the change in the laboratory field (theoretically at the position of the Ramsey cells but without the mu-metal and SC shields in place) and ΔB_{RC} to be the corresponding change at the centre of the Ramsey cells in the presence of the magnetic shielding. It is important to note here that if the TDSF is increased to 10^6 then:

(a) The sensitivity of the experiment is increased by one order of magnitude (to 10^{-28} e·cm) if we keep the applied electric field across the cells at 400 kV.

(b) We achieve the same sensitivity (10^{-27} e·cm) by applying only 40 kV across the RCs.

The three parts of the apparatus that contribute to the magnetic shielding of the Ramsey cells and part of the neutron guides are:

1. The three cylindrical μ-metal shields, end caps and noses, which are situated inside the vacuum between the liquid nitrogen tank and the OVC, as shown in Figure 2.13. The field changes at the centre of these shields is a factor of 50 less than the external fluctuations. However, as we shall see later, the more important factor is the attenuation at the entrance to the HS which is important. This means that the effective SF for the μ-metal is $\approx$12.

2. The superconducting parts around the Ramsey cells consisting of the Pb shield and the Nb-Ti solenoid. At low temperatures ($T<7K$), the combination of these two parts contribute to the total magnetic shielding and for this reason the SF associated with them is termed as "Cryogenic" SF. The Cryogenic Shielding Factor (CSF) of the Pb shield alone should be $+5 \times 10^5$ but the value for the combination is -175.

3. A pair of active compensation coils. These coils are placed around the ends of the OVC and are designed to compensate for temporal changes of the magnetic field along the central axis. The magnetic fluctuations are measured by three fluxgates at the centre of each OVC flanges and the average value defines the current in these coils via a feedback circuit. They can compensate field changes up to maximum frequency of 50 Hz and of magnitude up to several hundered μT. These coils were added to mitigate the reduced shielding factor but their use in a edm measurement could possibly lead to a systematic error or even a false edm signal. They are hence seen as a temporary measure. They are designed to give a SF of 10.

The TDSF defined above refers to the axial magnetic shielding and is given by the product of the individual shielding factors (SF) produced by each of these three items:

TDSF = SF(Mu metal) x SF(SC Pb Shield/Solenoid) [x SF(Active Compensation Coils)]

So instead of having a TDSF $= 50 \times 5 \cdot 10^5 = 2.5 \cdot 10^7$, without having to use the compensation coils, we currently have a shielding factor of $12 \times 175 \times 10 = 2.1 \cdot 10^4$ with them. This is a factor of $\approx$50 below our design requirement of 10^6 and it becomes $\approx$500

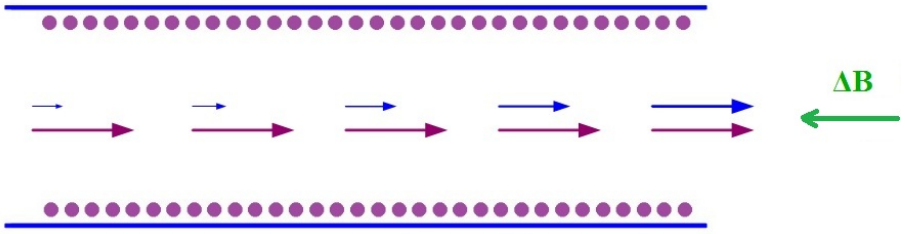

Figure 3.2: The response of the superconducting Pb shield (blue arrows) and Solenoid (purple arrows) to an external magnetic perturbation (green arrow).

without the use of the two compensation coils. Although the present CSF is very low, it is expected to lead to the almost identical variation in both Ramsey Cells. Hence, by comparing the frequency shifts from the HV and neutral cells the loss of SF can be mitigated further.

3.3 Improving the Cryogenic Shielding Factor (CSF)

3.3.1 Physical Explanation of the currently low CSF

In the cryo-nEDM experiment, described in Chapter 2, the solenoid that provides the static field of 5 μT lies inside the Pb shield. When a magnetic perturbation occurs at one end of this pair of superconducting items, circumferential screening currents are generated in the Pb shield, the current density of which decreases with distance from the end of the shield. The resulting magnetic field from these currents counteract the direct change at the centre of the Pb tube (see Figure 3.2 / blue arrows) and the axial Shielding Factor at the central area of the Pb tube alone is expected to be about $5{\cdot}10^5$ [3].

On the other hand, the response of the persistent-mode SC solenoid when magnetic flux is applied at its ends (see Figure 3.3) consists of a single-valued screening current, independent of the distance from the perturbation source, with the magnitude needed to cancel the total incoming flux across its cross sectional area. The resulting field in this case overcompensates the direct change in the central area (see Figure 3.2 / purple arrows) and the total SF drops from $5{\cdot}10^5$ to about -175, with the overcompensation reflected in the minus sign.

The case would be radically different if the solenoid were wound on the outside of the Pb shield. Then any imposed field from the solenoid would be screened by the shield and the SF would not be reduced. The strongest evidence for the validity of this hypothesis emerges from the different CSFs at the two ends of the shield/solenoid, where the Pb

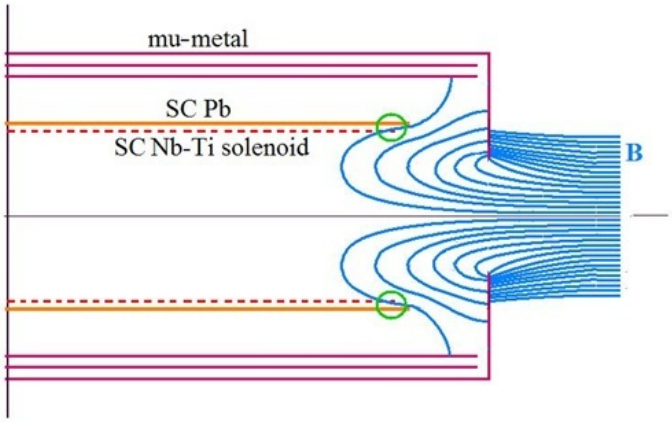

Figure 3.3: The flux from a perturbing magnetic field passes through the mu-metal end cap and penetrates a small distance inside the Pb cylindrical shield. Its interaction with the ends of the solenoid results in the reduction of the cryogenic SF by about three orders of magnitude [6].

shield projects by different lengths. As measured at Sussex in 2004/05 [6], the CSF at the high voltage (HV) end, where the Pb shield projects by 44 mm, is -440 ± 80 while a smaller CSF of -110 ± 17 is found for the six way section (6WS) end where the Pb shield projects by only 10 mm. These values were obtained in two separate ways; a) by changing the magnetic field with a coil placed 10 cm away from the end of the Pb shield but inside the mu-metal cylinders and b) by changing the overall external field with a perturbing source outside the mu-metal shields. The first is a direct way to obtain the CSF while in the latter case the contribution of the mu-metal shielding had to be taken into account. The fact that the worst CSF corresponds to the end where the solenoid ends are more exposed to external magnetic flux confirms the argument that the problem of the reduced SF stems from the relative position of the solenoid with respect to the Pb shield. It is worth pointing out that the problem with the persistent mode solenoid could be eliminated by not running it in this mode but by driving it from a constant current source. However, there are practical problems with this solution because modifications to the superconducting switches would involve cutting open the (welded) annular 4K tank containing the Pb shield and solenoid. In addition, the stability of the constant current sources would then become the dominant problem.

Analytical calculations of the response of the SC items were done by [3] using a series of consecutive current loops representing the effect of the Pb SC cylinder and with a single current in the solenoid. The values of these currents were defined by the physical principle that the flux through the cross sectional area of all the loops should not be changed by

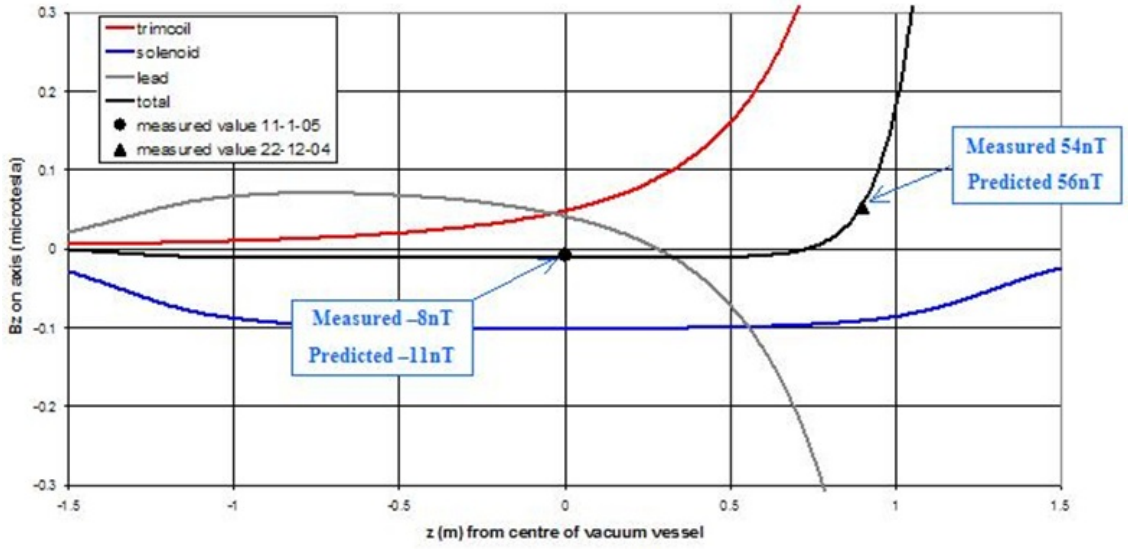

Figure 3.4: Theoretical predictions of the response of the SC Pb shield/solenoid to a 10 mA perturbation from the high voltage end trim coil. The symbols are for two positions for which experimental data were available as well. At z=0.75 m, the CSF becomes infinite.

the perturbing incoming flux. The results of these calculations, plus two experimental points taken by using the high voltage end trim coil at currents between 0 and 10 mA are shown in Figure 3.4. The interesting feature of these plots is that the CSF has a finite negative value at the centre of the solenoid and is gradually increasing up to 0.75 m from the centre where it becomes effectively infinite and then changes sign. A similar response was expected and found at the other end of the shields.

3.3.2 Adding an Inner Superconducting Shield (ISS) to mitigate the low CSF

One initial idea to restore the CSF was to add extra Pb "caps" at each end of the Pb cylinder and the solenoid in order to screen the solenoid ends from any perturbing field. A solution that seems to be easier to implement is to add an extra superconducting cylindrical shield inside the Pb shield/solenoid (see Figure 3.5). In this way, the perturbation propagated through the solenoid response induces circumferential currents into the Inner Superconducting Shield (ISS) where the current density now decreases with the distance from the solenoid ends. This is expected to improve the CSF.

From the basic physics point of view, this seemed a viable solution but it needed to be tested experimentally to confirm the expected enhancement of the CSF. For this reason, a $1/12.5^{th}$ scale model of the superconducting Pb/solenoid was built at Sussex and tested

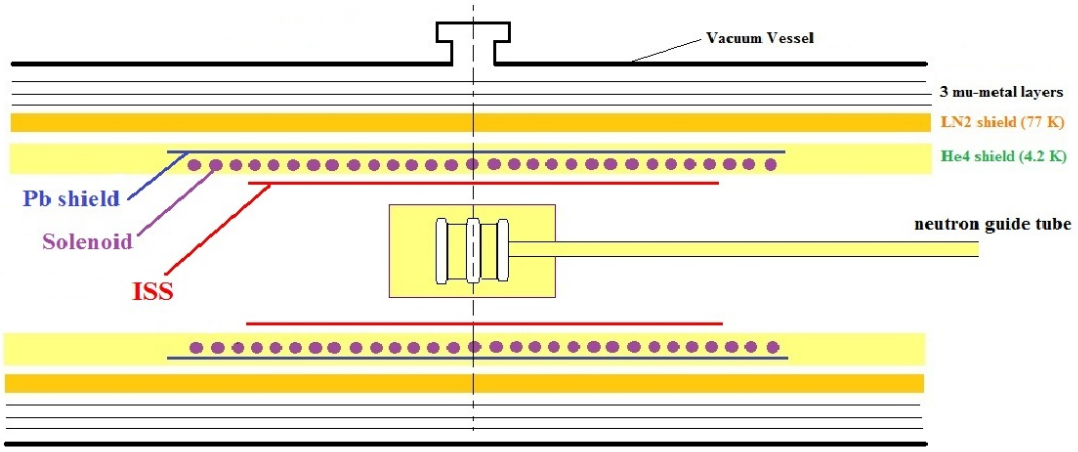

Figure 3.5: The addition of an Inner Superconducting Shield (ISS) inside the Pb shield/Solenoid combination is expected to restore the CSF to the required level.

on the basis that superconducting finite tubes with the same length/diameter (L/D) ratio must give the same SF at their central area according to the equation [63]:

$$SF = 0.5\ e^{3.83\ L/D} \tag{3.6}$$

In addition, since we are not only interested on the temporal stability of the magnetic field in the Ramsey cells but also on its spatial homogeneity, we had to investigate how this latter is affected by the geometric features of the ISS. To do this, both analytical calculations and magnetostatic simulations using the Quick Field program were done and are presented in the following sections.

3.4 Testing the ISS using a 12.5-th Scale Model of the SC Items of the Experimental Apparatus

3.4.1 Experimental Set-up

The heart of the experimental set-up consists of a $\approx 1/12.5^{th}$ scale model of the full-size superconducting Pb shield/solenoid in the Cryo-nEDM experiment, with an additional Inner Superconducting Shield (ISS). The model was thermally clamped to the cold stage of a cryocooler, protected from thermal radiation by a high purity aluminium radiation shield attached to the first stage of the cryocooler and placed in a vacuum chamber (see Figures 3.6 and 3.7). A rotary and a turbo pump were used to provide an adequate vacuum ($\approx 10^{-5}$ torr) before the cool-down procedure.

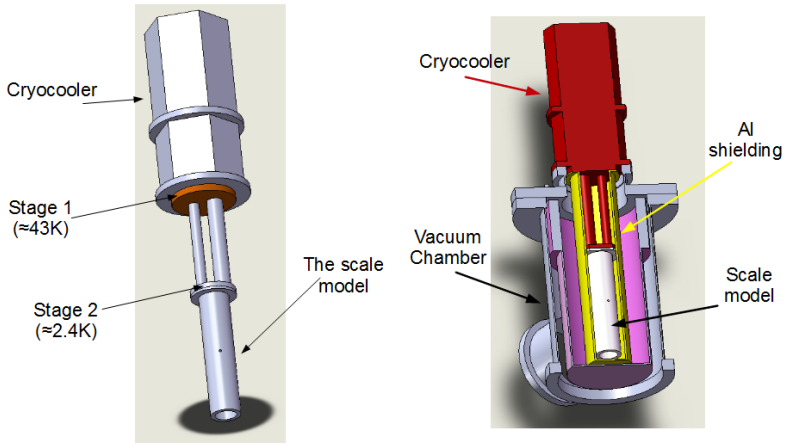

Figure 3.6: SolidWorks models of the Cryocooler with the $1/12^{th}$ scale model attached to the second stage at ≈2.4 K (left) and the Cryocooler with the high purity Aluminium radiation shield attached to the first stage inserted into the vacuum chamber (right).

The magnetic field outside the superconducting items could be changed by the use of two separate pairs of coils; a pair of thick high-current coils, attached on the outside surfaces of the top and the bottom flanges of the vacuum chamber and a pair of coils attached to the aluminium radiation shield inside the chamber. The temperature was recorded at both the top and the bottom of the scale model by the use of diodes. Finally, the changes in the magnetic field in the centre of the ISS were measured by a fluxgate magnetometer placed at the centre of the model.

In the following paragraphs, all these parts are described in more detail, accompanied by photos and drawings.

3.4.2 Pb shield/Solenoid

Initially, a cylindrical dural (an aluminium alloy of type Al 93.5/Cu 4.4/Mg 1.5/Mn 0.6) former was built to accommodate a $1/12.5^{\text{th}}$ scale model of just the Pb shield to reproduce the expected SF for a single superconducting shield of $5{\cdot}10^5$. A lead foil of 99.99% purity and 125 μm thickness was wrapped around the former and its longitudinal edges were soldered together and folded over to ensure electrical contact (see Figure 3.8 right).

A second dural former of the same dimensions but with its surface threaded to accommodate a "persistent mode solenoid" was made. After covering the thread with PTFE tape, a single layer of thin electronics solder was wound in the groove over the whole length of the former and the two ends were then brought together and joined by a solder blob (see Figure 3.8 left). The superconducting transition temperature of solder is $\approx 6.9K$, less

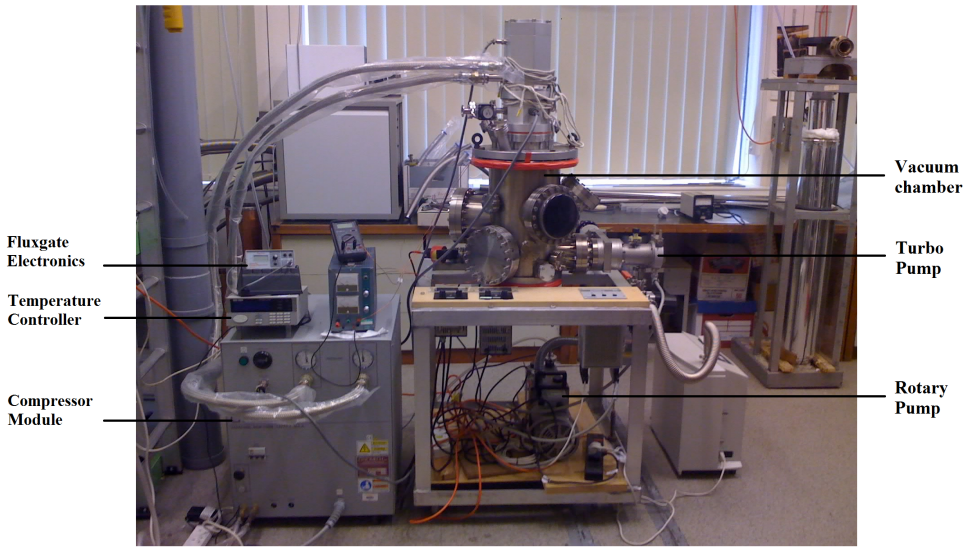

Figure 3.7: The apparatus used to measure the CSF improvement using an ISS.

than that of the Nb-Ti wire used in the actual apparatus ($\approx 9.3K$), but very close to that of lead ($\approx 7.2\ K$). The order by which the two items go superconducting does not affect the SF data quality so we proceeded with this setup. The solenoid was then covered with a 125 μm Pb foil soldered to form a cylinder. Considerable care was taken to ensure that the lengths and the end overlaps of the model shield and solenoid mimicked those in the full-size experiment (see Figure 3.9). Due to the relatively large pitch of the thread on the inner former ($\approx$ 1.5 mm), the ratios between the overlaps in the model and those in the full-size apparatus could not be made closer to the desired value of 12.5 than those shown in Table 3.4.2. Nontheless, the overlap on the 'HV'end was kept larger than the one on the '6WS'end. PTFE tape and GE varnish between the solenoid and the former ensures that there was no electrical connectivity between the two but they were in good thermal contact.

3.4.3 The Inner Superconducting Shield (ISS)

We made a total of three different types of ISS. The base of the first two types was another (smaller) dural former around which the superconducting material was attached. The first one tested was made of the same 125 μm Pb foil as used previously and this was wrapped around the former (Figure 3.9 (b)). The second one was made from copper foil which was formed into a cylinder and then coated with $\approx$ 20 μm solder to form a continuous layer (Figure 3.9 (a)). The thickness of the solder layer was determined by a scanning electron microscope. The signal detected was secondary electrons produced by the interaction of the primary electron beam and the material under investigation. This

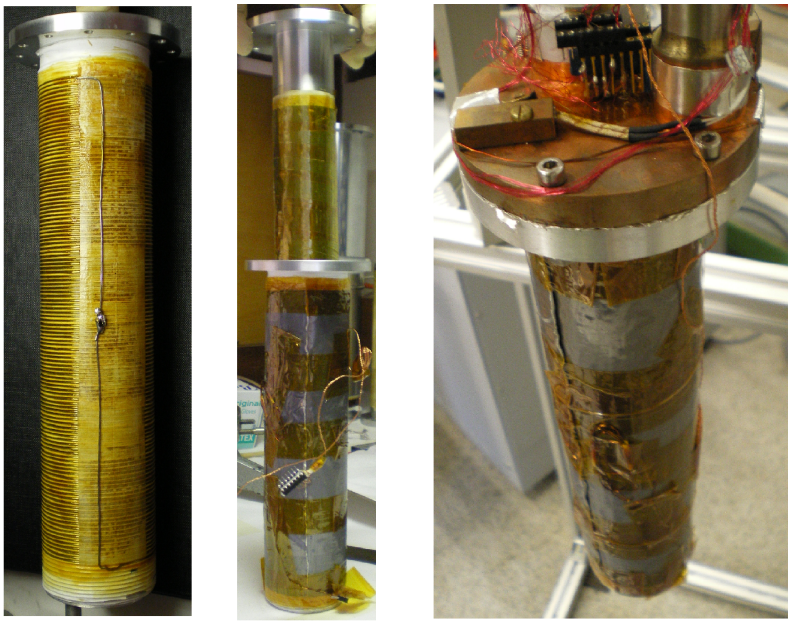

Figure 3.8: Left: The solenoid made of solder wire wound onto a threaded dural former. Centre: An ISS is inserted into the former which now carries the outer Pb shield and the solenoid. Right: A dural former with an outer Pb shield is attached to the second stage of the cryoccoler.

Item	Full size [mm] / Scale model [mm]	Ratio
Pb shield length	2680/214	12.5
Pb Shield diameter	724/57	12.7
Solenoid length	2627/206	12.7
Solenoid diameter	684/54	12.7
HV overlap	43/5	8.6
6WS overlap	10/3	3.3

Table 3.1: The ratios between the various dimensions of the full-size and the scale model shield/solenoid arrangement.

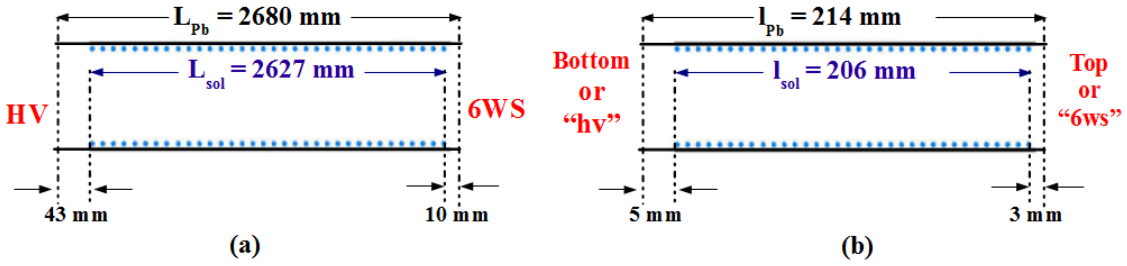

Figure 3.9: The dimensions of (a) the full-size and (b) the scale model of the shield/solenoid of the Cryo-nEDM apparatus.

signal was brighter for the higher atomic number materials (Sn/Pb of solder) and dimmer for the lighter Copper foil. The composition contrast between the solder and the copper, determined the thickness of the former. GE varnish was used to hold the copper foil to the dural former which also maximised the thermal contact between them. The third type of ISS was made by electroplating tin onto the central area of a copper tube into which a mounting flange had been brazed (see Figure 3.11). Permanent marker pen was found to give a very satisfactory mask to cover the areas on which tin was not to be coated. The electroplating was carried out by Thomas Gameson & Sons [64] onto three Cu tubes that were made at Sussex. They used an X-ray fluorescence method to determine the tin thickness and the values obtained for our samples at three different points are given in Table 3.2.

	Thickness [μm]		
Point no	Tube #1	Tube #2	Tube #3
1	5.93	6.66	6.21
2	6.17	5.40	7.42
3	7.27	5.86	6.22

Table 3.2: Values for the thickness of the tin plated area as determined by the electroplating company. These were determined by the intensity of the X-ray fluorescence radiation emitted by the sample.

The length of the superconducting region in the first two types of model ISS varied between 80 mm and 150 mm while for the tin plated copper tube it was kept constant at 80 mm. This latter dimension corresponds to about 1m in the full-size system. The diameter of all three types of model ISS was about 4.4 cm corresponding to ≈55 cm diameter full-size ISS. The geometry details of the outer former, and the ISS are given in Appendix

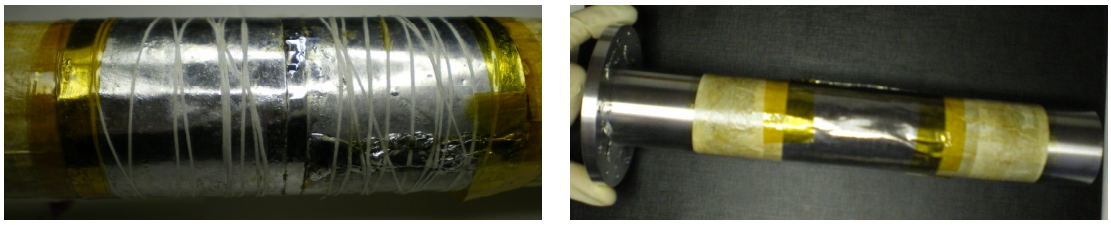

(a) (b)

Figure 3.10: Scale models of the ISS made of (a) solder coated copper foil and (b) lead foil wrapped around the (smaller) dural former.

Figure 3.11: Left: Copper tube used as a base for the electroplated tin ISS. Right: The Tin plated copper tube.

D.

3.4.4 Measuring the Magnetic Field

To record the changes in the magnetic field at the centre of the ISS at low temperature, we utilised a Mag-01H Bartington single-axis Fluxgate Magnetometer. This instrument can record slowly varying magnetic fields (up to 10 Hz) with maximum resolution of 0.1 nT. The cryogenic (MagF) probe is connected to the control unit with two sets of twisted pairs of enamelled copper wires and according to the manufacture's specifications can be used at down to liquid helium temperatues (4.2 K). The minimum temperature of the second stage of the cryocooler we used was 2.2 K and the probe still functioned normally. The orientation of the probe was such that it measured the vertical component of Earth's B-

field as positive.

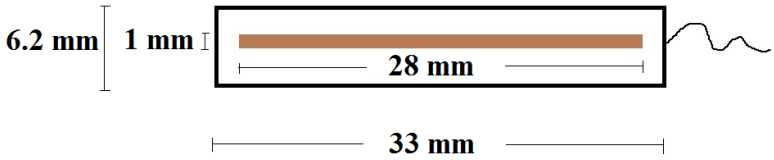

Figure 3.12: The dimensions of the cryogenic fluxgate probe (MagF) and its sensitive volume.

Inside the probe, there is a pair of high permeability cores which are driven in and out of magnetic saturation by an ac current in two excitation coils. The cores constitute the sensitive volume of the fluxgate probe which responds only to the component of the external field parallel to the axis of the cores. As shown in Figure 3.12, the cylindrical probe is 33 mm long and 6.2 mm diameter, while the sensitive area within it is 28 mm long and 1 mm diameter symmetrically positioned around the middle point of the probe. These dimensions would correspond in the full scale model to a $\approx 35.6\ cm$ long and $\approx 12.7\ cm$ diameter cylindrical volume about the centre of the Pb outer shield. This volume is about three times longer than the pair of the Ramsey Cells and about half their diameter.

A hole in the dural formers was drilled to accommodate the fluxgate probe in the middle of both the outer shield / solenoid and the ISS (see Figure 3.13). Low temperature (kapton) tape was used to keep the probe in place.

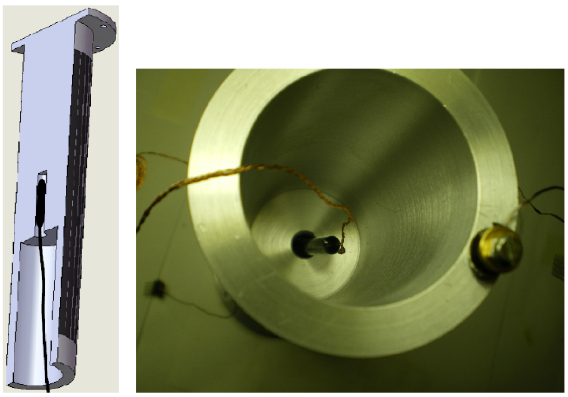

Figure 3.13: The fluxgate probe (MagF) was placed in a hole in the centre of the dural formers. The photo on the right shows also the DT470 diode attached on the bottom of the former.

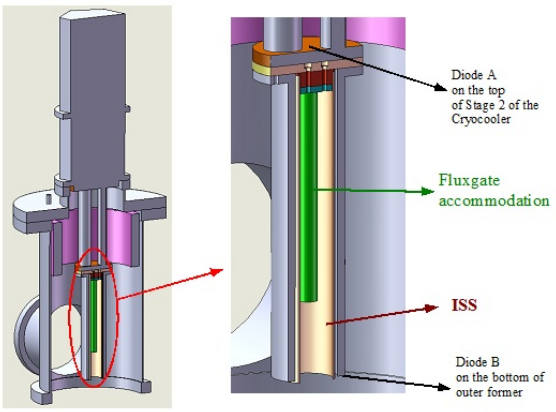

Figure 3.14: These drawings show the experimental set up we used for testing the tinned Cu tube as ISS. Note that neither of the diodes is directly attached to the ISS.

3.4.5 Measuring the Temperature

A SI 410 diode (Diode A) on the top of the second stage of the cryocooler and a DT 470 diode (Diode B) on the bottom (see Figures 3.13 and 3.14) of the outer dural former were used to record the temperature. The calibration of these diodes is given by the supplier and was checked experimentally against the superconducting transition temperature of lead and found to be in a good agreement.

The minimum temperature on the second stage was recorded to be in the range of $T_A = (2.2 - 2.5)\ K$ while the corresponding temperature at the bottom of the former was about $T_B = (3.4 - 3.5)\ K$. Both are well below the SC transition temperature of both the Pb foil and the Solder wire.

3.4.6 Applying a magnetic field

To change the magnetic field we used two pairs of coils. A pair of high-current coils are connected in series and are wound on the top and bottom flanges of the vacuum chamber, producing about 30 μT/A. These are not symmetrically positioned with respect to the ends of the scale model and they could be driven at up to about 60 A, producing $\approx 18 \times 10^{-4}\ T$ or 35 times the Earth's field.

To measure the SF separately at each end of the shield/solenoid system, we used a pair of low-current coils which are symmetrically positioned with respect to the centre of the Pb shield and wound on the aluminium radiation shield. At the centre of the scale model, these coils produce a magnetic field of about 100 μT/A each and can be driven up to about 1 A, giving up to $\approx 10^{-4}\ T$. The position and the geometry of both pairs of coils are shown in Figure 3.4.6.

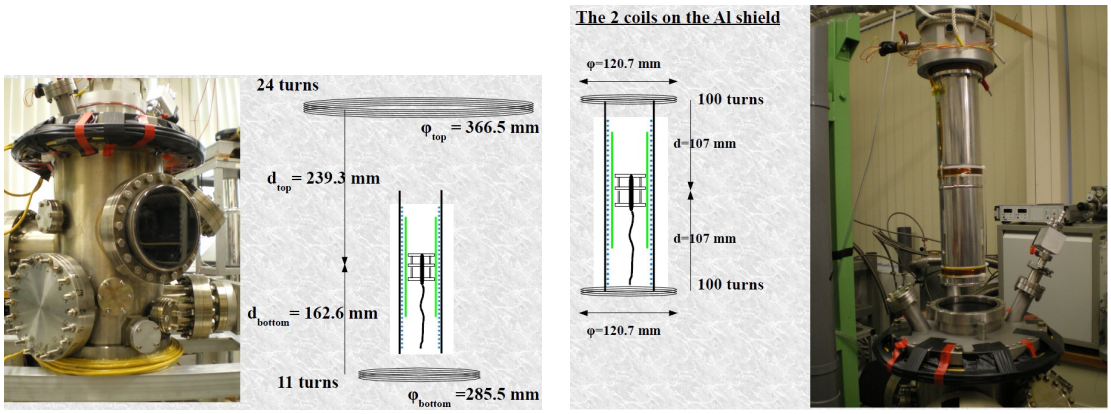

(a) (b)

Figure 3.15: (a) High current coils attached on the top and bottom flanges of the vacuum chamber. (b) Low current coils attached to the radiation shield.

The low-current coils were connected to a current source delivering up to ± 1.5 A. The high-current coils were connected to three different current sources; the first one could provide up to ± 12 A variable. The second source was a battery that delivered a current of order 30 A which decreased with time during data taking (typically it dropped from $\approx$ 33 A to $\approx$ 29 A within about 5 s). The current quoted in our plots of data below was the average of the initial and final currents during the measurements. Finally, a three-phase supply was used to deliver a variable current up to $\approx$ 60 A. It was actually a constant voltage source controlled manually by three ganged variable transformers. At high values, the current tended to decrease slowly with time as the coils became warm and their resistance increased.

In an attempt to reduce the noise in the field values from the fluxgate, a data logging system was used in conjunction with this 60A supply in the later SF experiments. In this, one DVM measured the voltage across a 0.001 shunt in the current leads and a second DVM read the output from the fluxgate, with the whole system running under LabView via IEEE-488. In operation, the current setting was changed manually in steps and the system was set to record data continuously from both channels in sequence at 0.1 s intervals. The data was then binned into current intervals and averages taken of both the current and field voltages. In practice, the variation in current within a single bin was insignificant.

At base temperature, the maximum applied field (1800 μT at 60 A) is below the critical field of all the superconducting parts of the model as shown in Table 3.4.6.

material	Pb	Solder	Tin
SC transition temperature [K]	7.2	6.9	3.7
Critical Field at 3.4 K [mT]	62	57	4.8

Table 3.3: The SC transition temperatures and the critical fields at 3.4 K for the three SC materials used in the model.

3.4.7 Cryocooler

A Cryomech PT405 pulse tube cryocooler with a cooling power of 0.5 W at 4.2 K was used. The first stage of this reaches a minimum of 43 K and stage two about 2.5 K within about 2 hours.

3.5 Extraction of Shielding Factors from Experimental Data

The CSF was calculated in two ways, depending on the type of data sets we had available;

3.5.1 Linear Fit

When the CSF was of the order of several hundreds, the B-field response with current was well above the sensitivity of the fluxgate and linear. This was also true for many cases with the SF to be of the order of 10^5. Data of this type are presented in the next two sections as plots of $B(I)$ where B is the field measured by the fluxgate at the centre of the shield arrangement and I is the current in either the radiation shield coils or those on the vacuum chamber. To obtain the CSF, we calculated the ratio of the slopes measured for the outer Pb shield/solenoid/ISS in the normal $(\frac{dB}{dI})_N$ and superconducting $(\frac{dB}{dI})_{SC}$ states:

$$SF = \frac{(\frac{dB}{dI})_N}{(\frac{dB}{dI})_{SC}} \tag{3.7}$$

with error σ_{SF} given by the standard formula:

$$\sigma_{SF} = SF \cdot \sqrt{(\frac{\sigma_N}{(\frac{dB}{dI})_N})^2 + (\frac{\sigma_{SC}}{(\frac{dB}{dI})_{SC}})^2} \tag{3.8}$$

and σ_N and σ_{SC} are the standard errors in these individual slopes and were found using the linear regression fitting command in Excel.

In each of the plots below, the data taken when the shield arrangement is superconducting is shown in blue. The data taken when all parts of the shielding are normal are

shown in red. Hence, the red field values are also the field values being applied to the outside of the shields when these are in the superconducting state.

3.5.2 Extremal Values

We experienced considerable difficulty with fluxgate noise in many of the experiments, particularly when measured CSF>10^5 (for example when testing the outer Pb shield/solenoid with the ISS in place). In such cases, it was only possible to obtain sensible values for B at the extremal values of I. In this case, the formula we used to calculate the CSF is:

$$SF = \frac{(\frac{B_{max}-B_{min}}{I_{max}-I_{min}})_N}{(\frac{B_{max}-B_{min}}{I_{max}-I_{min}})_{SC}} = \frac{(\frac{\Delta B}{\Delta I})_N}{(\frac{\Delta B}{\Delta I})_{SC}} \tag{3.9}$$

The error is given by:

$$\sigma_{SF} = SF \cdot \sqrt{(\frac{\sigma_N}{(\frac{\Delta B}{\Delta I})_N})^2 + (\frac{\sigma_{SC}}{(\frac{\Delta B}{\Delta I})_{SC}})^2} \tag{3.10}$$

with:

$$\sigma_{N,SC} = \sqrt{2}\sqrt{(\frac{\sigma_{B_{N,SC}}}{(\Delta B)_{N,SC}})^2 + (\frac{\sigma_{I_{N,SC}}}{(\Delta I)_{N,SC}})^2} \tag{3.11}$$

and where typical errors for the B readings being from ± 0.1 to ± 1 nT and for the I values being ± 1 A for the three phase supply, and about ± 0.5 A for the other two current supplies.

3.5.3 Data taking method

For the tests on the Pb foil and solder coated Cu foil ISSs, the data were taken manually by reading the field on the fluxgate unit. For most of the Tin-plated Cu tubes, the data logging system described in section 3.4.6 was used. A number of attempts were made to improve the noise levels by, for example, rewiring the fluxgate leads to the cryocooler and by taking data when the latter was switched off (which in turn leads to a rising temperature).

Finally, before we proceed to the CSF data and results, it is important to stress the fact that the fluxgate resolution limits the sensitivity of this experiment. As the lowest field that the fluxgate can record is 0.1 nT and the maximum field we can apply is about 1800 μT, the theoretical maximum CSF we can measure by the use of the fluxgate is:

$$SF = \frac{1800\mu T}{0.1nT} = 1.8 \times 10^7 \tag{3.12}$$

However, as detailed below, the actual noise levels reduced the maximum measurable CSF to much less than this value.

3.6 Initial Experimental SF Data

At temperatures ($\approx$ 10 K) well above the SC transition temperature of Pb, we activated the pair of coils on the vacuum chamber in order to compensate the background magnetic field; from $B \approx 15 \pm 1\ \mu T$ down to $B \approx 0.2 \pm 0.1\ \mu T$. Nonetheless, when the shield went superconducting (and without changing the current on the coils) there was a flux rearrangement inside the shield and the fluxgate reading increased rapidly by about one order of magnitude ($B \approx 2 \pm 1.5\ \mu T$).

When the temperature on the second stage of the cryocooler (denoted as T_A) reached $\approx$ 2.4 K and at the bottom of the scale former (denoted as T_B) $\approx$ 3.4 K, the cryocooler was switched off in order to eliminate the vibrations. The results of the tests for the various scale model configurations as described above are presented in the following sections.

3.6.1 Model Pb shield alone

First, the scale model of the outer Pb shield was tested alone. Two sets of data were taken at currents up to about $\pm$12 A. Figure 3.16 shows the data when the current was increased by small steps. The linear regression to model the dependence of the B-field response on the current change is shown as well. The low coefficient of determination when the Pb shield is in SC state ($R^2 \approx 0.3$) results in the high slope error for this data set. This finally reflects to a significant uncertainty to the calculated SF value:

$$SF_{Pb} = \frac{30.56 \pm 0.053\ \mu T/A}{0.162 \pm 0.091\ nT/A} = (1.88 \pm 1.06) \times 10^5 \tag{3.13}$$

A second set of data were taken only at the two extremes of the current (see Table 3.4). Using the same response of the fluxgate in the normal state as before, we take:

I [A]	$B[\mu T]$	$\bar{B}[\mu T]$
+12.12	0.4139 - 0.4158	0.41485 $\pm$ 0.00095
-12.33	0.4117 - 0.4130	0.41235 $\pm$ 0.00065

Table 3.4: Data taken at the maximum current values ($\approx \pm 12\ A$) when only the outer Pb shield was tested. The second column gives the recorded values between which the field was varying. The calculated average value with its error is given in the third column.

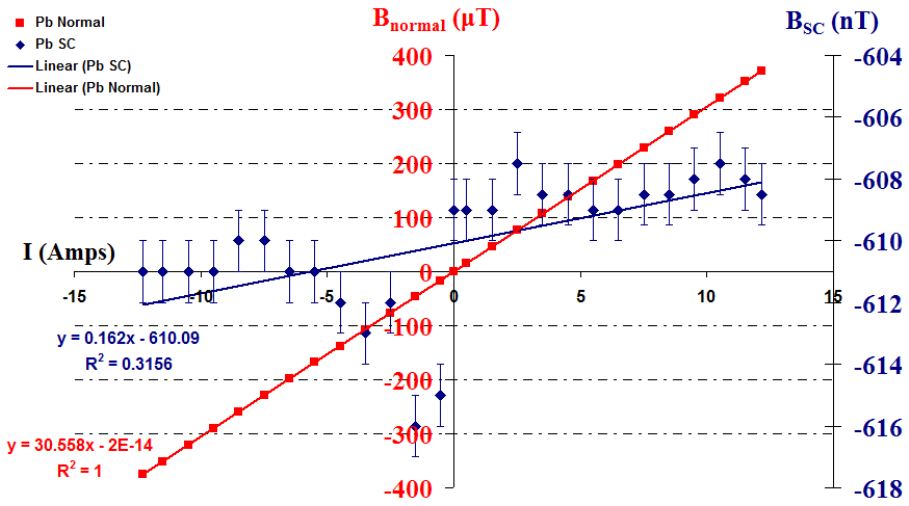

Figure 3.16: Testing the outer Pb shield alone ($SF \approx 1.88 \cdot 10^5$).

$$SF_{Pb} = (3 \pm 1.2) \times 10^5 \tag{3.14}$$

a figure which is in a good agreement with the first result.

3.6.2 Model of the full-size shield/solenoid

Using the symmetrically positioned pair of coils on the radiation shield, we reproduced the two end SFs recorded at Sussex in 2004/05 and the theoretically expected value for the total SF. The two end SFs were found by activating each coil separately while for the total SF tests they were connected in series.

The data for the "6WS" or top end of the scale model are shown in Figure 3.17 and yield:

$$SF_{6WS} = \frac{102.74 \pm 0.19\ \mu T/A}{-0.781 \pm 0.005\ \mu T/A} = -132 \pm 1 \tag{3.15}$$

The data shown in Figure 3.18 for the "HV" or bottom end of the scale model give us:

$$SF_{HV} = \frac{99.25 \pm 0.17\ \mu T/A}{-0.252 \pm 0.001\ \mu T/A} = -393 \pm 2 \tag{3.16}$$

Finally, for the Total SF (TSF) of the scale model, we first used the coils on the radiation shield. The results of the first are shown in Figure 3.19 and give a SF equal to:

$$TSF = \frac{204.43 \pm 0.05\ \mu T/A}{-0.871 \pm 0.003\ \mu T/A} = -234 \pm 2 \tag{3.17}$$

A summary of the scale model test results using the radiation shield coils and the data taken at Sussex in 2004/05, as well as the theoretically expected data for the full-size

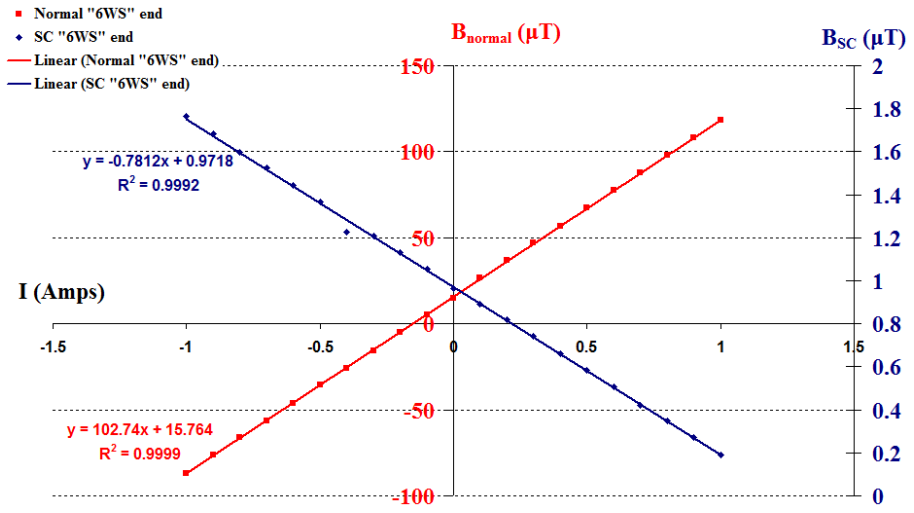

Figure 3.17: Data taken for the SF at the 6WS end of the scale model (SF=-132).

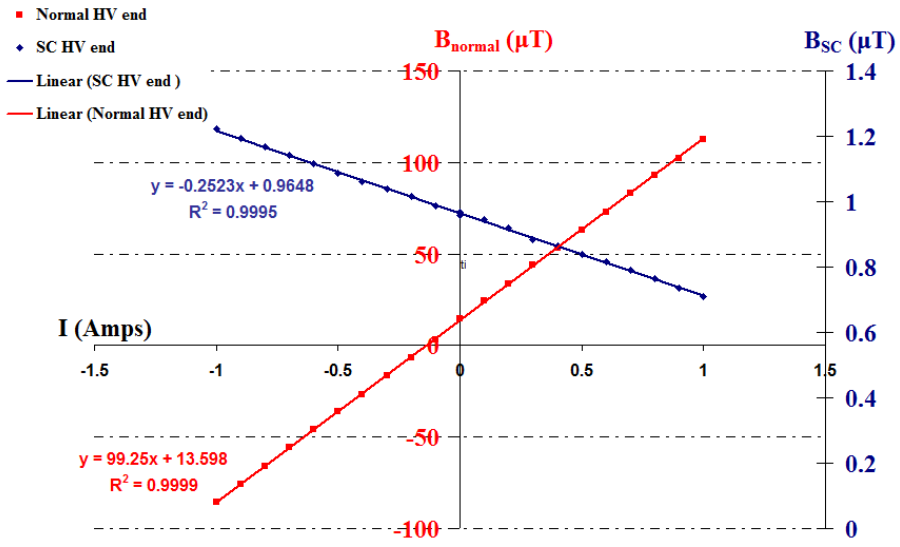

Figure 3.18: Data taken for the SF at the HV end of the scale model (SF=-393).

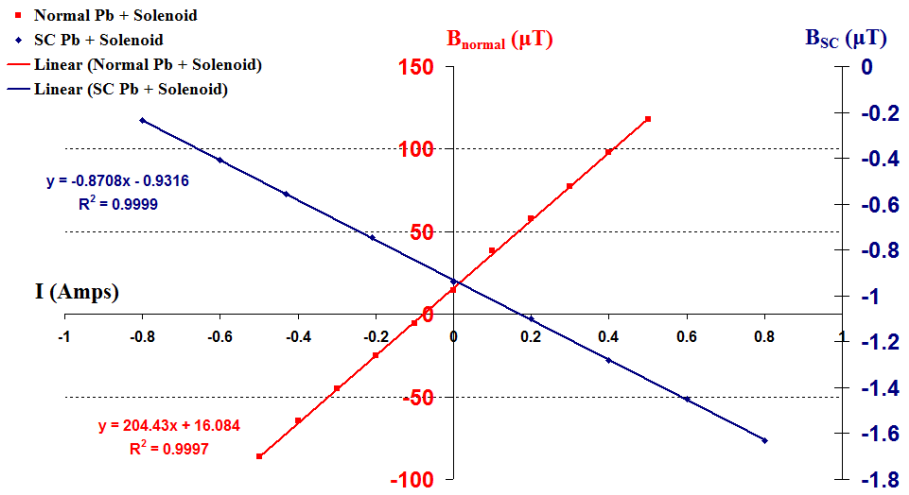

Figure 3.19: Data taken for the Total SF of the scale model using both coils on the radiation shield (SF=-234).

apparatus, are presented on Table 3.5. We note the good agreement and therefore we contend that our $\approx 1/12.5^{th}$ scale model mimics adequately the SC items of the full size apparatus.

	Full Size apparatus	$1/12.5^{th}$ scale model
Pb shield alone	$5{\cdot}10^5$ (theor.)	$(3 \pm 1.2){\cdot}10^5$
Pb Shield + Solenoid HV end	-440 ±80 (exper.)	-393 (±2)
Pb Shield + Solenoid 6WS end	-110 ±17 (exper.)	-132 (±1)
Pb Shield + Solenoid Total	-175 (theor.)	-234 ±2

Table 3.5: Comparison of the scale model SF data with the data taken at Sussex in 2004/05 and the theoretically predicted values for the full size apparatus [1].

In order to improve the sensitivity of the scale model experiment, it was essential to increase the applied field. For this reason, and before we made any other modification to the scale model (i.e. adding the ISS), we repeated the test for the total SF using the high-current coils on the vacuum chamber. This SF has been termed 'Global' (GSF).

Both Global and Total SFs reflect the shielding efficiency of the outer shield/solenoid when the external field is changed at both of their sides simultaneously. The only difference is that the Total SF refers to data for which the external field was changed by the use of the symmetrically positioned coils on the radiation shield, while the Global SF refers to tests where the vacuum chamber coils were used instead.

The test was carried with the ± 12 A power supply. The data obtained are shown in

Figure 3.6.2 and yield:

$$GSF = \frac{30.65 \pm 0.02\ \mu T/A}{-0.0355 \pm 0.001\ \mu T/A} = -863 \pm 24 \tag{3.18}$$

This number is significantly different from the value we found with the radiation shield coils. Nevertheless, this is expected as the geometric features of the two pairs of coils are different; the vacuum chamber coils are wider than the radiation shield ones and placed asymmetrically away from the ends of the scale model. The difference in the coils geometry is reflected on the fact that the slope $(\frac{dB}{dI})_{Normal}$ is about 6.7 times bigger for the radiation shield (rad.sh.) coils compared to that for the vacuum chamber (v.c.) coils. So, for $I_{rad.sh.} = 6.7 \times I_{v.c.}$ we apply the same field at the point where the fluxgate is placed, but at the same time it is easy to show that the total flux impinging the two sides of the shield/solenoid system is about 5.5 times more when we use the radiation shield coils. Therefore, for every μT we apply at the centre of the model, the current generated in the solenoid is expected to be larger in the case of applying the field with the radiation shield coils. Bigger current in the solenoid leads to a larger $|\Delta B_{int}|$ which in turn reduces the absolute value of the CSF. In any case, the solenoid overcompensates the imposed change at the centre of the model, so the CSF is always negative. The fact that the ratio of the incoming flux for the two pairs of coils (≈ 5.5) is very close to the ratio of the two SFs (i.e. Global SF / Total SF = 3.7) strengthens the above argument.

All the tests in the following sections were conducted with the high-current coils on the vacuum chamber and therefore the value of 863 is our reference SF. Hence, any change in the SF is to be compared with this number.

3.7 CSF Improvement by a continuous ISS

The next step was to insert the various types of ISS and repeat the measurements with the high-current coils on the vacuum chamber.

3.7.1 Pb foil ISS - SF data.

The Pb-foil was initially made to be 150 mm long and it was then progressively reduced in length to 120 mm, 100 mm and finally to 80 mm. Superconducting state data were taken for each of these lengths at extremal current values of ±12 A and ±30 A. The normal state data from the previous runs were used to calculate the SFs. These are shown in Figure 3.20, grouped for the different ISS lengths.

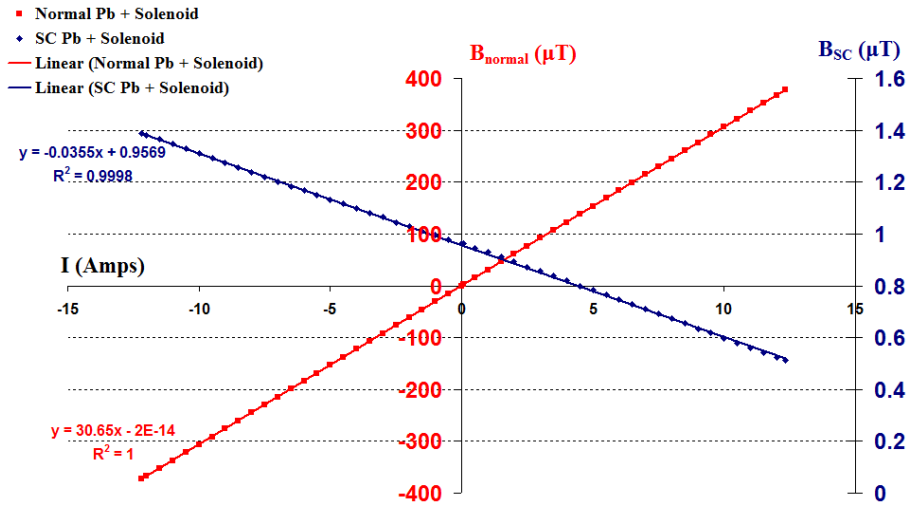

Figure 3.20: SF data taken for the Global SF by the use of the high-current coils wound on the vacuum chamber (SF=-863).

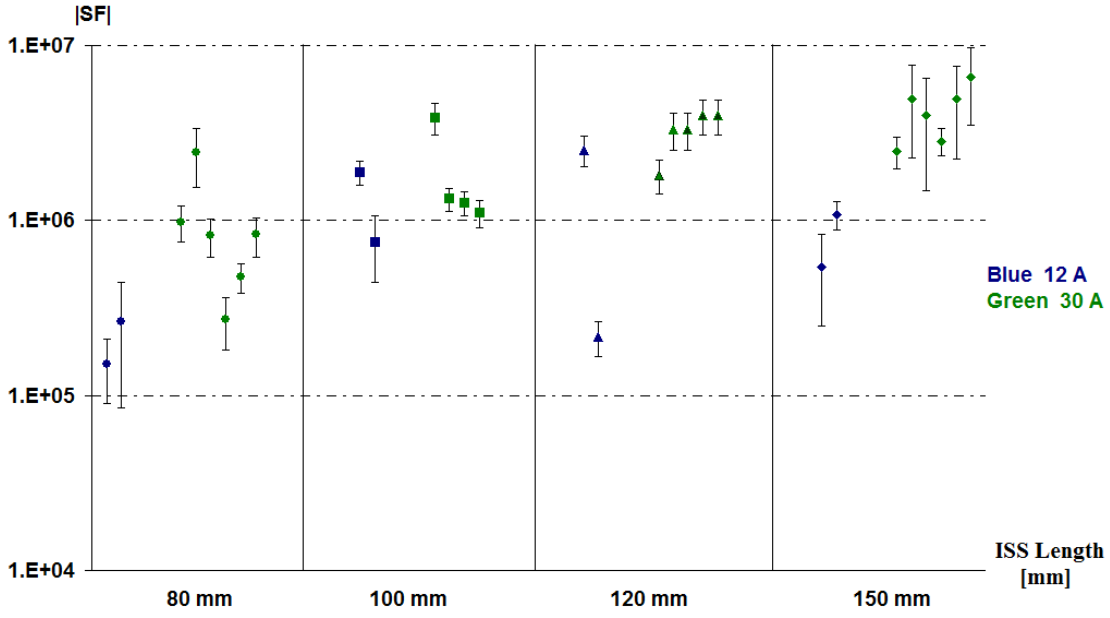

Figure 3.21: The modulus of the calculated SF using extremal current data taken for the model with Pb foil ISS. The blue points correspond to the data taken with the ± 12 A and the green with the ± 30 A current supplies.

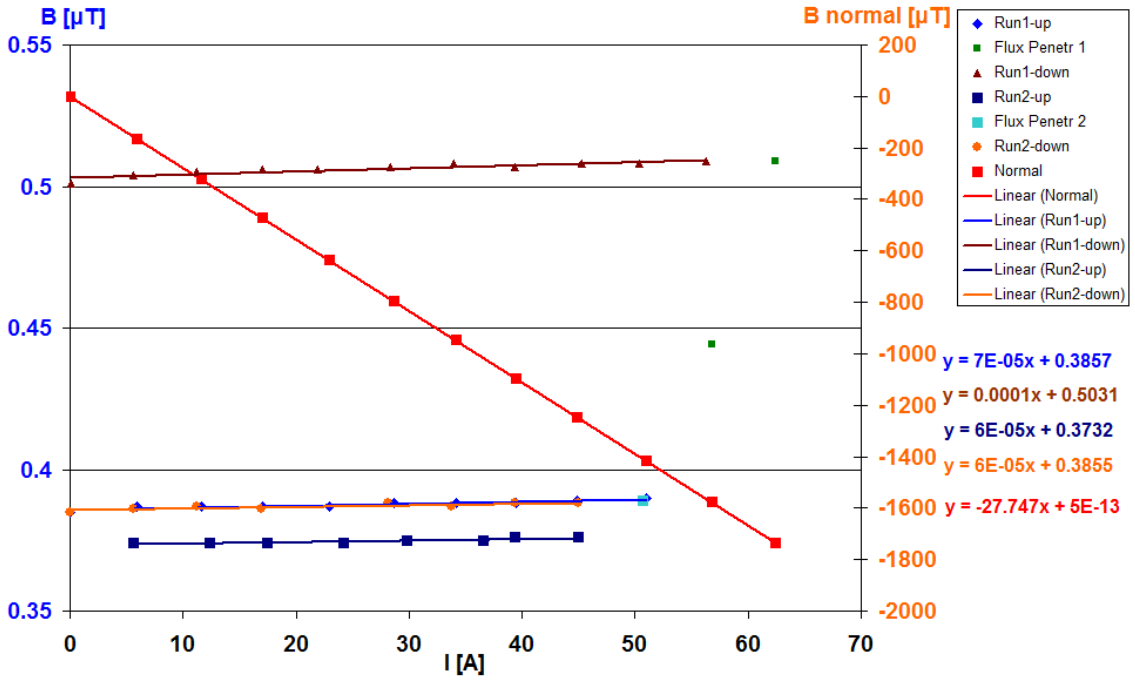

Figure 3.22: SF data for a 80 mm Pb foil ISS at higher currents and hence fields. Flux penetration occurs at the highest currents. For the SF calculations, only the 0-50 A regions were fitted to a linear dependence.

We note that the values of SF calculated from individual ±12 A data points can differ by up to one order of magnitude. This is because the applied field does not change the field inside the model by more than the noise in the fluxgate. On the other hand, most of the 30 A values seem to be better grouped and more consistent with each other.

Finally, we made measurements on the 80 mm Pb-foil ISS using the 60 A supply. The data are shown in Figure 3.22 and for currents up to 50 A, the SC state data can be sensibly fitted to a linear dependance. However, for currents above about 50 A (corresponding to a field of ≈ 1500) there is an abrupt increase of the B-field at the fluxgate, indicating that some part of either the outer Pb shield or the ISS, or both, goes normal. This is somewhat unexpected since the maximum applied field is 40 times weaker than the critical field of lead ($\approx 65mT$) at 3.5 K. Hence, we speculate that there may be a "weak link" in one of the SC elements (possibly on the longitudinal join in the outer Pb shield) which leads to the observed flux penetration at 50 A. When the current was reduced back to zero, the B-field response was again linear but remained at a higher level. We conducted the same test twice and in both cases we observed the same response. For this type of data, we calculated the SF separately for the two linear regions, using only the data for 0 to 50 A. The results are given in Table 3.6.

Run	$SF \times 10^5$	$\sigma_{SF} \times 10^5$
Run 1 - Increasing I	-3.8	0.6
Run 1 - Decreasing I	-2.5	0.4
Run 2 - Increasing I	-4.8	1.0
Run 2 - Decreasing I	-4.7	1.1

Table 3.6: Summary of SF data for the 80 mm Pb-foil ISS when the vacuum chamber coils are driven up to $\approx 60\ A$.

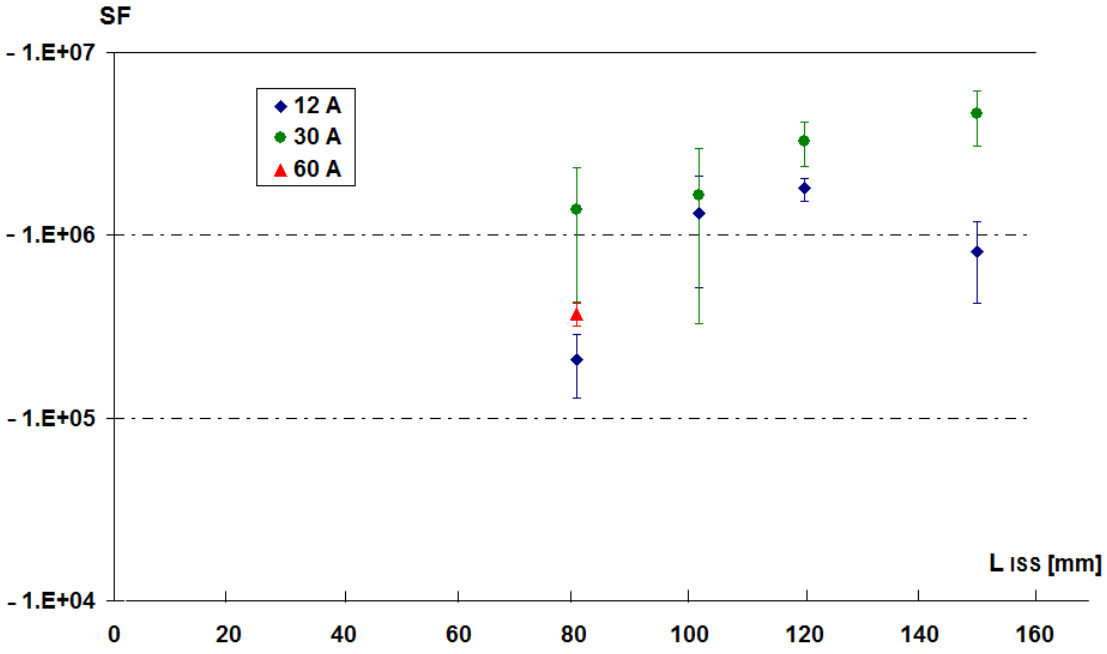

Figure 3.23: The SF data as a function of the Pb foil ISS length. Three sets of data are presented here: red: 60 A, green: 30 A and blue: 12 A). The most reliable value is the single 60 A point which suggests that with 1 m long ISS we can enhance the Global SF from 863 to $(-3.9 \pm 1.5) \times 10^5$.

Taking the average of the SF separately for the data sets of ± 12 A, ± 32 A and ± 60 A we obtain Figure 3.23 which shows the dependance of the SF on the length of the ISS. The 60 A data can be considered as those more reliable data for the SF calculation as they correspond to the strongest imposed B-field. The average of the two linear regions yields:

$$SF_{60A} = (-3.9 \pm 1.5) \times 10^5 \tag{3.19}$$

One interesting point in Figure 3.23 is that we do not see the SF become infinite at a length of 120 mm (which corresponds to 1.5 m in full scale) as was suggested from consideration of Figure 3.4. Furthermore, the SF does not become positive for an a ISS longer than this value.

3.7.2 Solder-coated Cu foil ISS SF data

The data taken with the 80 mm long solder-coated Cu foil ISS described in section 3.4.3 are presented in Figure 3.24. Using the average of the increasing and decreasing current slopes we obtain:

$$SF = \frac{30.4 \pm 0.55 \ \mu T/A}{(9.5 \pm 0.83) \times 10^{-5} \ \mu T/A} = (3.2 \pm 0.3) \times 10^5 \tag{3.20}$$

which is in a good agreement with the results taken with the 60 A power supply for the 80 mm Pb foil ISS.

For this solder-coated ISS, we did not observe flux penetration at the highest current and the field response was linear over the full range of the applied current (0-63 A). However, when the current is increased the slope is about 10% steeper compared to that for decreasing current. One possible explanation for this is that the ISS might was brought at thermal equilibrium as time was passing. In this case, supercurrents would be developed along longer part of the ISS, the response of the fluxgate would be weaker and therefore the slope less steep and the SF higher.

Nonetheless, as we will see on the next sets of data, the slopes for increasing and decreasing currents can be different by about the same percentage as well. Thus, we can not claim that this discrepancy is a characteristic behaviour of this particular type of the ISS setup, but probably is caused by the experimental procedure and conditions in general.

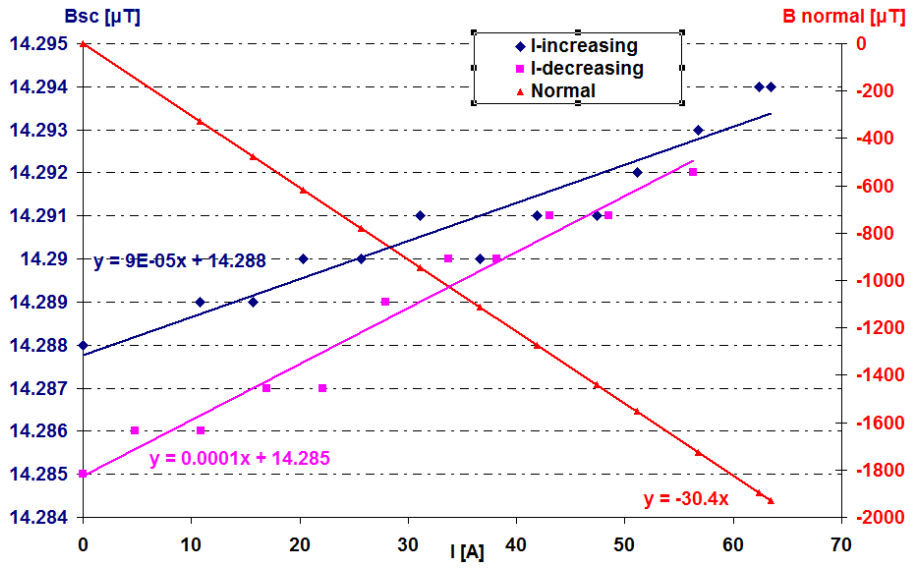

Figure 3.24: SF data for a 80 mm Solder-coated Copper foil ISS. ($SF = (-3.4 \pm 0.3) \times 10^5$).

3.7.3 Electroplated Tin ISS - SF data

Before discussing in detail the data for the SF of the combined Sn ISS and Pb shield / solenoid, it is worth reiterating the basic problem we encountered in making these measurements. The overall SF is expected to be close to the product of the two separate SFs and hence to be of the order of 5×10^5. Given that the maximum field we can apply before flux penetration occurs (see section 3.7.1 and also below) is about 1500 μT, the maximum variation expected inside the combined shields is about 3 nT. Although this is well above the quoted 0.1 nT sensitivity of the fluxgate, it proved impossible to achieve this latter limit in the actual apparatus at low temperature. The noise level varied considerably but in general was never much below 1 nT. On occasions, the noise levels were such that it was impossible to determine a linear dependence of $B(I)$.

As described in section 3.5.3, a number of attempts were made to improve the noise levels. For the later measurements on the Sn-coated ISS, the LabView (LV) data logging system described in section 3.4.6 was used to average the readings.

The difficulty in determining the SF due to these elevated noise levels is evident when we now consider the raw $B(I)$ data. Some of the data sets were taken after the system had been cooled in zero field, after compensating the laboratory field.

Figure 3.25 shows two data sets taken on different days with the apparatus having been dismantled between the two runs. Data set (a) used the LV system and the lab field was compensated before cooling whereas set (b) was taken manually and no compensation was applied. The small differences in the slope of the normal state response is attributed

to a small difference in the position of the fluxgate on reassembly.

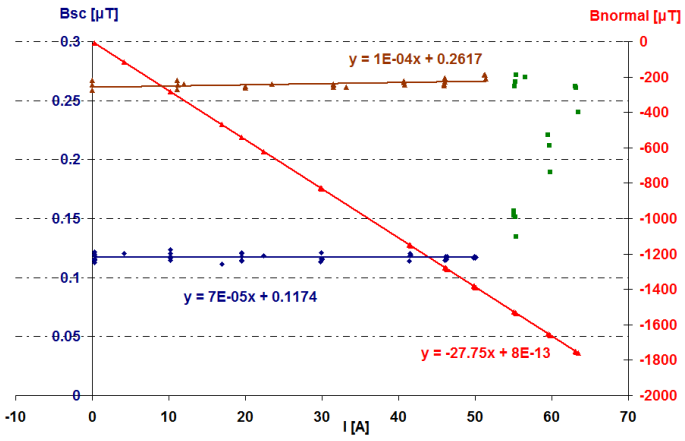

(a)

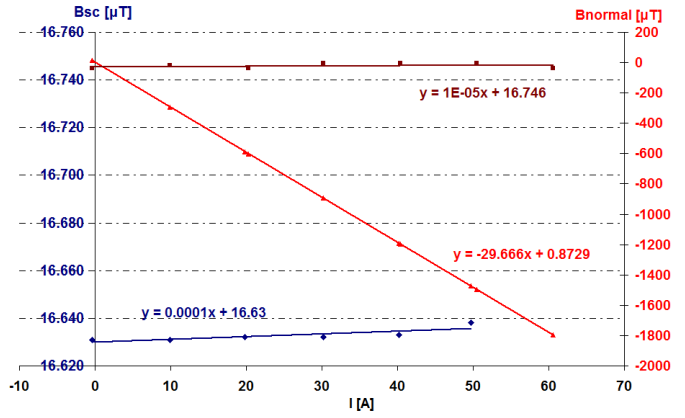

(b)

Figure 3.25: Outer Pb shield/solenoid with Sn-ISS SF data. For both increasing (blue) and decreasing (brown) currents between 0 and 50 A, there is a linear response of the B-field. At about 50 A, a flux penetration occurs (green) so the B-values suddenly increase. Both data sets, were taken manually using LabView system. The background field was compensated in (a), using the vacuum chamber coils before the start of measurements. There was no attempt to cancel out the background field in (b).

In a similar manner to the data from the Pb foil ISS, flux penetration is observed at the higher currents. This occurs at the same 50A value as was found for the Pb foil case, suggesting that this behaviour is associated with the shield/solenoid, which is common to both configurations and not to the (different) ISSs.

As with the Pb foil data, the SF was determined from such data by a linear regression fit to the data below 50A for both increasing and decreasing current.

Figure 3.26 shows, on an expanded scale, a typical data set taken with the LV system

and after compensation of the lab field. The scatter in the data even after averaging is considerable, but a linear regression fit yields a SF of (-5.9 ± 1.5)×10^5. In this data set, as in several others with the Sn-coated ISS, there is no evidence of flux penetration even at 60A. We can find no clear correlation of the occurrence or absence of flux penetration with any other parameter in the experiment. Since flux penetration is expected to occur when some part of the superconducting shields is driven normal by the applied field, any slight change in temperature will affect strongly the field value required to do this. We thus attribute this variability to small changes in the temperature at which the specific data set was taken, recalling that some of the data were taken after the cryocooler had been switched off.

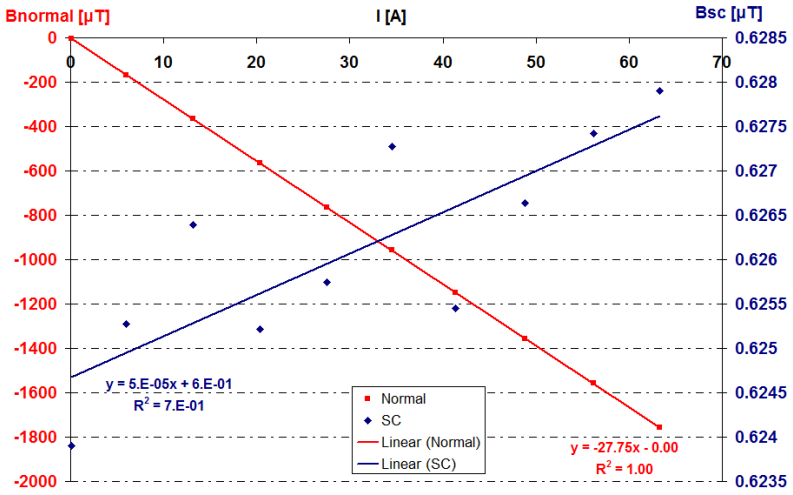

Figure 3.26: Linear response of the B-field for the Sn-ISS. The field varies more than the fluxgate intrinsic noise levels. For these data: $SF = (-5.9 \pm 1.5) \cdot 10^5$

Figure 3.27 shows the data from a representative selection of the data sets from those which were used to determine the SF of the Pb shield/solenoid plus the Sn-coated ISS. This shows the $B(I)$ data up to 50 A only and each set has been offset by an arbitrary B_{off} for clarity. The top two data sets (purple and orange points) were taken all manually and are just one fluxgate reading for each current value. The next two (green and brown points) are taken with LabView program which recorded several fluxgate outputs for a given current without any averaging. Finally, in the last two data sets (blue and red points) LabView gave the averages of both the current and field voltages. One set of data (labeled as "LV Integrate I-increasing 1") in which the noise was such that it was impossible to determine any linear dependence, has been included for comparison.

All the SF determined from linear fits to data sets giving statistically significant values of dB_{sc}/dI are shown in Figure 3.28, plotted as a function of the vertical component of

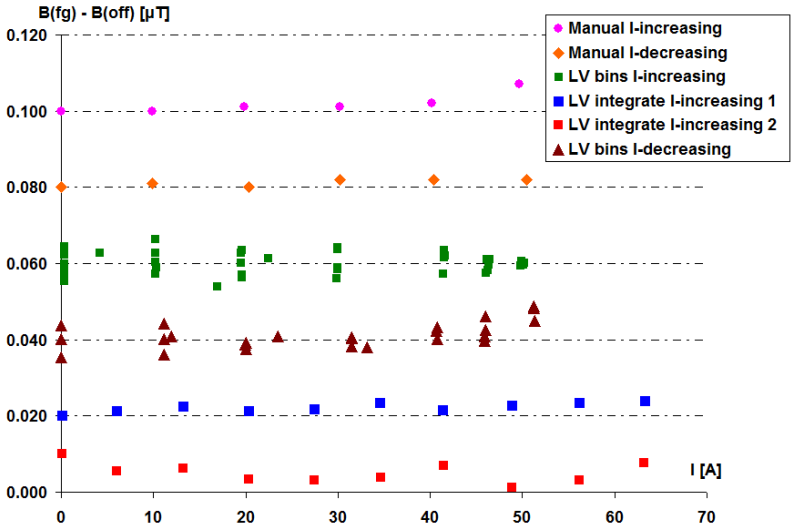

Figure 3.27: Three pairs of data sets for testing the Sn-ISS, following different data acquisition method (see text) for comparison. Arbitrary offsets (B_{off}) have been applied for clarity.

the field in which the shields were cooled. As is evident from this figure, there is no clear dependence of the SF on the cooling field and therefore the flux that was trapped within the shields during the SC transition. Neither is there evidence that the SF is different after flux penetration has occurred nor whether the data had been taken with increasing or decreasing current. Taking the unweighted average of all the data in Figure 3.28, we arrive at a final value for the $SF = 3.95 \pm 1.65 \times 10^5$.

3.7.4 Summarising the ISS SF tests results

All the results with the three different types of ISS, show conclusively that by adding an $80\ mm \times 12.5 = 1\ m$ long ISS within the present Pb shield/Solenoid we expect to enhance the SF by about:

$$\frac{3.9 \times 10^5}{863} \approx 450 \tag{3.21}$$

This number refers to the Global SF improvement. Similarly, we expect the Total SF to be improved by the same factor and become:

$$TSF = 450 \cdot (-235) = -1.06 \times 10^5 \tag{3.22}$$

The minus sign is not important in terms of magnetic shielding. We are only interested in minimising the magnitude of the changes within the Ramsey Cells region, whatever the sign.

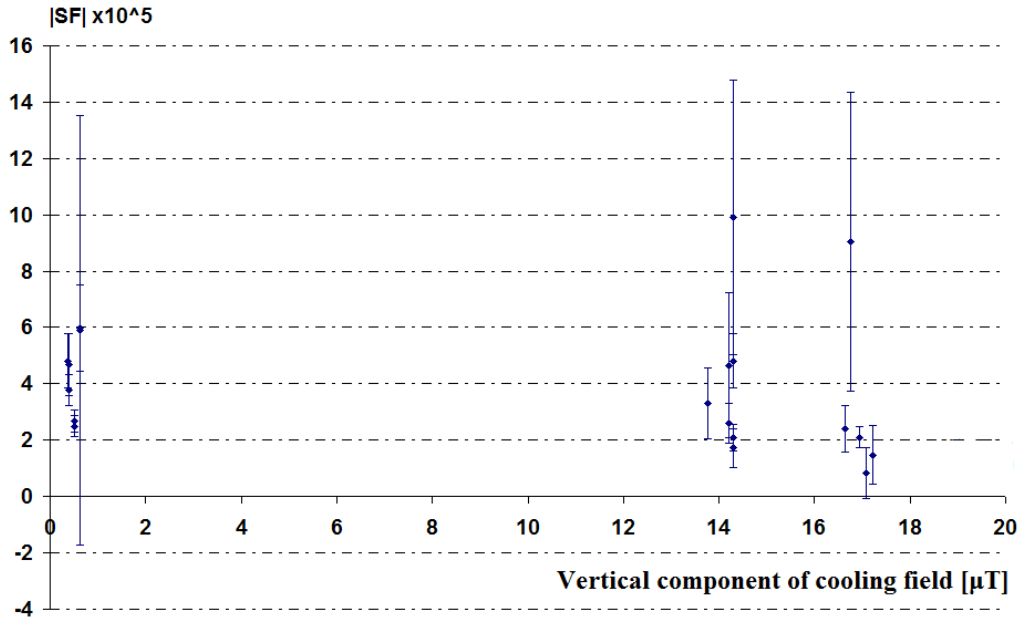

Figure 3.28: SF for the outer Pb shield/solenoid with the Sn-plated ISS as a function of the cooling field. The plot shows no correlation of the SF value with the trapped flux through the SC transition.

3.7.5 Electroplated Tin ISS T_c

The superconducting transition temperatures of the Sn-plated ISS and the outer Pb shield/solenoid were checked several times by carrying out the procedure described here.

At T >10 K and while cooling, the background field was compensated by activating the two vacuum chamber coils with current of about 0.5 A. This current was kept constant until the system reached the base temperature of ≈2.4 K. At this point, we increased the current up to 60 A and at about 50 A flux penetration occured and the field at fluxgate increased by about 0.15 μT. The current was then brought back to zero but the value of the field remained at the higher level. This is taken as evidence that some flux remains trapped within the outer shield/solenoid, either between it and the ISS or distributed over both.

Next, the cryocooler was switched off and the system allowed to warm. As shown in Figure 3.29, an abrupt increase of about 70 μT in the fluxgate field occurs at 3.95 K. This jump is presumed to occur when the ISS goes normal and the flux which had been trapped between the two shields reaches the fluxgate.

For 3.95 K <T <7.45 K, the outer shield/solenoid goes gradually normal (from bottom to the top) so the total flux is slowly released. The field is finally restored to the background level ($\approx 17\mu T$) when the shield/solenoid goes completely normal.

The sharp changes at 7.45 K and 3.95 K are hence interpreted as the transition temperatures of the (Pb) shield/solenoid and the (Sn) ISS, respectively. However, these values are each about 0.25 K higher than the accepted values for the bulk materials. The temperature plotted is that indicated by diode A (see section 3.4.5). This diode is clamped to the second stage cold plate of the cryocooler which is the coldest point of the system. The discrepancy between the expected and measured transition temperatures is thus attributed to the diode no longer being in good thermal with the SC parts of the model. Despite this, the fact that the T_c of the $\approx 6\mu m$ tin coating is very close to the bulk value indicates a high purity of the electroplated layer.

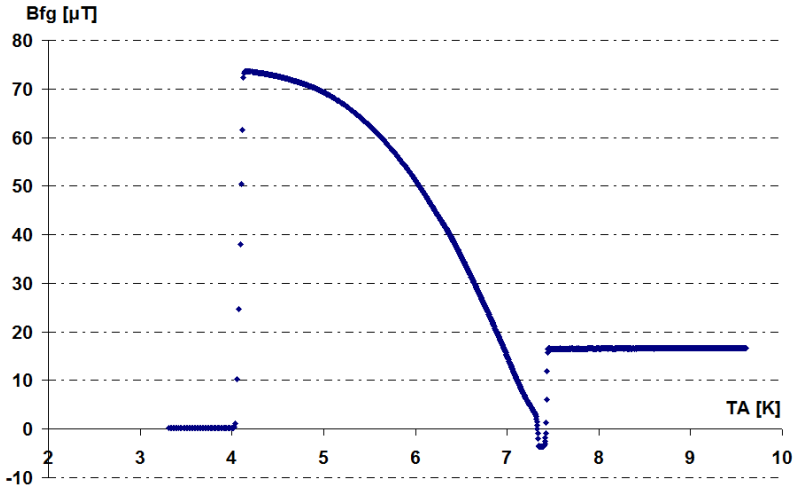

Figure 3.29: While warming the model, the recorded superconducting transition temperature of the Sn-coated Cu tube (3.95 K) occured well below that of the outer shield/solenoid (7.45 K). There is a 0.25 K discrepancy between the recorded and the expected values for Sn (3.7 K) and Pb (7.2 K) transition temperatures. This discrepancy is attributed to the fact that the diode we used was not directly attached on the SC items of the model but actually measured the temperature of the second stage of the cryocooler instead.

3.8 Quick Field Simulations of B-field in the ISS

For an ISS of arbitrary Length to Diameter ratio and thickness, we wish first to be able to calculate the dynamic shielding factor and then the distortion of an (initially) uniform field that will be caused when the shield is cooled through its superconducting transition. As will be explained in detail in Chapter 5, there is homogeneity requirement on the field for resonance. The design criterion in the Cryo-nEDM experiment is that the longitudinal field gradient $\frac{dB_z}{dz}$ does not exceed 1 nT/m over the Ramsey Cell volume. The "Quick

Field" (QF) software package [65] has been used to do both of these calculations and initially we consider a cylindrical ISS of uniform thickness.

3.8.1 Calculation of the Shielding Factor

This is done by simulating a tube that is initially zero-field cooled (ZFC) below its SC transition temperature such that there is no flux inside it. An external field (ΔB_{ext}) is then applied and the field which penetrates to the centre (ΔB_{in}) is evaluated. Figures 3.30 and 3.31 shows the QF outputs for a tube with L/D = 1.90, which corresponds to the 80 mm long and 42 mm diameter ISS in the scale model. The external field is screened inside the ISS and the minimum field occurs at the centre.

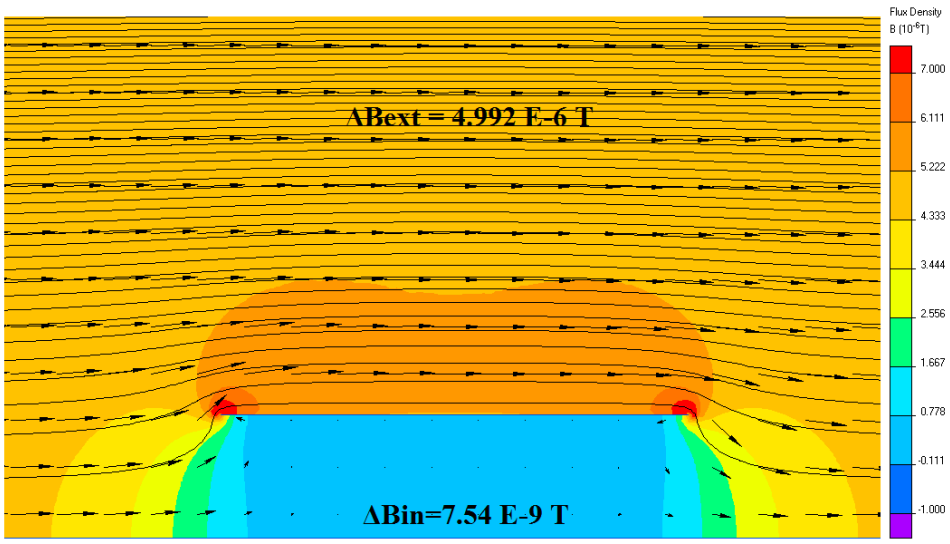

Figure 3.30: Quick Field output for a superconducting shield with L/D = 80mm/42mm = 1.90 after cooling in zero field and then application of an external field of 5 μT. The colour scale on the right hand side giving the magnitude of B varies from -1×10^{-6} T to 7×10^{-6} T. The ratio ($\Delta B_{ext}/\Delta B_{in}$) corresponds to a $SF \approx 660$.

According to these simulations, the SF is ≈660 which is in reasonable agreement with our experimental results if we think that this value is calculated using only the B-filed values at the centre of the ISS (z=r=0). In reality, the fluxgate measures the B-field changes over a finite volume (28 mm × 1 mm). The sensitive volume of the fluxgate with respect to the ISS models size is shown in Figure 3.32. As we move away from the centre of the ISS, the magnetic shielding becomes less effective, the changes of the magnetic field will be larger and hence the SF, as this is measured by the fluxgate, is expected to be smaller than the above value of 660.

A more realistic calculation of the SF would have to take the sensitive volume of the

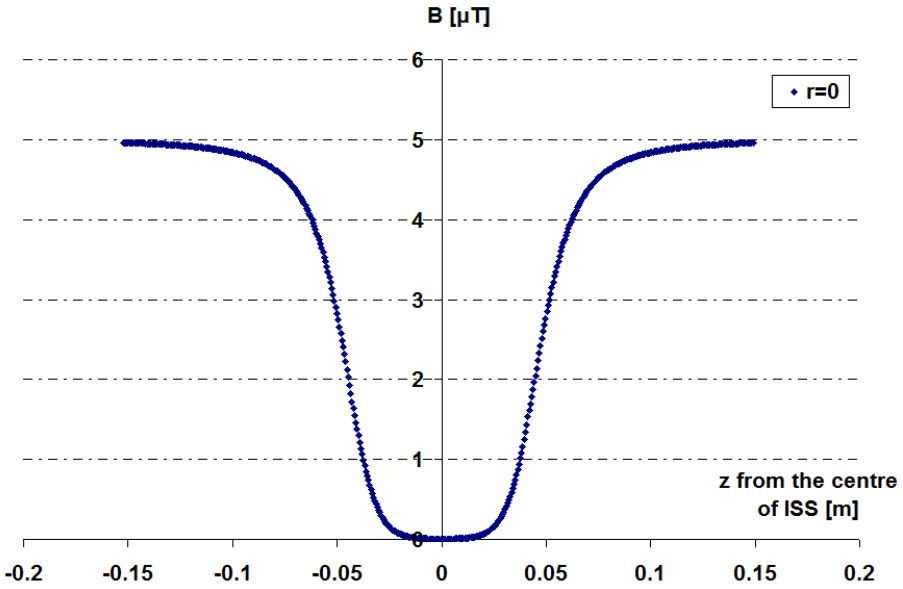

Figure 3.31: Bz as a function of z along the main axis of the ISS model of Figure 3.30. The ISS lies between -0.04 m <z <+0.04 m.

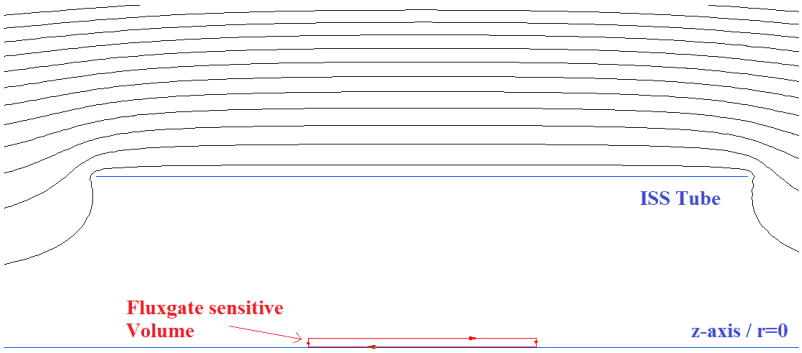

Figure 3.32: The fluxgate sensitive volume within the ISS of the scale model.

fluxgate into account. We do this by dividing the flux within this volume when the ISS tube is in normal state over the flux when it is in SC state (as this calculated with QF). This ratio yields:

$$\frac{\Phi_{ext}}{\Phi_{in}} = \frac{1.4 \times 10^{-10}\ \text{Wb}}{3.45 \times 10^{-13}\ \text{Wb}} \approx 405 \tag{3.23}$$

As expected, this number is smaller than the first calculation of 660 at the centre of the ISS and it is closer to our experimental results of ≈450 for the CSF improvement of the scale model when we add the ISS. Having in mind that, in full-size, the fluxgate sensitive volume corresponds to three times the length of the Ramsey Cells, it is safe to say that by adding an ISS with L/D=1.90, the SF improvement over the Ramsey Cells region is expected to be between 450 and 660. This can be considered as a satisfactory

improvement, as we aim for about 500 (see section 3.2). Additionally, as it is suggested by our results with the Pb-foil ISS (Figure 3.23), adding a longer ISS (with the same diameter) could enhance this improvement even more.

3.8.2 Calculation of dBz/dz and dBz/dr after Field Cooling (FC)

This is done by simulating a tube that is initially in the normal state and in a uniform field. It is then field cooled (FC) through its SC transition and the distortion of the field due to the Meissner effect is evaluated. This was done for a series of cylinders with different effective thicknesses but with the same L/D =1.90 as previously. A full-size ISS with this latter ratio is likely to have a length of 1m and diameter of 0.525 m. The calculations of the effect on field homogeneity were done for this size of ISS with thicknesses from 1mm to 5mm.

Figure 3.33 shows the QF field map output for such an ISS in a $\approx 5\mu$T field. As expected, the maximum distortion occurs near the edge of the ISS but the region in the centre is rather uniform.

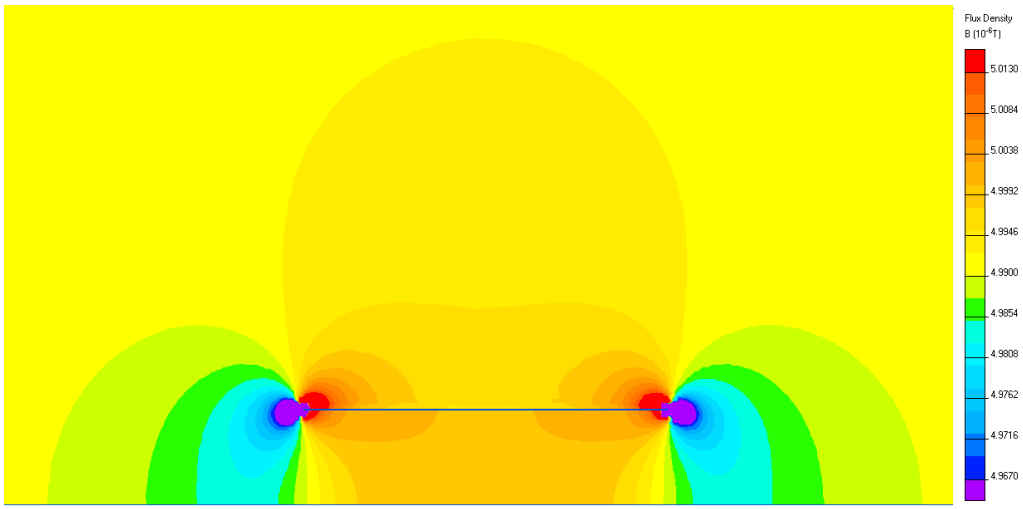

Figure 3.33: Quick Field output for a superconducting 1m long cylinder with diameter 0.525m and thickness 3 mm after cooling in a 5 μT field. The colour scale on the right hand represents a total variation of $\approx$ 50nT (from about 4.967 to 5.013 μT).

Figure 3.34 shows the z-component of the flux density as a function of z along the main axis, r=0, and for radial distances of 75 mm and 150 mm from it. z=0 corresponds to the centre of the ISS tube. We note that just before the entrance of the SC tube, the field drops by about 12 nT within from the value of 4.992 μT of the applied field. The field then smoothly increases as we move inside the tube exceeding the background level, due to the Meissner effect. The Ramsey Cells lie between -0.06 m <z <+0.06 m and 0

mm <r <125 mm, where the field gradient is about 0.6 nT/m for r=0 and even less as we move away from the main axis. This number is less than our design figure of 1 nT/m.

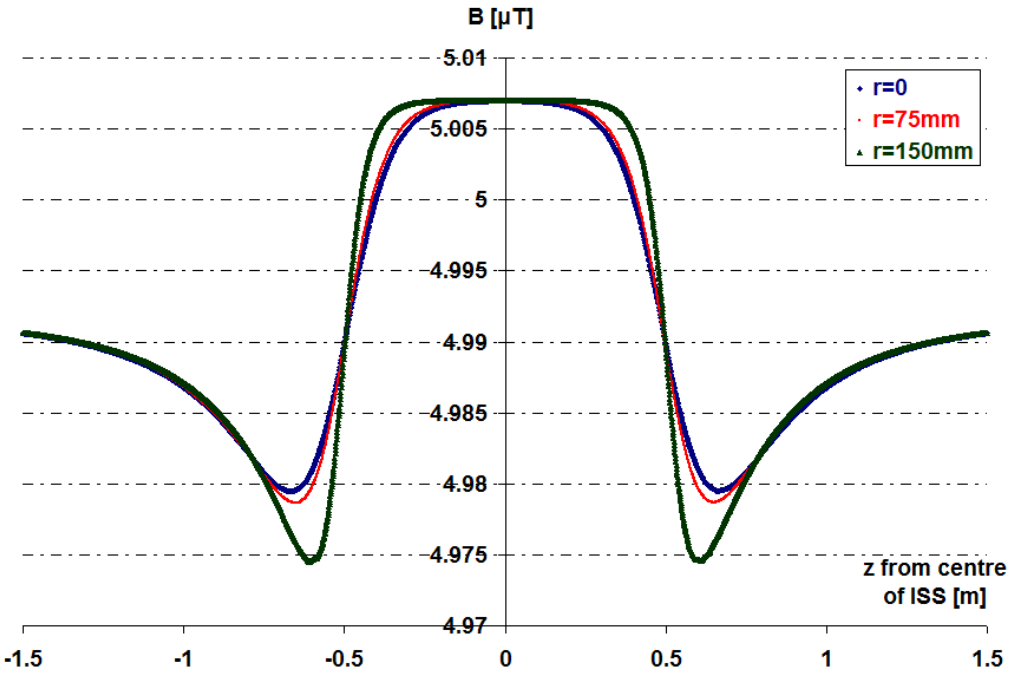

Figure 3.34: Plot of Bz as a function of z obtained from Quick Field for 1m long/0.525m diameter 3 mm thick cylinder after cooling in a ≈5 μT field for three different radial distances. The field drops before the entrance of the SC ISS tube and then increases above the level of the applied field (4.992 μT) inside. The field is quite uniform (dBz/dz = 0.6 nT/m for r=0 and even less away from the main axis) within the volume of the Ramsey Cells (-0.06 m <z <+0.06 m and 0 mm <r <125 mm).

Figure 3.35 shows the value of dBz/dz calculated by QF as a function of the thickness of the ISS. The gradients are again measured from -0.1 m <z <+0.1 m on the axis of a 1m long and 0.525 m diameter shield. As expected, dBz/dz is increasing with tube thickness but for all values below 5 mm the gradient is below our design criterion of 1 nT/m.

3.9 The Effect of Geometrical Imperfections in the ISS on B-field Homogeneity.

At some level, any practical realisation of an ISS will be neither perfectly cylindrical nor perfectly uniform in thickness. Providing that the cross section is constant over the length of the shield, any departure from circularity should not cause problems. The same is not obviously true for a variation in thickness of the superconductor.

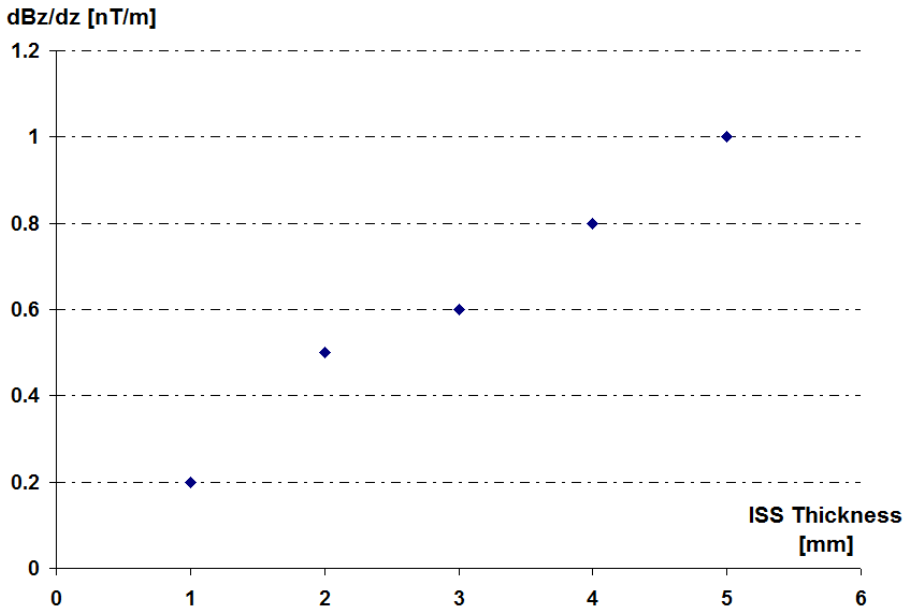

Figure 3.35: Quick Field results for dBz/dz for 1m long/0.525m diameter SC tube of thicknesses between 1 to 5 mm along its main axis and for -0.1m < z < +0.1m (Ramsey Cells region). The maximum gradient we can tolerate within this region (dBz/dz < 1nT/m) corresponds to a 5 mm thick tube.

In an attempt to estimate this latter effect, we have modelled the case of a SC lump on the inner surface of the ISS.

3.9.1 Effect of a SC lump on B-field homogeneity

We assume that the departure from homogeneity at the Ramsey Cell can be treated as the extra field coming from a dipole on the surface of the ISS. We first calculate the maximum allowed value of the dipole moment satisfying our design requirement that dBz/dz <1 nT/m everywhere inside the cell. We then estimate the size of the SC lump which would produce this value of the moment.

The geometry is given in Figure 3.36. We consider the case where the lump is at the closest possible position (P) to the Ramsey cells, that is at z=0.

The magnetic field at position $\vec{r}$ (point Q) from the dipole is given by the known equation [66]:

$$B(\vec{r}) = \frac{\mu_o}{4\pi} \left(\frac{3\vec{r}\,(\vec{m}\cdot\vec{r})}{r^5} - \frac{\vec{m}}{r^3}\right) \tag{3.24}$$

We consider that $\vec{m} = m\hat{k}$, thus the z-component of the B-field is equal to:

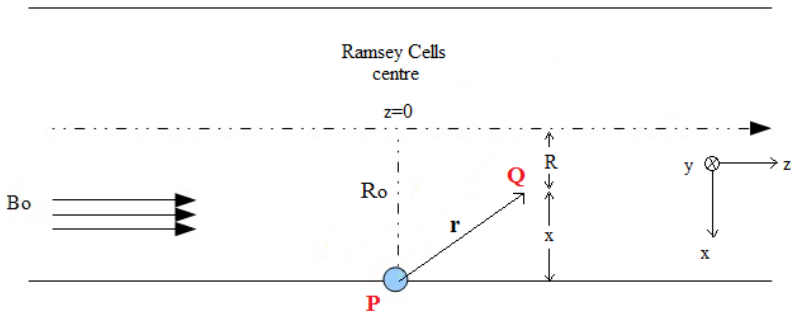

Figure 3.36: The SC lump on ISS (blue area) placed at the closest position to the Ramsey Cells. The dashed line shows the symmetry axis of the 0.525 m diameter ISS tube.

$$B_z = \frac{\mu_o}{4\pi} m \frac{2z^2 - x^2}{(x^2 + z^2)^{5/2}} \tag{3.25}$$

Therefore:

$$\frac{dB_z}{dz} = \frac{\mu_o}{4\pi} m \frac{9zx^2 - 6z^3}{(x^2 + z^2)^{7/2}} \tag{3.26}$$

with $x = R_o - R$ where R_o is the radius of the ISS and R is the distance off axis. For our usual value of $R_o = 0.525/2$ $m = 0.2625$ m and with $R = 150$ mm and $-0.06m \leq z \leq +0.06m$, means that m<8.4×10^{-7} Am^2 to get $dB_z/dz \leq 1$ nT/m over the whole Ramsey Cells volume (see Figure 3.37).

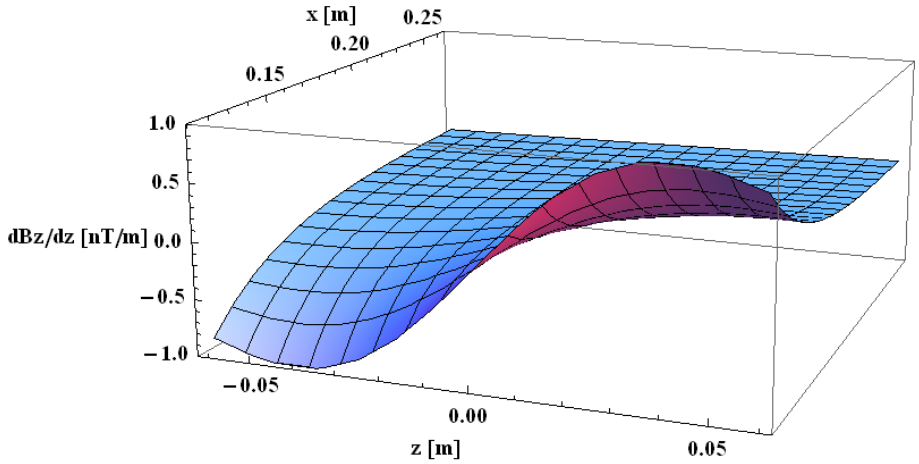

Figure 3.37: $dB_z/dz < 1nT/m$ within the Ramsey cells region ($-0.06m \leq z \leq +0.06m$ and $0.1125m \leq x \leq 0.2625m$) for $m_{max} = 8.4 \times 10^{-7} Am^2$.

By equating the lump to a single ring of superconductor and using the standard result for the inductance of a thin loop ($L \approx \mu_o b \ln(\frac{8b}{\alpha} - 2)$), it is easy to show that:

$$b = (\frac{\mu_o m \ln(8\frac{b}{\alpha} - 2)}{\pi^2 B_o})^{1/3} \tag{3.27}$$

where b is the radius of the loop and α its thickness. With $B_o = 5\ \mu T$ and $\alpha \approx 1$ mm, this gives:

$$b_{\max} \approx 4 \text{ mm} \tag{3.28}$$

The above estimates are based on meeting the design field gradient at the outside edge of the Ramsey Cell, where the effect of the lump will be about ≈40 more severe than on axis. Given that the thickness of the ISS will be about 10 μm, it is very unlikely that there will be imperfections of millimeter dimensions and hence the occurrence of realistically sized SC lumps on the inner surface would not seem to pose any potential threat.

3.10 Specification and Implementation of a Full-size ISS

3.10.1 Geometry

The diameter of the ISS, d_{ISS}, is rather closely restricted since it has to fit between the SCV and the Horizontal Shield (HS), i.e. 500mm $\leq d_{ISS} \leq$ 593mm. A larger d_{ISS} reduces the effect of imperfections whilst a smaller one increases the shielding factor. The length is not so constrained although in the experimental model and in many of the calculations we have chosen lengths equivalent to 1m at full size. This length would not decrease the field homogeneity significantly and would give a sufficient increase in shielding. There is rather weak evidence from Figure 3.23 in section 3.7.1 that the SF increases with length, but there was no indication of a sharp increase at any "magic value". As detailed in section 3.8.2, the thickness of the shield could actually be of the order of a mm but the most important geometrical parameter is the uniformity in thickness. It is also necessary that the ISS is very well aligned parallel to the B-field produced by the solenoid when it cools through its superconducting transition. If this is not the case, it will lead to a reduction in homogeneity.

3.10.2 Shield Material

Of the three types of $1/12^{th}$ scale model ISS tried experimentally, electroplated Sn on Cu is the best in terms of uniformity of thickness. Pb foil is very soft and vulnerable to mechanical damage and deformation and it is difficult to control the thickness of a solder

coating on Cu. The plated Sn layer is clearly sufficiently thick and pure to have a transition at the bulk value and there has been no evidence of any corrosion or reduction in TC with ageing over a two year period. The commercial electroplating specialists who made our samples are also confident that a full-size shield can be made in the same manner.

The stable mechanical support of the Sn option would be provided by the Cu tube, although it may be advisable to mount this on a composite former. The same would apply to a solder-coated Cu tube, although a Pb or solder-coated Cu foil would need support.

3.10.3 Thermal

In order to ensure a uniform field, with no trapped flux, the whole ISS needs to go superconducting at the same time. This in turn means it must be in good thermal contact with a support which itself is at a uniform temperature and thus needs to be a good thermal conductor. Again, a Cu support is indicated with the thermal contact being best in the case of the Sn plated option.

Attention will need to be paid to the thermal links between the ISS support and the thermal reservoirs to ensure that there are no thermally induced electrical currents flowing when the shield goes superconducting.

3.10.4 Configuration

The ISS can be mechanically coupled to either the SCV or the HS, and it can be (independently) thermally linked to either, giving four possible configurations. These options are shown in Table 3.7. Clearly, it is simpler to link it both mechanically and thermally to one or to the other, but this brings other disadvantages. Mechanical linking to the HS gives the best alignment whereas the stability of the field is best when the ISS is locked to the SCV. A permanent thermal link to the HS means Sn cannot be used but the ISS can be cycled above its superconducting transition more rapidly to allow field changes. Permanent thermal linkage to the SCV permits the use of Sn but the cycle time is much longer. The best option would appear to be to have a switchable thermal link between the ISS and the SCV if this can be arranged (the fifth configuration in the following Table).

3.11 Conclusions

We have shown experimentally that by building and using a scale model of the SC parts of the real apparatus that we can reproduce the present shielding factor from the outer shield/solenoid combination. We have proposed a technique to increase the cryogenic SF

Configuration	T_{ISS}	Sn	Pb	B Cycle	B Align	B Stability
Thermal:SCV Mechanical:SCV	0.6K	Yes	No	8 days	OK	Best
Thermal:SCV Mechanical:HS	0.6K	Yes	No	8 days	Best	OK
Thermal:HS Mechanical:HS	4.2K	No	Yes	2 days	BestK	OK
Thermal:HS Mechanical:SCV	4.2K	No	Yes	2 days	OK	Best
Thermal:SCV/HS Mechanical:SCV	0.6K	Yes	No	2 days	OK	Best

Table 3.7: ISS thermal and mechanical configurations.

to the required level and have shown experimentally that an ISS of ≈0.5 m diameter and ≈1 m long is expected to enhance the magnetic shielding by at least a factor of 450.

We have investigated several methods of construction for the ISS and conclude that a ≈10 m thick Sn layer electroplated onto a copper cylinder is a feasible and relatively simple method for the construction of a full-size shield.

We have made a number of calculations and simulations to investigate the effect that an ISS, including thickness imperfections, would have on the homogeneity of the main magnetic field for resonance. We conclude that, particularly for a practical realization of a Sn-coated copper ISS, any changes to the homogeneity should be well within the design criteria.

Finally, various configurations for the incorporation of the ISS into the HS have been considered. The most convenient of these would need to have a switchable thermal link between the SCV and the ISS.

Chapter 4

The Polarisation Holding Field Along the Neutron Guides

The magnetic field along the neutron guides from the exit of the polariser to the Ramsey Cells is discussed in this chapter.

As described in Chapter 2, the cold neutron beam passes through the polariser in which there is a vertical magnetic field of ≈30 mT (≈300 Gauss). The maximum polarisation of the exiting cold beam is expected to be about 90%. In order to maintain their spin polarisation, the neutrons must remain in a well-defined holding field throughout the rest of the apparatus. Depolarisation can occur if the motion of a neutron through a local gradient in the field gives rise to a time-varying transverse component of the B-field at the Larmor (resonance) frequency corresponding to the mean local (quasi-static) field. This fluctuating B-field thus induces a spin-flip and the rate at which this occurs is characterised by a local value of T_1, the longitudinal relaxation time, where:

$$P_z(t) = P_z(0)\ e^{-t/T1} \tag{4.1}$$

and P_z is the projection of the vector sum, $\vec{P}$, of the neutron spins in a field $\vec{B} = B_z\hat{z}$, as shown in Figure 4.1

The degree of depolarisation of a beam of cold or ultra cold neutrons passing through the apparatus from the polariser to the Ramsey cell, and eventually to the detectors, thus depends on the average field, the field gradient and the speed of the neutrons at each point in their trajectories.

For neutrons travelling quasi-ballistically along the guides (which is certainly the case for the cold neutrons in the source), it is sufficient to consider just their mean translational velocity. The holding field requirements can then be expressed rather simply in terms of

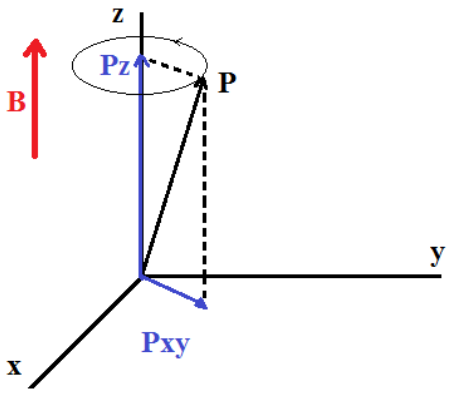

Figure 4.1: The polarisation vector and its projections on z-axis and xy-plane.

the adiabaticity condition mentioned in Chapter 2 and developed further below. On the other hand, for UCN, whose motion is essentially a random walk, much like molecules in a low density gas, a more detailed approach may be needed. We outline below an analytic calculation of T_1 which takes into account this motion of the neutrons within the guides of our apparatus. For the case of a UCN population drifting through regions where the field geometry is rather complicated, a Monte Carlo (MC) calculation, in which the spin of each neutron is tracked, is a more appropriate technique. We have two MC routines available at Sussex and some results from these for the effect of the expected holding fields are presented here.

There are a number of complicating hardware-related factors involved in determining the actual holding fields in the apparatus, mostly due to the presence of various μ-metal and other high-permeability shields. In order to optimise the holding field, we have simulated the full experimental apparatus in OPERA [67], a finite-element electromagnetic simulation package. This has allowed us to model the effect of changing the currents in the various coils and hence to produce vector B-field maps of the critical regions, particularly at the entrance to the horizontal shields. These maps were then used in MC simulations to estimate T_1 and the degree of depolarization.

4.1 Specification of the Polarisation Holding Field

We discuss here three ways which can be used to estimate whether a particular holding field will preserve the polarization.

4.1.1 The Adiabaticity Condition

In order for the neutron magnetic moment to retain its orientation with respect to $\vec{B}$, its Larmor precession frequency, ω_L, has to be large compared to the frequency ω_P associated with the change of the magnetic field as this is seen by the moving neutron. This yields the adiabaticity condition ([47], section 2.1.3) that :

$$\frac{1}{B}\left|\frac{\partial B}{\partial t}\right| = \omega_P << \omega_L = \gamma B \tag{4.2}$$

For azimuthial symmetry and assuming $\nabla \cdot \vec{B} = 0$, ω_P reduces to:

$$\omega_P = \frac{1}{B}\left|\frac{\partial B}{\partial t}\right| = \frac{1}{B}\left|\frac{\partial B_z}{\partial z}\frac{\partial z}{\partial t}\right| = \frac{1}{B}\left|\frac{\partial B_z}{\partial z}\right| v_n \tag{4.3}$$

where v_n is the velocity of the neutron moving parallel to z. The adiabaticity condition becomes:

$$\left|\frac{\partial B}{\partial z}\right| \ll \gamma B^2 / |v_n| \tag{4.4}$$

or in terms of the adiabaticity parameter k:

$$k = \frac{\gamma B^2}{\left|\frac{\partial B_z}{\partial z}\right|} \gg 1 \tag{4.5}$$

Figure 4.2 shows the maximum values of the field gradient such that $k \geq 10$ for UCN having $v_n = 7\ m/s$, over the range of values of B relevant to our experiment. For cold neutrons with $v_n = 400\ m/s$ the permitted values of the gradient are ≈ 60 times lower.

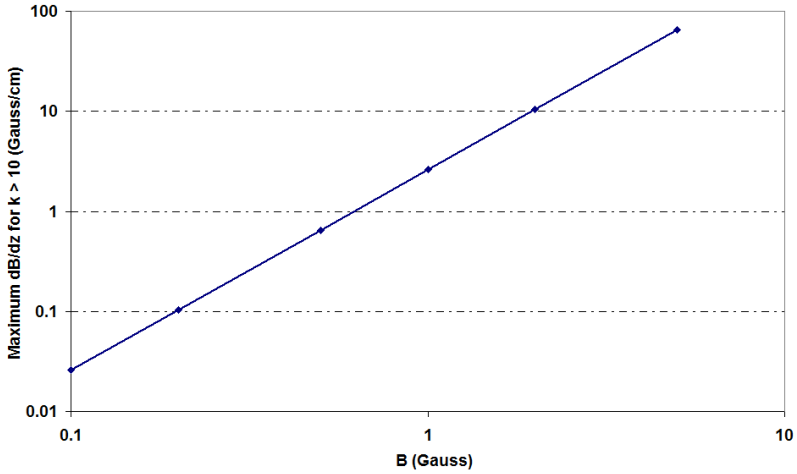

Figure 4.2: Maximum values of $\left|\frac{\partial B_z}{\partial z}\right|$ such that the adiabaticity condition is met for UCN with $v_n = 7\ m/s$, over a relevant range of B.

4.1.2 Analytic Calculation of T1 for UCN

The adiabaticity condition is strictly relevant only to neutrons moving through a field gradient without collisions. This is not the case for UCN since they move like a low pressure ideal gas, bounce off the containment surfaces and diffusing slowly along guides. Pendlebury [68] has derived formulae for T_1 for UCN in a field gradient, taking account of their actual motion.

In this section, we attempt to give a more detailed approach based on his work. The underlying idea of the following analysis is that the magnitude of the polarisation of the ensemble of neutrons is directly related to the z-projection (P_z) of the vector sum ($\vec{P}$) of the neutron spins (see figure 4.1). Any alteration of the orientation of ($\vec{P}$) will result in the change of its z-projection and therefore to neutrons polarisation. So essentially, we are trying to estimate the time dependence of the ($\vec{P}$) vector alignment in space.

We consider a square guide tube with its symmetry axis along z (see figure 4.3). The magnetic field within the tube is provided by a series of circular coils whose diameter is about one order of magnitude bigger than the width of the guide tubes (0.5-1 m compared to ≈7 cm / see also section 2.5.3). This results in a total field ($B = \sqrt{{B_x}^2 + {B_y}^2 + {B_z}^2}$) which does not change significantly with $r = \sqrt{x^2 + y^2}$. The change between the central axis (r=0) and the extremes of the tubes ($r \approx 7cm$) for the narrowest coils ($\phi = 0.5m$) is about 7% and about 2% for the widest one ($\phi = 1m$). So it is a very good approximation to consider that the magnitude of the total B field remains the same. However, the vector $\vec{B}$ deviates from the z-axis as we move radially outwards and thus the neutrons heading to the walls experience a rotating field in their reference system. We consider here the idealised case of a neutron moving perpendicularly to the z-axis, say along x-axis.

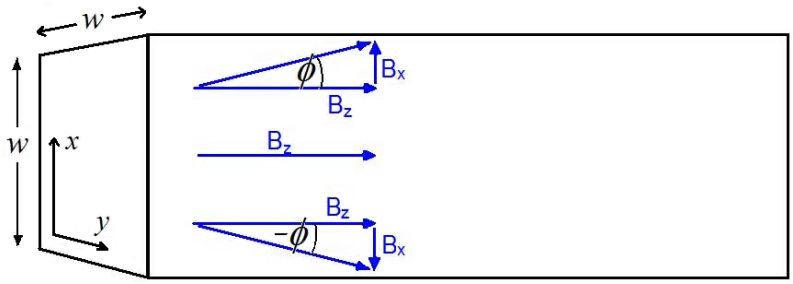

Figure 4.3: $\vec{B}$ field in the guide tubes as seen by a neutron traveling along the x-direction

If f_c is the collision frequency of a UCN on all four walls (2 perpendicular to the x-axis and 2 perpendicular to the y-axis), then, given that in a square tube the collisions are equally frequent along the x and y directions, then $f_c/2$ describes how often UCNs hit the

walls perpendicular to the x-axis:

$$f_c^x = \frac{f_c}{2} \tag{4.6}$$

The time between two successive collisions for UCN in our guides is about:

$$t_c^x = \frac{w}{v_{ucn}} \approx \frac{7\ cm}{7\ m/s} = 0.01\ s \tag{4.7}$$

so the collision frequency is about $f_c^x = 100$ Hz. The assuption that is quietly hidden here is that the neutron spin must always be able to follow the $\vec{B}$ vector. That can be achieved only if its Larmor frequency is bigger (or at least equal) than (to) the frequency by which $\vec{B}$ changes direction. In other words, the neutron spin must precess at least once (over 2π) during the maximum change in $\vec{B}$. Ideally, the UCN should precess many times. The minimum field that satisfies this requirement is tiny:

$$\omega = \gamma B_{min} \Rightarrow B_{min} = \frac{2\pi/0.01}{1.8 \cdot 10^8}\ T = 3.5\ \mu T = 35\ mG \tag{4.8}$$

Hence, as a neutron moves across the tube and precesses around the holding field, the latter seems to rock through the small angle 2ϕ which is the total opening angle between the two walls perpendicular to the x-axis (see Figure 4.3):

$$2\phi \approx 2tan\phi = 2\frac{B_x}{B_z} \tag{4.9}$$

Here B_x is the x component of the magnetic field at the extremes of the tube. The $\vec{B}$ field rotation frequency is:

$$\vec{\omega}_{rock} = \frac{2\phi}{t_c^x}\ \hat{y} = \frac{2\phi}{2/f_c}\ \hat{y} = \frac{B_x}{B_z} f_c\ \hat{y} \tag{4.10}$$

By moving to another coordinate system which rotates with a frequency equal to $\vec{\omega}_{rock}$, we see the $\vec{B}$ vector as static and neutron's spin as still precessing. The equation of motion for the magnetic moment:

$$\frac{d\vec{\mu}}{dt} = \vec{\mu} \times (\gamma \vec{B}) \tag{4.11}$$

has to change in order to adjust to the rotating frame whose unit vectors are rotating with frequency $\vec{\omega}_{rock} = \omega_{rock}\ \hat{y}$:

$$\frac{d\hat{x}_i}{dt} = \vec{\omega}_{rock} \times \hat{x}_i \tag{4.12}$$

where i=1,2,3 correspond to the $\hat{x}, \hat{y}, \hat{z}$ unit vectors. We have:

$$\frac{d\vec{\mu}}{dt} = \frac{\delta\mu_i}{\delta t}\hat{x}_i + \mu_i\frac{d\hat{x}_i}{dt} = \frac{\delta\vec{\mu}}{\delta t} + \mu_i(\vec{\omega}_{rock} \times \hat{x}_i) \Rightarrow$$

$$\frac{d\vec{\mu}}{dt} = \frac{\delta\vec{\mu}}{\delta t} + (\vec{\omega}_{rock} \times \vec{\mu}) \tag{4.13}$$

where $\frac{\delta\vec{\mu}}{\delta t}$ is the time derivative of $\vec{\mu}$ in the rotating reference frame. Substituting into equation 4.11 leads to:

$$\vec{\mu} \times (\gamma\vec{B}) = \frac{\delta\vec{\mu}}{\delta t} + (\vec{\omega}_{rock} \times \vec{\mu}) \Rightarrow \frac{\delta\vec{\mu}}{\delta t} = \vec{\mu}\gamma(\vec{B} + \frac{\vec{\omega}_{rock}}{\gamma}) \tag{4.14}$$

where the extra magnetic field term is along the y-direction:

$$\vec{B}^* = \frac{\omega_{rock}}{\gamma}\ \hat{y} = (\frac{B_x}{B_z})(\frac{f_c}{\gamma})\ \hat{y} \tag{4.15}$$

Equation 4.14 implies that the magnetic field $\vec{B}$ in the rotating reference frame has to be replaced by an effective or resultant field $\vec{B}_R$ which is the vector sum of $\vec{B}_z$ (recall that our main field is along the z axis) and $\vec{B}^*$ (see figure 4.4(a)):

$$\vec{B}_R = \vec{B}_z + \frac{\vec{\omega}_{rock}}{\gamma} = B_z\ \hat{z} + \frac{\omega_{rock}}{\gamma}\ \hat{y} \tag{4.16}$$

We consider the spin vector ($\vec{s}$) which initially precesses about the resultant field $\vec{B}_{R1}$ (see figure 4.4(b)) where we can see the trajectory of its tip (not of the neutron itself) on the xy plane. A collision takes place at the point P_{col} which is on a surface perpendicular to the x-axis. At the moment of collision, $\vec{B}_z$ remains the same but $\vec{\omega}_{rock}$ changes orientation abruptly and therefore so $\vec{B}^* = \frac{\vec{\omega}_{rock}}{\gamma}$ does too.

As we mentioned at the beginning of this section, we are interested in finding the orientation of the spin vector with respect to the holding field at any given time. The magnitude that we can use and have to follow for this purpose is the "distance" of the spin tip from the resultant magnetic field just before and just after the collision. From the geometry of figure 4.4(c) we see that the coordinates of the $\vec{r}_1$ and $\vec{r}_2$ vectors are:

$$\vec{r}_1 = r_1 sin\phi\ \hat{i} + r_1 cos\phi\ \hat{j} \tag{4.17}$$

$$\vec{r}_2 = r_1 sin\phi\ \hat{i} + (r_1 cos\phi + S(2\theta))\ \hat{j} \tag{4.18}$$

Thus the distance before the collision is r_1 while after is:

$$r_2 = \sqrt{r_1 + (2S\theta)^2 + 2S\theta r_1 cos\phi} \tag{4.19}$$

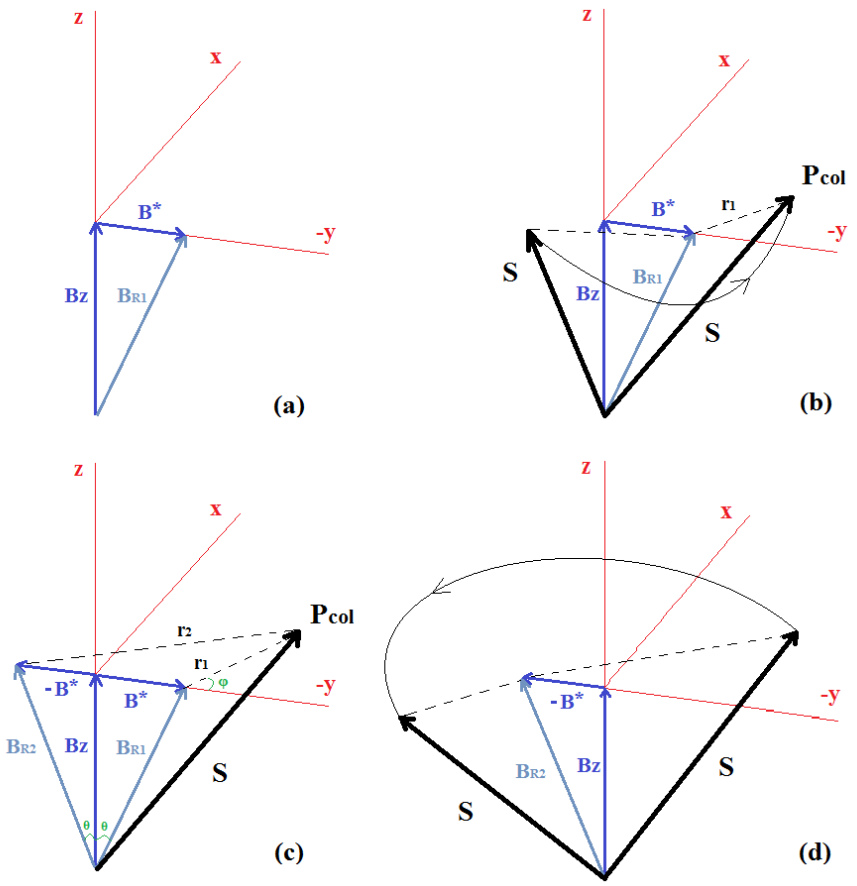

Figure 4.4: The spin tip motion -with respect to the rotating frame- before and after a collision where an abrupt change in the magnetic field occurs: (a) Before the collision, the resultant magnetic field $\vec{B}_{R1}$ in the rotating reference frame is the vector sum of $\vec{B}_z$ and $\vec{B}^*$ which depends on the collision frequency of neutrons (for relative equations see text). (b) The neutron spin vector ($\vec{s}$) precesses about the resultant field $\vec{B}_{R1}$. (c) At the collision point P_{col}, the resultant magnetic field -as this is seen by neutron- changes abruptly from $\vec{B}_{R1}$ to $\vec{B}_{R2}$, due to the abrupt orientation change of the rocking frequency $\vec{\omega}_{rock}$ ($\vec{B}_z$ remains unchanged). (d) Finally, neutron spin vector precesses around the new resultant field $\vec{B}_{R2}$.

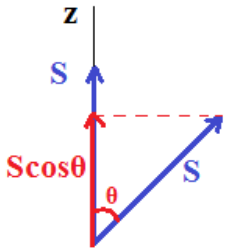

Figure 4.5: The spin vector deviation from the z-axis

Averaging over all ϕ's (we consider a uniform distribution between 0 and 2π), the expectation value of r_2 becomes:

$$\langle r_2^2 \rangle = \langle r_1^2 \rangle + (2S\theta)^2 \tag{4.20}$$

which leads to:

$$\langle S_{xy2}^2 \rangle = \langle S_{xy1}^2 \rangle + (2S\theta)^2 \tag{4.21}$$

where S_{xy} is the projection of the spin vector onto x-y plane. Equation 4.21 tells us that after each wall collision the square of this projection changes by $(2S\theta)^2$. Isolating the angle term, the average total change in the angle between the spin and the field after N_x collisions on the walls perpendicular to the x-axis is given by:

$$\langle \theta_{tot}^2 \rangle = N_x(2\theta)^2 = t f_c^x (2\frac{B^*}{B_z})^2 = t\frac{f_c}{2}(2\frac{B^*}{B_z})^2 \tag{4.22}$$

where in this last equation we consider that the inhomogeneities in the applied field are relatively small, and that therefore B^* and θ are also quite small such that $tan\theta \approx \theta$.

Keeping the classical approach of this analysis, if we consider that the spin vector of a neutron was initially aligned along the z-axis, then after N_x collisions on half of the walls, it has deviated by the angle θ_{tot} (see figure 4.5) and the new S_z is now:

$$S_z = S - S\ cos\theta_{tot} \tag{4.23}$$

Hence, the reduction in the z-component, and therefore in the contribution of each spin unit to the polarisation of neutrons is given by:

$$-\frac{dP}{P} = \frac{S(1-cos\theta)}{S} \approx \frac{\theta_{tot}^2}{2} = \frac{t}{T_{1x}} \tag{4.24}$$

Substituting θ_{tot} and B^* from equations 4.22 and 4.15 respectively we find [68]:

$$T_{1x} = \frac{\gamma^2 B_z^4}{B_x^2 f_c^3} \tag{4.25}$$

Similarly for collisions on the walls perpendicular to the y-axis, we have:

$$T_{1y} = \frac{\gamma^2 B_z^4}{B_y^2 f_c^3} \tag{4.26}$$

with B_x to be given by:

$$\frac{\partial B_x}{\partial x} = \frac{B_x - 0}{w/2} \Rightarrow B_x = \frac{w}{2}\frac{\partial B_x}{\partial x} \tag{4.27}$$

and a similar expression for B_y. In the case of cylindrical symmetry, and using $\nabla \cdot \vec{B} = 0$ we can substitute the gradients along x and y with:

$$\frac{\partial B_x}{\partial x} = \frac{\partial B_y}{\partial y} = -\frac{1}{2}\frac{\partial B_z}{\partial z} \tag{4.28}$$

The total spin relaxation time is then given by:

$$\frac{1}{T_1} = \frac{1}{T_{1x}} + \frac{1}{T_{1y}} \tag{4.29}$$

Since $T_{1x} = T_{2x}$ this leads to:

$$\frac{1}{T_1} = \frac{2}{T_{1x}} \Rightarrow T_1 = (\frac{8\gamma^2}{w^2 f_c^3})\ \frac{B_z^4}{(\partial B_z/\partial z)^2} \tag{4.30}$$

or:

$$T_1 = \frac{8\gamma}{f_c} k^2 \tag{4.31}$$

where k is the adiabaticity parameter defined previously. Figure 4.6 shows T_1 as a function of field gradient for UCN having $v_n = 7\ m/s$ moving in a rectangular guide of ≈7 cm width over the range of values of B relevant to our experiment.

It is important to note that since the collision frequency, f_c, for UCN in our guides is about 100Hz, just satisfying the usual adiabaticity condition that $k \geq 10$ leads to a T_1 of only 10 seconds. Since this value is smaller or comparable with the fill and emptying times in the experiment, values of $k \approx 100$ or higher are required to ensure that no significant depolarisation can occur.

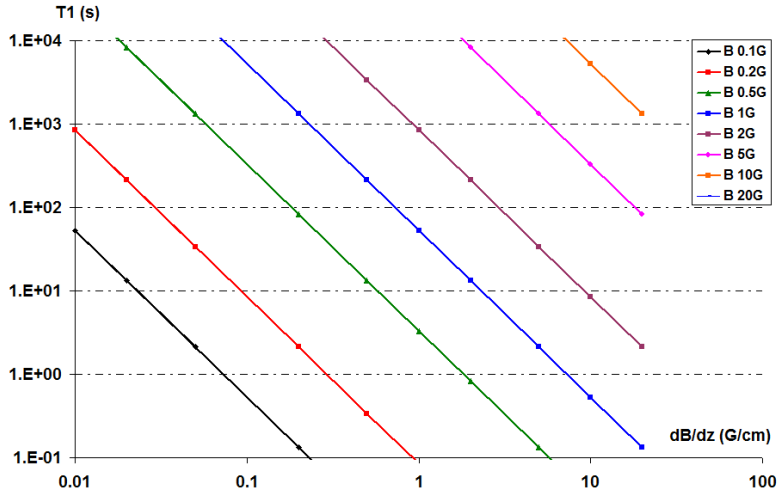

Figure 4.6: T_1 as a function of field gradient for UCN having $v_n = 7\ m/s$ moving in a rectangular guide of ≈7 cm width in various strength fields.

4.1.3 Monte Carlo Simulations

The adiabaticity condition and the analytic calculation of T_1 outlined above are most easily applied to cases where both the average value of the field and its gradient are roughly constant. However, in the actual experiment, the magnitude of the B-field the neutron encounters varies by four orders of magnitude as it moves in a diffuse random walk between the polarizer and the Ramsey Cell. This can be treated by considering each high-gradient region separately, or by attempting some integration over the different regions. The problem with such an approach is that the internal geometry of the guide is relatively complicated and may lead to the neutrons spending more time in some regions than in others, all the while bouncing off the walls. The most elegant way of determining the neutron depolarisation is to use a Monte Carlo technique which calculates and tracks both the motion of the neutron in the guides and the motion of the neutron spin in the magnetic field at the same time. Two MC simulations are available at Sussex. The first can deal with individual regions of the apparatus at a time whereas the second, which is still under development, models almost the entire system from the source to the Ramsey Cells. In both cases a map of the magnetic field is loaded into the simulation and the output is then usually the density and the net polarization of the neutron population at a specific location as a function of time. The details of how these MC simulations work is beyond the scope of this thesis but full descriptions are given [69] [70].

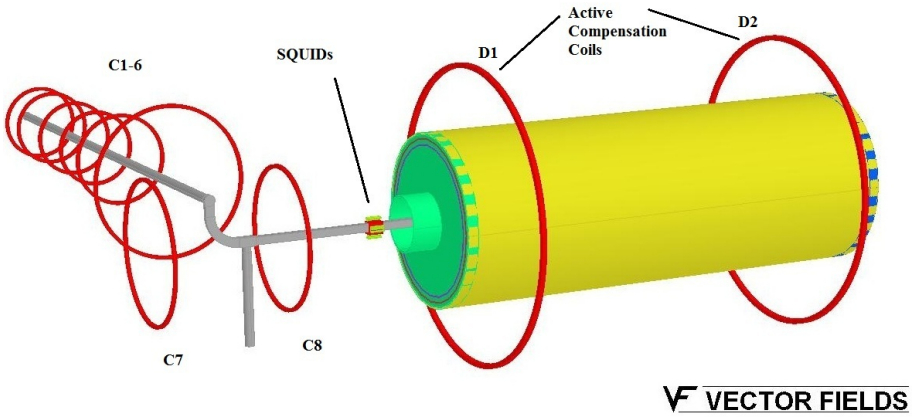

Figure 4.7: The first six of the holding field coils (C1-6) are aligned along the source tube while the last two (C7,8) are on each side of the transfer section. The active compensation coils on the outside of the Horizontal Shields and the SQUID sensors are shown too.

4.2 Experimental Holding Field Profile

At any point in the apparatus, there are a number of different contributions and factors which go to make up the actual holding field seen by the neutrons.

The neutrons see a vertical ≈30 mT (≈300 Gauss) field in the polariser and this has to decrease smoothly in magnitude to ≈1 mT and rotate to become horizontal at the entrance of the source volume. From this point, through the production volume and then along the neutron guides up to the horizontal shield the field is provided by a set of 8 circular coils. Along most of this length, the field from these coils is simply given by the Biot-Savart law for conductors in free space and the condition for an adiabatic change should be relatively easy to determine.

Between the last of the 8 holding field coils (HFC) and the horizontal shields, around the six-way section, the field should ideally decrease smoothly from ≈0.6 mT (6 Gauss) to eventually ≈5 μT inside the solenoid. However, the situation is rather complicated in this region since the field from the last HFC is strongly perturbed by the μ-metal layers within the horizontal shields.

A further final complication is provided by the presence of twelve SQUID sensors, each in its own high permeablilty shield, which are installed very closely around the neutron guide tube, just before the entrance of the horizontal shields.

Figure 4.7 shows the overall arrangement of the holding field coils, the guides and the shields and the position of the SQUIDS. Two further active compensation coils (ACC) are shown in this figure. These are normally intended to be operated in conjunction with an

active feedback loop to offset temporal variations in the laboratory field at each end of the SCV. Not shown in this figure are the two solenoid end correction coils (SECC) at each end of the solenoid and the solenoid coil itself.

It is also important to note that the magnitude of the holding fields can be such that the Earth's field in the laboratory cannot be ignored. This is particularly true near the entrance to the horizontal shields.

The neutron guides sit mostly inside tubes of ≈160 mm diameter which contain the superfluid ^4He. As will become painfully apparent in Chapter 6, some of the seals on these tubes are made of superconducting Indium. The resulting superconducting rings are hence concentric with many of the coils shown in Figure 4.7.

4.2.1 Earth's Field

The Earth's field has been measured about 5 meters away from the horizontal shields (on the platform above the entrance to the source tube) and found to be about 40.6 μT (≈ 0.4 G) with components as presented on Figure 4.8. These are the values used in the OPERA simulations presented later in this chapter.

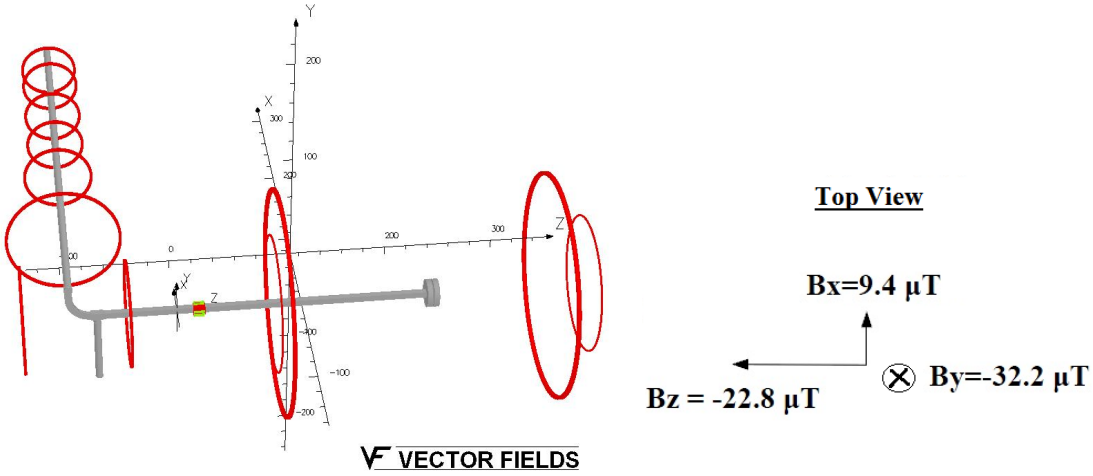

(a) Axes Convention (b) B_{earth} components

Figure 4.8: Earth's magnetic field as measured above the entrance of the source tube and coil C1, ≈ 5 m away from the mu-metal shields. Axes convention is shown on the left. The solenoid end compensation coils (small diameter) and the active compensation coils (large diameter) are also shown here on each side of the Ramsey cells.

It should be noted here that the z-component of the Earth's field along the guide tube after the 90^o section is opposing the field from the coils on this axis (C7 and C8); it points from the HV flange towards the rectangular box while the coils are normally set up to

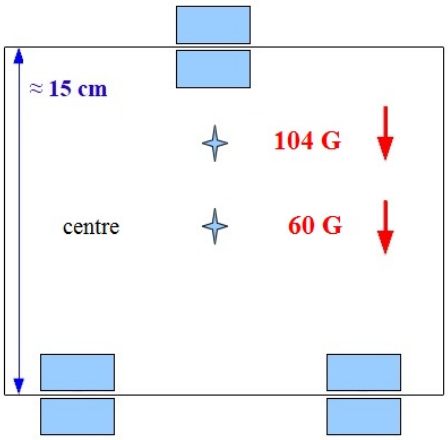

Figure 4.9: The field after the polariser as measured with a Hall Magnetometer during November 2010.

produce a field in the downstream direction.

4.2.2 Field after the polariser

The field just after the exit of the polariser has been measured during November 2010 run. The field in the polariser is about 30 mT (300 Gauss) downwards and at the nozzle of it, three pairs of small (about 2cm x 2cm x 1cm) permanent magnets are placed in a square frame (see Figure 4.9). Their distance from the polariser is about 10 cm and about 15 cm from the cryostat flange while the first holding field coil (C1) is about 10cm further along, inside the concrete wall of the casemate.

Over this distance of about 35 cm, the magnets have to turn the field orientation from vertically downwards to horizontal. After having turned all the holding field coils off and using a Hall magnetometer, we measured the field at the centre of the metallic frame and at about 4.5 cm off-centre finding 10.4 mT and 6 mT (104 G and 60 G) respectively. These data give us an idea about how the field is decreasing after the polariser but they are insufficient to have a clear picture of it. Due to lack of space, no further measurements could be made at that time but it is strongly suggested to take more data when an opportunity occurs.

On the basis of the very limited information above, the maximum field gradient in the region between the polariser and the first holding field coil is estimated to be less than 4×10^{-2} T/m, at a mean value field of 1 mT. For cold neutrons with $v_n \approx 400$ m/s, this correspond to an adiabaticity parameter $k \approx 11$ which should be sufficient to preserve their polarisation.

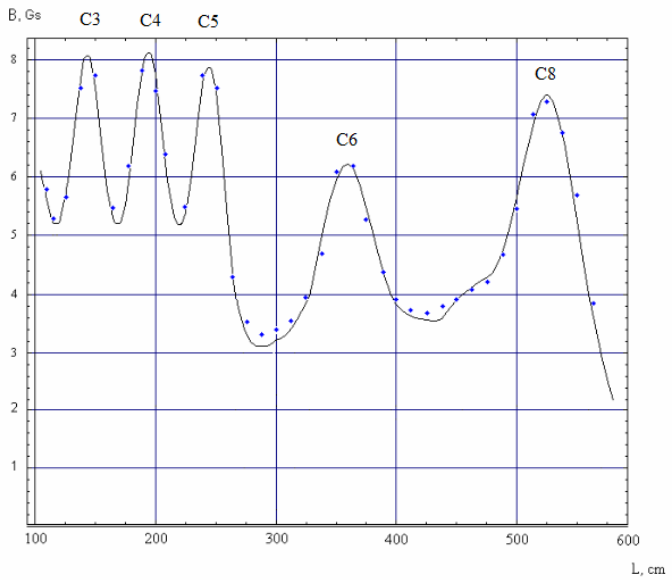

Figure 4.10: The guide field as function of distance along the neutron guide, as measured by Balashov [4] (blue dots) at excitation currents of 6 A for C1-4 and 20 A for C5-8. There is good agreement with the calculated field (continuous line). The field is in the upstream direction from C5 to C3 and downstream at C8.

4.2.3 Magnetic Field from the Holding Field Coils

There are eight circular polarisation holding field coils placed at points along the guide tubes. The first six of these (C1-6) are aligned along the source tube while the last two (C7,8) are on each side of the transfer section, setting up the field along the guides between the rectangular box and the entrance of the horizontal shields. The arrangement is shown Figure 4.7 and the dimensional details were given in section 2.5.3.

The field from these coils has been measured experimentally by Balashov [4]. Figure 4.10 shows the field plotted as a function of the distance along the guide (which is not the same as the distance between the coils), together with the calculated value. The first two coils are not included but they are expected to give very similar fields to coils C3 and C4 as they have a approximately the same geometry. No peak is seen corresponding to C7 since the guide tubes do pass through this coil. It should be noted that these measurements were taken with the field the in the upstream direction in the source tube region and downstream in the region of guides parallel to the horizontal shields. The coil currents for these measurements were 6 A for C1-4 and 20 A for C5-8, values which had been used previously when polarizations of 77% were observed.

The maximum field gradient in Figure 4.10 is approximately 2×10^{-3} T/m (0.2 Gauss/cm).

To get an idea about whether this field configuration is suitable, we consider both cases of neutrons with and without wall collisions. For cold neutrons in the source tube (up to C6) that do not hit the walls, this values of gradient in a field of 0.5 mT leads to an adiabaticity parameter $k \approx 56$. It is worth noting that for such fields k will be directly proportional to the coil currents.

For UCNs with vn $v_n \approx 7$ m/s and taking the guide width as 6 cm, leads to a collision frequency, $f_c = 115$ Hz. Equation 4.31 leads to a spin relaxation time:

$$T_1 \approx 10^7 \ s \tag{4.32}$$

4.2.4 Magnetic Field at the Entrance of the Horizontal Shields

The area between the last holding field coil (C8) and the entrance of the horizontal shields is the most complicated region, as mentioned above, due to the presence of high permeability parts and the fact that the holding fields become comparable to the laboratory field. Nevertheless, it is instructive to make a simplistic calculation ignoring these factors for the moment.

We do this by assuming that the 0.7 mT field at the position of C8 falls as linearly to 5 μT just inside the shields. We then use equation 4.31 for T_1 and integrate this over the region.

We consider the simplest case of a linear drop of the field along z:

$$B_z = B_{C8}(1 - F\frac{z}{L}) \tag{4.33}$$

where B_{C8} is the field value on axis at the position of C8 coil and F is the reduction that B_{C8} has suffered after $z = L$. The axial gradient is:

$$\frac{\partial B_z}{\partial z} = -\frac{B_{C8}F}{L} \tag{4.34}$$

Therefore:

$$\frac{1}{T_1} = \frac{w^2 f_c^3}{8\gamma^2} \int_0^L \frac{(\partial B_z/\partial z)^2}{B_z^4} \, \mathrm{d}z = \frac{w^2 f_c^3}{8\gamma^2} \frac{F^2}{B_{C8}^2 L^2} \int_0^L \frac{1}{(1 - Fz/L)^4} \, \mathrm{d}z \tag{4.35}$$

By doing the following substitutions:

$$1 - F\frac{z}{L} = \alpha \tag{4.36}$$

$$dz = -\frac{L}{F} d\alpha \tag{4.37}$$

we take:

$$\frac{1}{T_1} = \frac{w^2 f_c^3}{8\gamma^2} \frac{F}{B_{C8}^2 L} \int_{1-F}^{F} \frac{1}{\alpha^4} \, \mathrm{d}\alpha \Rightarrow$$

$$\frac{1}{T_1} = \frac{w^2 f_c^3}{8\gamma^2} \frac{F}{3B_{C8}^2 L} \{ \frac{1}{(1-F)^2} - \frac{1}{F^2} \} \tag{4.38}$$

Thus for a reduction factor of $F = (7 - 0.05)\ G\ /\ 7\ G = 6.95/7$, wall collision frequency of $f_c = v_{ucn}/w = 4\ ms^{-1}/\ 0.06\ m \approx 67\ Hz$, $B_{C8} = 7\ G$ and for a linearly decreasing field, the average spin relaxation time of UCNs over the 1m long region between C8 coil and the entrance of the horizontal shields is found to be:

$$T_1 = 1.8\ 10^4 \tag{4.39}$$

Assuming 40 sec to fill the cells and another 40 sec to empty both of them we have a total time of 80 sec for neutrons to move around this area. The contribution to the polarisation loss is then:

$$-\frac{\Delta P}{P} = \frac{T_{storage}}{T_1} = \frac{80}{1.8\ 10^4} \approx 0.5\% \tag{4.40}$$

Hence, if the field could be made to fall linearly, the depolarization would be negligible. Unfortunately, this ideal field profile does not apply here.

4.2.5 Installation of SQUID Sensors on the Neutron Guide

Prior to the November 2010 run, 12 SQUID sensors were installed around the rectangular neutron guide tube near the centre of the six-way section, as shown in Figures 4.11 and 4.12. These particular sensors are encased in tubes made of cryoperm, a low-temperature μ-metal. Placing 12 high permeability tubes about 10 cm long and 1 cm diameter, very close to the neutron guide tubes, is expected to distort significantly the local holding field. They were placed there to have them as close as possible to the SCV, thereby reducing the length of the pick-up loop and therefore electronic noise.

To deal with the expected distortion of the holding field, two coils were wound directly onto the guides and beneath the SQUID cryoperms (Figure 4.11). Ideally one coil would be used but this was not possible due to the presence of two bolts and studs. The two coils were made of two layers of 300 m wire, with density of 66 turns per centimetre. The

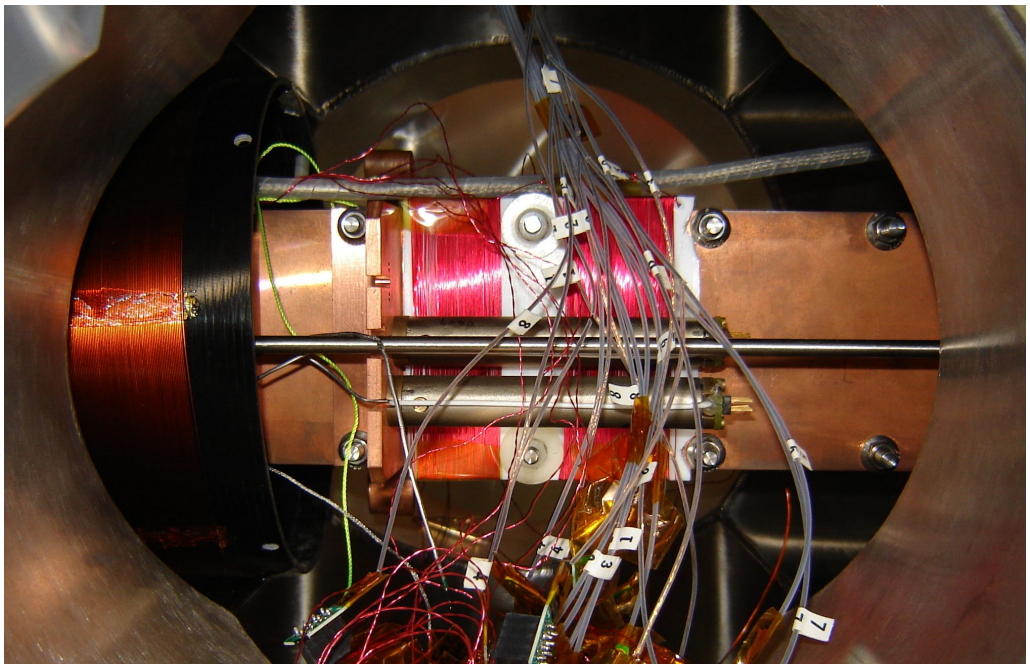

Figure 4.11: A view into the six-way section showing the SQUIDs compensation coils wound directly on the neutron guide. Two of the cryoperm housings can be seen.

first was centred at 2.1 cm from the middle of the SQUIDs with 4.2 cm length and the other one, 3.4 cm long, was positioned at about 2.5 cm on the other side of the SQUID's centre.

More details of the position of the SQUIDs and the compensation coils are shown in Figures 4.13 and 4.14. The axis orientation and the dimensions used for the OPERA simulations can be seen in these figures too. The shape and size of the coils are identical to the outer dimensions of the guide tubes. This information was extracted from the technical details of the SQUIDs mounting given in Appendix D.

The objective goal of the conducted magnetostatic simulations was to find the optimum current values for the coils around the SQUIDs such as we would achieve minimum polarisation losses. Initially, we reproduced experimentally taken data for the field within the SQUIDs. Then we visualised the field configuration for various currents that were already set-up at ILL. Finally, we proposed various sets of currents to compensate for the cryperms effect and two of these were the input of P.H. Harris Monte Carlo simulations to estimate the resulted T_1 relaxation time in this region.

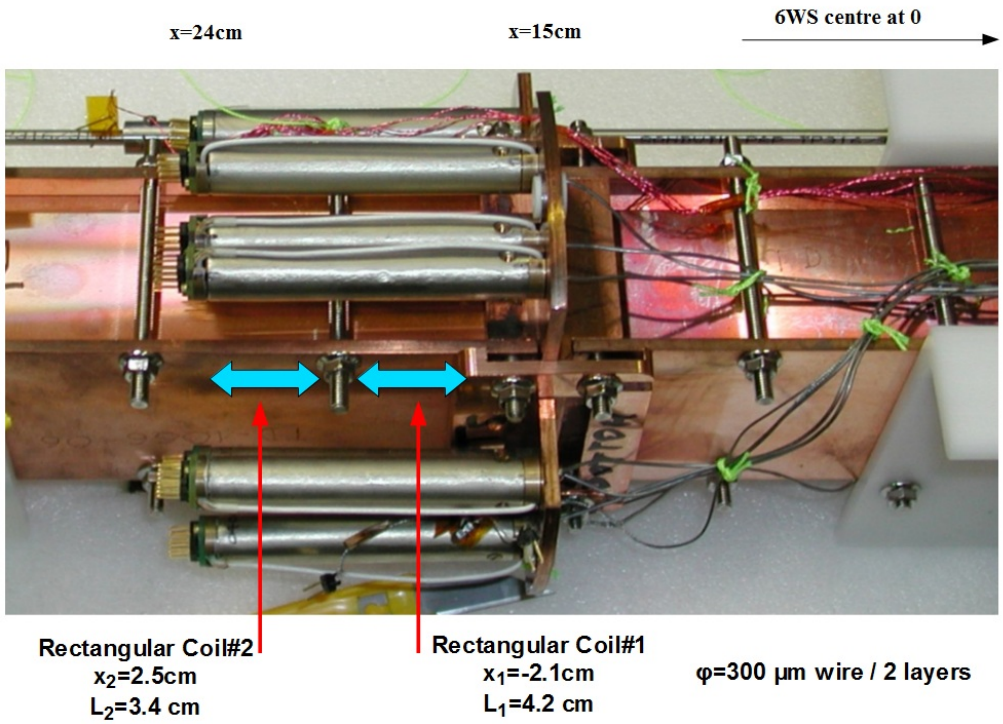

Figure 4.12: A view of the full array of the SQUIDs cryoperm housings mounted on the neutron guide when outside of the apparatus. The compensation coils are not present in this case but the dimensions are given.

4.3 Magnetic Modeling of the Holding Field

The goal of the magnetostatic simulations reported here was to find the optimum values of currents in the various the coils contributing to the holding field, particularly in the region at the entrance to the horizontal shields. Once the full experimental apparatus was modeled in OPERA, the coil currents were adjusted to produce the smoothest field. A full vector field map was then produced and the results of this used as the input for Monte Carlo simulations to estimate T_1.

4.3.1 The Magnetic Model

The full model contains all coils the relevant to the holding field: the holding field coils (HFC) along the neutron guides, the SQUIDs compensation coil (SQCC), the active compensation coils (ACC), the solenoid end compensation coils (SECC) and the solenoid itself. It also incorporates the three μ-metal shields, the μ-metal nose at the 6WS end, and the twelve cryoperm SQUID housings.

The various coils mounted on the carbon fibre former around the SCV have not been included. OPERA is not able to handle superconductors and hence the behaviour of the

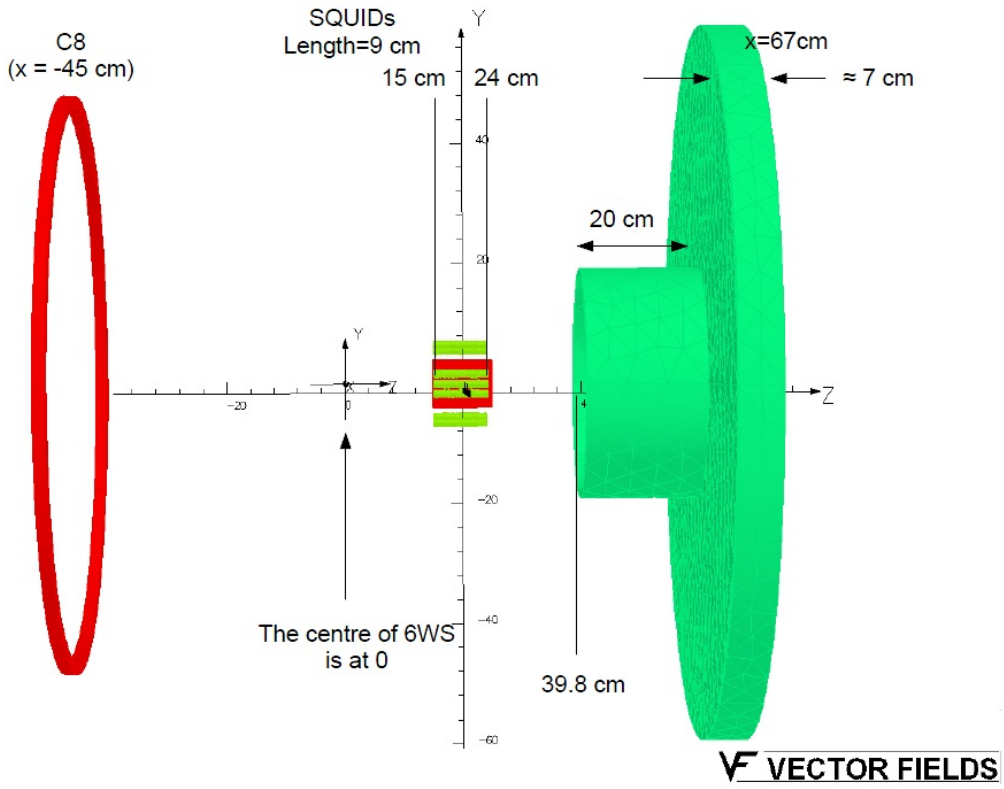

Figure 4.13: The arrangement of the SQUIDs cryoperm housings, coil C8 and the mu-metal nose from the OPERA model. The Horizontal Shields and some of the other coils have been omitted.

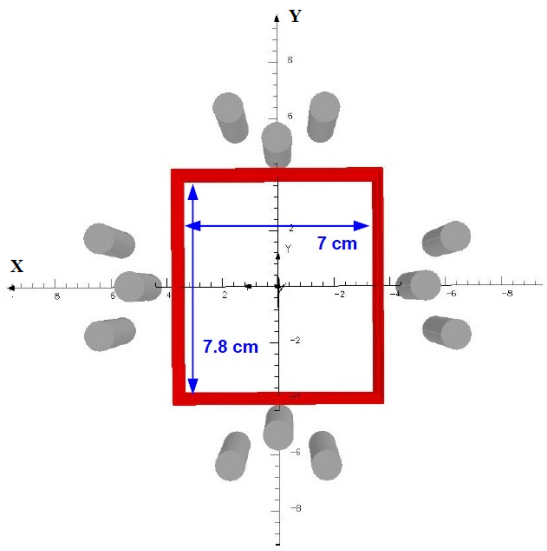

Figure 4.14: Details of the arrangement of the cryoperm housings and the SQUID compensation from the OPERA model.

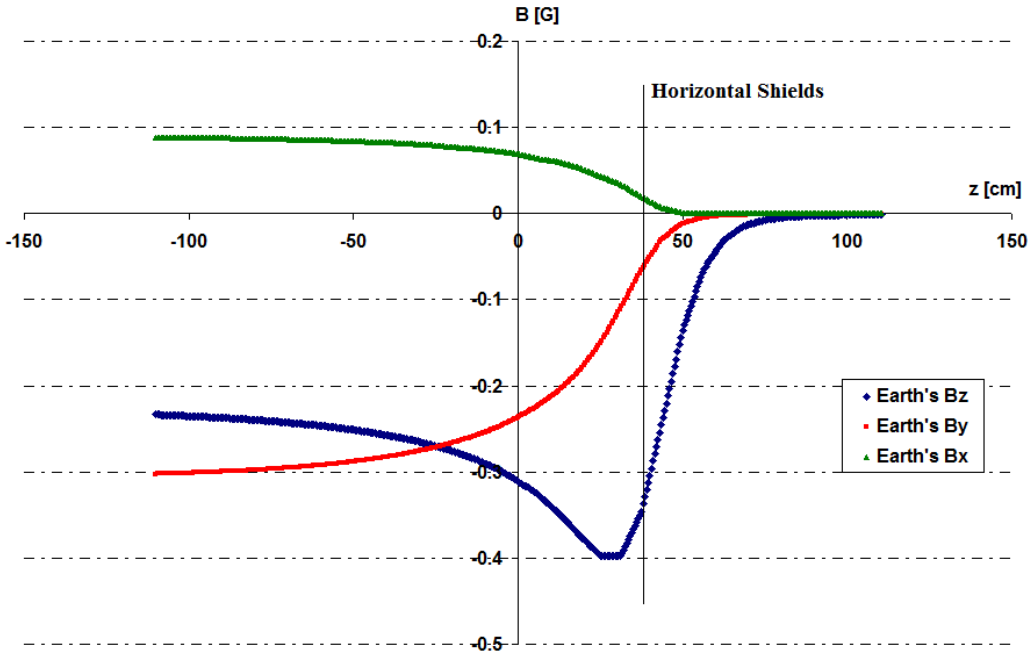

Figure 4.15: Output from the OPERA model showing the effect of the μ-metal in the horizontal shield on the Earths B-field along the central axis of the guide tube.

superconducting items (Pb shield and solenoid) has not been examined here.

Figure 4.13 shows the spatial relationships of the μ-metal nose and shield end cap, the cryoperm housings and C8, the last HFC. Figure 4.14 details the arrangement of the cryoperms around the guide.

The OPERA model files and the corresponding tables are stored on Sussex computers and can be considered as the basis for any future modeling if modifications are needed. The code of the model that includes all the above parts of the apparatus is given in Appendix A.

4.3.2 Results of the Magnetic Modeling

Effect of the μ-metal shields on the Earth‘s field. Close to the entrance of the horizontal shields, the Earth‘s magnetic field is strongly deformed by the presence of the μ-metal layers, end cap and nose. The output from the model can be seen in Figure 4.15. Just before the entrance of the on the 6WS side, the z-component (parallel to the main axis of the tubes) is increased by about 75%, while the other two components, perpendicular to the shields axis, are gradually decreasing to about the tenth of their initial value. As expected, all three components reduce to close to zero inside the shields. We recall that the sense of positive Bz is upstream.

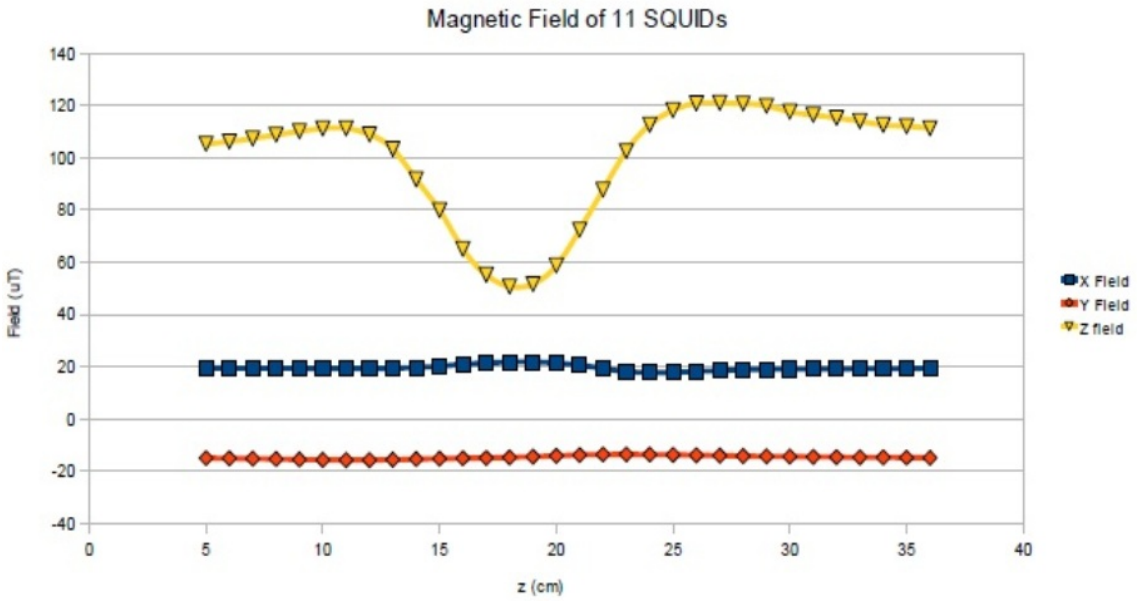

Figure 4.16: B-field distortion inside the SQUIDs cryoperm array when applying 110 T with the SQUID compensation coils.

Effect of the cryoperm array on a uniform field One of our Oxford collaborators, Christine Clarke, measured the field reduction inside the cryoperm array by driving the two SQUID compensation coils at 8.8 mA. With this current, the free-space field in the centre should be about 110 T. The results of magnetic scans shown in Figure 4.16 indicated that the z-component of the field was reduced by about 60%. As expected, the other two components do not suffer any significant change [71]. As is demonstrated in Figure 4.17, we were able to reproduce this experimental data with the model when taking $\mu = 10^4$ for the magnetic permeability of cryoperm.

Combining multiple effects The output shown in Figure 4.18 is from a model which includes the μ-metal nose and shields and the cryoperm housings and it shows all three field components. C8 is driven at 9 A and the Earth's field is included. Both active compensation coils are off but the 6WS solenoid end correction coil and the solenoid are activated with their standard currents of 10 mA and 0.981 mA, respectively. These latter two coils generate the small peak at $z \approx 0.75$ m (the position of the SECC) and cause the field for $z \geq 1$m to reach a constant 5 μT well inside the solenoid.

The value of 9A for C8 was used here as this was the value initially used in the Autumn 2010 run instead of the proposed 20 A. We see that using this lower current causes the on axis component B_z to drop to a value comparable to the Earth's field at the centre of the SQUIDs cryoperm array. The B_x and B_y components are due to Earth's field and not

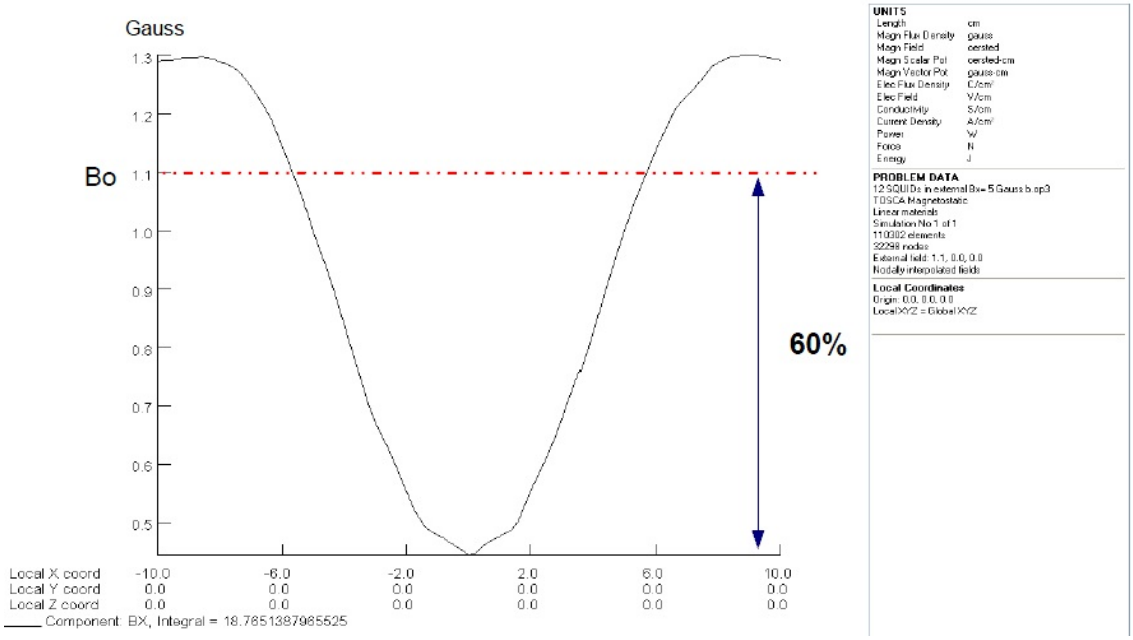

Figure 4.17: Output from the OPERA model for 12 high permeability tubes placed in a homogeneous 110 μT field reproducing the experimentally observed 60% reduction in field.

due to C8 coil.

It is clear that the cryoperm array absorbs the field strongly, creating a "magnetic valley" in their vicinity.

The effects produced by the Earth's magnetic field and that from C8 are visualized separately and in combination in Figure 4.19. The z-component of Earth's field is opposing that from the C8 coil and effectively produces a peak in the SQUIDs area. By energizing the 6WS active compensation coil (D1) at 2A we can lift the field in this area, but we also make the valley deeper.

Figure 4.20 shows Bz on axis for a variety of combinations when the current in C8 is restored to its expected value of 20A. To the free-space C8 field are then added consecutively the effects of:

- 12 SQUID cryoperms
- 6WS end mu-metal nose/end cap
- SQUID compensation coils with I=13.2 mA (this value initially chosen by Oxford)
- three μ-metal layers and the second end cap (at the HV end)
- 6WS active compensation coil energised at 2A (generating 0.1 mT at the SQUIDs).

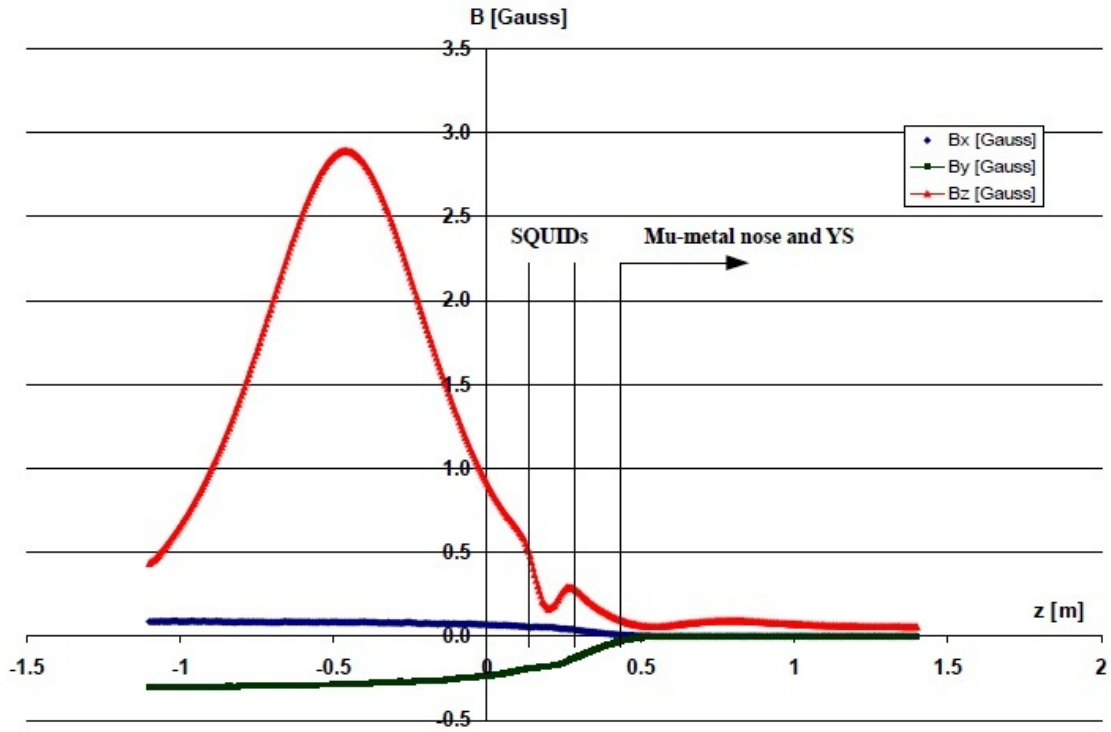

Figure 4.18: Bx, By and Bz along the central axis for 9A on C8, 10 mA on 6WS SECC and 0.981 mA on the Solenoid in the presence of the μ-metal nose and end cap and the cryoperm array. The Earth‘s field is also included.

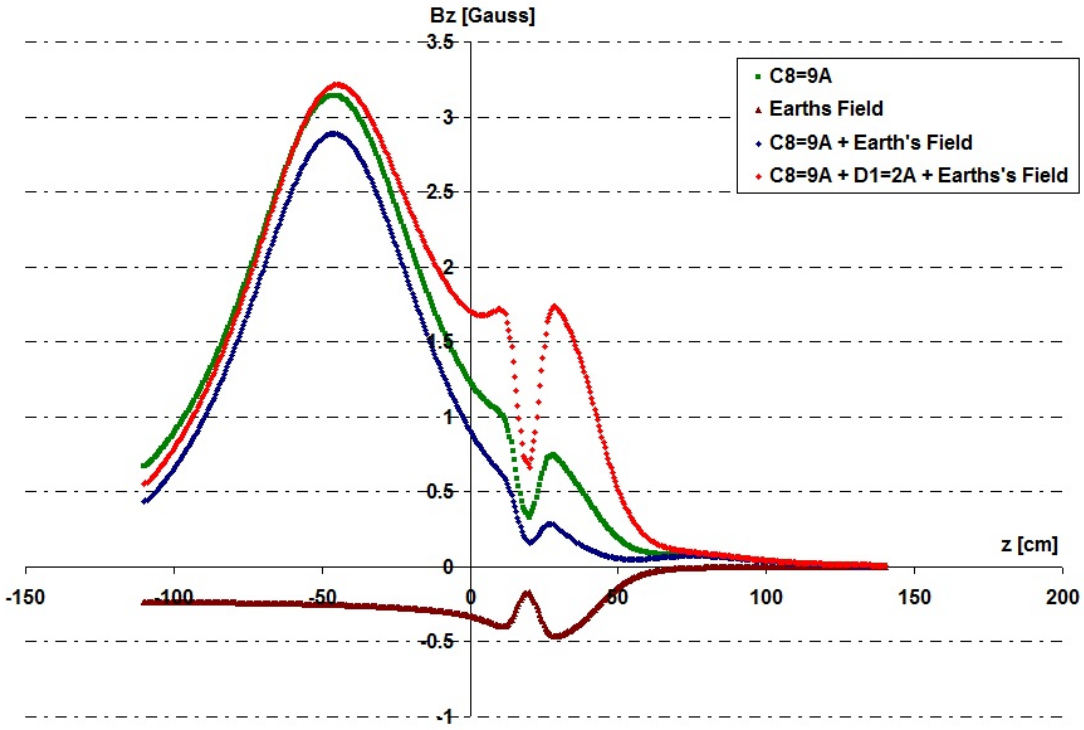

Figure 4.19: Bz along axis in the presence of the μ-metal nose and end cap and the cryoperm array various combinations of 9A on C8, the Earth‘s field and 2A on the 6WS end active compensation coil.

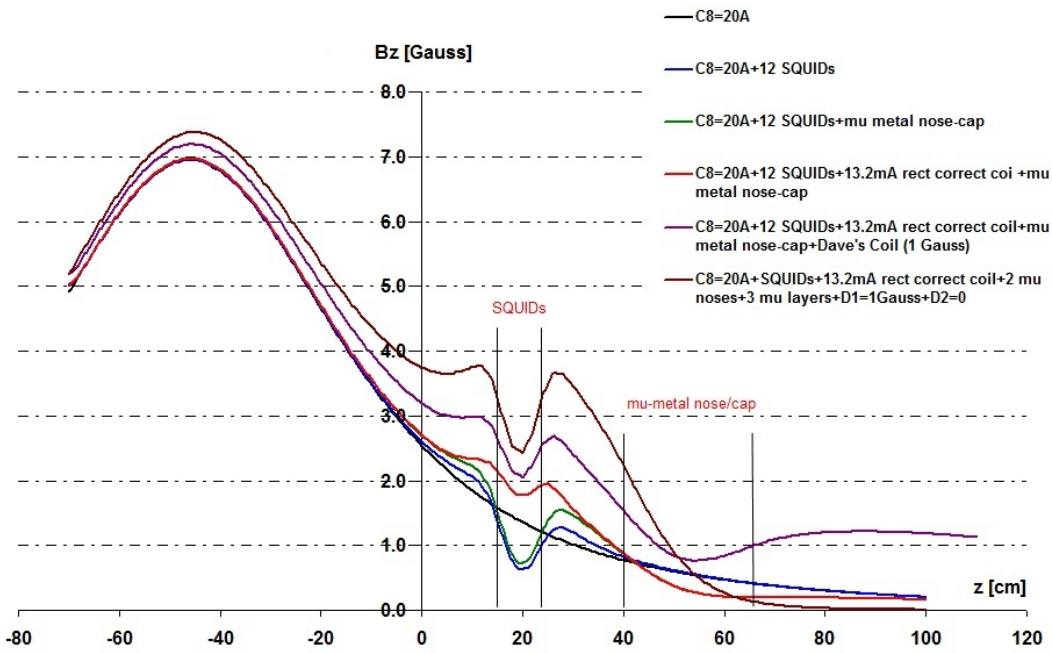

Figure 4.20: Bz along central axis for a variety of combinations shown in the key and discussed in the text.

The presence of the SQUIDs array is the reason for the valley around z = 20 cm (blue line). The 6WS end μ-metal nose and end cap combination increases slightly the field in front of it (green line). Activating the SQUID compensation coils with 13.2 mA (red line) irons out the dip and lifts the minimum of the valley from 1 to 2 Gauss. The 2A in the (D1) active compensation coil increases both the field level (by about 1 G) and the depth of the valley (from ≈20% to ≈30 % (magenta line)). In this case, the relatively high field at $z \approx 50$ cm is because the field from the D1 coil is not (yet) screened by the horizontal shields. The addition of the latter (brown -top- line) increases the field at the front of the shield by about 0.7 G and increases the depth of the valley to ≈35%. We note that when all the factors are included, the B_z component drops from about 7 Gauss at the position of C8 to about 2.6 Gauss at the minimum of the valley which is 5 times the Earth‘s field. Inside the horizontal shields, B_z goes smoothly to zero as expected since in this case the solenoid and the end correction coils at its ends are not energised.

Optimising the field and T_1 Keeping C8 at the value of 9A set initially in the Autumn 2010 run, we ran the full model trying different combinations of currents in the SQUIDs compensation coil and in the active compensation coil on the 6WS end to see what con-

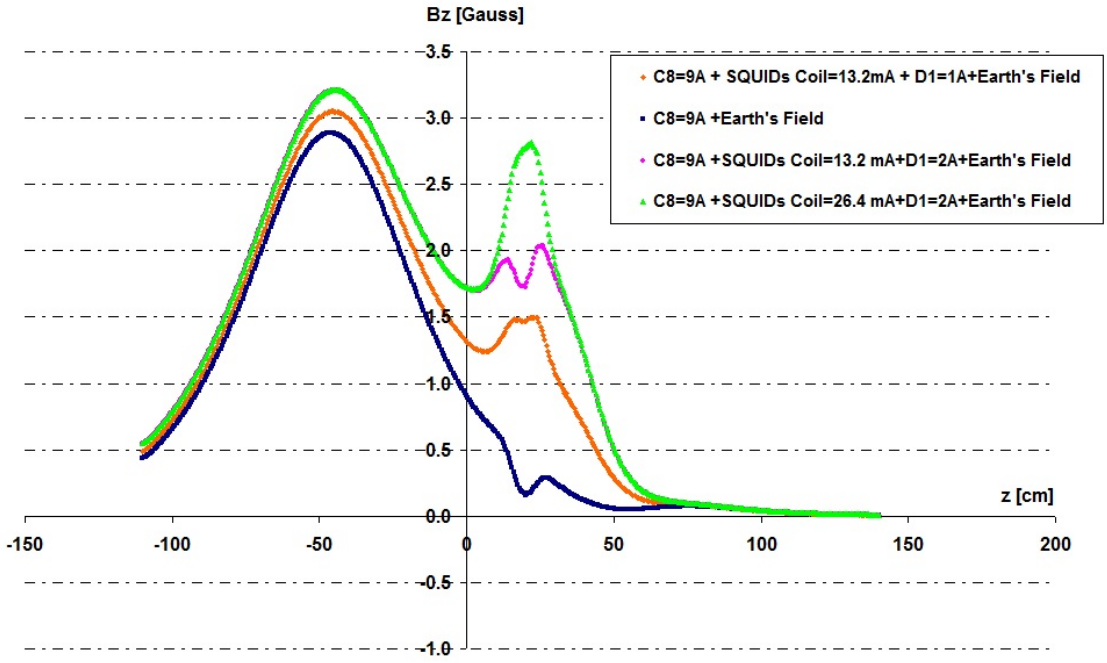

Figure 4.21: The effect of varying the SQUIDs compensation coil current is to transform the B-field valley to a peak.

figurations could eliminate the B_z valley, increase the field at the entrance of the μ-metal nose and ultimately increase the T_1 spin relaxation time. As can be seen in Figure 4.21 for the B_z component on axis, with the D1 coil at 1A changing the SQUIDs compensation coils from 13.2 mA to 26.4 mA transforms the valley to a peak.

In the Autumn 2010 run we wanted to test whether we could improve or worsen noticeably the polarisation of neutrons. For this reason we sought two simple sets of currents for which we would be able to get distinct changes in UCN polarization. We eventually found two combinations of currents ($C8 = 9\ A$, $D1 = \pm 2\ A$ and SQUIDs coil $= \pm 26.4$ mA) which transformed a peak to a very deep valley around the SQUIDs array, as shown in Figure 4.22.

Figure 4.23, shows the three field components along the surface of the neutron guide for the current combination which gave the peak in Figure 4.22. Position (a) corresponds to the corner of the guide and (b) to the middle of a face. The field is far from smooth for any of the three field components and B_x and B_y exhibit cusps at each end of the cryoperm array. In such a case the most effective way to calculate T_1 was by was by using Harris'Monte Carlo simulations where neutrons sample the whole volume within the SQUIDs array.

The MC simulation was run using as input the OPERA B-field grid for the two extreme

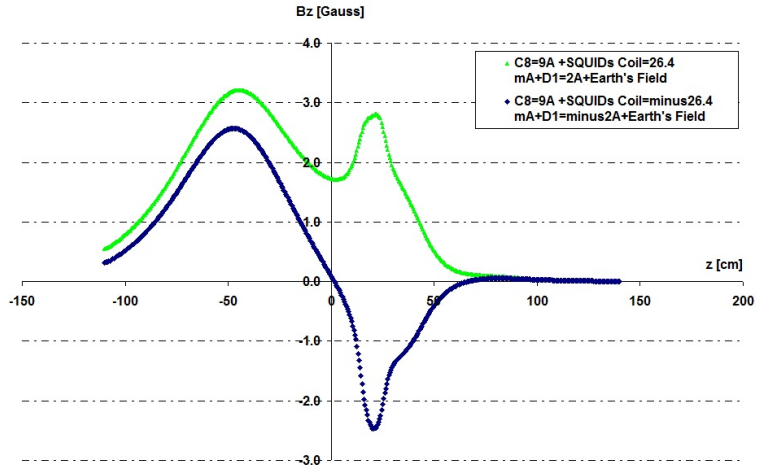

Figure 4.22: Two extreme cases of trimming the magnetic field in the SQUIDs area.

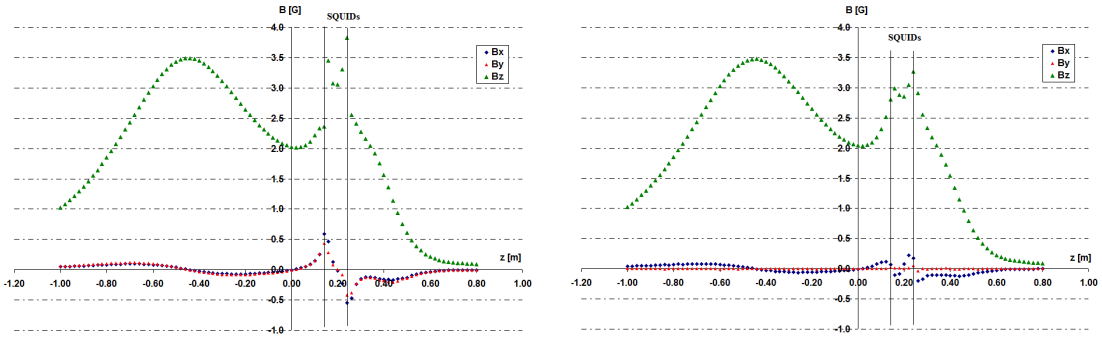

(a) x=3.1cm and y=3.7cm

(b) x=3.1cm and y=0cm

Figure 4.23: B_x, B_y and B_z components of the field at the surface of the neutron guide for the current configuration: C8=9A, D1=+2A, SQUIDs coil =+ 26.4 mA. This is the "peak" Bz profile of Figure 4.22. The plot on the left refers to the corner of the guide tubes while the one on the right refers to the mid-point of the side.

current cases of Figure 4.22. The calculated polarization as a function time for neutrons confined to a region around the SQUIDs array is shown in Figure 4.24. This indicates T_1 is expected to be about 150 seconds for the "peak" case and less than 10 seconds when the "valley"is made even deeper.

4.4 Conclusions

In this chapter, the profile of holding field along the neutron guide tubes was described with three different approaches:

1. The fulfilment of the adiabaticity condition

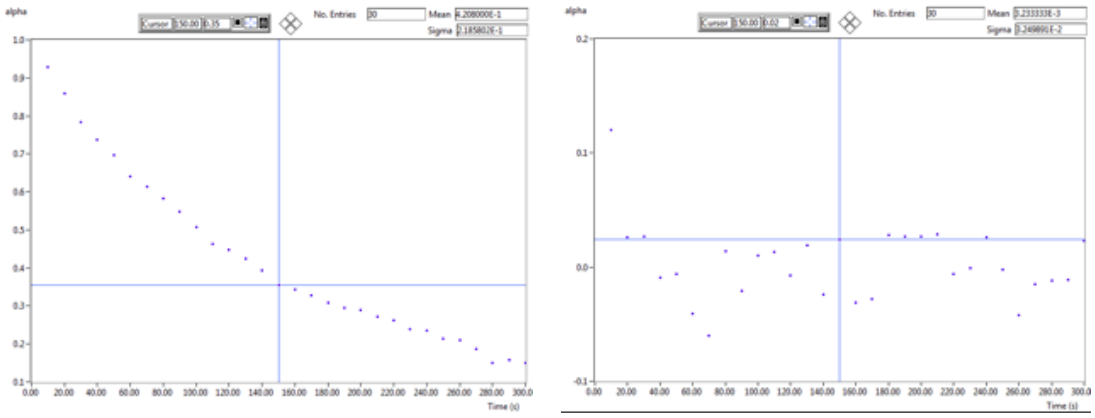

Figure 4.24: Neutron polarization as a function of time for neutrons in the region around the SQUIDs array for the current configurations of Figure 4.22. In the "peak" case (left) T_1 is ≈150 seconds and less than 10 seconds for the "deaper valley" case (right).

2. The T_1 spin relaxation time analytical calculation and

3. The OPERA electromagnetic models whose B-field map outputs can be used by MC simulations to estimate the expected polarisation of neutrons.

In particular, using the OPERA software package, the case of placing 12 SQUID magnetometers along the guides was examined with various current combinations for the holding field coils lying around them. We were lead to the conclusion that the field "valley" caused by the 12 high permeability SQUID cryoperms, can not be smoothed adequately in order to restore the field profile as it is without their presence.

Instead, the optimum result that can be achieved using the existing coils is to create in the same place a peak. The resulted field configuration has about the same axial gradient, but the magnitude of the holding field at the entrance of the μ -metal nose is enhanced well above the (opposing) Earth's field and therefore can retain neutrons' polarisation by increasing their T_1 spin relaxation time.

Chapter 5

Optimising the Resonance Magnetic Field

5.1 Introduction

Before we attempt an EDM measurement, we have to bring the experiment to a level where a clear resonance curve can be obtained. In Spring of 2010 the collaboration decided to focus on this goal. The precondition for seeing the Ramsey resonance is that the magnetic environment seen by neutrons is temporaly stable as explained in Chapter 3 but also spatially homogeneous. For this reason it was first decided to investigate the magnetic field due to the SCV within which the Ramsey cells would be placed. Any magnetic impurities in the SCV material can have a significant effect on the field experienced by UCN and reduce the T_2 relaxation time.

A first set of magnetic scans conducted at room temperature revealed that the axial field gradient within the SCV was two orders of magnitude worse than the design specification. We then carried out a full characterisation of the **B** field at low temperature as well.

To compensate these magnetic anomalies by the use of the 21 correction coils mounted on the carbon fibre former around the SCV had also to be explored. The actual response of all the trim coils was measured rather than relying on the fields calculated from the Biot-Savart law. This was done because the presence of the three μ-metal shields is expected to modify the free-space fields.

Using the above information (i.e. the **B** field configuration and the trim coils response), Professor P. G. Harris, M. Raso-Barnett and I developed a systematic method determine the optimum currents to be set in the compensation coils in order to improve the **B** field

homogeneity in the region of the Ramsey cells. Further magnetic scans were conducted to check our predictions for the resultant magnetic field configuration. The new field maps were then used in Monte Carlo (MC) simulations to calculate T_2 in the Ramsey Cells.

The optimisation method is explained in this chapter and the comparisons between the predicted and measured magnetic field configurations and the T_2 relaxation times are given as well.

5.2 Static Resonance Field Specification

In order to perform a nEDM experiment we require a stable and homogeneous B-field over the Ramsey Cells volume. As with temporal changes, any variation of B-field in space results in different precession frequencies for neutrons in different parts of the cells.

Since the UCN move with speed of about 6 m/s, during a 300 s storage time they cross the Ramsey Cells about 9000 times. Therefore, to a first approximation, it might be reasonable to assume that they sample the B-field throughout the cell volume and at the end of the storage period their spin vector is still aligned as if the field had been uniform at some average value.

This approach is only correct if we assume that the neutrons are uniformly distributed throughout the Ramsey Cells. Neutrons' velocity follows the Maxwellian quadratic distribution [72] with mean value of $\overline{v} = 5.22$ m/s ($E_{KIN} \approx 140$ neV) and most probable velocity equal to $v_p = 4.62$ m/s ($E_{KIN} \approx 110$ neV), very close to the mean value. That means that most of the neutrons are narrowly distributed over the velocity range. Golub and Pendlebury showed [73] that the gravitational energy gradient for neutrons is of the order of 100 neV/m, so within the 125 mm high Ramsey Cells, the UCN gravitational potential varies by about 25 neV, a significant fraction (about 10 %) of their kinetic energy. Thus, the UCN are not expected to be distributed in a uniform manner, since there will be more of them in the lower parts of the cells. This means that any spatial variations of the B-field will not be sampled equally by all neutrons. This results in neutrons having different precession frequencies which decreases the T_2 relaxation time and hence limits the time for which they can be stored.

Ideally, we need a constant B-field throughout the cells volume, perfectly aligned to the z-axis, with no radial component. The latter is needed in order to eliminate the $\vec{v} \times \vec{E}$ effect as described in section 2.1.3. Our target value for the axial gradient is:

$$\left| \frac{dB_z}{dz} \right| \leq 0.83 \text{ nT/m} \tag{5.1}$$

or approximately 1 nT m. A detailed derivation of this figure can be found in [3]. Pendlebury [74] has alos calculated the corresponding limit for the radial gradient of the B_z. This should not exceed 0.1 nT over the width of the cells, or equivalently:

$$\left|\frac{dB_z}{dr}\right| \leq 1 \text{ nT/m} \tag{5.2}$$

These two restrictions, which are approximately the same, are our guide for optimising the field homogeneity within the Ramsey Cells in order to perform a nEDM experiment.

5.3 Experimental set-up for the magnetic scans

The magnetometer array (see Figure 5.1) used for the magnetic scans in the summer of 2010 consisted of five Bartington (Mag-01H) low temperature single-axis fluxgate (FG) magnetometers. Their alignment was such as they all measured the component of the B field parallel to the symmetry axis of the horizontal shields (B_z).

Four of them were mounted on a $\approx$ 3 m long perspex tube that was free to move along the main axis of the SCV and rotate by $\pm$180 degrees. Two of them were placed on axis (r=0), one was at r=7.5cm and the fourth one at r=15cm. All four of them were aligned such as they indicated negative field when the solenoid field was in the downstream sense.

The fifth fluxgate was firmly attached on a hole on the G-10 ring to which the 6WS end Baseplate of the SCV was bolted to. Its radial distance was $\approx$ 25 cm from axis and it was reading positive values for field downstream. This fluxgate was used to record the temporal changes of the background field.

The signals from all five magnetometer were read by the DAQ computer controlled by the Oxford collaborators. The calibration was done by comparing the amplified voltage output recorded on the Oxford computer with the raw readings on the FG control boxes. A colour was assigned to each FG that was recorded in the data file headers and in all the plots presented in this chapter.

The perspex tube was inserted into the OVC from the HV end (see Figure 5.3 (a)) and could move along the main axis through a sliding vacuum seal. The mechanism to facilitate the axial movement of the tube consisted of three stainless bars with 25 holes every 2 cm over a distance of $\approx$ 0.5 m. The angular rotation was controlled by a aluminium flange attached to the three metal rods with 24 equispaced notches on its periphery, giving 15 degrees steps. A metal pin on the top of the flange locating into one of the notches kept the whole support structure stable while sliding. The precise axial and angular positions

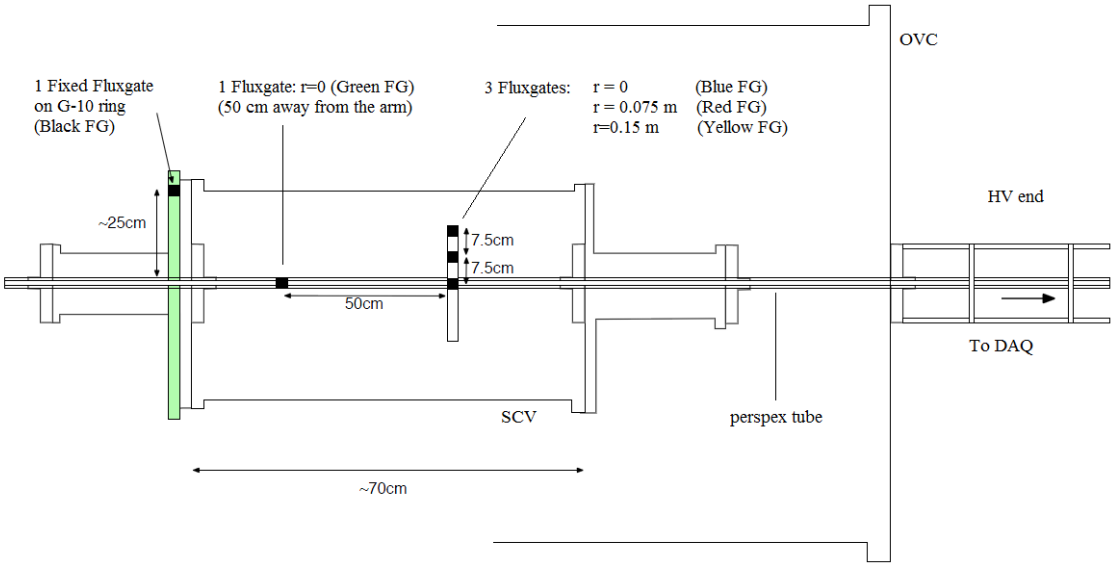

Figure 5.1: The magnetometer array used for the Summer 2010 magnetic scans at ILL. The centre of the SCV corresponds to $z \approx 30$ cm. The colour labels for each FG is also shown. Apart from the fixed (Black) FG, the other four FGs indicated negative values for B_z pointing downstream from the 6WS towards the HV end.

of the magnetometers were actually recorded on the Oxford computer via potentiometers, but these positions were manually entered into the data header..

The angular convention was different from previous magnetic scans with theta taking values between -180 $< \theta <$ +180 (Figure 5.3 (b)). $\theta = 0$ corresponds to top centre and positive values to clockwise rotation. While cooling the apparatus down, the position of the fluxgates arm was been found to have an angular offset of about $+20^o$. After an accident with the perspex tube on the 22^{nd} of June 2010, this offset changed to -55^o. Both of these offsets were found by comparing the measured position of the maximum response of an azimuthial coil with its expected peak position.

5.4 Trim Coils Response

We measured the field-current response of the 19 compensation coils on the carbon fibre former and the two solenoid end compensation (or trim) coils (TC) over the region -10 cm $\leq$ z $\leq$ +10 cm around the centre of the SCV for three radial distances of r = 0, 7.5 cm and 15 cm. This region covers the entire volume of the two Ramsey cells which extend $\pm$ 6 cm along z and 12.5 cm in r. The readings were taken every 2 cm (giving 11 z positions) and with angular steps of 15 degrees between -6 cm $<$ z $<$+6 cm and with angular steps of 90 degrees at z = $\pm$ 8 cm and $\pm$ 10 cm. This gives 552 measurements for each of the

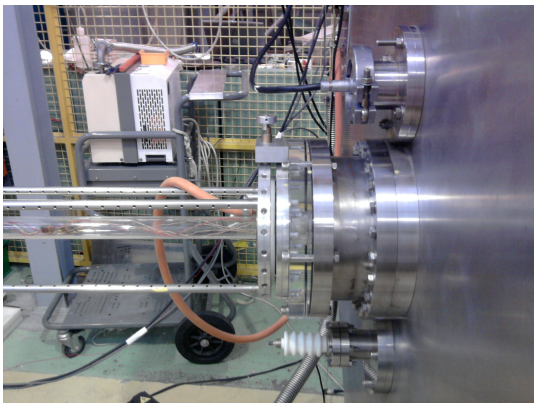

(a) Magnetometer Array

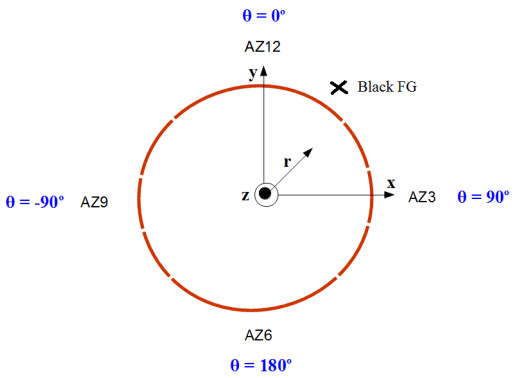

(b) θ convention

Figure 5.2: (a) Picture of the magnetometer array insertion device at the HV end of the OVC. The 24 notches on the periphery of the Aluminium flange and part of the three 25-notched metal bars are also shown. (b) The angle (theta) convention looking from the HV to the 6WS end. The position of the fixed (Black) fluxgate probe on the G10 ring is also shown at about +30 degrees.

21 coils and 11592 data points in total.

To avoid any possible hysteresis effect from the surrounding mu-metal parts, the current sequence was 0 mA, +20 mA, -20 mA and finally 0 mA again, with each measurement lasting for 5 seconds. This gave a time interval of 10 seconds between tests with non zero current. Any hysteresis would then lead to different readings for the two zero current data points. In the following three subsections, plots of some of the coils response are shown.

The reason for testing the coils response experimentally is because the field produced by each of these is expected to be affected by the presence of the three mu-metal layers whose magnetic permeability is not accurately known. The deviation from the Biot-Savart law is expected to be larger as we move away from the coils.

The scans were conducted with the Pb shield and the solenoid in their normal states, since the compensation coils will have to be activated at temperature above the superconducting transition temperature of the solenoid ($\approx$ 9K). All the 19 coils on the carbon fibre former exhibited linear responses with current. We used these data to calculate the "proportionality factors" (f) between the magnetic field produced along z (B_z) and the current (I_c) in each coil ($B_z = fI_c$) at given point in space. This information was later used in the current optimisation method to reduce the magnetic field inhomogeneities. The data for the two solenoid end trim coils, on the other hand, showed a non linear behavior due to hysterisis.

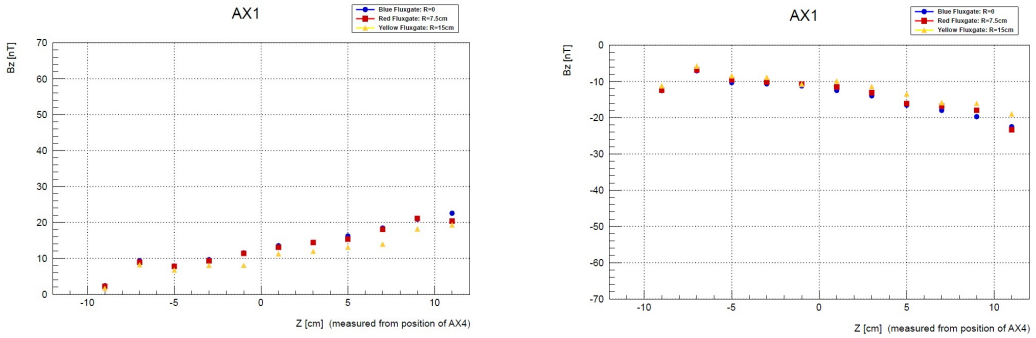

Figure 5.3: AX1 response along z for ±20 mA.

Axial Coils

The responses from the first (AX1), the middle (AX4) and the last (AX7) Axial correction coils at ± 20 mA are shown in Figures 5.3 to 5.5. In these Figures, the position of the AX4 coil is displaced from the centre of the SCV (z=0) by about 1.4 cm (see Appendix E). We note the experimental data do not differ from the theoretically expected from these coils in free space by more than 0.2 nT (close to the resolution of the magnetometer), so the effect of the mu-metal shields is considered insignificant.

	AX1 response [nT/mA]			AX4 response [nT/mA]		
z cm	r=0 cm	r=7.5 cm	r=15 cm	r=0 cm	r=7.5 cm	r=15 cm
0	0.64 (0.62)	0.61 (0.59)	0.53 (0.50)	2.33 (2.37)	2.48 (2.53)	3.01 (3.19)
-6	0.46 (0.44)	0.44 (0.42)	0.38 (0.37)	2.27 (2.22)	2.40 (2.33)	2.83 (2.69)
6	0.90 (0.86)	0.89 (0.82)	0.75 (0.70)	2.10 (2.17)	2.18 (2.26)	2.30 (2.54)

Table 5.1: The theta-averaged experimental data for the AX1 and AX4 coils, compared with the values expected from the Biot-Savart law in free space (in parenthesis). z=0 cm corresponds to the centre of the SCV and of the RCs while z=-6 cm and z=6 cm are at the extremes of the RCs.

Finally, Figure 5.6 shows the response of the AX2 coil as we change the current from 0 mA to ±20 mA and then back to 0 mA again, at about 10 cm away from the centre of the SCV and at $\theta = 0^o$. We note that the two zero points have the same value, therefore hysterisis is not observed.

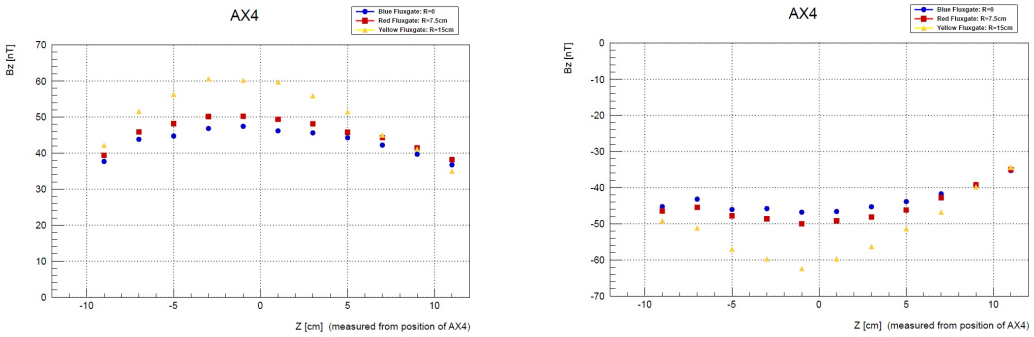

Figure 5.4: AX4 response along z for ±20 mA.

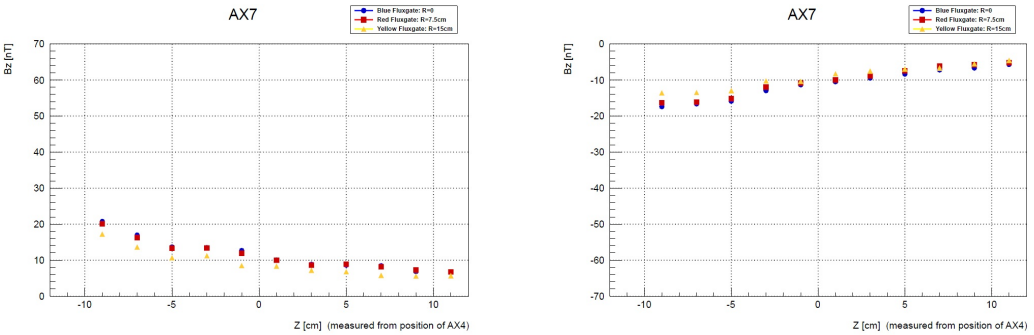

Figure 5.5: AX7 response along z for ±20 mA.

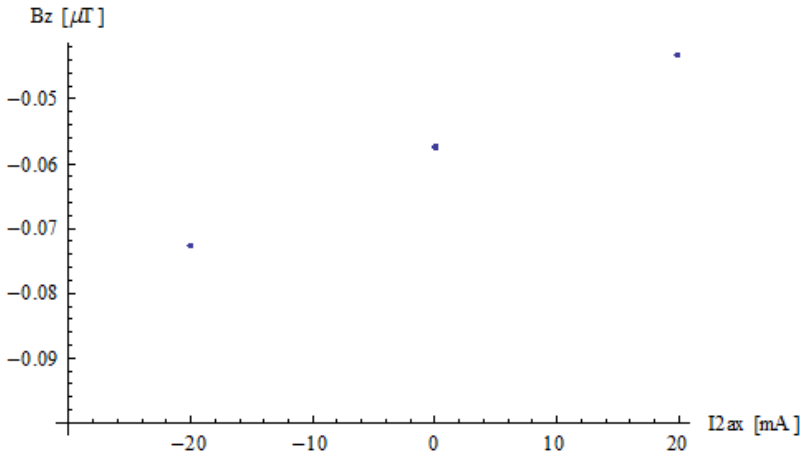

Figure 5.6: The recorded response of the AX2 coil for the current sequence of 0 mA, +20 mA,- 20 mA and finally 0 mA again at z=-10 cm from the centre of the SCV showing no detectable hysterisis (the two zero current values are indistinguishable).

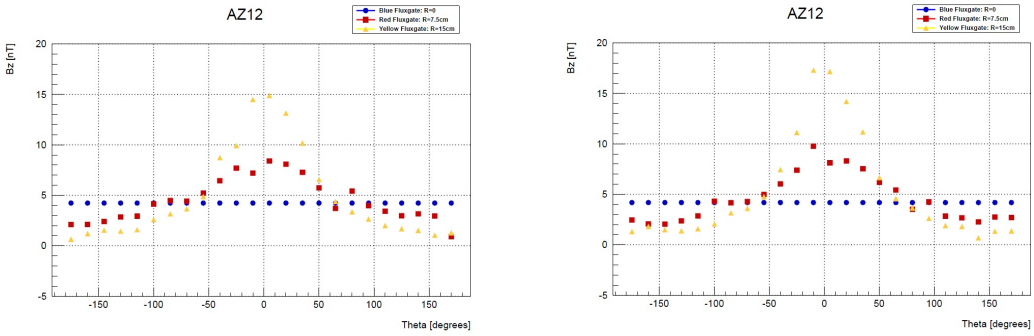

Figure 5.7: AZ12 coil response to + 20 mA at z = 2 cm and z = 6 cm from the centre of the SCV

Azimuthial Coils

Because the azimuthial coils symmetrically position around the centre of the RCs, only the AZ#12 response at 20 mA is shown in Figure 5.7 at the centre and at the (HV side) extreme of the Ramsey cells. The maximum corresponds to the expected angular position of the coil ($\theta = 0^o$) and the shape of the field is also as expected.

Again, as shown in Table 5.2 we see no significant deviation of the experimental data from the Biot-Savart values given by the Biot-Savart law nor any hysterisis effect (see Figure 5.8).

	AZ12 responce [nT/mA]		
θ^o	r=0 cm	r=7.5 cm	r=15 cm
5	0.22 (0.22)	0.40 (0.42)	0.75 (0.77)
50	0.21 (0.22)	0.31 (0.31)	0.33 (0.32)
95	0.22 (0.22)	0.19 (0.19)	0.13 (0.13)
140	0.21 (0.22)	0.13 (0.13)	0.07 (0.08)
-175	0.22 (0.22)	0.12 (0.12)	0.06 (0.07)

Table 5.2: The experimental data for AZ12 coil at about the centre of the SCV/RCs are compared with the values expected from Biot-Savart law in free space (in parenthesis).

Solenoid End Compensation Coils

To test the current dependence of the magnetic field produced by the two solenoid end compensation coils we activated them by the following current sequence: 0, +40, -40, 0, +60, -60, 0, +20, -20, 0 mA. These data were taken immediately after the μ-metal shields

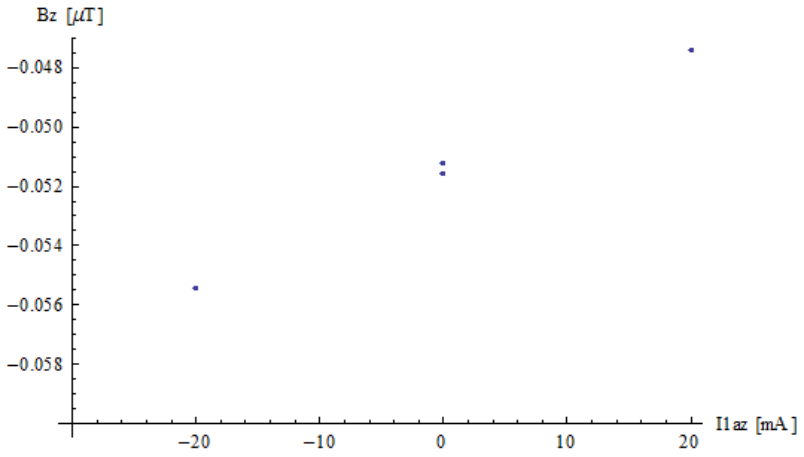

Figure 5.8: No hysterisis effect was observed in AZ1 coil response to ±20 mA at z = -10 cm from the centre of the SCV.

had been demagnetised. The results for the 6WS end coil are shown in Figure 5.9. We obtain identical results for the HV end coil. No hysteresis effect was observed in this case.

Nevertheless, when these (solenoid end compensation) coils were tested with a different current sequence we did see a non-linear response and a hint of a hysterisis. In Figures 5.10 and 5.11 we see that the two zero points are separated by about 40 nT inside the SCV and we saw a corresponding change in the external fluxgate horizontal component by about tenth of that (≈ 10 nT). This behaviour was observed at all the positions along z and theta for both coils. These data were taken along with the 19 carbon fibre former coils tests, which lasted for about 3 days. During this time, the μ-metal shields were not demagnetised.

5.5 Characterisation of the SS SCV magnetic field configuration

5.5.1 Inherent Magnetic Impurities on the SCV Baseplate

In April of 2010, a first magnetic scan of the SCV was conducted at RAL to investigate the magnetic field profile on its interior. The SCV body with each baseplate attached were moved on a non-magnetic trolley while a 3-axis magnetometer was held in a fixed position. One set of data was taken with the fluxgate probe on the SCV axis and one taken with the probe at 4 cm off-axis. The outcome (Figure 5.12, red points) showed an axial gradient of about 300 nT/m over the Ramsey cells region (±6 cm along the central axis) which is 2 orders of magnitude bigger than our design limit.

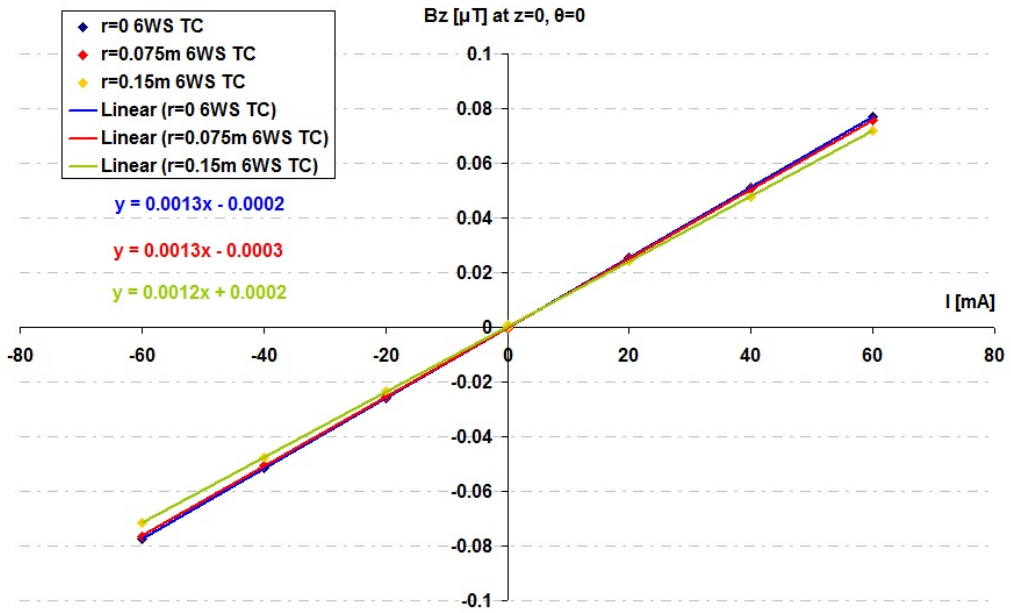

Figure 5.9: 6WS solenoid end compensation coil response for three radial positions at z=0 as a function of current. No hysteresis effect is observed.

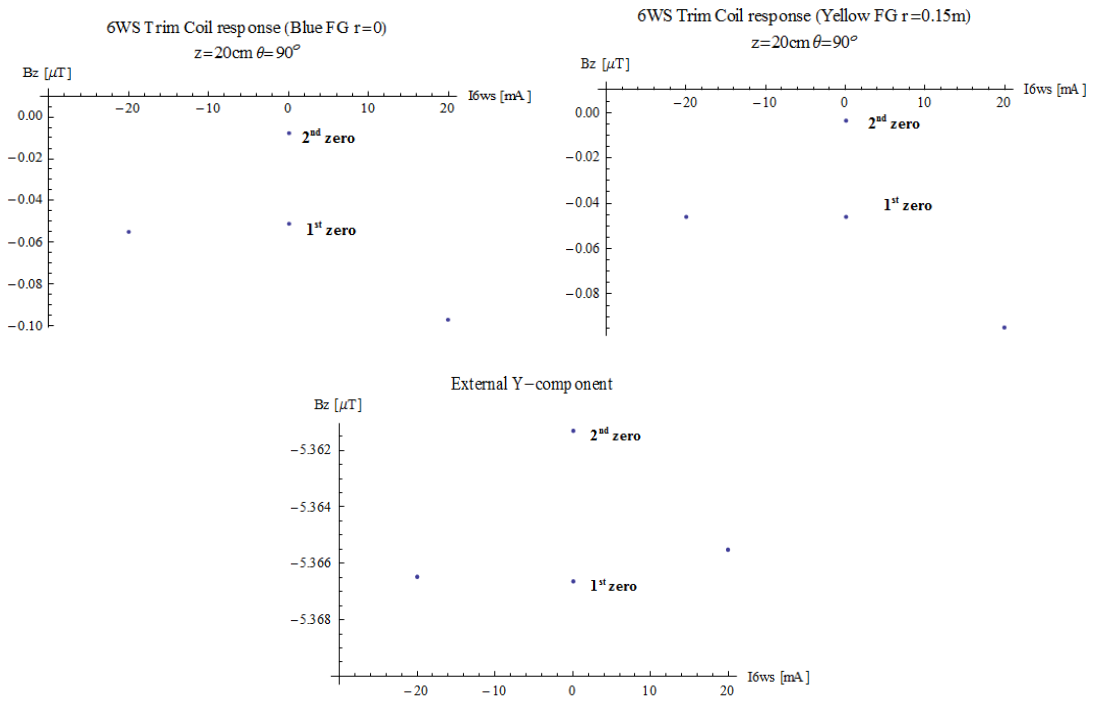

Figure 5.10: The 6WS end TC response to ±20 mA at z=-10 cm and $\theta = 90^o$.

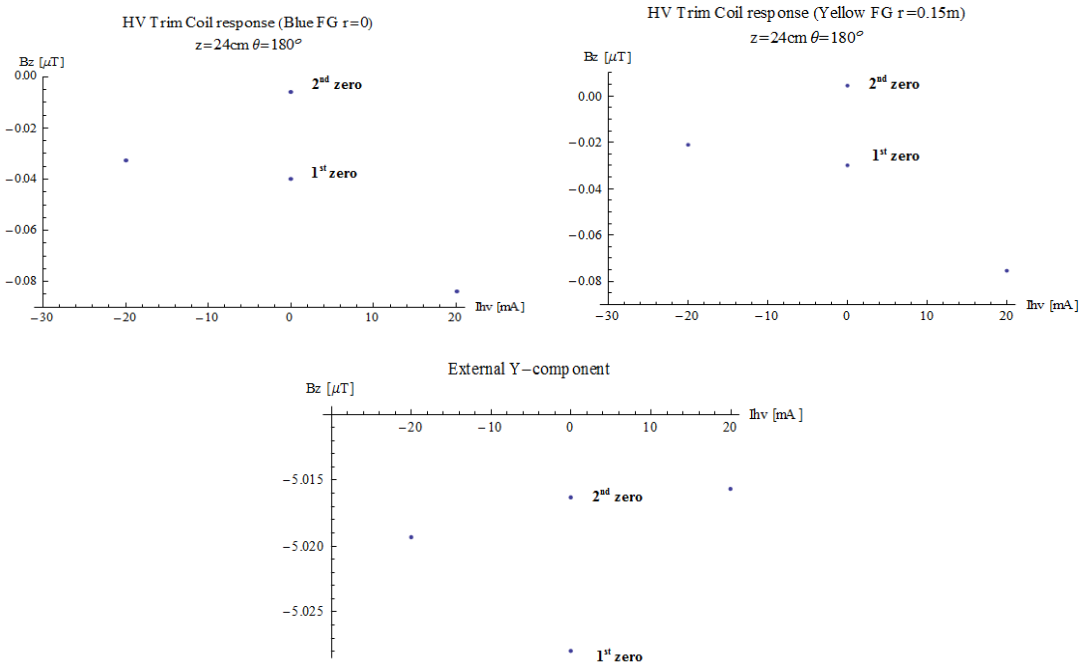

Figure 5.11: The HV end TC response to ±20 mA to ±24 mA at z=-10 cm and $\theta = 180^o$.

In May 2010, the SCV and attached baseplates were placed inside the horizontal shields at ILL without the Ramsey cells and a new magnetic scan was performed at room temperature. The new results, shown in blue in Figure 5.12, confirmed the previous measurements for the field on axis; the measured gradient dBz/dz was the same. The observed offset can be explained by the presence of the mu-metal shields and possible differences in fluxgate calibrations.

Both sets of data show large features at ±0.35 m which correspond to the positions of the baseplates at the end of SCV body. These features have since been shown to be associated with the welded joint between the base plate and the 160 mm diameter tube extending from it. The further feature at -0.7 m is at the position of a further welded joint between the tube and a flange. It is clear that the gradient at the centre of the SCV is largely as a result of the magnetic anomaly on the baseplate. The off-axis data taken at ILL inside the shield (the red and yellow data in Figure 5.13) highlight the localised nature of this anomaly. As will be evident from data presented below, that the extra field associated with the (circular) weld does not have axial symmetry.

Not only does this anomaly affect the field for resonance in the RCs, its possible depolarising effects needs to be considered.

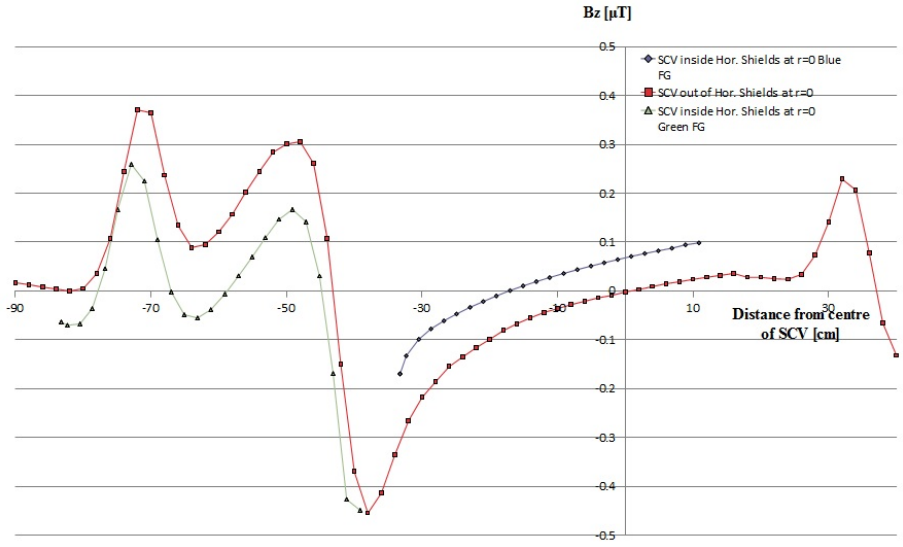

Figure 5.12: Magnetic scans of the SCV and baseplates at room temperature taken on axis. Brown data points: measurements taken in the laboratory field at RAL; Green and Blue data points: measurements taken in the horizontal shields at ILL from the Green and Blue fluxgates respectively.

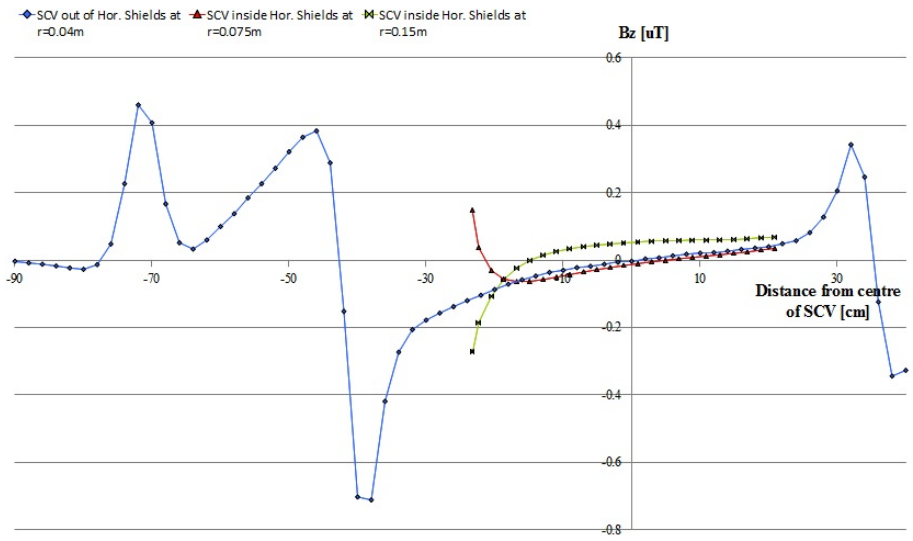

Figure 5.13: Magnetic scans of the SCV and baseplates at room temperature taken off axis. Blue data points: measurements taken in the laboratory field at RAL at 0.04 m off axis; Red and Yellow data points: measurements taken inside the horizontal shields at ILL at 0.075 m and 0.15 m off axis respectively.

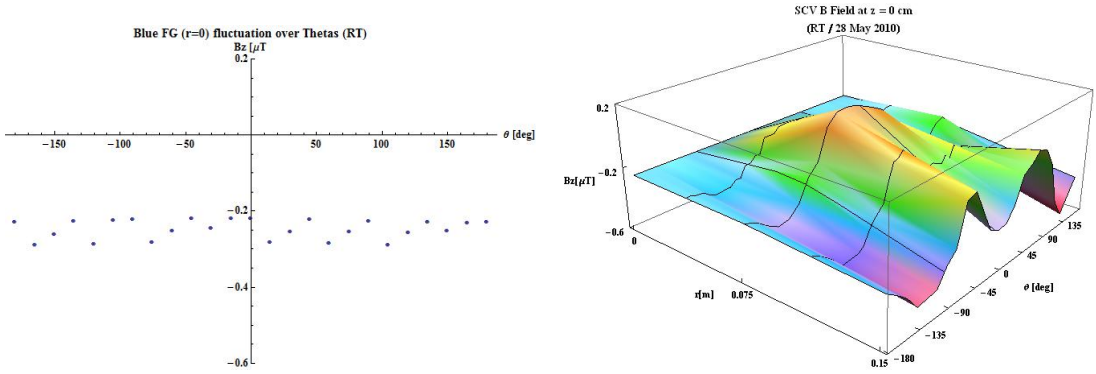

Figure 5.14: Room temperature data showing temporal variation in the Blue fluxgate output and the 3D SCV B field about the centre of the RCs (z=0) for all azimuthial positions.

5.5.2 B Field Dependence on Temperature

A series of magnetic scans of the interior of the SCV were conducted as the apparatus cooled. We were mainly interested in the magnetic field profile as close as possible to the base temperature of 0.5 K. The minimum temperature of the SCV that was finally reached was about 10 K with the solenoid and lead shields below 7 K and therefore at superconducting state.

During the room temperature scans, the magnetic environment inside the SCV was quite noisy as can be seen by the field recorded by the on axis (Blue) fluxgate (FG) over all thetas; no changes are expected on a FG at r=0 while rotated, so the observed fluctuations must be attributed to temporal variations in the field due to (large scale) external pertubations. These variations which were coherent in all the fluxgates, were then subtracted from all channels to produce the 3D image of the magnetic field profile shown in Figure 5.14.

When the magnetic shield was superconducting the noise was drastically reduced. The corresponding 3D picture at ≈10 K (Figure 5.15 (b)) is quite similar to that at room temperature (the two ripples at about ± 90 degrees appear in both cases) but slightly smoother. The azimuthial average of the axial gradients across the RCs region is 20% less (see Table 5.3). The values given in this table are the mean of the absolute values of the axial gradients (dBz/dz) for all angles over the region of -6 cm $<$ z $<$ +6 cm.

A table giving the axial gradients as a function of theta over the RCs region for the two scans can be found in Appendix F1.

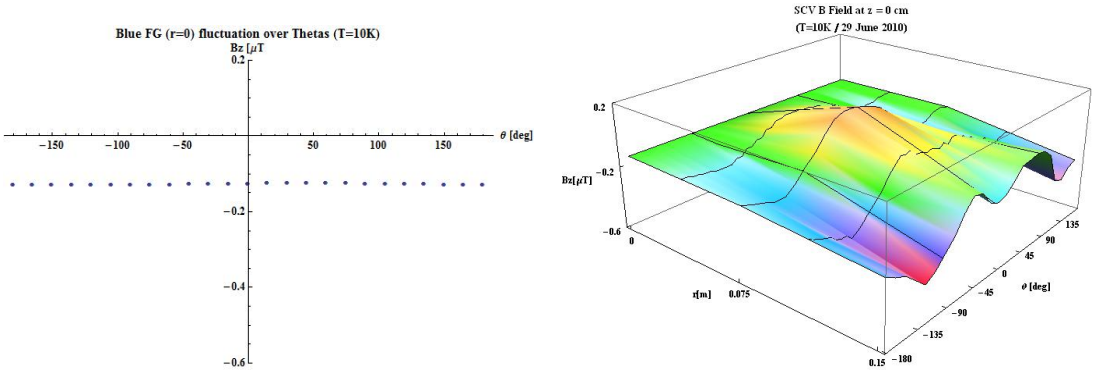

Figure 5.15: Low temperature data for $T_{scv} = 10$ K and $T_{shields} < 7$ K. The Blue fluxgate data do not show any temporal variation. The 3D B_z field map has the same profile with that obtained at room temperature.

	Room Temperature		T=10K	
Fluxgates	Mean Axial Gradient [nT/cm]	Standard Deviation [nT/cm]	Mean Axial Gradient [nT/cm]	Standard Deviation [nT/cm]
r=0 (Blue FG)	3347	243	2702	36
R=0.075 m (Red FG)	3253	802	2672	786
R=0.15 m (Yellow FG)	3530	2385	3309	2513

Table 5.3: The azimuthial average of the modulus of the axial gradients over the RCs region.

5.6 Improving the Longitudinal and Azimuthial Deviation of the Magnetic Field

A systematic method to calculate the optimum currents for the 19 correction coils in order to minimise the axial gradient and azimuthial deviation of the magnetic field inside the SCV has been developed in the summer of 2010 [75]. The manner in which the compensation coils need to be trimmed had not been specified before and a trial and error process will be inefficient when dealing with 19 currents and an enormous amount of magnetic data. Any attempt to change the magnetic field profile in a controlled way requires knowledge of the existing field characteristics and the accurate response of each coil at each point within the Ramsey cells region.

5.6.1 Optimisation Method

Having found linear responses for the 19 correction coils, the field compensation problem has been approached as a linear function minimisation. The total magnetic field at any point with position vector $\vec{r}$ -from say the centre of the RCs- is given by:

$$\vec{B}(\vec{r}) = \vec{B}_S(\vec{r}) + \sum_{k=1}^{N_c} I_k \vec{f}_k(\vec{r}) \tag{5.3}$$

where the first term $\vec{B}_S$ represents the static background field of the SCV minus the 5 μT holding field of the solenoid. The second term gives the contribution of the $N_c = 19$ coils. For each coil k, driven by current I_k, the proportionality factors f_k relate the current to the magnetic field at the given point.

Given that the magnetometer array used gave only the axial (z) component of the magnetic field, the function that has to be minimised is the single component scalar:

$$\chi^2 = \sum_{i=1}^{N_p} \left(B_S(i) + \sum_{i=1}^{N_c} f_k(i) I_k \right)^2 \tag{5.4}$$

where N_p is the number of spatial points which in the first approach are all given equal weighting. We minimise χ^2 with respect to the I_k:

$$\begin{aligned} &\frac{\partial}{\partial I_m}\chi^2 = 2\sum_{i=1}^{N_p} \left\{ f_m(i) \left[B_S(i) + \sum_{i=1}^{N_c} I_k f_k(i) \right] \right\} = 0 \Rightarrow \\ &\Rightarrow \sum_{i=1}^{N_p} B_S(i) f_m(i) = -\sum_{i=1}^{N_c} I_k \sum_{i=1}^{N_p} f_k(i) f_m(i) \end{aligned} \tag{5.5}$$

Doing this for all the currents we get:

$$\begin{pmatrix} \sum_{i=1}^{N_p} B_S(i) f_1(i) \\ \dots \\ \sum_{i=1}^{N_p} B_S(i) f_{N_c}(i) \end{pmatrix} = \begin{pmatrix} \sum_{i=1}^{N_p} f_1(i) f_1(i) & \dots & \dots \\ \dots & \dots & \dots \\ \dots & \dots & \sum_{i=1}^{N_p} f_{N_c}(i) f_{N_c}(i) \end{pmatrix} \begin{pmatrix} -I_1 \\ \dots \\ -I_{N_c} \end{pmatrix} \tag{5.6}$$

or

$$\underline{\beta} = \alpha \underline{a} \tag{5.7}$$

where β is the column vector with elements:

$$\beta_n = \sum_{i=1}^{N_p} B_S(i) f_n(i) \tag{5.8}$$

and a is the matrix with elements:

$$\alpha_{mk} = \sum_{i=1}^{N_p} f_k(i) f_m(i) \tag{5.9}$$

The optimised currents are then the elements of the vector matrix a:

$$-\underline{a} = \alpha^{-1} \underline{\beta} \tag{5.10}$$

After applying the calculated optimum currents, another scan needs to be done to check whether the effect is as predicted and to apply further iterations if necessary.

5.6.2 Predicted and Measured Magnetic Fields and T_2 relaxation time

As stated above, the magnetic scans of the residual SCV B-field covered only 168 out of the 264 positions. After using the above optimisation method, 5 different optimisation currents were applied. Once a set of 19 currents was decided upon, the apparatus waas warmed above the superconducting transition temperature of the solenoid (at about 9.1 K), the two inner mu-metal shields were demagnetised and then the compensation coils were activated before the system was cooled again to below 7 K.

In the following two tables, the details of the labelling of the configurations and the coil settings for the reference and the optimised fields are given. As a reference field, we considered the field profile taken during the 6th of July 2010 magnetic scan.

Of the 5 optimisation configurations, only the 1^{st} and 4^{th} use the outcome of the minimisation routine without any further manual fitting. In our first configuration, we

No.	Date	Comment
0	07/06/10	No compensation coils. Solenoid and Guide Field ON (reference field)
1	07/07/10	Config. 1. Axial Coils Only
2	07/08/10	Config. 2. Axial+Azimuthal Coils + Hand-fit
3	07/08/10	Config. 3. Axial+Azimuthal Coils + Hand-fit
4	07/09/10	Config. 4. Axial+Azimuthal Coils
5	07/09/10	Config. 5. Config 4. but with +10% to all axial coil currents

Table 5.4: Labelling of the reference and the optimised field configurations.

Configuration No.	0	1	2	3	4	5
AX1 (mA)	0	-24.1	103.7	-46.63	-44.4	-48.87
AX2 (mA)	0	-5.17	-29.515	2.695	6.64	7.3
AX3 (mA)	0	-9.18	-27.802	-4.25	-12.1	-13.3
AX4 (mA)	0	2.78	-19.345	-1.21	-9.99	-10.99
AX5 (mA)	0	4.73	-0.08	1.522	0.3	0.33
AX6 (mA)	0	8.99	-4.153	12.989	6.74	7.42
AX7 (mA)	0	-9.89	90	-6.387	0.4	0.44
AZ1 (mA)	0	0	18	18	-6.94	-6.94
AZ2 (mA)	0	0	20	20	87.9	87.89
AZ3 (mA)	0	0	20	20	30.16	30.16
AZ4 (mA)	0	0	18	18	22.47	22.47
AZ5 (mA)	0	0	0	12	43.63	43.63
AZ6 (mA)	0	0	0	20	3.07	3.06
AZ7 (mA)	0	0	0	-12	35.2	35.16
AZ8 (mA)	0	0	-18	-18	-4.15	-4.15
AZ9 (mA)	0	0	-20	-20	-43.54	-43.55
AZ10 (mA)	0	0	-20	-20	-28.8	-28.83
AZ11 (mA)	0	0	-18	-18	8.37	8.36
AZ12 (mA)	0	0	13.878	-5.651	25.41	25.41
6WS TC (mA)	-10	-10	-10	-10	-10	-10
HV TC(mA)	-12	-12	-12	-12	-12	-12

Table 5.5: Coils settings for the reference and the five optimised fields.

attempted to smooth only the axial gradient of the field by activating the 7 axial coils and keeping the azimuthial coils off. The other four configurations were also intended to compensate for the azimuthial deviation but different weighting factors were given to B-field data points at different distances from the main axis.

When conducting the magnetic scans, at each z position the central fluxgate (Blue FG) at r=0 took 24 measurements while the other two fluxgates took only one at each angular position. For this reason we reduced the weight given to the central points by a factor of 1/24 in all five optimisation configurations. On the other hand, the space points covered by the yellow fluxgate are not part of the Ramsey cells volume. Therefore, as neutrons do not sample these points, it was decided to reduce the weighting factor of the r=0.15 m points in one of the optimisation sets to 0.25 (configuration number 2). Finally, the r=0.075 m points (recorded by the Red FG) lie on a circle of radius equal to half that of the RCs and therefore their weighting factor was kept at 1 (see Table 5.6).

The reason that some of the currents were adjusted manually in configurations 2 and 3 is because, for the given weighting factors, is because the values given by the optimisation method required more powerful current supplies than the ones available at ILL (the maximum current that can be delivered by the existing current suppliers is 150 mA). In these cases, the minimisation routine has been run again with fewer free parameters.

Configuration No.	Blue Fg	Red FG	Yellow FG
0	N/A	N/A	N/A
1	1/24	1	0
2	1/24	1	1/4
3	1/24	1	0
4	1/24	1	1
5	1/24	1	1

Table 5.6: Weight factors for the three fluxgates.

The ultimate goal in this exercise is to increase T_2 for the neutrons in the actual resonance field in the RCs. To extract this information, Monte Carlo (MC) simulations were run by P. G. Harris. These simulations consider the UCN moving as an ideal gas inside a cylinder and in a given magnetic field. For each of the proposed sets of currents we produced a theoretical field map given by the optimisation routine and an experimentally measured map. Running the MC for these two grid maps we found that there is a good agreement between the expected T_2 values for either cases (Figure 5.16).

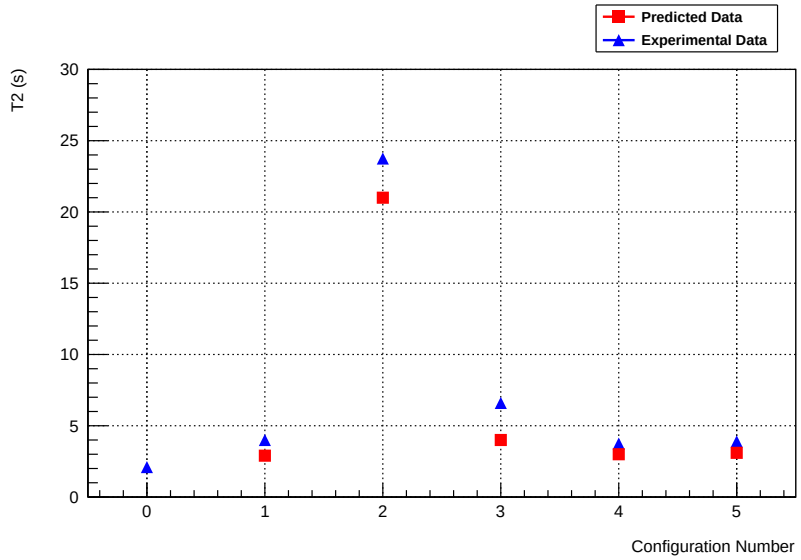

Figure 5.16: Monte Carlo simulations results for T_2 relaxation times for the predicted (red squares) and measured (blue triangles) B-field configuration.

According to these simulations, trimming the axial gradient only Configuration 2 makes a significant difference to T_2 value; When the outermost points contribute with a non-zero weighting factor but less than that of the middle points, the optimisation routine changes the B-field in a way that T_2 relaxation time of UCN is increased from about 2 seconds to more than 20 seconds.

5.7 Conclusions

We measured the field-current response of all the 19 carbon fibre former compensation coils within the region of the RC in the presence of the three μ-metal shields. This information was then used to calculate the optimum currents for these coils with a new routine which approaches the problem as a linear (19 parameter) function minimisation. Attaching different weighting factors to points at different axial distances, we improved the T_2 relaxation time (as this calculated by MC simulations) by one order of magnitude.

It is worth mentioning that the set of the 19 compensation coils were originally designed to correct for very small inhomogeneities (few tens and not hundreds of nT) in the solenoid windings. On the other hand, the applied minimisation routine with the existing maximum current restrictions clearly works as it improves T_2 by a factor of 10.

Further improvement would require first of all a detailed scan of the SCV magnetic field by using 3D fluxgates and then a modification of the minimisation routine as appropriate

to incorporate the additional information. Also, the current supplies should probably be replaced with others which can deliver currents higher than 120 mA.

Nonetheless, the ideal way to proceed with an EDM measurement is to eliminate all the existing magnetic anomalies. The safest solution would be to replace the SCV with a non magnetic one and operate the 19 compensation coils for their original purpose.

Chapter 6

Polarisation Data Analysis for November 2010 Run

A considerable amount of data was taken over winter of 2010 run. The aim was to observe the Ramsey resonance curve and extract information about the neutron number density and the time we can store ultra cold neutrons. However, the preliminary analysis showed very quickly that neutrons were highly depolarised (polarisation levels reached 40% maximum) and a lot of effort was put in during the run to identify the source of this problem and to investigate possible solutions.

By the time the run was finished, the polarisation of neutrons could not be increased to the level in previous runs of about 77%. This unexpected result led to us looking at these data more closely. The aim of the analysis in this chapter is to extract information about the reasons that led the neutrons to be depolarised and determine what we have to do in the future to eliminate the problem.

At the beginning of this chapter, detailed descriptions of the different types of data files and sequences of the data taking are given. The method of analysing the raw data and some new analysis routines which take into account various issues are then presented. The results of the different types of analysis have revealed issues that have to be resolved in a more consistent and systematic way in future runs.

6.1 Data Files

All data files referred to here are available on nedm@minostux.uscs.sussex.ac.uk data repository in nedm/rundata/cycle160 directory.

6.1.1 Files Selection

The range of files where the temperature was low enough for UCN production and observation is between file #1353 (T=0.9 K -on cooling) and file #1591 (T=0.98 K -on warming). The majority of these files (163 out of 239) do not provide any useful information either because:

1. They were ranked as "junk files", i.e. runs used to resolve issues like checking different parts of the electronics, valve operations, the DAQ software etc. For these files, the neutron beam was always off.

2. The neutron beam was on but the count rate was very low such that the different valves settings were not distinguishable on the MCS spectra.

In the table *"Detection Settings"* in Appendix F2 all the (76) useful for analysis files are listed accompanied by the information about MCAs and MCSs labelling.

6.1.2 Types of Experimental Data

As has been discussed in Chapter 2, there are two sets of data available for analysis, those from the MCS and MCA spectra. Before proceeding to the analysis, a detailed description is given below of the way in which the spectra were categorised.

It is useful here to briefly review the experimental arrangement. Figure 6.1 shows the relevant valves which are used to control the movement of the neutrons around the apparatus. The main gate valve, V1, is immediately after the polariser and allows the cold neutron beam to enter the apparatus, via an aperture which can be varied in size. The Source Valve, SV (see Figure 6.2(a)), is of the plug type, i.e. it has a cylindrical plug which can be rotated inside the valve body to allow or block flow through the valve. When it is closed, allows the UCN density to build up in the source volume. Opening the SV allows the neutrons to enter the curved guide section in the transfer section. The Flap Valve, FV (see Figure 6.2(b)), is situated in the horizontal guide tube, directly above a vertical guide (the detector tube), at the bottom of which the detectors are located. In the "open" position, the plate of the FV is horizontal and (in principle) closes the entrance to the detector tube, thus allowing neutrons from the source to move into the horizontal section of guide leading to the Ramsey Cells. In the closed position, the FV plate is vertical, blocking the path from the transfer section and allowing neutrons in the horizontal tube to fall into the detector tube and hence to the detectors. At the end of the horizontal guide a "pre-volume" at the back of the Ramsey Cell assembly contains

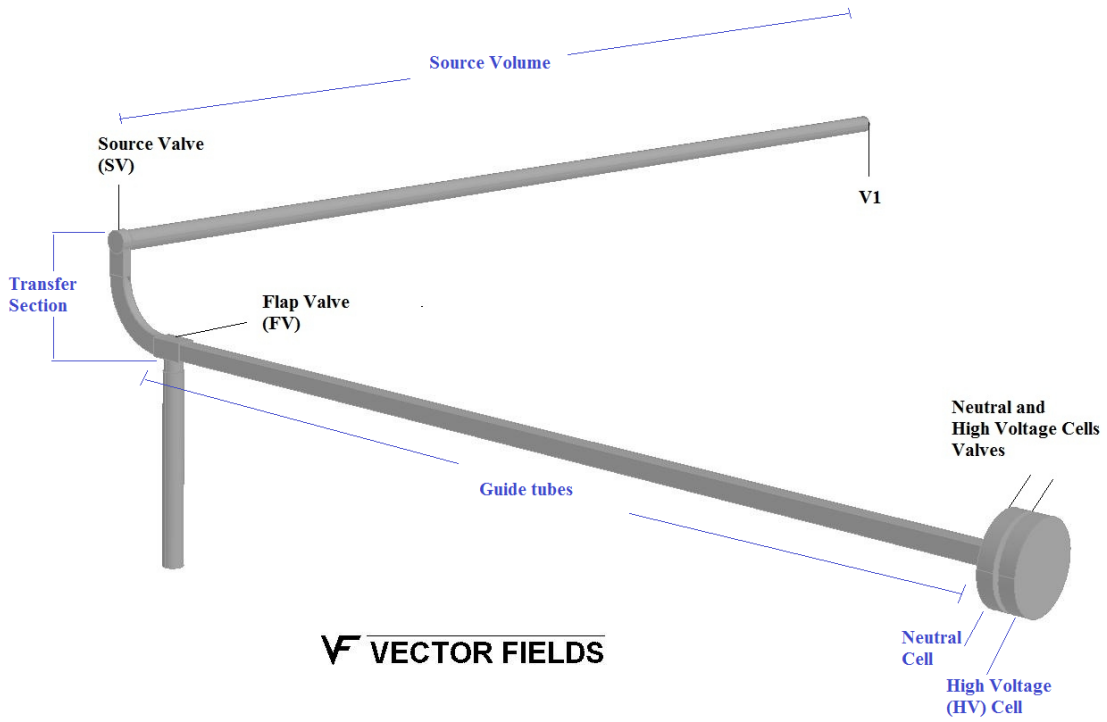

Figure 6.1: The position of the five available valves along the neutron guides. V1 controls the entrance of the neutron beam and signals the beginning of data taking. The other four valves are used to manipulate the transit of neutrons through the different parts of the apparatus as described in the text.

two further plug valves which allow neutrons to be stored in the HV and Neutral cells. At the end of Ramsey resonance cycle, these two valves are opened consecutively (first the neutral and then the HV cell valve) and with the FV in the closed (vertical) position, the neutrons are detected and analysed. It should be noted here, and will be shown below, that in the November 2010 run, the FV did not move completely to either the fully vertical or horizontal positions. A similar problem occurred with the SV not closing completely, but to a much lesser degree.

MCS Spectra and Neutron Sampling

Each Multi-Channel Scaler (MCS) spectrum gives essentially the number of neutrons counted in a given detector as a function of time. The shape of the spectrum is then defined by a series of different valve settings and the sequence and times at which they occur. In the Autumn 2010 experiment there were 8 different types of MCS spectra that correspond to 10 different valves settings (see Table 6.1). All figures below in this section show MCS spectra of UCN1 detector which detects neutrons of both spin states.

Valves configuration	**V1**	**SV**	**FV**	**Neutral Cell Valve**	**High Voltage Cell Valve**
1a	Open	Open	Open	Open	Open
1b	Open Open	At least partially Open Closed	Open Open	Open Open	Open Open
2	Open	Closed	Closed	Open	Open
3	Open	Closed	Closed	Closed	Closed
4	Open	Open	Closed	Open	Open
5a	Closed	Open	Closed	Open	Open
5b	Closed Closed	At least partially Open Closed	Closed Closed	Open Open	Open Open
6a	Closed	Open	Closed	Open	Closed
6b	Closed Closed	At least partially Open Closed	Closed Closed	Open Open	Closed Closed
7a	Closed	Open	Closed	Closed	Closed
7b	Closed Closed	At least partially Open Closed	Closed Closed	Closed Closed	Closed Closed
8	Closed	Open	Open	Open	Open
9	Closed	Closed	Closed	Open	Open

Table 6.1: Indicated and actual position of the various Valves for the different configurations. For Valve Configurations 1b, 5b, 6b and 7b the actual positions could not have corresponded to those indicated in the DataView header file (see text for why is this so). For these configurations, the table shows the (deduced) actual valve positions (top line) and the the recorded in DataView header settings (bottom red).It is important to note that the FV did not move completely to either the fully vertical or horizontal positions.

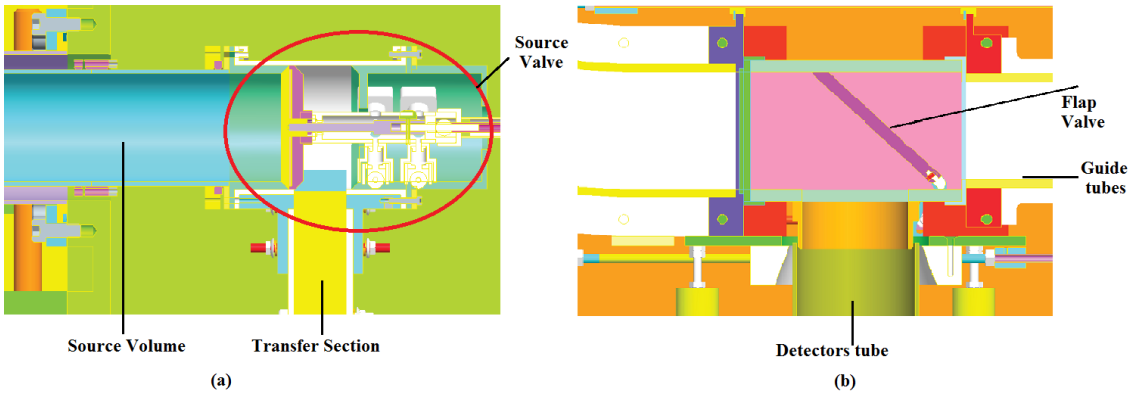

Figure 6.2: A depiction of (a) the Source Valve (SV) and (b) the Flap Valve (FV).

Type A.

Files #1353 to #1365, #1533, 1543, 1548 and finally files from #1565 to #1575 fall into this category. Their MCS spectrum is shown on Figure 6.3. The sequence of this type of run consists of two parts:

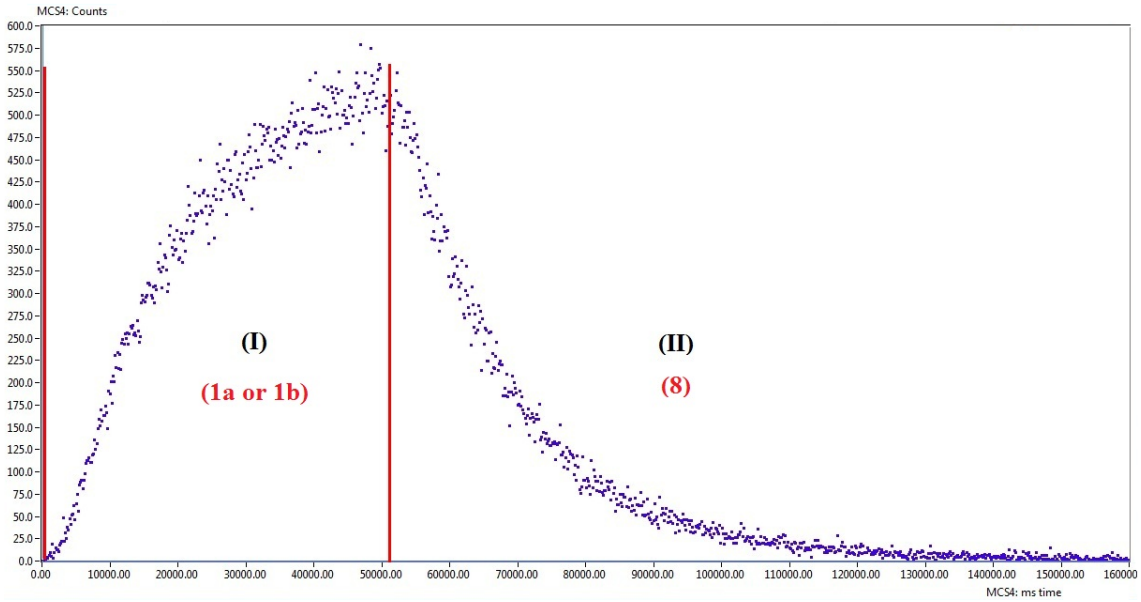

Figure 6.3: Type A (file #1359)MCS spectra from the UCN1 open detector. The valve configurations are shown as red numbers.

(I) **Fill the Source Volume, the guide tube and the cells:** V1 is open to let cold neutrons enter the Source Volume while the SV and FV are at least partially open allowing ultra cold neutrons to diffuse as an ideal gas to all the available volumes of not only the Source tube but also the guide tube and the cells. We note that neutron count rate did not reach a constant maximum value or settle on a plateau, which means that the neutron density on these volumes has not reached its equilibrium

value. This is probably because V1 was not left open long enough time to fill them.

(II) **Empty all volumes (Source/guide tube and cells):** V1 is now shut and neutrons are falling into the detectors tube where captured by the LiF layer.

With the FV in the horizontal position the detector volume should be isolated from the guides and one might expect that no neutrons should be recorded. Nevertheless, even though the FV appears to be horizontal, it is not closing off the tube above the detectors since neutrons are being detected.

Area	**Type of Valves Settings**
I	1a or 1b
II	8

Table 6.2: Valves settings as recorded on the DataView Header for Type A files. The rapid increase of neutron counts while filling the Source (region I) implies that the SV was half-open instead of closed. The FV and the cells valves were not yet connected.

In these files, having the FV and the cell valves permanently open to the beam, means that the neutrons being detected are a mixture of neutrons coming from all parts of the guides and the cells. Neutrons in area I are mostly coming directly from the Source Volume and these are considered in our analysis to be the "neutrons from the Source". There are no regions in this type of spectra where we detect neutrons coming solely from the cells.

NB: It is important to know that the indicators in the DataView header giving the valve positions are not always reliable. In the case of files #1353 to #1365, the actual SV position is inconsistent. The reason for this is as follows: The SV (according to the DataView Header) is closed to build up neutron density, but the neutron rate is constantly increasing in area I, instead of being zero. This implies that the SV was actually set open or at least half-open instead of closed. This argument is enhanced by the similarity of the spectra between this group of files and those files where the SV is recorded open.

Type B.

Files #1382 and 1384 fall into this category. The MCS spectra of this type (see Figure 6.3) can be analysed into three parts:

(I) **Fill the Source Volume:** V1 is open to let cold neutrons enter the Source Volume while SV is kept closed to build up neutron density. The FV is now in the vertical (at about 70 degrees) position, valving off neutrons that have escaped from the

Source tube. The neutron count rate is increasing slowly, instead of being zero, which means that the SV is leaking again but this time to a lower degree than in the previous group of files (Type A).

(II) **Fill the guide tube and cells:** V1 is now shut and both the SV and FV are open to empty the Source Volume and let neutrons fill the guide tube and the cells.

(III) **Empty the guide tube and the cells:** FV is closed (set at vertical position) exposing the detector tube to the neutrons from the guide tube and the cells.

Through all these steps, the cell valves were open. The valves settings for this type of file are given in the following table:

Area	**Type of Valves Settings**
I	2
II	8
III	5a

Table 6.3: Valves settings as recorded on the DataView Header for Type B files. The slow increase of neutron counts while filing the Source tube (region I) implies that there is some leakage through the SV. The Cell valves were not operated.

Neutrons in area II can be considered as coming mainly out of the source tube, but there is an unavoidable mixing with neutrons that have spent some time in the transfer section and the cells. Neutrons in area III come from the transfer section and the cells. Neutrons from area II have been considered as "neutrons from the source". Again, neutrons have not been trapped in the cells, so there is no part of this type of spectra either which we can consider that we detect neutrons from the cells.

Type C.

The valves settings for files #1406 to 1408 (see Figure 6.5) were intended to manipulate neutrons as follows:

(I, II) Fill the Source Volume, the guide tube and the cells: V1, SV and FV are all open into the Source Volume and then allow UCN to fill the guide tube and the cells. On the DataView Header, the SV is recorded as closed at region (I), but this seems not to be the case as we see the neutron counts increase with a constant rate over these two areas. If the SV was initially shut, a relatively abrupt increment in neutron counts should have been recorded when it was opened (see files of Type D).

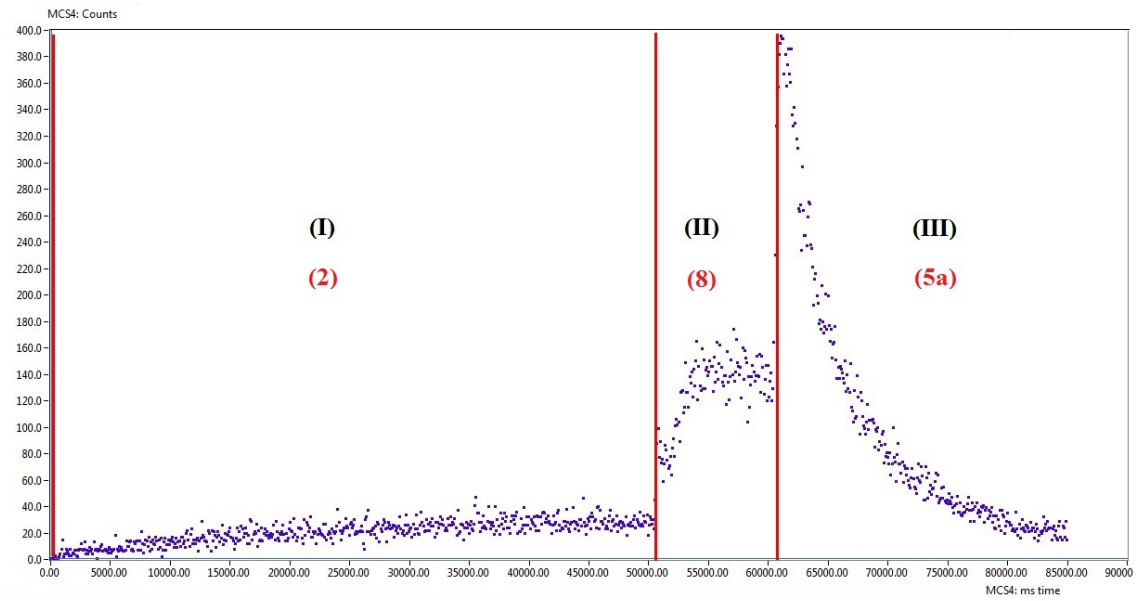

Figure 6.4: Type B (file #1382) MCS spectra from the UCN1 open detector. The Valve Configurations are shown as red numbers.

(III) Empty the guide tube: V1 is now shut and the FV closes (set at vertical position) to empty the guide tube. The cell valves are both shut to trap the neutrons already in there.

(IV) Empty the neutral cell: The neutral cell valve only opens to release neutrons. No change to the rest of the valves.

(V) Empty the high voltage cell: Finally, the high voltage cell is emptied by opening its valve.

These are the first files in which the cells are isolated for some period of time from the rest of the guide tubes. Neutrons in regions I and II can been considered to be coming mainly from the source volume with some mixing with the neutrons ffrom the transfer section guide tubes and the cells. Neutrons in areas IV and V are those which have been stored in the cells. In our analysis, region II has been used to calculate the polarisation of the "neutrons coming from the source" (to be consistent with the DataView header) and regions IV and V for that of "neutrons coming from the cells".

Type D.

File #1427 MCS spectrum is shown on Figure 6.6 and consists of five parts:

(I) **Fill the Source Volume:** V1 is open to let cold neutrons enter the Source Volume while SV is kept closed to build up neutron density. FV is also closed, and according to a comment on the electronic logbook, is the valve that actually operated as a SV

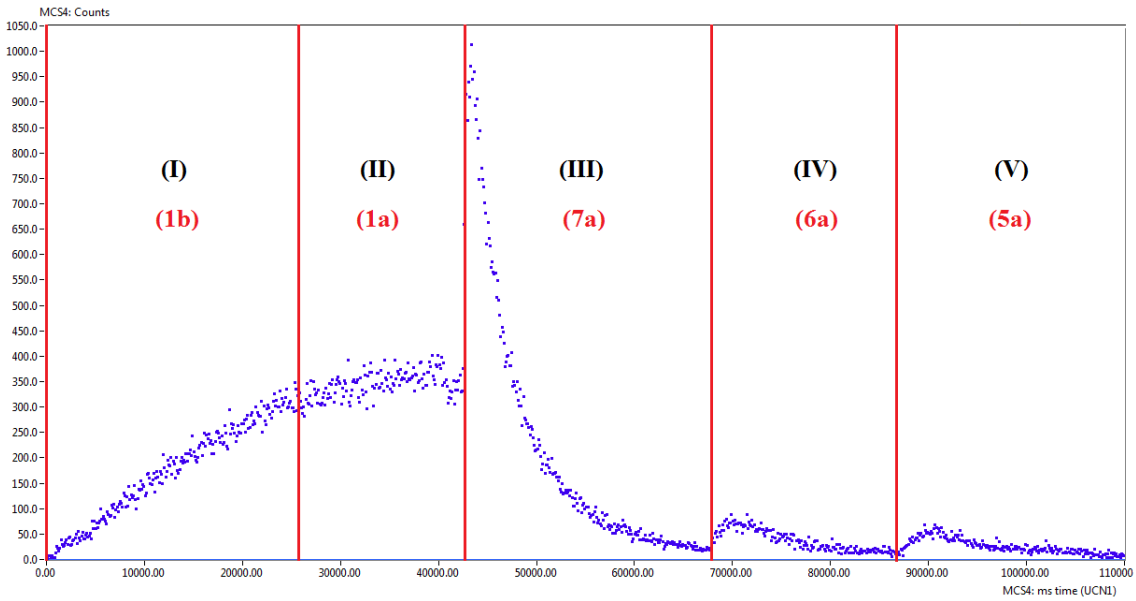

Figure 6.5: Type C (file #1408) MCS spectra from the UCN1 open detector. The Valve Configurations are shown as red numbers.

Area	**Type of Valves Settings**
I	1b
II	1a
III	7a
IV	6a
V	5a

Table 6.4: Valves settings as recorded on the DataView Header for Type C files. The linear rise in neutron counts in regions I and II, implies that the SV was open contrary to the DataView Header recorded information. This group of files are the first where neutrons are stored in the cells.

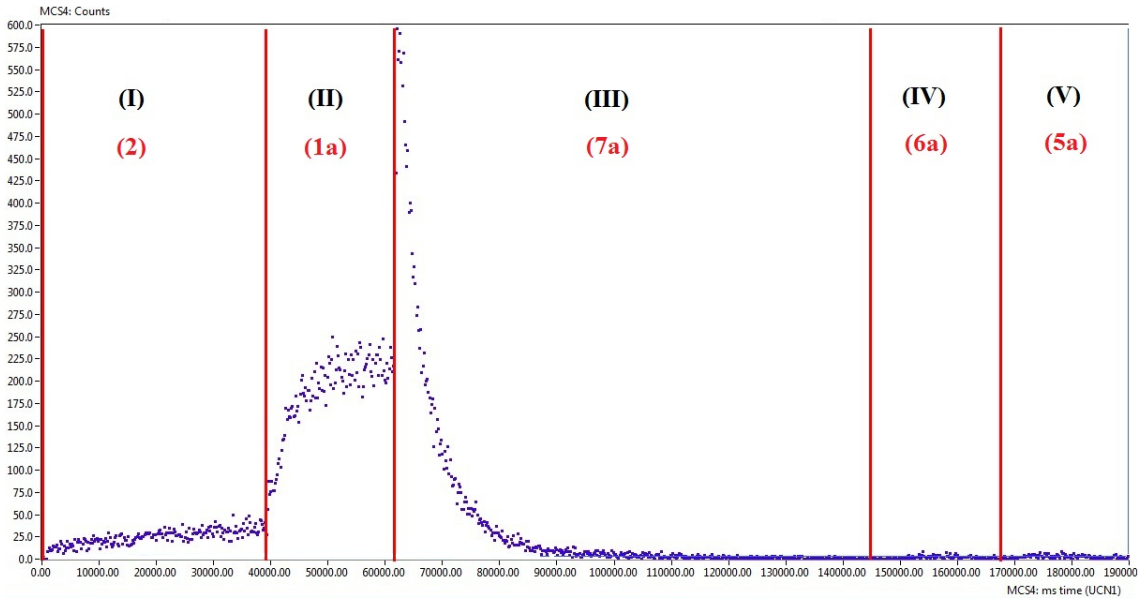

Figure 6.6: Type D (file #1427) MCS spectra from the UCN1 open detector. The Valve Configurations are shown as red numbers.

since the latter had been moved to far open before this run begins, so it could not seal the Source Volume properly. The cell valves are open.

(II) **Fill the guide tube and the cells:** V1 is kept open while the SV and FV are also open to allow neutrons to fill the guide tube and the cells, whose valves are both open.

(III) **Empty the guide tube:** V1 is shut and FV now closes (set at vertical position) to empty the guide tube. The cell valves are both shut to trap the neutrons already in there.

(IV) **Empty the neutral cell:** Neutral cell valve only opens to release neutrons from there. No change to the rest of the valves.

(V) **Empty the high voltage cell:** Finally, the high voltage cell is emptied by opening its valve.

Region II, has been chosen to calculate the polarisation of neutrons that "come from the source". In reality, there is some mixing with the neutrons in the transfer section guide tubes and the cells. Neutrons of regions IV and V are again those stored in the cells while the guide tubes are being emptied. Both regions have similar polarisation values and region V is selected for our polarisation analysis of "neutrons coming from the cells".

Area	Type of Valves Settings
I	2
II	1a
III	7a
IV	6a
V	5a

Table 6.5: Valves settings as recorded on the DataView Header for Type D files. This type of MCS spectrum is the closest to the ideal run for the nEDM experiment as described in section

Type E.

File #1448 MCS spectrum (see Figure 6.7) is divided into four sections:

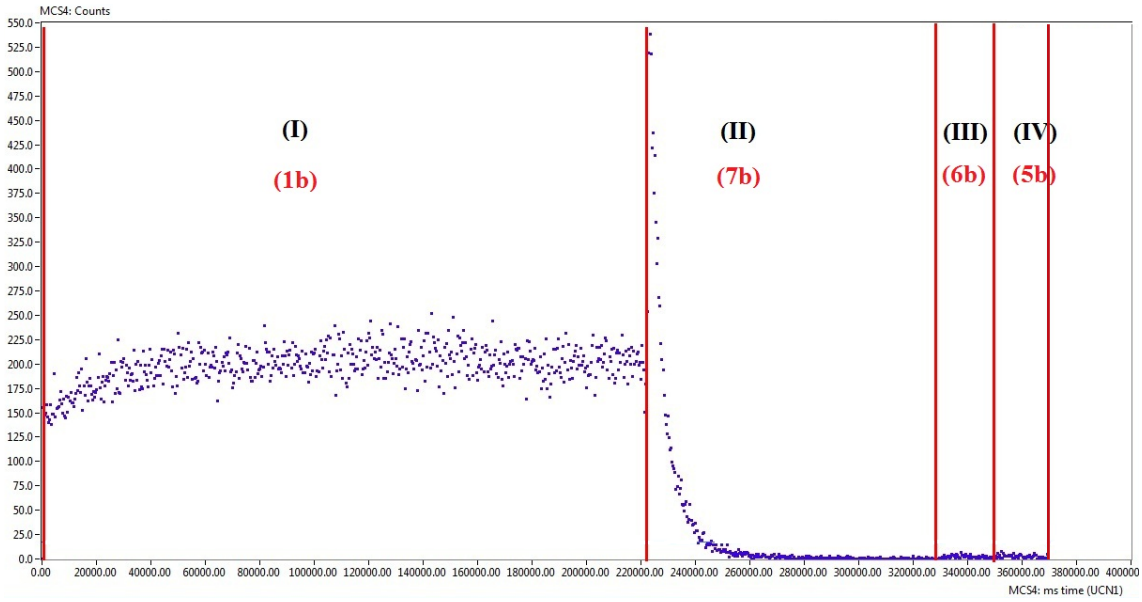

Figure 6.7: Type E (file #1448) MCS spectra from the UCN1 open detector. The Valve Configurations are shown as red numbers.

(I) **Fill the Source Volume, the guide tube and the cells:** V1 is open for the whole period of 220 seconds of this area letting cold neutrons into the Source Volume. However, on the DataView Header, the SV is recorded as closed over this period and during the whole run. This is clearly incorrect since the neutron count rate is constant over most of this area. In fact, since the neutron counts do not start from zero means that V1 actually opened before the set time. The FV and the cell valves are open as well.

(II) **Empty the guide tube:** V1 is now shut and the FV closes (set at vertical position) to empty the guide tube. The cell valves are both shut to trap the neutrons already in there.

(III) **Empty the neutral cell:** FV remains shut and the neutral cell valve opens to release neutrons.

(IV) **Empty the high voltage cell:** Finally, the high voltage cell valve opens.

Area	Type of Valves Settings
I	1b
II	7b
III	6b
IV	5b

Table 6.6: Valves settings as recorded on the DataView Header for Type E files. The SV here is recorded as closed through the whole run but the shape of the MCS spectrum implies that it must have been open.

Neutrons in region I have been considered as coming "from the source", even though there is a strong mixing with neutrons from the guide tube and the cells. Regions III and IV are the neutrons from the two cells separately, after emptying the guide tubes. In our analysis, we chose region IV to represent the polarisation of "neutrons from the cells".

Type F.

File #1464 and also files from #1471 to #1527 fall into this category (see Figure 6.8 for their MCS spectrum). The valves sequence is described below:

(I) **Fill the Source Volume:** V1 is open to let cold neutrons enter the Source Volume while SV and FV are kept closed to build up neutron density. The neutron count rate is non-zero but rather constant which indicates a small leakage through the SV and FV. The neutrons that manage to escape the Source Volume are either falling into the detector tube or diffusing in the guide tube and the cells since their valves are open from the beginning of the run.

(II) **Fill the guide tube and the cells:** Keeping V1 open, SV and FV are open as well to allow neutrons to fill the guide tube and the cells whose valves are both

open. The new neutron density in the detector tube is increasing abruptly while emptying the Source tube.

(III) **Empty the guide tube:** V1 is kept open but the SV is now closed, preventing most of neutrons in the Source Volume from reaching the guide tube. On the other hand, FV closes (set at vertical position) to empty the guide tube while the cell valves are both kept shut.

(IV) **Empty the cells:** The neutral and high voltage cell valves open simultaneously to release neutrons giving only one peak. V1 closes only now.

Area	**Type of Valves Settings**
I	2
II	1a
III	3
IV	9

Table 6.7: Settings as recorded on the DataView Header for Type F files.

Region II can be considered as corresponding to "neutrons coming from the source", again with some mixing of neutrons that have spent time in the guide tube and/or the cells. Finally, region IV is used to calculate the polarisation of "neutrons coming from the cells".

Type G.

Files #1528, 1529, 1534 and 1542 (see Figure C.1) are runs during which an rf pulse was applied. The valves sequence that has been followed is a double iteration of Type F files with the rf pulse being applied in the first part of the runs, as described below:

(I) **Fill the Source Volume:** V1 is open to let cold neutrons enter the Source Volume while SV and FV are kept closed to build up neutron density. V1 will remain open during the whole run.

(II) **Fill the guide tube and the cells:** SV and FV are open in order to allow neutrons fill the guide tube and the cells.

(III) **Empty the guide tube + rf pulse:** SV and FV close to empty the guide tube while cell valves are both shut to trap the neutrons there. The rf pulse is applied to the stored neutrons.

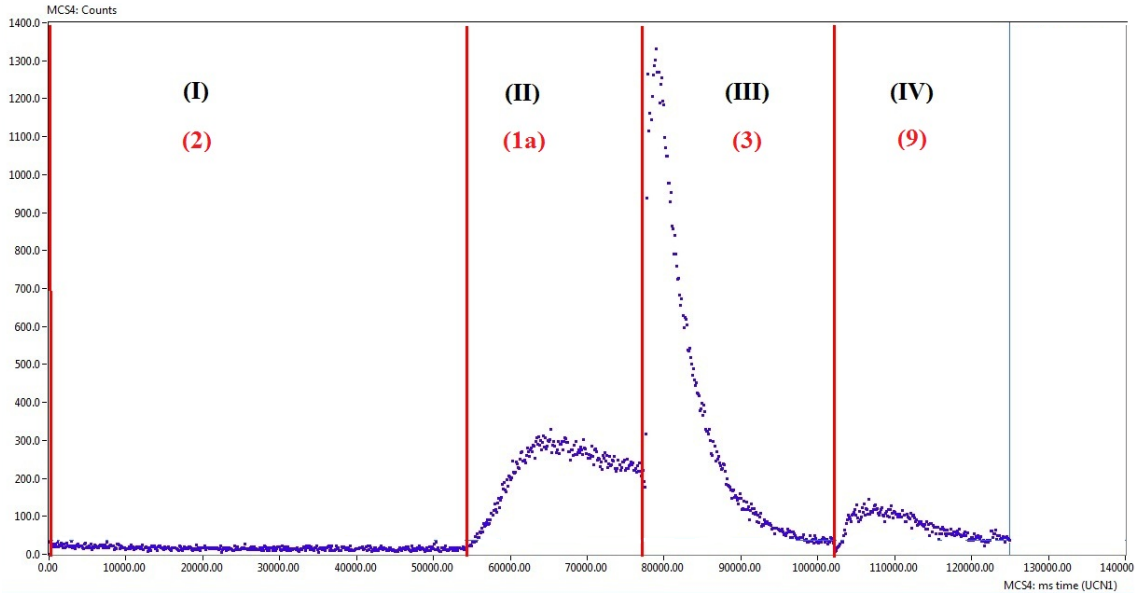

Figure 6.8: Type F (file #1471) MCS spectra from the UCN1 open detector. The Valve Configurations are shown as red numbers.

(IV) **Empty the cells:** The neutral and high voltage cell valves open simultaneously to release neutrons.

Regions (V) to (VIII) are an iteration of the previous four steps but now no rf pulse is applied while the neutrons are stored in the Ramsey Cells. For these runs, we are mainly interested in the neutrons that come out of the cells (regions IV and VIII) to compare their polarisations. The polarisation of neutrons that come directly from the source has been calculated for areas II and VI.

Area	Type of Valves Settings
I	2
II	1a
III	3
IV	2
V	2
VI	1a
VII	3
VIII	2

Table 6.8: Valves settings as recorded on the DataView Header for the runs where an rf pulse was applied while storing the neutrons in the Ramsey Cells (files Type G).

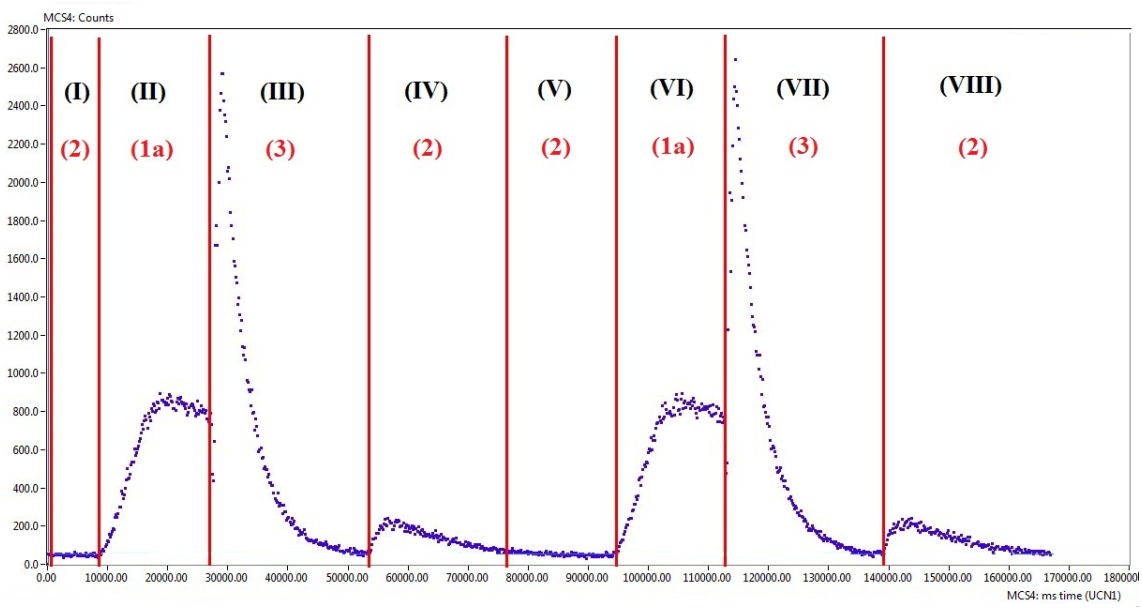

Figure 6.9: Type G (file #1528) MCS spectra from the UCN1 open detector. The Valve Configurations are shown as red numbers.

Type H.

For files #1552 to #1563 the SV was not functional and kept open during the runs. These spectra (see Figure 6.10) can be divided into five sections:

(I) **Fill the Source Volume:** V1 is open to let cold neutrons enter the Source Volume. SV is open so the FV is effectively operating as the source valve and used to build up the neutron density by keeping it closed in the vertical position. Since the FV is not sealing the Source tube properly, the neutron count rate is constantly increasing in this area. The cell valves are open.

(II) **Fill the guide tube and the cells:** V1 closes, the SV remains open and the FV is open as well to allow neutrons to fill the guide tube and the cells.

(III) **Empty the guide tube:** FV now closes (vertical position) to empty the guide tube. The cell valves are both shut to trap the neutrons.

(IV) **Empty the neutral cell:** Neutral cell valve only opens to release neutrons from there. No change to the rest of the valves.

(V) **Empty the high voltage cell:** Finally, the high voltage cell is emptied by opening its valve.

Similarly to files of type D, the neutrons in region II are essentially those coming from

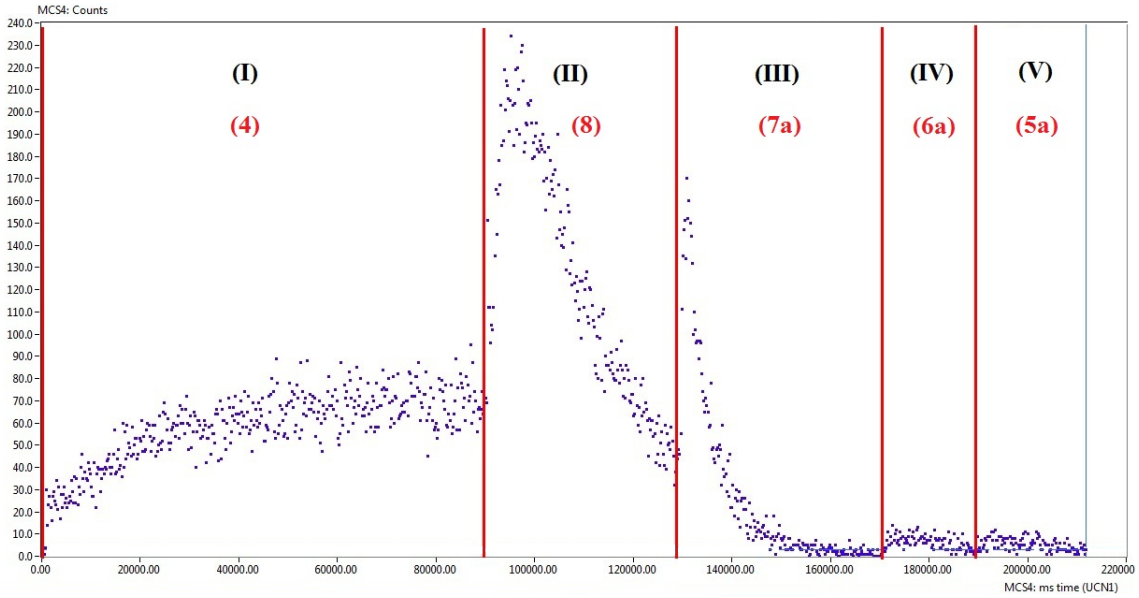

Figure 6.10: Type H (file #1555) MCS spectra from the UCN1 open detector. The Valve Configurations are shown as red numbers.

Area	Type of Valves settings
I	4
II	9
III	8
IV	7
V	6

Table 6.9: Valves settings as recorded on the DataView Header for files of Type H. The spectra of this type are similar to these of type D but here the SV was static open.

the source tube again with some mixting with neutrons from the other volumes. Neutrons in regions IV and V are coming from the two cells after the guides have been emptied.

MCA Spectra

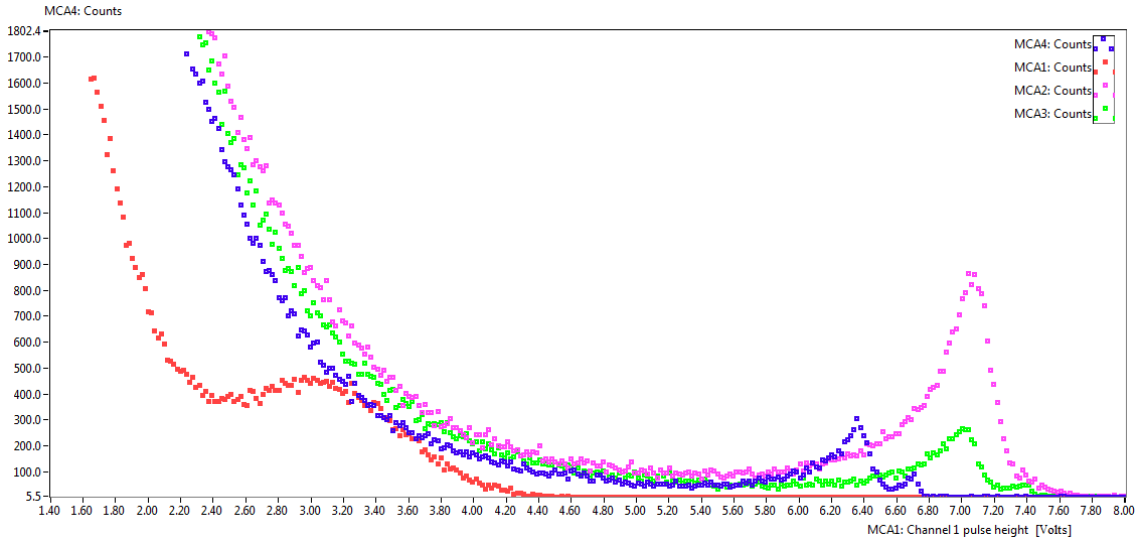

Figure 6.11: Typical MCA spectra for the UCN1 (red dots), UCN2 (purple dots) open detectors and the UCN3 (green dots) and UCN4 (blue dots) iron detectors for run #160 (Data refer to file #1382).

The typical Pulse Height (MCA) spectra for the Open (UCN1/UCN2) and the Iron (UCN3/UCN4) detecors for the run #160 are shown in Figure 6.11. We expect to see both alpha and triton peaks in each of these plots but only the latter is clearly visible. In all four cases the presence of background or electronic noise seems to dominate the low pulse height area where the alpha peak is expected. For the UCN1 Open detector (red dots) it affects the triton peak as well. As can be seen in the same Figure, this is because the settings of the amplifiers before the detectors have placed the UCN2/UCN3 and UCN4 triton peaks at about 6.5 Volts –well away from the background/noise. The UCN1 triton peak, on the other hand, is set at about 3.0 Volts which largely overlaps with the background/noise. We note here that the UCN2 Open detector started exibiting a deformed MCA spectrum after the tenth useful run file (#1384). Hence, most of our Open detector data are based on the UCN1 and not on UCN2 detector.

For the vast majority of the 76 useful files, the MCA spectra are similar to those shown in Figure 6.11. For the first 8 files, however, the spectra are slightly different. The positions of the peaks are more or less the same but the background/noise levels are significantly diminished by about two orders of magnitude. For these 8 files and for all

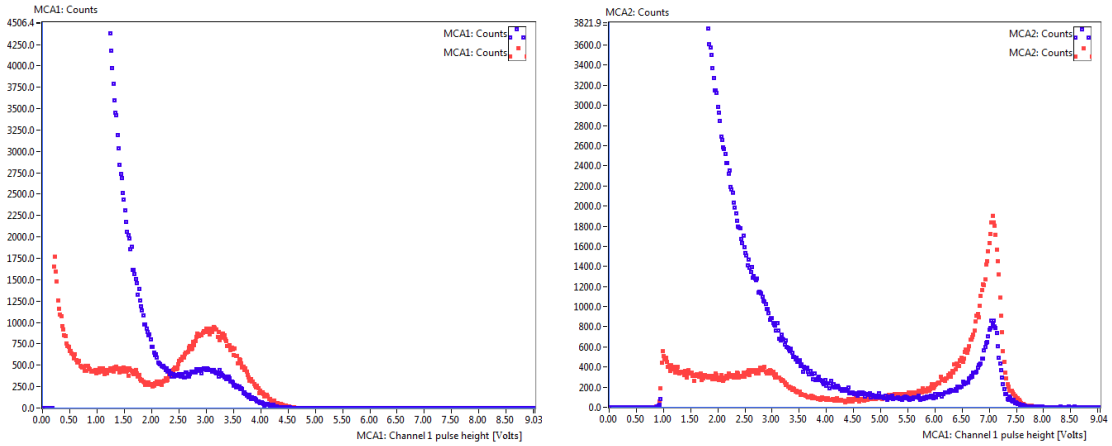

(a) UCN1 Open Detector

(b) UCN2 Open detector

Figure 6.12: Comparison of the MCA spectra of the UCN1 and UCN2 open detectors before (red dots for file #1365) and after (blue dots for file #1382) the FV connection.

detectors, we can even see a clear sign of the alpha peak. According to the information recorded on the electronic logbook, this change occured (according to what is recorded in the electronic logbook) when the flap valve (FV) was connected. That means that before it was electrically disconnected and in a static open position and after this point was in full operation. A comparison of the MCA spectra for each of the detectors before and after the FV connection is presented in Figures 6.12 and 6.13.

The effect of the background/noise –mainly in the UCN1 open detector data– on the polarisation analysis has been a serious concern. Our approach to deal with this problem is presented in section 6.5 while the results so derived are given in section 6.6.4.

6.2 Neutron Sampling and Polarisation Analysis

The polarisation analysis aims to determine the polarisation of neutrons released from the cells after they have been stored there for some period of time and undergone a Ramsey sequence. However, because of the unexpectedly low polarisation that was found in the Autumn 2010 run, we were also interested in the polarisation of the neutrons before they enter into the cells. Ideally, we would like to know the polarisation of the neutrons at all points in the apparatus separately, starting after the polariser, in order to see where it degrades.

Although there were two detectors on the Source Volume, these detected both spin states ("open"). Hence, a polarisation could only be determined by using the two "open"

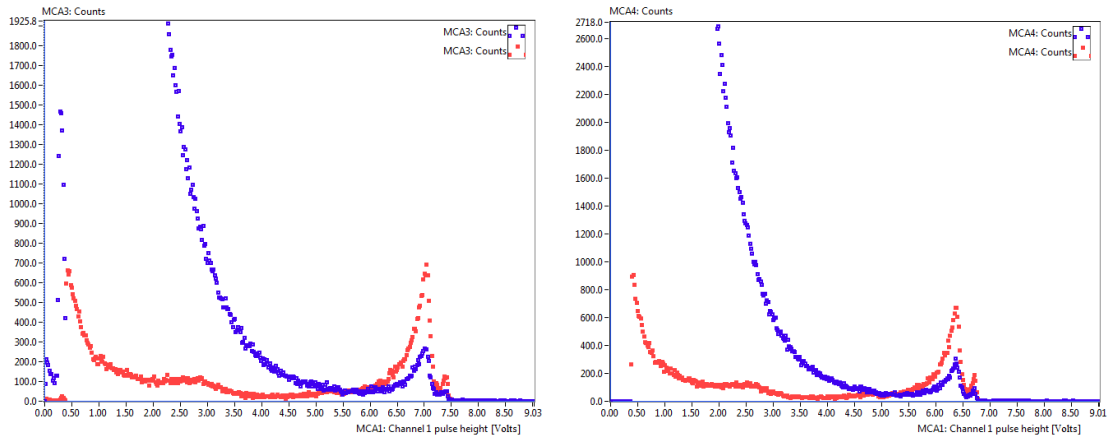

(a) UCN3 Iron Detector

(b) UCN4 Iron Detector

Figure 6.13: Comparison of the MCA spectra of the UCN3 and UCN4 iron detectors before (red dots for file #1365) and after (blue dots for file #1382) the FV connection.

and the two "closed" detectors at the bottom of the detector tube. In order to measure the polarisation in different parts of the apparatus, we selected different time regions of the MCS spectra in the following two ways:

1. Neutrons that come largely from the source. Ideally, these would be only neutrons that exit from the Source Volume when we open the SV and the FV and are led directly to the detectors tube. However, as explained below, the actual situation is more complicated.

2. Neutrons coming from the cells.

It has to be stressed that, for different types of MCS spectra, these two categories will correspond to different areas of the spectra and to different valve settings. This mainly affects the analysis made for neutrons coming from the source and rather less for those coming from the cells. In this latter category, it is a lot more straightforward as we can only choose the one or two peaks on the MCS spectra after emptying the guide tube. In the first category however, the region that has to be chosen is subtly different for different types of MCS spectra depending on the SV and FV settings as the averaging of the volumes differs.

The regions that have been chosen in our analysis have already been stated in the previous section when describing the different MCS spectra, but they are also summarised in Table 6.10.

Type of files	Area that corresponds to Neutrons from the Source	Area that corresponds to Neutrons from the cells
A	I	N/A
B	II	N/A
C	II	V
D	II	V
E	I	IV
F	II	IV
G	II and VI	IV and VIII
H	II	V

Table 6.10: The regions of all the different MCS spectra chosen for the polarisation analysis for neutrons coming from the source and the cells.

6.3 Calculating the Neutron Polarisation

6.3.1 General Formula

The neutron polarisation is given by:

$$P = \frac{N_\uparrow - N_\downarrow}{N_\uparrow + N_\downarrow} \tag{6.1}$$

where $N_\uparrow$ and $N_\downarrow$ are the counts of neutrons with spin up and spin down respectively. In the Autumn 2010 run, the spin flipper was not operating so we were able to record neutrons of both spin states $N_{\uparrow\downarrow}$ (with the open detectors UCN1 and UCN2), and spin down neutrons $N_\downarrow$ (with the iron detectors UCN3 and UCN4). Thus, the above formula has to be modified in order to contain the measured parameters:

$$P = \frac{N_\uparrow - N_\downarrow}{N_\uparrow + N_\downarrow} = \frac{N_\uparrow + (N_\downarrow - N_\downarrow) - N_\downarrow}{N_{\uparrow\downarrow}} = \frac{N_{\uparrow\downarrow} - 2\ N_\downarrow}{N_{\uparrow\downarrow}} = 1 - 2\ \frac{N_\downarrow}{N_{\uparrow\downarrow}} = 1 - 2\ R \tag{6.2}$$

where: $R = \frac{N_\downarrow}{N_{\uparrow\downarrow}}$ and $N_{\uparrow\downarrow} = N_\uparrow + N_\downarrow$.

The neutrons coming out of the polariser are considered having their spin upwards so the fewer the counts recorded by the iron detectors the higher the polarisation. The uncertainty in the polarisation is:

$$\sigma_P = 2\ \sigma(\frac{N_\downarrow}{N_{\uparrow\downarrow}}) = 2 \cdot R\sqrt{(\frac{\sqrt{N_\downarrow}}{N_\downarrow})^2 + (\frac{\sqrt{N_{\uparrow\downarrow}}}{N_{\uparrow\downarrow}})^2} = 2\ R\sqrt{\frac{1}{N_\downarrow} + \frac{1}{N_{\uparrow\downarrow}}} \tag{6.3}$$

Time Binning

Given that we want to calculate the polarisation of neutrons in different time periods of the MCS spectra, we have analysed the data by binning them in time using Excel spreadheets (see Figure 6.14). For each of these time bins, we have estimated the polarisation and its error.

In general, the width of the time bins does not correspond to the duration of emptying the source or the cells. It was made shorter as we were interested in checking whether the polarisation level of directly detected neutrons was different from those that had been bouncing around for some period of time before being detected. Unless the statistics were low, the analysis for the different time bins corresponding to the same valve settings showed that the polarisation was the same within 3-4% uncertainty. The values presented on the following plots are the mean value of all the bins within a given area.

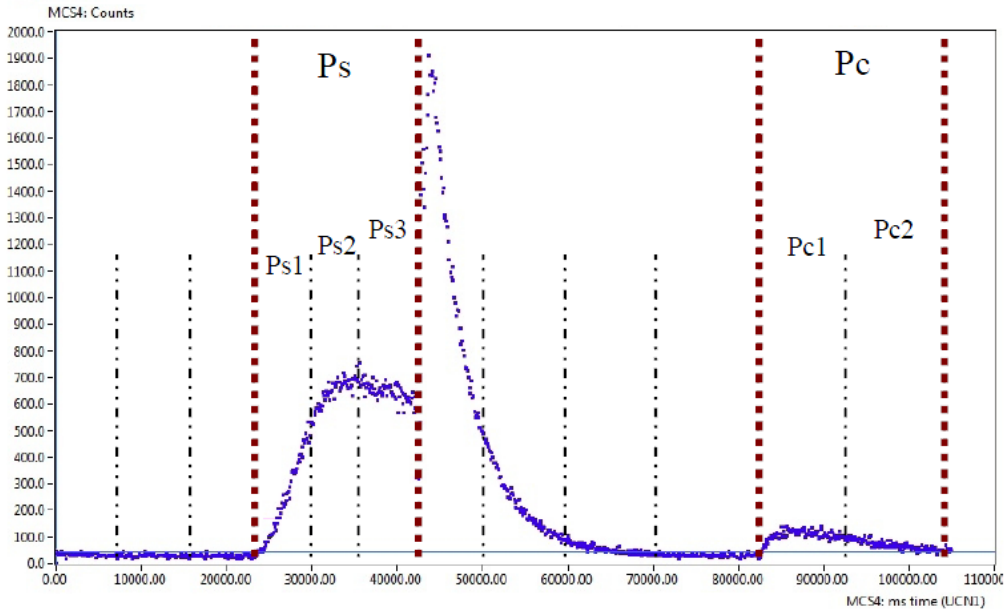

Figure 6.14: Neutron counts and polarisation analysis in time bins. The polarisation values for the neutrons coming from the source (Ps) and the cells (Pc) are the mean values of those from the bins.

6.3.2 Neutron Counts Calibration

For an unpolarised neutron beam we expect the iron detector to record half the counts of the open detector. In practice, however, this might vary slightly (for example due to different detection areas) and we need to perform a calibration.

This was done by depolarising the incoming cold neutron beam by placing a demag-

netised ($\approx$ 0.3 mm thick) iron sheet on their passage before the entrance of the Source Volume. The principle of this method, first proposed and explained by Halpern and Holstein [76] in 1941, is that the spin vector of neutrons interacts with the randomly orientated magnetic field of the ($\approx 10 - 100$ μm) magnetic domains within a ferromagnetic material like iron. This results in a fully unpolarised neutron beam at the exit of the sheet of the ferromagnetic material.

The correction factor (CF) which sets the Iron detector counts to half of those from the Open detector, is given by:

$$(CF) \cdot N_{\downarrow} = \frac{1}{2} \cdot N_{\uparrow\downarrow} \Rightarrow (CF) = \frac{N_{\uparrow\downarrow}}{2 \cdot N_{\downarrow}} \tag{6.4}$$

With an uncertainty of:

$$\sigma_{CF} = \frac{1}{2}(CF) \cdot \sigma(\frac{N_{\uparrow\downarrow}}{N_{\downarrow}}) = \frac{1}{2}(CF)\sqrt{(\frac{\sqrt{N_{\downarrow}}}{N_{\downarrow}})^2 + (\frac{\sqrt{N_{\uparrow\downarrow}}}{N_{\uparrow\downarrow}})^2} \Rightarrow$$

$$\sigma_{CF} = \frac{1}{2}(CF)\sqrt{\frac{1}{N_{\downarrow}} + \frac{1}{N_{\uparrow\downarrow}}} \tag{6.5}$$

The formula to use for calculating the polarisation becomes:

$$P_{CF} = 1 - 2 \cdot \frac{(CF) \cdot N_{\downarrow}}{N_{\uparrow\downarrow}} = 1 - 2 \cdot R_{CF} \tag{6.6}$$

with $R_{CF} = \frac{(CF) \cdot N_{\downarrow}}{N_{\uparrow\downarrow}}$ and uncertainty of:

$$\sigma_P = 2 \cdot \sigma(\frac{(CF) \cdot N_{\downarrow}}{N_{\uparrow\downarrow}}) = 2 \cdot R_{CF}\sqrt{(\frac{\sqrt{N_{\downarrow}}}{N_{\downarrow}})^2 + (\frac{\sqrt{N_{\uparrow\downarrow}}}{N_{\uparrow\downarrow}})^2 + (\frac{\sigma_{CF}}{CF})^2} \Rightarrow$$

$$\sigma_P = 2 \cdot R_{CF}\sqrt{\frac{1}{N_{\downarrow}} + \frac{1}{N_{\uparrow\downarrow}} + (\frac{\sigma_{CF}}{CF})^2} \tag{6.7}$$

The last two formulae were used to calculate the "Raw Polarisation Data" presented later on.

6.4 Amplifiers Stability

6.4.1 Raw Data

Any change in the amplifiers gain can change the position and the shape of the triton peak. For fixed discriminator settings, the count rate in the MCS spectra can change, as

more or fewer background counts are recorded. This, in turn, can change the apparent polarisation.

To investigate any possible effect of this kind, the position of the triton peak maximum and the width of the peak were plotted for all useful runs for all the three detectors that were mostly used (UCN1-open, UCN3-Fe3 and UCN4-Fe4 detectors). Figures 6.15 to 6.19 show that both the open (UCN1) and the UCN3 detectors were unstable for most of the run files with respect both the maximum position and the width of the triton peak. As far as the open detector is concerned, the triton peak overlapped significantly with the background so the (second) half width at half maximum is plotted instead of the FWHM (Figure 6.17).

On the other hand, the UCN4 detector, the older of the two iron detectors, seems to be the most stable and reliable detector (Figures 6.16 and 6.19). Unfortunately, no MCS data were taken from this detector before run number 1487, and there was no calibration test between this file and run number 1552 when the discriminator levels settings were last changed for this detector. The first calibration test was conducted just after run 1408 (no numbering was attached to it) and the second at run number 1573.

We note that the full width at half maximum of the triton peak is about the same for the two iron detectors (about 0.3 V) but about 4 times wider (1.2 V) for the open detector.

6.4.2 New Discriminator Levels

The shift and the width variation of the triton peak on the open (UCN1) and the two iron (UCN3, UCN4) detectors can result in the peak drifting partially outside the discriminator levels. To determine the effect of amplifiers instability on the apparent polarisation the following procedure was followed: the polarisation (and its error) was calculated from the pulse height spectra (MCA) using the same formulae (equations 6.6 and 6.7) and the same calibration factors as for the MCSs for two different cases:

1. Integrating the spectra between the set discriminator levels and
2. Integrating between two new values for the lower and upper "discriminator levels", the position of which is shifted with respect to the set levels in the same ratio as the peak maximum has been shifted with respect to some reference value.

Firstly, for UCN1 and UCN3 detectors the data were split into two groups, based on the fixed discriminator settings (see Table 6.11). Each of these groups contain a calibration

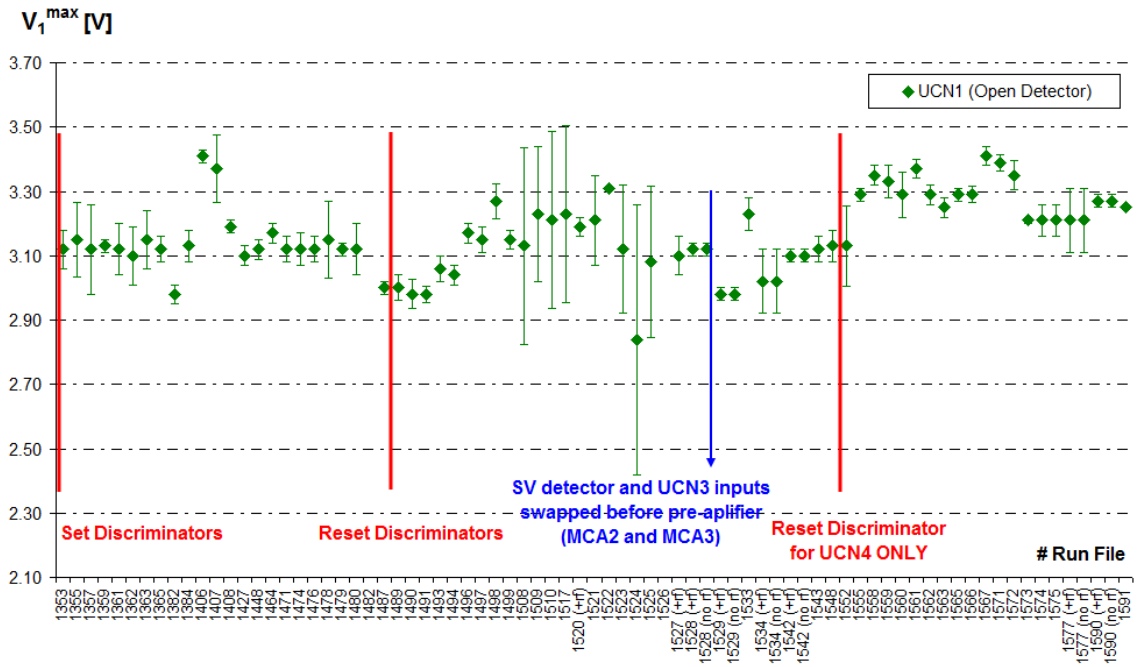

Figure 6.15: The position of the triton peak maximum on the pulse height spectra of the open (UCN1) detector for all the useful run data files. There is a fluctuation of about ± 10 % around the average value of 3.12 V.

test. The first group consists of the files between 1353-1487 and the second of all the rest of the files (1489-1591).

Files Range	UCN1 (LL/UL)	UCN3 (LL/UL)	UCN4 (LL/UL)
1353–1487	2.22/5.18	5.9/8.05	5.40/7.26
1489–1548	2.32/4.71	5.06/7.42	4.50/6.85
1552–1591	2.32/4.71	5.06/7.42	5.00/6.80

Table 6.11: Discriminator settings for the three detectors for all the useful run files. UCN1 and UCN3 settings have been set twice while there was one more modification for UCN4 levels.

As already mentioned, unlike UCN1 and UCN3, for the UCN4 detector there were three different discriminator levels. Therefore, the second group of files (1489-1591) do not correspond to constant discriminator settings for UCN4 detector. Given that these intermediate values (4.50/6.85) are closer to the final settings (5.00/6.80) rather than the initial ones (5.40/7.26), we chose the second calibration test (#1573) as a reference file, as we had for the other two detectors.

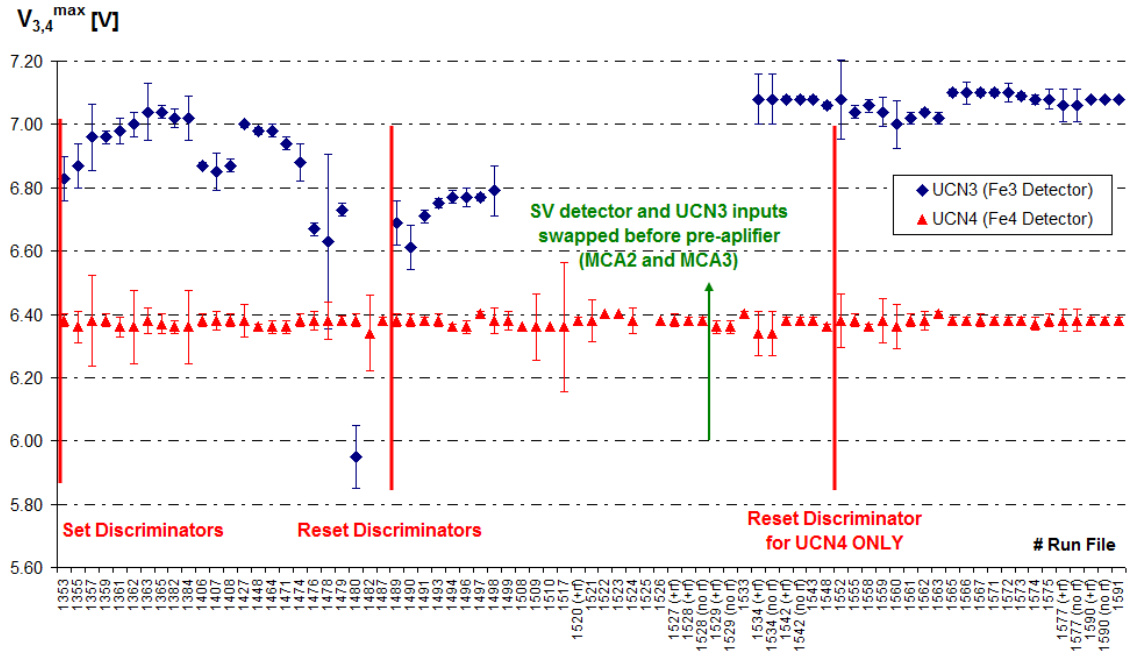

Figure 6.16: The position of the triton peak maximum on the pulse height spectra for the two Fe detectors (UCN3 and UCN4) for all the useful run data files.

The "reference" runs to define the position of the triton peak maximum were #1408 (taken just before the calibration) for the first group and the calibration file #1573 for the second group. So for each for these two "reference" runs, the peak maximum was at some V_{ref}^{max} while for the rest of the runs it was at V^{max}. The new integration limits had to satisfy the following equation:

$$\frac{LL^{new}}{LL^{set}} = \frac{V^{max}}{V_{ref}^{max}} = \frac{UL^{new}}{UL^{set}}$$

where LL^{set}/UL^{set} are the actual lower and upper discriminator levels respectively that were set in reality and LL^{new}/UL^{new} are the new lower and upper integration limits.

The selection of the "reference" runs was a rather arbitrary choice as we cannot associate any run with a "right" result but can only draw conclusions for the relative changes of the polarisation.

The results for the polarisation from both iron detectors are presented in section 6.6.3.

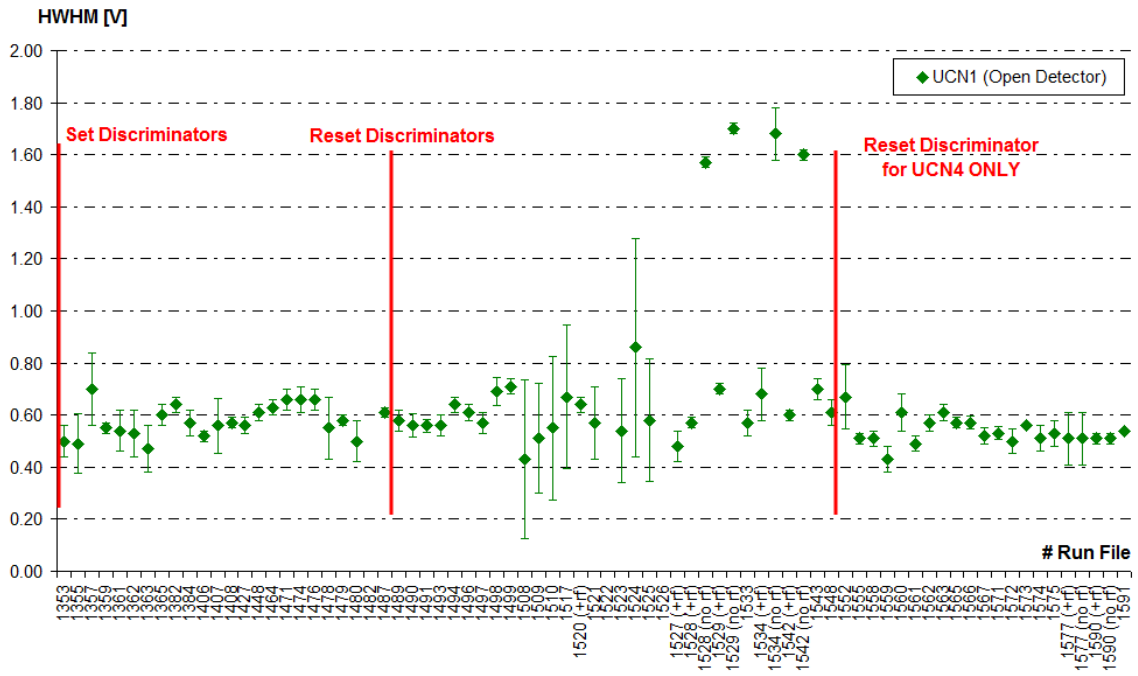

Figure 6.17: The half width at half maximum of the triton peak as seen by the open (UCN1) detector. There is a fluctuation of 30% around the average value of about 0.55 V for the half width or about 1.1 V for the full width at half maximum.

6.5 Background Subtraction

6.5.1 Introduction and General Formula

On the pulse height spectra (MCA) the alpha peak has never been seen clearly as it is buried under the background/electronic noise whereas, the triton peak sits on top of some background (see Figures 6.12 and 6.13). The calculation of the polarisation can only be reliable if we extract the peak from the background.

In order to calculate the net counts in the peak, we need to know the Background Count Rate (BCR) to be subtracted from the raw MCS counts (N) over the time interval (δt) of our interest. For the iron detectors we get:

$$IC_{Net} = (N_{\downarrow} - BCR \times \delta t) \times CF \tag{6.8}$$

where IC_{Net} to be the net Iron detector Counts. For the open detector, the formula is slightly different as there is no calibration factor attached to it:

$$OP_{Net} = N_{\uparrow\downarrow} - BCR \times \delta t \tag{6.9}$$

where OC_{Net} to be the net Open detector Counts. The formula for calculating the polar-

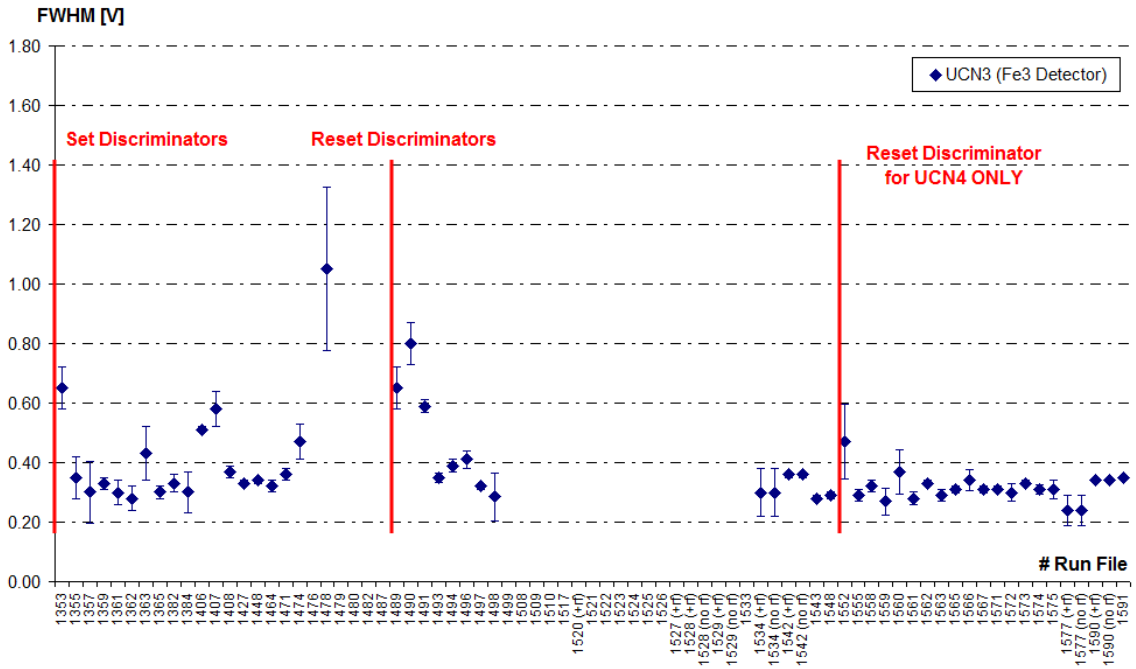

Figure 6.18: The full width at half maximum of the triton peak as seen by the Fe3 (UCN3) detector. There are many missing data as this detector was not connected for many runs.

isation after the background subtraction then becomes:

$$P = 1 - 2 \cdot \frac{(N_{\downarrow} - BCR_{\downarrow} \times \delta t) \times CF}{(N_{\uparrow\downarrow} - BCR_{\uparrow\downarrow} \times \delta t)} \tag{6.10}$$

By setting $BC = BCR \times \delta t$ to be the Background Counts for the given time period δt, the uncertainty of the BCR is given by:

$$\sigma_P = 2 \cdot \sigma(\frac{(N_{\downarrow} - BC_{\downarrow}) \cdot CF}{N_{\uparrow\downarrow} - BC_{\uparrow\downarrow}}) =$$

$$= 2 \cdot \frac{(N_{\downarrow} - BC_{\downarrow}) \cdot CF}{(N_{\uparrow\downarrow} - BC_{\uparrow\downarrow})} \cdot \sqrt{(\frac{\sigma(N_{\downarrow} - BC_{\downarrow})}{N_{\downarrow} - BC_{\downarrow}})^2 + (\frac{\sigma(N_{\uparrow\downarrow} - BC_{\uparrow\downarrow})}{N_{\uparrow\downarrow} - BC_{\uparrow\downarrow}})^2 + (\frac{\sigma_{CF}}{CF})^2} \tag{6.11}$$

With:

$$(\frac{\sigma(N_{\downarrow} - BC_{\downarrow})}{N_{\downarrow} - BC_{\downarrow}})^2 = \frac{(\sigma_{N_{\downarrow}})^2 + (\sigma_{BC_{\downarrow}})^2}{(N_{\downarrow} - BC_{\downarrow})^2} = \frac{\sqrt{N_{\downarrow}}^2 + \sqrt{BC_{\downarrow}}^2}{(N_{\downarrow} - BC_{\downarrow})^2} = \frac{N_{\downarrow} + BC_{\downarrow}}{(N_{\downarrow} - BC_{\downarrow})^2} \tag{6.12}$$

Similarly:

$$(\frac{\sigma(N_{\uparrow\downarrow} - BC_{\uparrow\downarrow})}{N_{\uparrow\downarrow} - BC_{\uparrow\downarrow}})^2 = \frac{N_{\uparrow\downarrow} + BC_{\uparrow\downarrow}}{(N_{\uparrow\downarrow} - BC_{\uparrow\downarrow})^2} \tag{6.13}$$

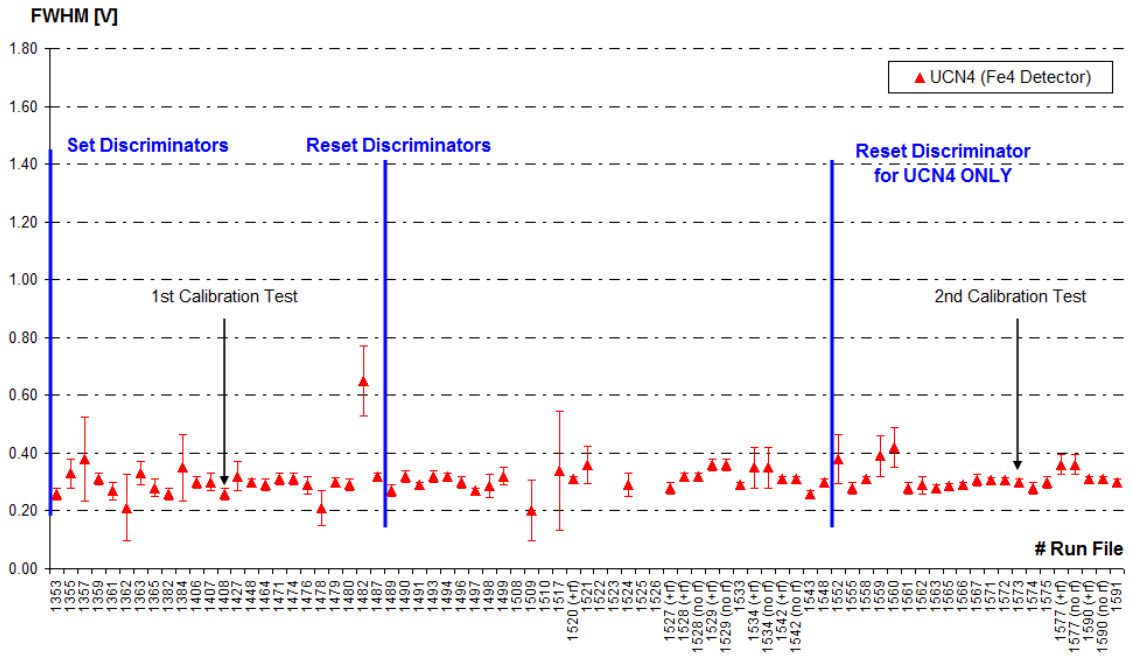

Figure 6.19: The full width at half maximum of the triton peak as seen by the Fe4 (UCN4) detector. Similarly to the peak maximum position (Figure 6.16), it seems to be quite stable with maximum fluctuation of about 30%. Unfortunately, no calibration test was conducted between run files 1489 and 1552 where the discriminator settings for this detector were changed.

Thus, the error in calculating the polarisation taking into account both the calibration for the iron detectors and the background subtraction is given by:

$$\sigma_P = 2 \cdot \frac{(N_\downarrow - BC_\downarrow) \cdot CF}{(N_{\uparrow\downarrow} - BC_{\uparrow\downarrow})} \cdot \sqrt{\frac{N_\downarrow + BC_\downarrow}{(N_\downarrow - BC_\downarrow)^2} + \frac{N_{\uparrow\downarrow} + BC_{\uparrow\downarrow}}{(N_{\uparrow\downarrow} - BC_{\uparrow\downarrow})^2} + (\frac{\sigma_{CF}}{CF})^2} \tag{6.14}$$

6.5.2 Methods of Subtracting the Background Counts

There are two ways of removing the background counts from the "real" neutron data: either by using the MCS data alone, or by estimating a background count rate from the MCA spectra and applying the correction to the MCS data.

MCS Spectra

In many MCS files, illustrated in Figure 6.20, there is a non-zero "plateau" on which the neutron counts set. In principle, this value should be zero, at least at the beginning and at the end of the run. This value, defined as Background Counts (BC), has to be translated

into Background Count Rate (BCR) by dividing it with the time width of each bin on the MCS spectra. This is given in the DataView header and is equal to the total duration of the run divided by the number of time bins (usually 1000).

$$BCR = \frac{Offset}{bin\ size} = \frac{BC}{Total\ Duration} \cdot 1000$$

The BCR is then multiplied by the time of the area of our interest and finally subtracted from the raw MCS counts (see equation 6.10).

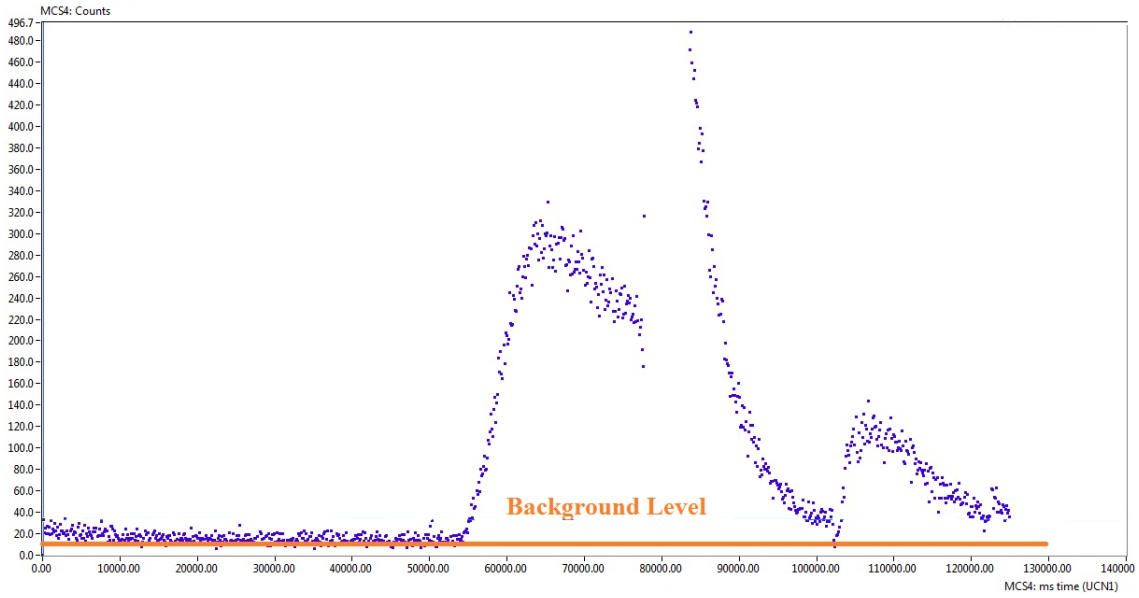

Figure 6.20: MCS spectrum of run file #1471. There is a clear offset of about 9 counts. The duration of this run was 125 sec, therefore the time bins were 125/1000 = 0.125 sec wide. Having these two numbers known, we find the Background Count Rate (BCR) = 9 / 0.125 = 72 Counts/s.

MCA Spectra

The first step to determine a BCR using MCA data is to define a region of background that is close to the triton peak but not underneath it. A background function is fitted to this region and is then extrapolated under the peak. This function is then integrated between the discriminator settings to give a total background count for the time that the MCA gate is open. The BCR can then, in principle, be calculated and applied to the MCS spectra.

The lower voltage limit of the background was set as the first or second non-zero counts point. This point never corresponded to 0 Volts but to about 0.2 Volts. The upper limit

was set by visual inspection as the point where the triton peak reaches zero if extrapolated leftwards. This is shown schematically in Figure 6.21.

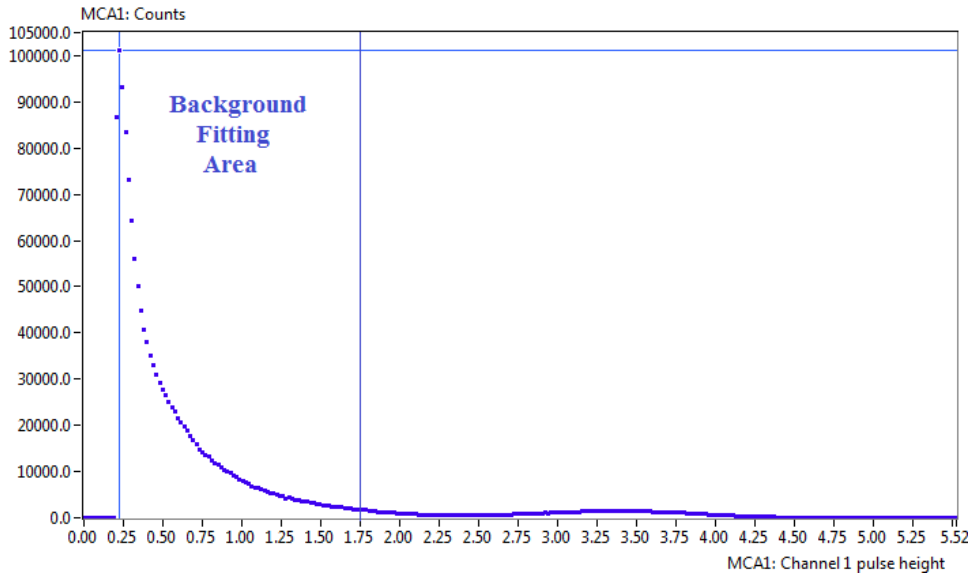

Figure 6.21: The pulse height spectrum of the open detector (UCN1) for run number 1406 before any background subtraction. The triton peak is clearly visible while the alpha peak is buried under the background. The background fitting area is between 0.23 V and 1.75 V.

The first attempts to fit a single exponential were not very accurate. The background is dominated by the high count area which decays more rapidly than the lower count area of the background. To get a simple and quick approximation to the background, the following proceedure was carried out. First a single exponential was fitted to the total background, crossing it at 2 (or 3) points (Figure 6.22(a)). These points define three (or four) different regions where the background can be fitted to a single exponential (Figure 6.22(b)). This is done for the region closest to the triton peak and this function then extrapolated under the peak, as shown in Figure 6.23. The outcome of this process is shown in Figures 6.23 for the open detector and 6.25 for the iron UCN3 detector.

In order to calculate the Background Counts, we need to integrate the fit line under the true discriminator settings and find the sum of the counts. This is done with the following way:

Consider X_i and X_f the LL and UL values of the discriminator. The MCA sorts the pulses in 512 bins between 0-10 Volts. That means that the width of each bin is 10V / 512 = 0.01953 V ($\sim$ 0.02 V). The total number of points between X_i and X_f is therefore:

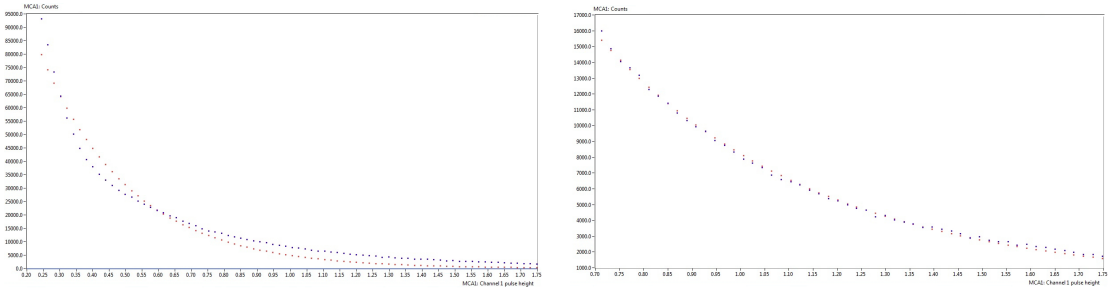

(a) Fitting the total area of the background

(b) Fitting the tail of the background

Figure 6.22: A single exponential fit (red dots) to the total background (blue dots) 6.22(a) crosses it at a minimum of at two points and leads to very few background counts under the triton peak. The equation of a single exponential fitted to the part of the background after the last crossing point 6.22(b) was finally used.

$$N = \frac{X_f - X_{in}}{\delta x}$$

where $\delta x = 0.02V = const.$

By integrating the fit curve we calculate the following quantity:

$$I = \sum_{i=1}^{N} \frac{(x_{i+1} - x_i) \cdot (y_{i+1} + y_i)}{2}$$

which represents the area of the trapezium under the fitting curve between the discriminator limits. Therefore, given that X_{i+1}-X_i = δx:

$$\sum_{i=1}^{N}(y_i + y_{1+1}) = \frac{2 \cdot I}{\delta x} = \frac{2 \cdot I}{0.02} = 100 \cdot I$$

But:

$$\sum_{i=1}^{N}(y_i + y_{i+1}) = \sum_{i=1}^{N}(2y_i) - (Y_{in} + Y_f)$$

as all y_i's are counted twice apart from the first y_{in} and the last y_f values. So finally, the total counts under the fitting curve are given by:

$$\sum_{i=1}^{N} y_i = 50 \cdot I + \frac{1}{2} \cdot (Y_{in} + Y_f)$$

6.5.3 Timer Box Issue

Having found the total background counts from the MCA spectra we can translate this to the BCR by dividing by the time during which the MCA gate was open. This time,

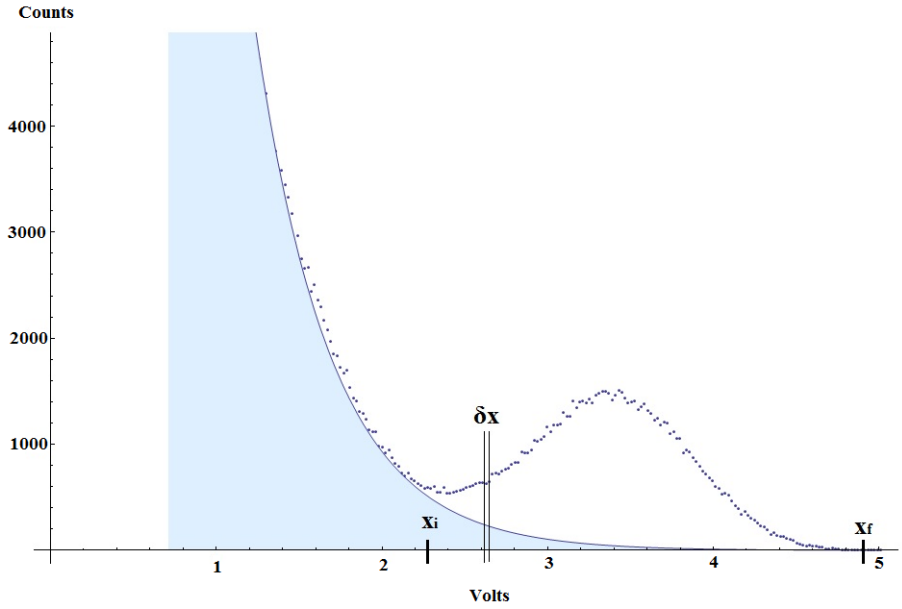

Figure 6.23: MCA spectrum (dotted line) of the open detector UCN1 for Run file #1406 with a fit line (solid line). The width of each of the 512 bins is δx = 1000/512 $\approx$ 0.02 Volts. The area under the fit line (coloured with blue) was integrated between the discriminator settings (X_i and X_f) to calculate the background counts. The result, when subtracting these counts from the triton peak, is expected to be equal to the MCS counts within the MCA gate time window.

τ_{MCA}, is recorded in the DataView header along with the other timing information about when the valves are open and closed, when the scalers are on etc.

We expect the counts in the MCS spectra during this period and the counts in the MCA spectra between the discriminator settings to be the same within some confidence level. In other words, we expect:

$$R = \frac{\text{MCS Counts during } \tau_{MCA}}{\text{MCA Counts between the dicriminator levels}} \approx 1 \tag{6.15}$$

Figures 6.26 and 6.27 present the results of calculating this ratio for all the useful run files. We note that for 5 runs, R >1, for 1 run R=1 and for all the rest R <1.

If the discriminator levels were actually set differently from the recorded values, R should be again different from 1, but constant for all the runs for which the levels were the same. Hence, the parameter that we has to be incorrect is τ_{MCA}. If the actual time is more or less than that recorded, then $R \neq 1$.

The fact that the R values are grouped and not randomly spread led us to search for common features among the files that fall into the same groups. It was found that

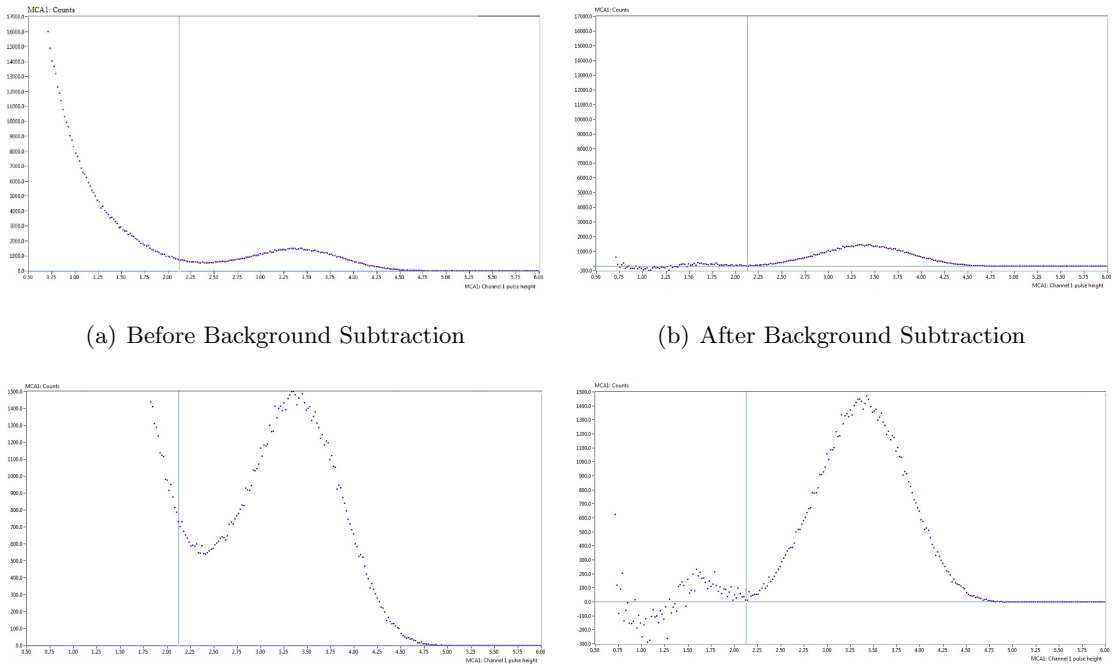

(a) Before Background Subtraction

(b) After Background Subtraction

(c) Before Background Subtraction

(d) After Background Subtraction

Figure 6.24: Pulse height spectrum of the open detector for run number 1406 before (left) and after (right) background subtraction. The lower two Figures present a magnified section of the two top ones.

for a sequence of successive files for which the timing settings were unchanged, R is the same. When the timer box settings were altered from one file to the next, for example by changing the valve settings, R changed as well.

The next step was to claculate the true τ_{MCA}. We knew that at least one of the opening and/or closing times (as recorded in the DataView header) for the MCA gate window were wrong and hence tried to find new timings which gave R close to unity. The possible times were, in principle, only those when the timer box was set to perform some kind of change. By trial and error, in comparing the MCS counts over different time periods with the MCA counts between the discriminator levels, new timing settings for the MCA gate were found which gave R $\approx$ 1 for most of the runs, apart from 4 files (see Figure 6.28). For the 4 'rogue' runs, even integrating the total MCS spectra still did not give enough counts to equal those from the MCA between the discriminator levels. These files (in addition to those where the MCA gate was meant to be closed) were not used to correct the raw polarisation by subtracting the background.

The new timing settings found for the MCA gate are given in Table F3 in Appendix F. For most of the cases, the MCA gate either opens or closes when the source valve is

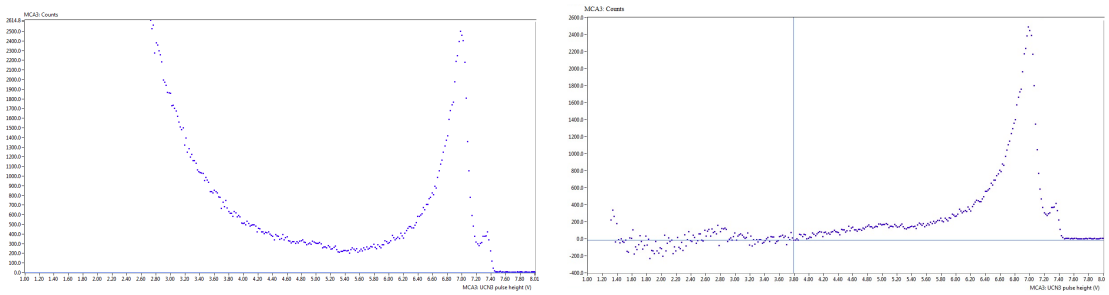

(a) Before Background Subtraction (b) After Background Subtraction

Figure 6.25: The MCA spectrum of the iron UCN3 detector for file #1448 before and after background subtraction.

operated -it seems to follow the status of the source valve.

It is worth mentioning the case of file #1499 separately. Even though it has the same time settings as the previous 5 files (#1493 to #1498), the MCA gate operated at a different time from these, and opened at the beginning of the run. The only change made at file #1499 is that the source valve was unplugged so it was open from the beginning of the run.

After correction, the less than 10% deviation from unity shown by Figure 6.28 (ignoring the 'rogue'files) can be explained by the fact that the valves did not operate when expected but at earlier times. An example of this for file #1590 is given in Figure 6.29. According to the time sequence recorded in the DataView header, emptying of the guide should occur at the 42 and at 175.6 seconds, shown at the two ends of the highlighted area. It is clear, however, that the count rate starts to rise before either of these times. This affects the MCS/MCA ratio and for the cases of deviations of R from unity very close to 10% this time drift corresponds to areas with high count rates. No additional correction for this drift was made in our background count rate calculations.

6.6 Polarisation Analysis Results

6.6.1 Calibration Test

The results of the two calibration tests are shown in Figures 6.30(a) and 6.30(b). The correction factor (CF) was calculated as explained in section 6.3.2 and found to be 1.18 for the UCN3 iron detector in the first test. The discriminator settings were changed once for the UCN1 and UCN3 detectors and twice for the UCN4 detector before the second test. This gave CF to be about 1.25 for both iron detectors. The accurate values are given

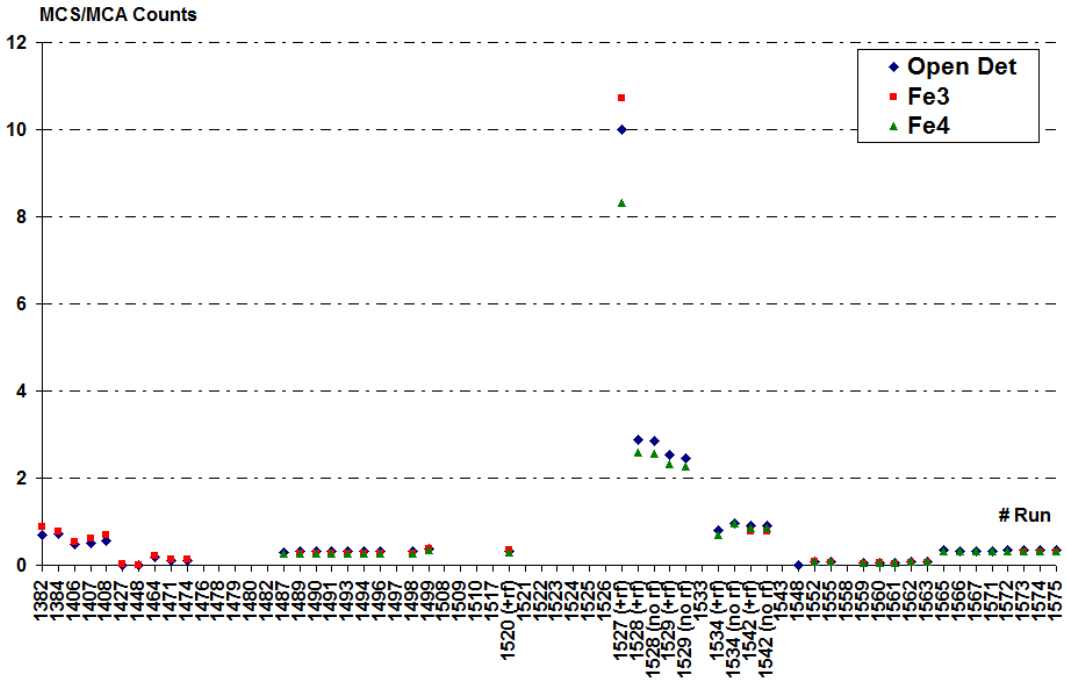

Figure 6.26: This plot shows the ratio MCS Counts –within the MCA time window– over the MCA Counts between the discriminator settings. The expected value is 1.

in Table 6.12.

Calibration Test	CF UCN3	σ_{CF} UCN3	CF UCN4	σ_{CF} UCN4
1st	1.184	0.011	–	–
2nd	1.252	0.005	1.242	0.005

Table 6.12: The correction factors as calculated from the two calibration tests.

6.6.2 Raw Polarisation (MCS Spectra)

Polarisation of neutrons coming from the source and the cells

Figure 6.31 shows that the run files can be divided into three regions with respect to the discriminators settings: Files #1365 to #1487 from the UCN3 MCS spectra (UCN3 was the only iron detector connected up to run file #1482) show polarisations between 20% and 40% before this detector started exhibiting erratic behaviour (run file #1476). After the first resettings of all the discriminators, UCN3 seemed to give random numbers a behaviour that disappeared when it was connected to a different preamplifier before run file #1529. Over this period, the UCN4 polarisation was initially very close to zero and then increased up to ≈10% before its discriminator was reset again. Over the final region,

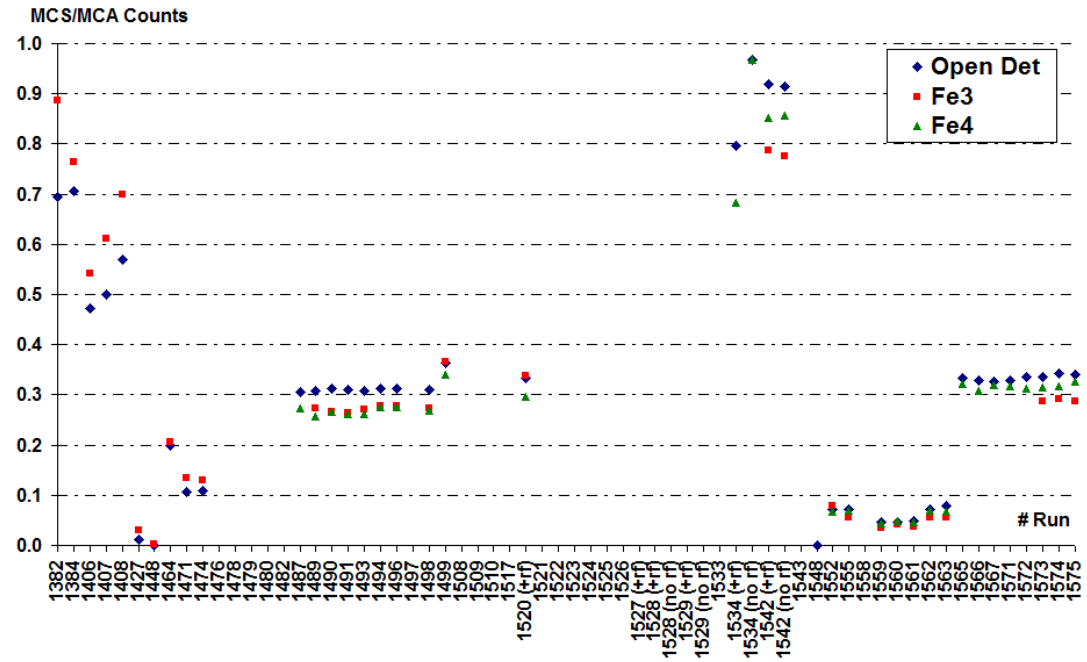

Figure 6.27: Rescaling the vertical axis to zoom in to Figure 6.26.

after the UCN4 discriminator reset, both detectors showed polarisation between zero and about 20%. We should mention here that for the first 8 useful files (#1353 to #1365), the MCS data for the open detector corresponded to the UCN2 detector. For run file #1382 and onwards the UCN1 open detector was used instead.

We get the same pattern for the polarisation out of the cells as shown in Figures 6.32, 6.33 with the only difference being that the error bars are bigger since the neutron counts are much less. In these plots, the polarisation of neutrons from the neutral and high voltage cell are given seperately. When both cells were open simultaneously, the data points have been incorporated into the 'neutral cell' data. The number of data in these plots are less compared to that for polarisation from the source simply because for many runs neutrons were not stored in the cells.

For some files, and for neutrons coming from both the source and the cells, we derive negative polarisation values. From equation 6.2, this corresponds to the case when the iron detector counts are more than the half of those from the open one. This could mean that there had been some polarisation reversed, but this is highly unlikely. We note that these negative values are only observed when the counts are very small and hence the statistical fluctuations are large. Such fluctuations can also give rise to completely unphysical values where $|P|>100\%$. Negative values are only observed when the counts for both open and iron detectors are very small ($\approx$ tens or hundreds).

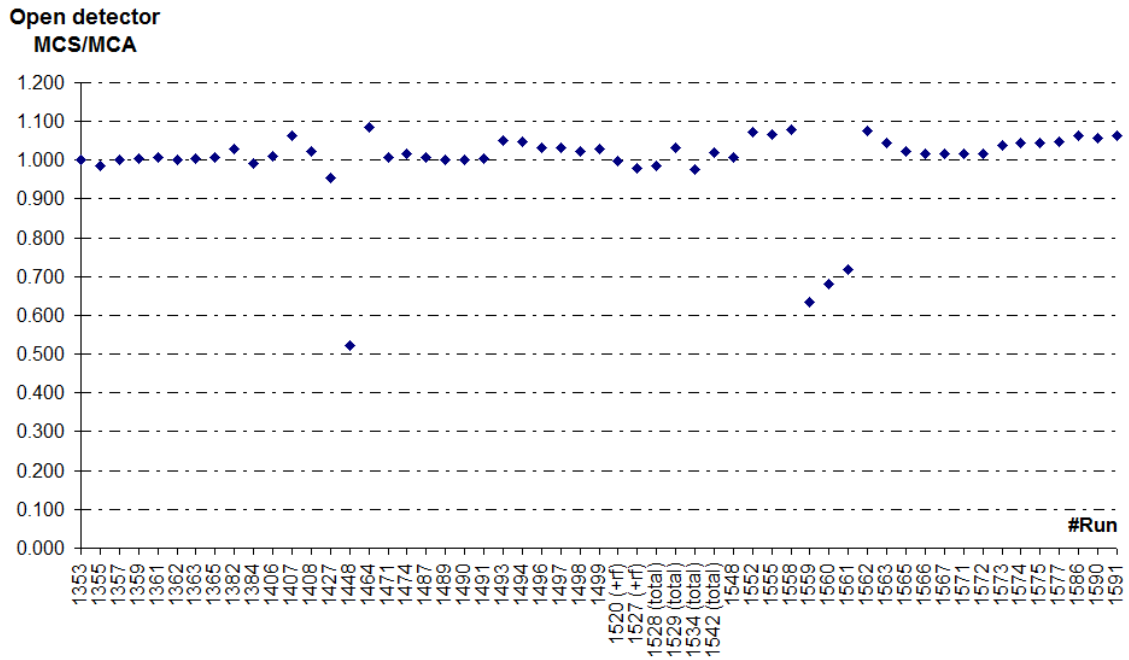

Figure 6.28: MCS/MCA counts ratio for the open detector (UCN1) with our estimated MCA gate time window

Polarisation Data for runs when an rf pulse was applied

Figure 6.34 shows the polarisation data for neutrons coming from the cells for cases where an rf pulse was applied during the storage in the Ramsey cells. Within error bars, neither detectors showed any significant change due to the rf pulse. As a comparison, Figure 6.35 shows the polarisation of the neutrons coming from the source for the same runs in which the rf was applied to the cells. Any hints of polarisation changes for the neutrons coming out of the cells are also seen in the data for the source tube and are not due to rf pulses applied.

6.6.3 Correction for New Discriminator Settings (MCA spectra)

The pattern of polarisation we obtain by using the pulse height (MCA) spectra shown in Figures 6.36 6.37 for the recorded and corrected discriminator settings, is similar to that from the MCS spectra. The only difference is that after run file #1487 (when the discriminators were reset for first time) the values drift to lower levels and become more negative. Again, this is due to the iron detector counts being more than the half of the open detector counts.

It should be stressed here that when using the pulse height spectra, we cannot separate the polarisation from the source or the cells. Although the MCA gate time window was

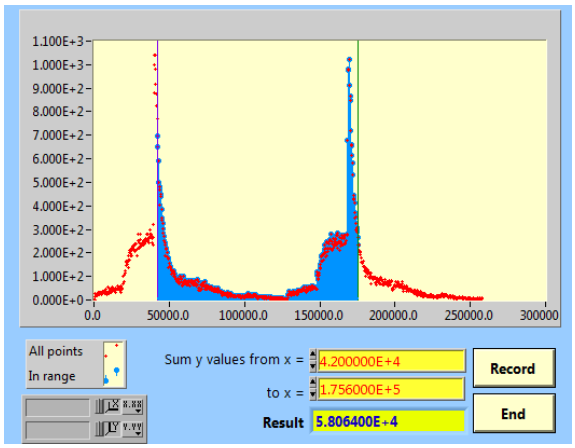

Figure 6.29: Valves timing discrepancy for File #1590. The DataView header indicates that emptying the guides should occur at the two ends of the (blue) highlighted region. However, it is clear that the count rate (red) increases earlier each time.

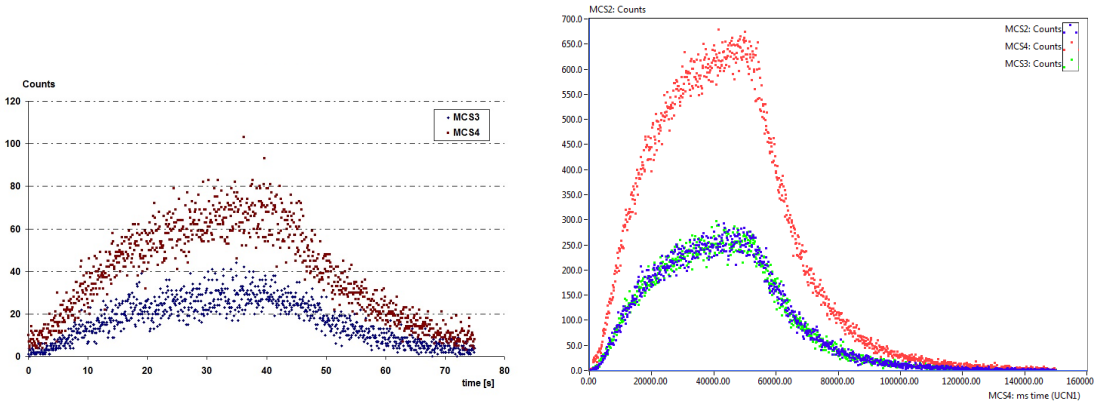

(a) 1st Calibration Test (b) 2nd Calibration Test

Figure 6.30: The results of the two calibration tests.

scheduled to be open for specific time sections of the MCS spectra, as we have seen above, it was actually open for different periods that did not correspond to neutrons coming exclusively from the source or the cells.

The correction to the discriminator settings does not seem to alter the polarisation values significantly. Therefore, the changes observed in the polarisation levels can not be attributed to amplifier instability.

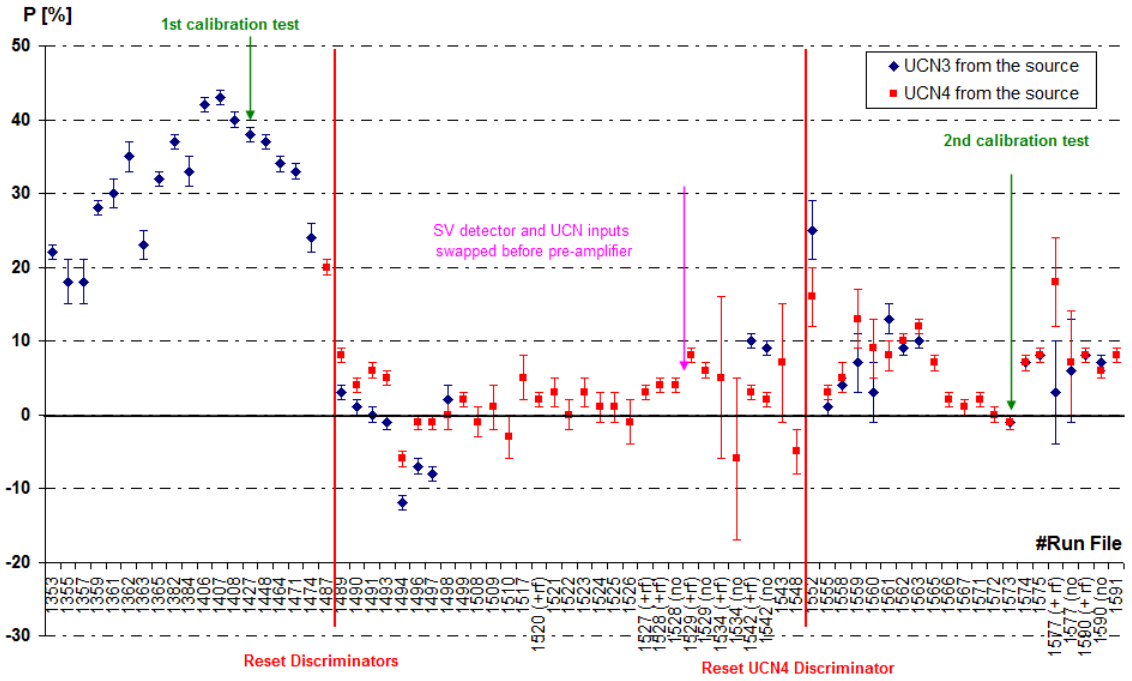

Figure 6.31: Raw polarisation of neutrons coming from the source using the MCS data from both iron detectors. UCN2 was used as an open detector for the first 8 files, and UCN1 for the rest.

6.6.4 Polarisation after background subtraction

MCS Spectra

The background subtraction analysis described in section 6.5.2 was carried out and Figures 6.38 and 6.39 show the corrected polarisation for neutrons from the source and the cells, respectively, taken with the UCN3 detector. Figures 6.40 and 6.41 show the corrected polarisation for the same groups of neutrons but taken with the UCN4 detector. In these plots, only the run files with a non zero offset are included and the new polarisation (after the background subtraction) is compared with the raw polarisation values from the MCS spectra.

The values do not change significantly for either detectors and the general trend is that after the background subtraction the polarisation has decreased or become more negative. This is not what we were hoping for when doing this analysis. If the offset on the MCS spectra corresponds to non-neutron counts, then after subtracting it we should be left with real data that would lead to physically meaningful polarisation values. But can be seen in Table F4 in Appendix F, the background counts for the iron detectors were always less than those for the open detector. In other words, by extracting a bigger number from the open detector counts and a smaller or zero value from the iron detector counts, the ratio

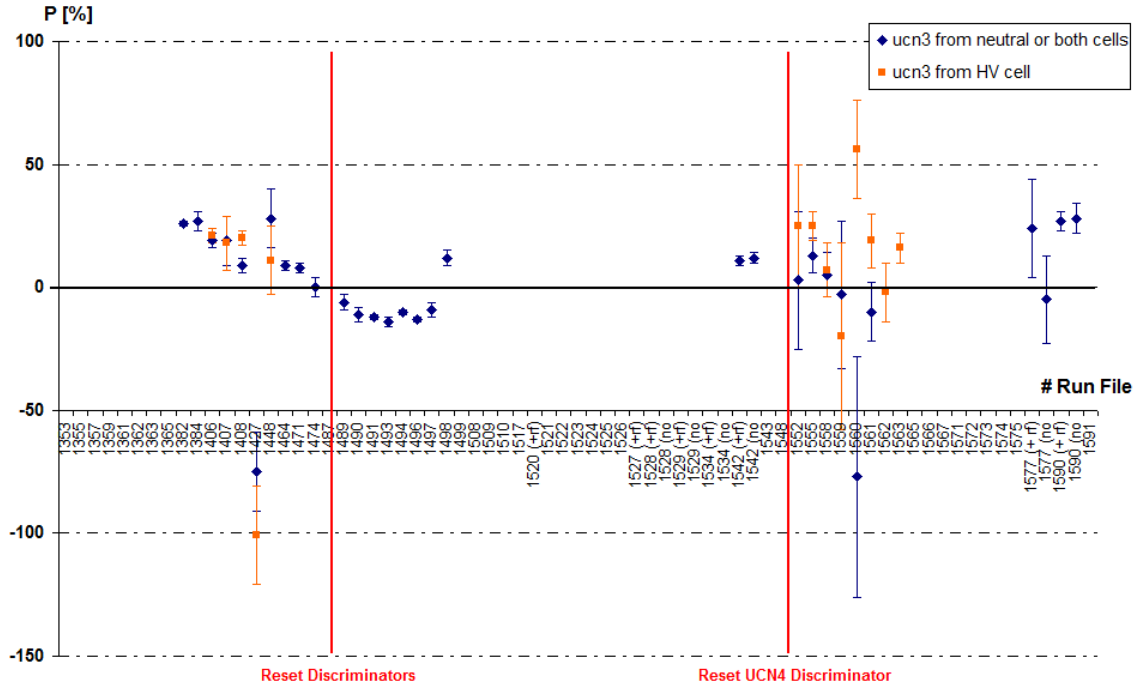

Figure 6.32: Raw polarisation of neutrons coming from the cells as calculated using the MCS spectra of the UCN3/UCN1 detectors.

$2 \cdot N_{\downarrow}/N_{\uparrow\downarrow}$ (which was already >1) increased further and the polarisation became more negative.

Pulse Height (MCA) Spectra

The final part of our analysis involves the background subtraction using the pulse height spectra (see section 6.5.2). The results are shown in Figures 6.42 to 6.44 for UCN3 detector and 6.45 to 6.47 for UCN4 detector. Only the run files for which the MCA gate was set to be open are included into these plots. The background counts for the open detector are, as expected, much more than those for the iron detectors. For most of the cases, they differ by one order of magnitude. Therefore, as was the case when subtracting the background using the MCS spectra, this analysis resulted also in more negative polarisation.

For the neutrons coming from the source, the polarisation does not change significantly after background subtraction and, within error bars, we can say that remains essentially the same. Things are radically different for the polarisation of neutrons coming from the cells, and for cases of low statistics (few tens up to a couple of hundred counts). The background counts, as calculated from the MCA spectra for the open detector, are more than its MCS counts for the time window over which the MCA gate was open. This leads to a negative figure for $N_{\uparrow\downarrow}$ and a polarisation above +100%. These high polarisation

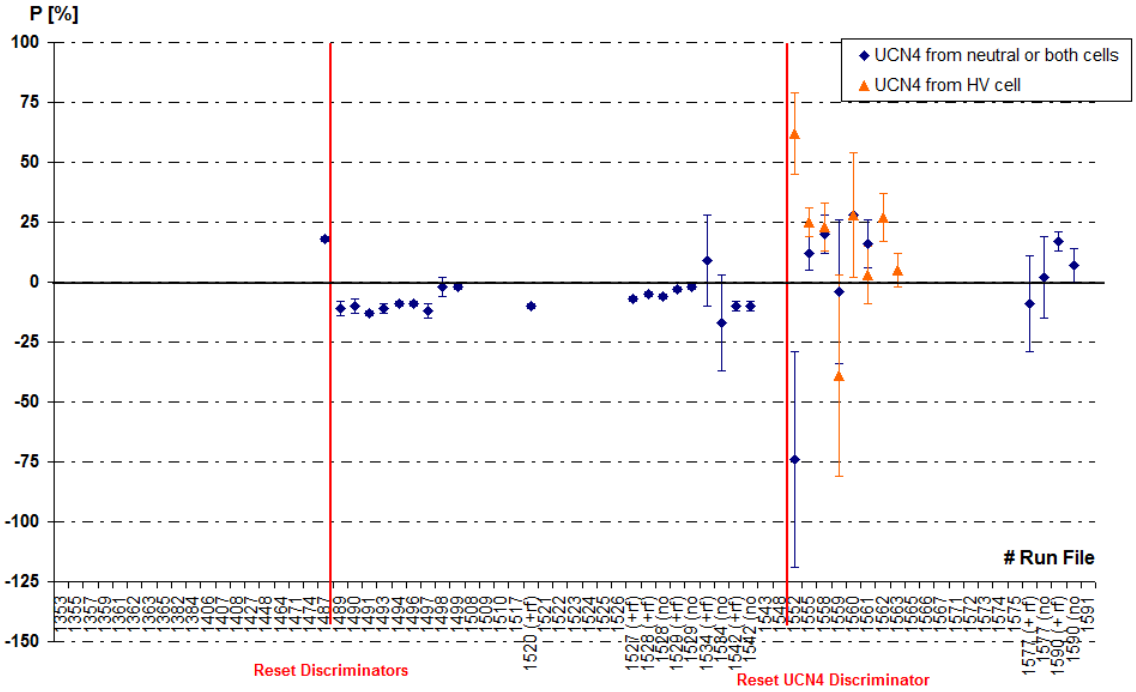

Figure 6.33: Raw polarisation of neutrons coming from the cells as calculated using the MCS data of UCN4/UCN1 detectors.

values are shown on Figures 6.43 and 6.46 and obviously have no physical meaning.

The actual values for the background count rates for all three detectors as calculated from their MCA spectra are given in Table F4 in Apendix F. We note that they are not only different for the different detectors but they do not agree with the values found from the MCS spectra either. The major difference is that the offset, that has been attributed to the existence of some kind of non-neutron counts, is zero for almost all but 8 of the MCS files. This is clearly not the case for the MCA files for which at least the open detector's triton peak is strongly affected by the background.

6.7 Polarisation Values, the Holding Field Configuration and Other Changes

The plot in Figure 6.48 shows the raw polarisation data, including those when the UCN3 detector was malfunctioning, and to this has been added the information giving the holding field configuration.

For the first two data points in this plot (#1353 to #1355), the holding field coils (HFC) C(1-8) were set at half the currents used in the past when observing ≈77% polarisation. The initial currents were then doubled and tripled (from #1357 to #1471) whilst the

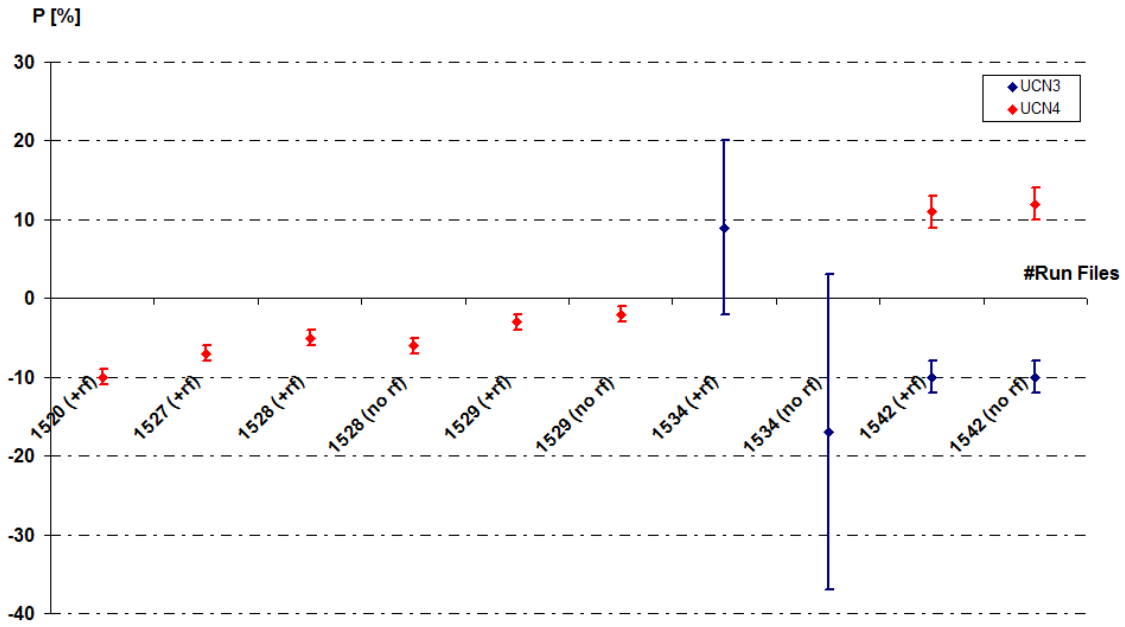

Figure 6.34: Polarisation values of neutrons coming from the cells for runs when an rf pulse was applied during the storage time. The first 2 values correspond to files for which the rf pulse was on continuously. The next four pairs of data correspond to runs when the rf pulse was initially on and then off. The negative values are due to low statistics and can be considered as zero polarisations. Within error bars, there is no change in neutron polarisation induced by the rf pulse.

polarisation rose from ≈20% to ≈40%. Another further change made during this set of runs was to increase the diameter of the beam aperture from 30 mm to 43 mm between #1357 and #1359. This size aperture then remained in place for subsequent runs until the last ten when various diameters from 15 mm to 48 mm were used.

For the data points from #1365 to #1471, both active compensation coils were set such as to produce an upstream field, opposing that produced by C7 and C8 with the HV end coil also being on from #1353.

At run #1474 it was decided to systematically set different field configurations and attempt to correlate these with corresponding changes in the polarisation. In the first such configuration (#1474) all the currents were set to zero and the neutrons were expected to be fully depolarised. This did not happen and instead the polarisation remained at ≈25%. We then tried various configurations, changing both the orientation and the magnitude of the holding fields. Full details are given in Appendix F.

Unfortunately, when these changes were being made (grey zone in Figure 6.48), the UCN3 detector began to malfunction in a way such as to indicate an increasing polarisa-

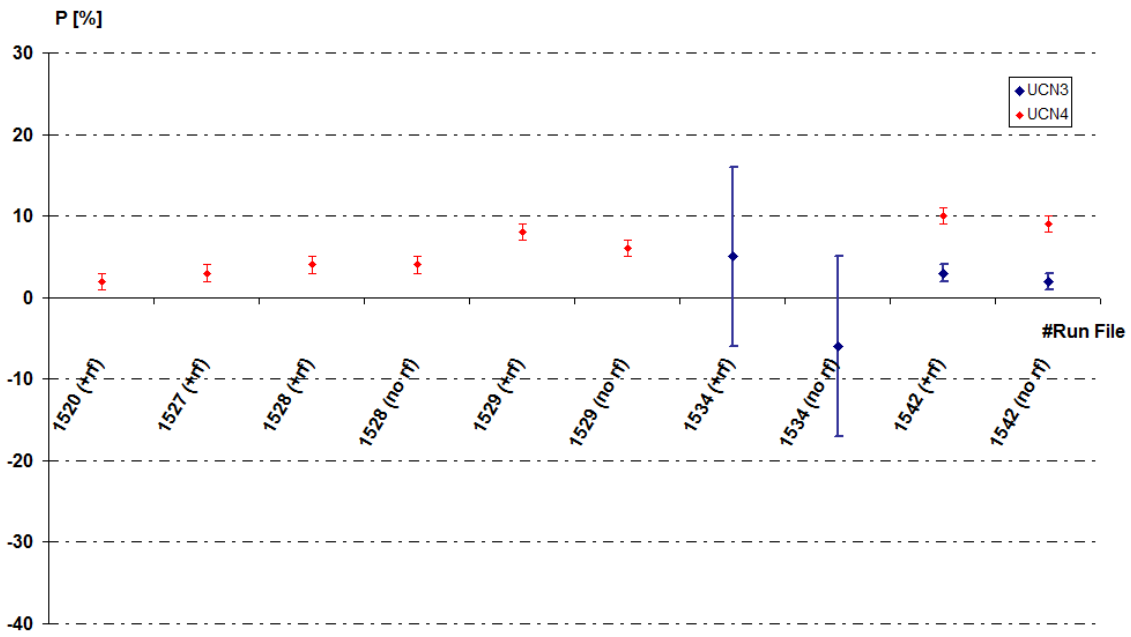

Figure 6.35: Polarisation values of neutrons coming out of the source tube for the runs that an rf pulse was subsequently applied while neutrons were stored in the Ramsey cells. This plot is given for comparison with the data coming out of the cells for the same runs (Figure 6.34). We note that, within error bars, the data of both plots follow the same pattern so any hints of polarisation changes are not due to the applied rf pulse.

tion. Since, at that point this was the only detector for which MCS data were available, it was some time before the correct cause of the apparent increase in polarization was identified. The amplifiers and connections to the detector were then changed as discussed above, and the discriminators were reset.

Only at the end of this process was it realised that some of the vacuum seals on the tube containing the guides were made of Indium and at 0.6 K these are well below their superconducting transition temperature of 3.4 K. The first effect of superconducting rings concentric with the holding field coils will simply be to oppose any changes to the flux locked into the ring when it cooled through its T_c. However, if applied field is sufficient to cause extra flux to be locked in, the initial field configuration will be effectively scrambled and it is likely that this happened here. After this point, even when the HFC currents were reset to values that had given higher polarisations earlier, these levels were never recovered thereafter.

Between the two discriminator resets, P=0%, and only after #1552 and for the last 21 runs (#1552 to #1591), P seemed to rise up to ≈10%. For the first 12 of these 21 runs

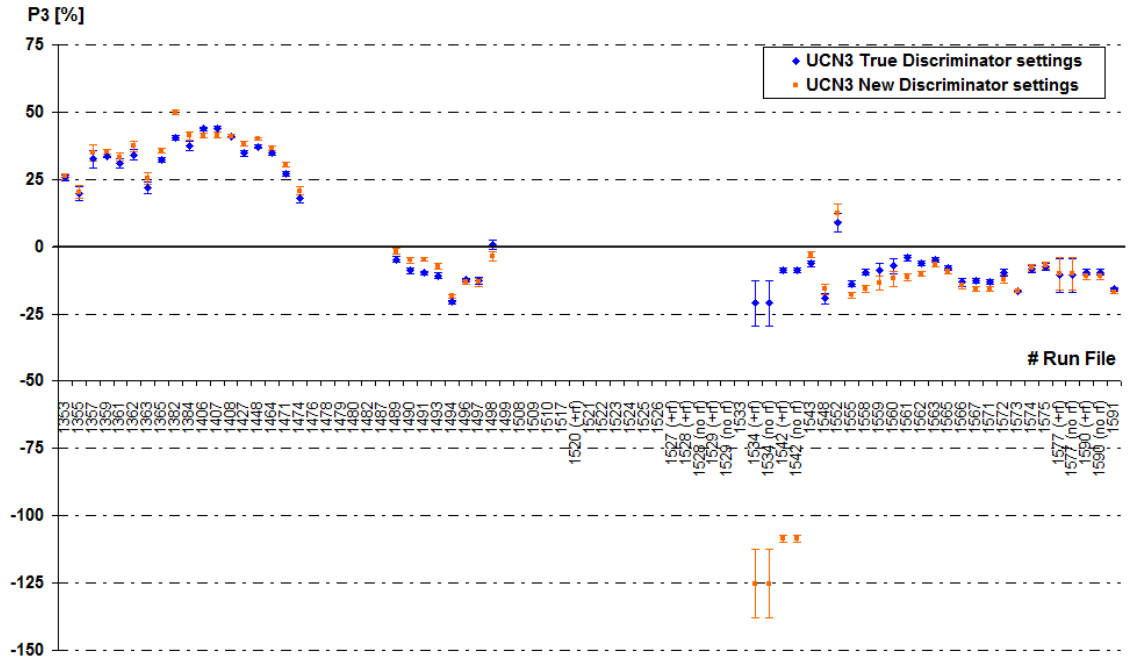

Figure 6.36: Polarisation of UCN3 detector from the pulse height spectra. Data were taken by integrating between the actual discriminator levels (blue diamonds) and between the new calculated integration limits (orange squares) calculated as described in section 6.4.2.

(#1552 to #1572), the three pairs of permanent magnets after the polariser were replaced with a 35 cm diameter / 1000 turns circular coil (labeled 'C0') in an attempt to provide a smoother transition between the field at the exit of the polariser and the holding field from the coils along the guides. No clear correlation of changes in polarisation with the use of this coil was been observed.

The SQUIDs compensation coil was turned off for most of the runs. In Figure 6.48, a red or a blue circle around a data point indicates that this coil was activated with a positive (red) or negative (blue) polarity. Apart from runs #1362 to #1365 at the beginning of the sequence, no significant change in the polarisation was observered when switching reversing the current in this coil.

It is very difficult to make clear correlations between changes to the holding field configuration and the observed polarisation, given the number of parameters being changed at the same time, the problems with the detectors and the complicating effects of the superconducting seals. We speculate that this latter problem led to the main drop in polarisation after #1489. It is not really clear why the polarization recovered a little towards the end of the run. The steady increase in the earlier data may be due to improving

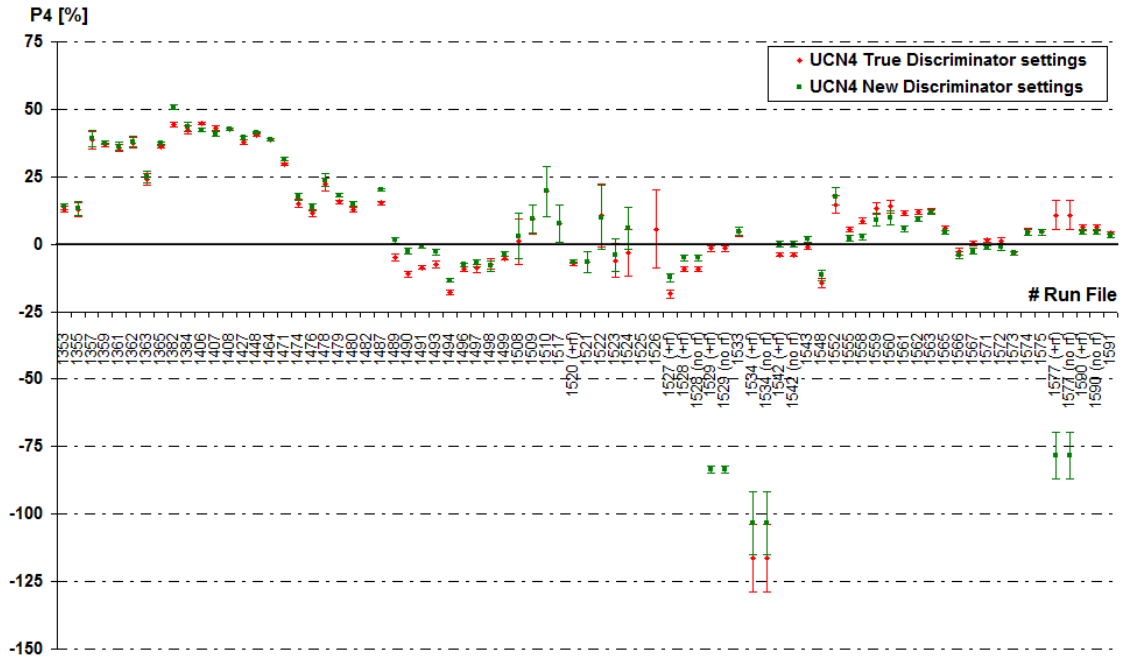

Figure 6.37: Polarisation of UCN4 detector from the pulse height spectra. As for the UCN3 detector, the data were taken by integrating between the actual discriminator levels (red diamonds) and between the new calculated integration limits (green squares).

the holding field, although it should be noted that the first increase of the polarisation actually occur at the same time as the the apperture was increased. The early variation with the SQUIDs is actually in the correct sense.

6.8 Discussion on the Polarisation Analysis

In this chapter, the analysis procedures followed and the results obtained for the polarisation in the Autumn 2010 run data have been presented. This shows that the polarisation reached a maximum of about 40% near the start of the run, then dropped to zero with non-zero values being obtained again after changing many parameters, finally reaching about 10%. The effect of making corrections for various factors, such as amplifier instability and background/electronic noise has been shown to be relatively small and did not produce significant change betweent the raw and corrected polarisation levels.

We then considered the polarisation data in conjuction with the changes made to the polarisation holding fields. We concluded that the uncontrolled nature of these field changes, resulting from the previously unsuspected presence of superconducting rings around the guides, may well explain at least some of the variations seen in the polari-

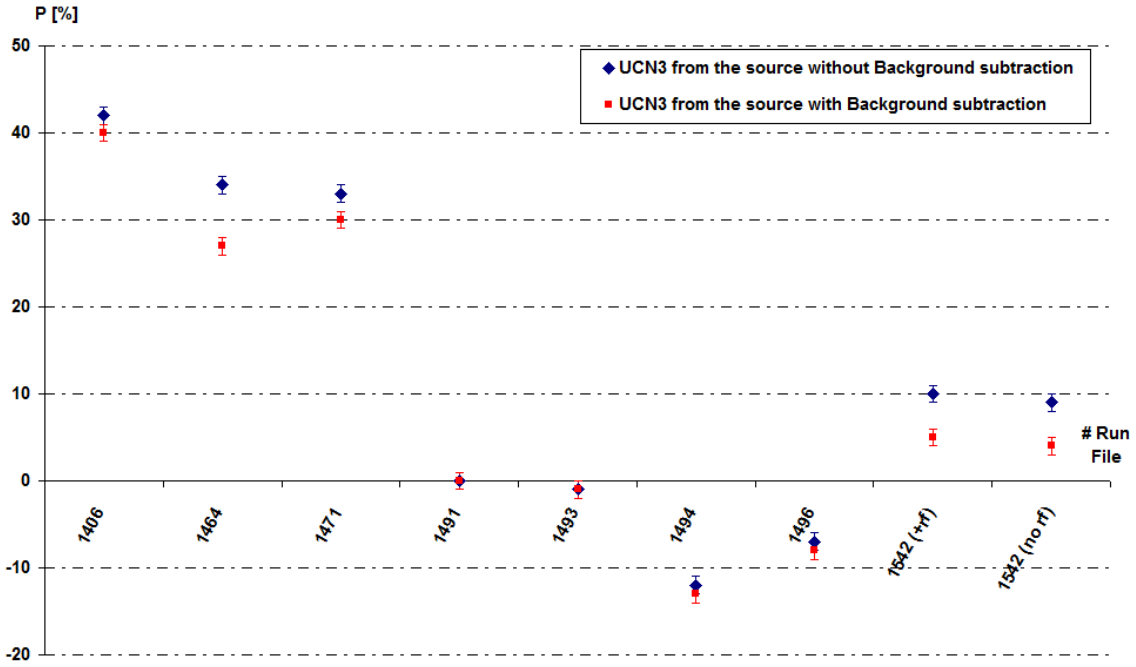

Figure 6.38: Comparison of polarisation data from the UCN3 detector for neutrons from the source with and without background subtraction using the MCS spectra.

sation.

A number of other issues arose during the analysis of the data which we discuss here.

1. Background Subtraction Methods

One can argue that in order to remove the background from the true neutron data, only the MCS spectra should be used. Defining any existing offset in these spectra is a quite straightforward, can be done consistently and will never produce negative neutron counts. Defining the background in the MCA spectra is much more difficult and somewhat subjective. The fact that we saw a hint of the alpha peak and a clear triton peak suggests that the method we followed is in the right direction. However, the small area of any broadened alpha peak, leads us to conclude that this method did not give ideal results and it is likely that the background was overestimated

2. Origin of the Background

There are three arguments why the background counts are due to electronic noise and not due to gamma-rays coming from the source volume;

Firstly, the background count rates are different for the different detectors for both MCS and MCA spectra. It is reasonable to assume that the detectors are exposed to the

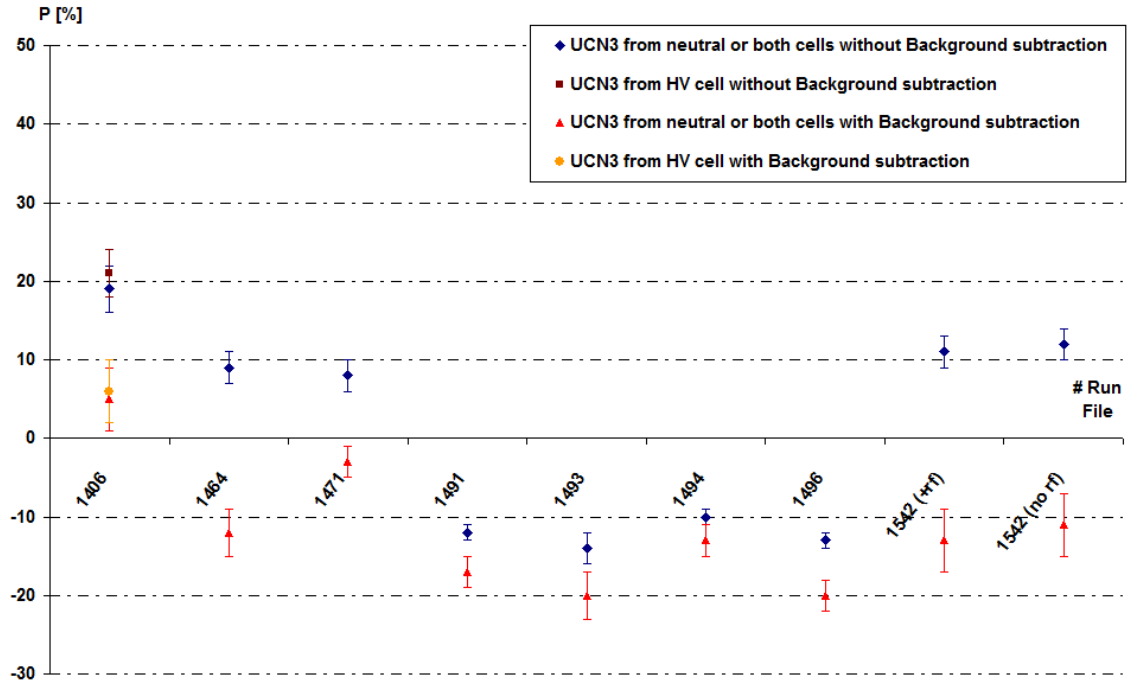

Figure 6.39: Comparison of polarisation data from the UCN3 detector for neutrons from the cells with and without background subtraction using the MCS spectra.

same radiation emitted from the source volume since they are at equal distances from it and have the same geometry.

Secondly, the fact that the shape of the background changed for all the detectors at the same time when the FV was connected, while nothing else was different according to the electronic logbook ((see section 6.1.2 and Figures 6.12 and 6.13)), is a strong indication that poor connections or ground loops are involved. It is also important to mention here that for the two files chosen just before and just after the FV connection, the aperture diameter was the same and V1 was open for exactly the same time.

Thirdly, if the origin of the background is gamma-rays, we do not really expect to see it in only about 10 run files (on the MCS spectra) but in others as well where the aperture diameter was the same and the V1 opening time was about the same or longer.

Finally, a background is always present on the MCA file of the open UCN1 detector but this is not the case for the MCS spectra and the other detectors. Whilst this is not a proof, it is at least suspicious, indicating the existence of electronic noise predominantly on the pulse height spectra of the UCN1 detector.

3. Electronic Interactions

Connecting the FV and SV seems to influence other parts of the apparatus. There

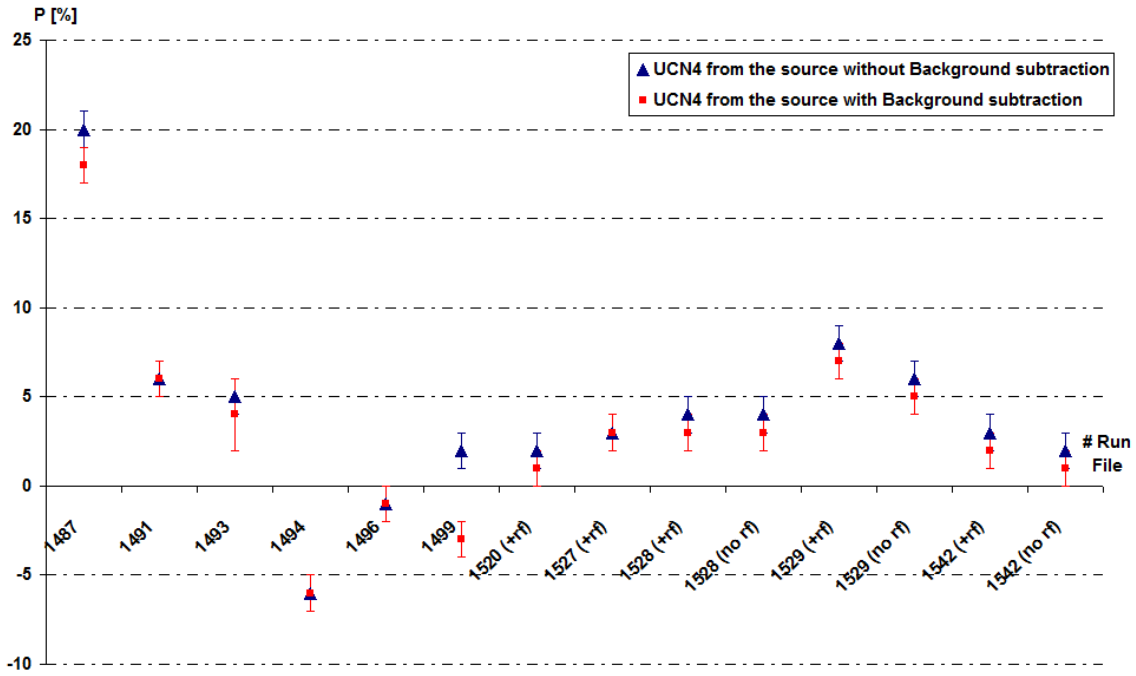

Figure 6.40: Polarisation analysis for neutrons from the source with and without background subtraction using the MCS spectra based on UCN4 detector data.

were strong indications that the electronic noise/background seen on the MCA spectra is related to the FV, while the SV operation affects the timer box.

4. Detector Performance It is suggested here that the performance of the detectors and amplifier chains should be examined, particularly that of the UCN1 open detector. As shown in Figure 6.11,the peak from this detector appeared at a very low voltage and was heavily influenced by the background. The shape of the peak was also different from those from the other detectors. Furthermore, during the analysis using time bins and when the statistics were low, there were cases when its MCS counts were fewer than those from the iron detector. It is not clear whether this detector recorded fewer counts than it should.

The only real suggestion for why this detector may be defective comes from one of the conclusions of Baker et al. paper [5] concerning the ORTEC silicon detectors. In this paper, the performance of these detectors was examined after radiation damage. In Figure 6.49 the spectra of two detectors are presented: a new one which had never been exposed to a neutron beam and a relatively old one which had received a radiation dose of 8×10^9 neutrons. These detectors used a ^{10}B (and not ^{6}LiF) converter, which has different reaction products:

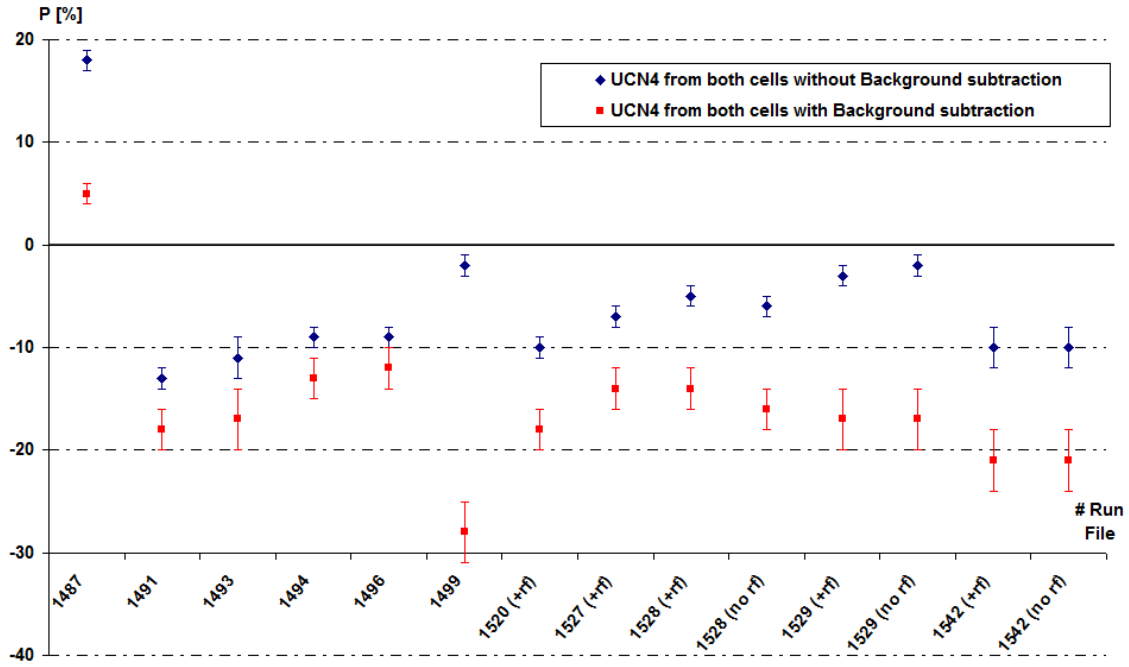

Figure 6.41: Polarisation analysis for neutrons from the cells with and without background subtraction using the MCS spectra based on UCN4 detector data.

$$n + {}^{10}B \rightarrow \alpha + {}^{7}Li$$

This is why the two peaks are different from those shown in section 2.7 for the same silicon detectors covered by ^{6}LiF layer. Nonetheless, we can see clearly that when the detector degrades, the two peaks are no longer resolved and a "background" suddenly appears which strongly overlaps with the only visible peak. According to the same authors, the threshold for replacing a detector should be 4×10^9 α particles detected, a number that is quite unlikely to have been reached even with a maximum UCN flux of the order of $10^5/\text{cm}^2/\text{s}$.

Nonetheless, this plot (6.49) is suspiciously similar to what we see not only on the open UCN1 detector but on the pulse height spectra from all the detectors. If this speculation is valid, then the loss in efficiency can not be estimated. And if, as seems to be the case, the UCN1 detector is in the worst state, then the actual polarisation would always be higher than we have observed.

5. Systematic Errors

It has been pointed out that the negative polarisation values have no physical meaning (that is why are interpreted as zero polarisation) and in many cases are due to low

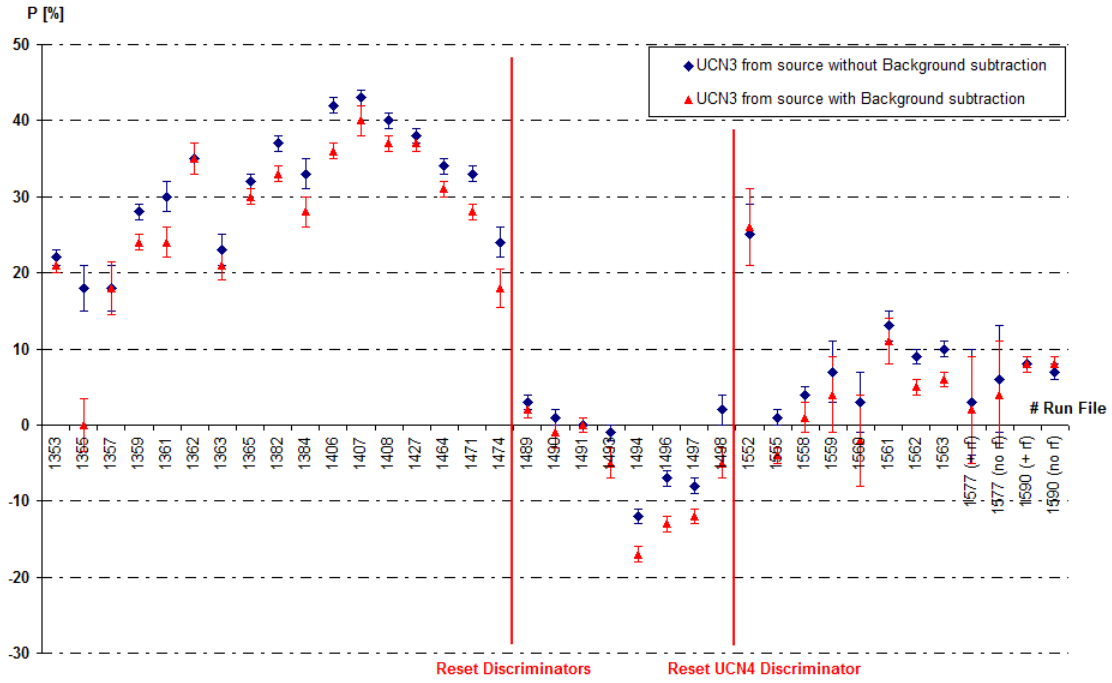

Figure 6.42: Comparison of polarisation data from the UCN3 detector for neutrons from the source with and without background subtraction from the MCA spectra.

statistics. Nonetheless, the fact that the statistical errors attached to them are often quite small implies the presence of systematic errors.

Having changed so many parameters at the same time while running the experiment, it is difficult to indentify with confidence the origin of these errors and estimate them. However, one possible source could be the determination of the discriminator settings, mainly those of the UCN1 (open) detector which is affected by the existence of the electronic noise the most.

All the plots showing the calculated polarisation of different parts of the apparatus and under different conditions (i.e. magnetic field configuration, valves operation, V1 aperture diameter etc), have something common: the polarisation level clearly drops by about 30% when the discriminator settings were first altered. After this point, the polarisation was never restored to its initial state.

The change of these settings did not only change the upper and lower values but also the width of the window between them. Using the values of Table 6.11, a rough calculation shows that this width dropped by $\approx 20\%$ for the UCN1 open detector and increased by $\approx 10\%$ for the UCN3 iron detector. For sake of simplicity and at first approximation, we assume that these changes correspond to counts changes. In that case the new polarisation, P_2, is expected to be equal to:

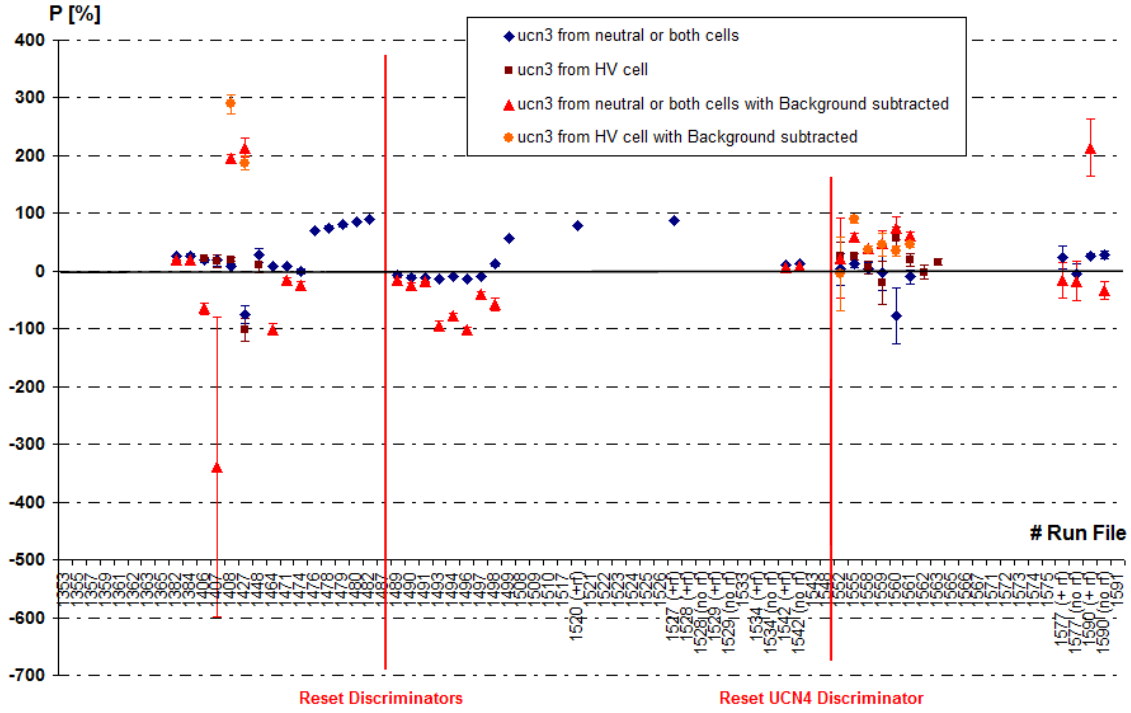

Figure 6.43: Polarisation data from the UCN3 detector for neutrons from the cells with and without background subtraction from the MCA spectra. Figure 6.44 is a magnified version of this Figure.

$$P_2 = 1 - 2\,\frac{(1+0.1)\;N_{\downarrow}}{(1-0.2)\;N_{\uparrow\downarrow}} = 1 - 2\cdot 1.375\;\frac{N_{\downarrow}}{N_{\uparrow\downarrow}} \tag{6.16}$$

Given that the polarisation before the discriminator settings change, P_1, was about 30%, the ratio of the iron over the open detector counts is found to be about:

$$P_1 = 1 - 2\;\frac{N_{\downarrow}}{N_{\uparrow\downarrow}} \approx 0.3 \Rightarrow \frac{N_{\downarrow}}{N_{\uparrow\downarrow}} \approx 0.35 \tag{6.17}$$

Substituting this in equation 6.16 the new polarisation is found to be:

$$P_2 \approx 3\% \tag{6.18}$$

This figure is getting worse if we recall the fact that by changing the lower limit of the discriminator window for the UCN1 open detector, we changed significantly its counts as it is in the area of the (quite high with respect to the observed peak) electronic noise. Even worse, when we subtract the background noise, we subtract a much bigger figure for the open detector than that for the iron detectors and therefore the count ratio becomes easily greater than 1 and the calculated polarisation a negative number.

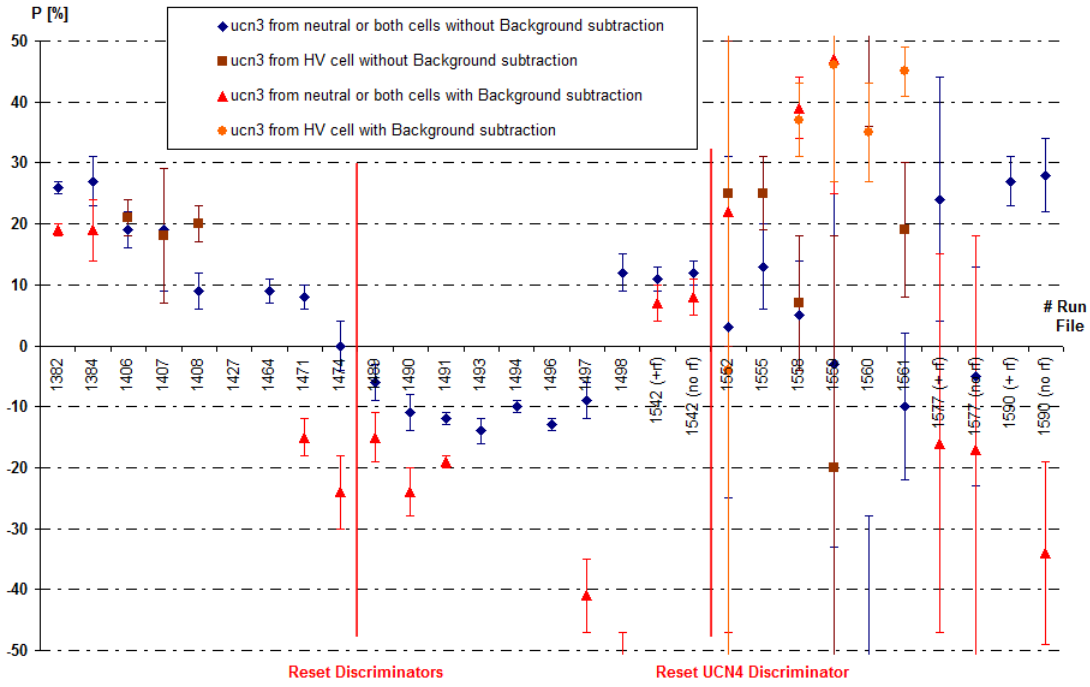

Figure 6.44: A magnified section of Figure 6.43 (Polarisation data from the UCN3 detector for neutrons from the cells with and without background subtraction from the MCA spectra).

If this assuption is correct, then the observed minor (between 0 and 10-15% fluctuations of the polarisation after the first discriminator settings change could be attributed to the fluctuations of the maximum and the width of the observed peaks of mainly the UCN1 (open) and UCN3 (Fe3) detectors (See Figures 6.15 and 6.18).

Additionally, it is quite possible that the correction factors found by two separate measurements at the beginning and at the end of the run, do not necessarily apply to the measurements between.

Finally, the open detector counts were used to calculate other parameters as for example the neutron density, assuming a specific efficiency (0.41). The files that were used were after the discriminator change and it is quite possible that using files before this change would give different result.

6.9 Suggestions for improvements

At a general level, it is evident that in future the type of detailed polarisation analysis described in this chapter has to be done automatically and in real time. If such a system had been in place during the last run, the lack of polarisation would have been evident

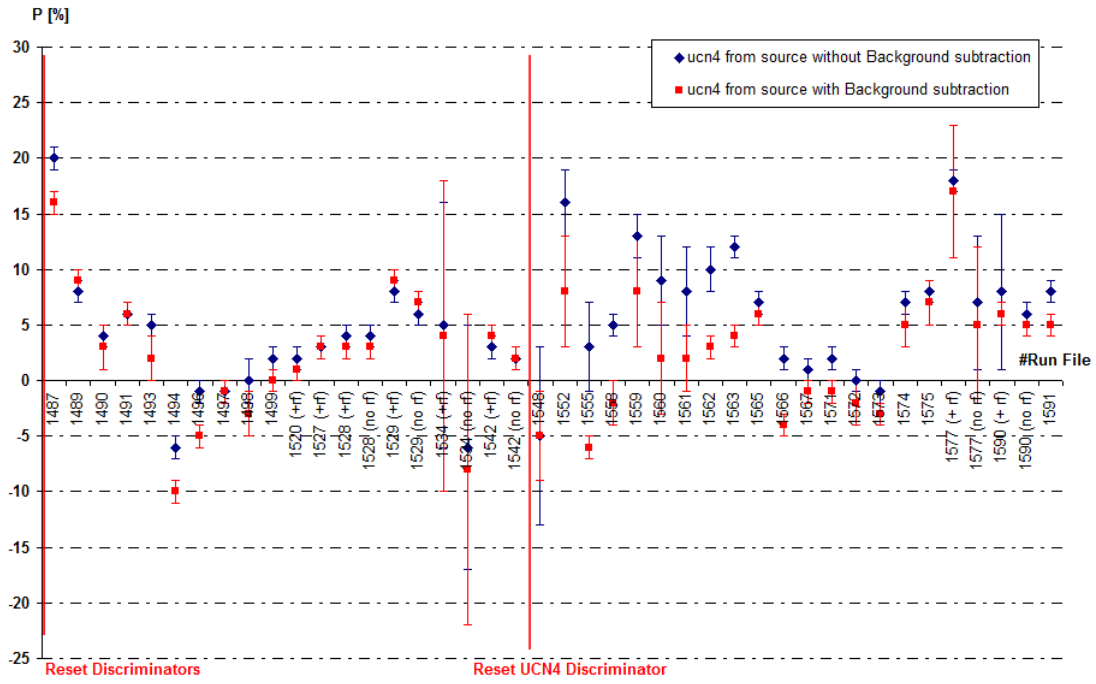

Figure 6.45: Polarisation from the UCN4 detector for neutrons from the source with and without background subtraction from the MCA spectra.

sooner and steps taken to remedy the situation, by, for example warming the supefluid volume to above T_c of Indium. It is also very clear that the management of the holding fields needs to improved.

Turning to more specific points, the suggestions below are towards two directions; firstly to monitor and store information that currently is not recorded, and secondly to take action on things that can easily slip someones attention.

Monitor and record with time (i.e. #run file) and for all the detectors information related to the neutron counts:

1. The position of the alpha and triton peaks maximum on the MCA spectra. This would show immediately any potential instability of the amplifiers.

2. The ratio of the MCA spectra integral between the discriminator settings over the MCS spectra counts within the MCA gate time window. Any deviation from unity would reveal problem with the timer box functionality.

3. The ratio of the MCS total counts for the two open detectors and the two iron detectors separately (i.e. Open1/Open2 and Iron1/Iron2). Do the same for the MCA integral between the discriminator settings. This is a good way to double

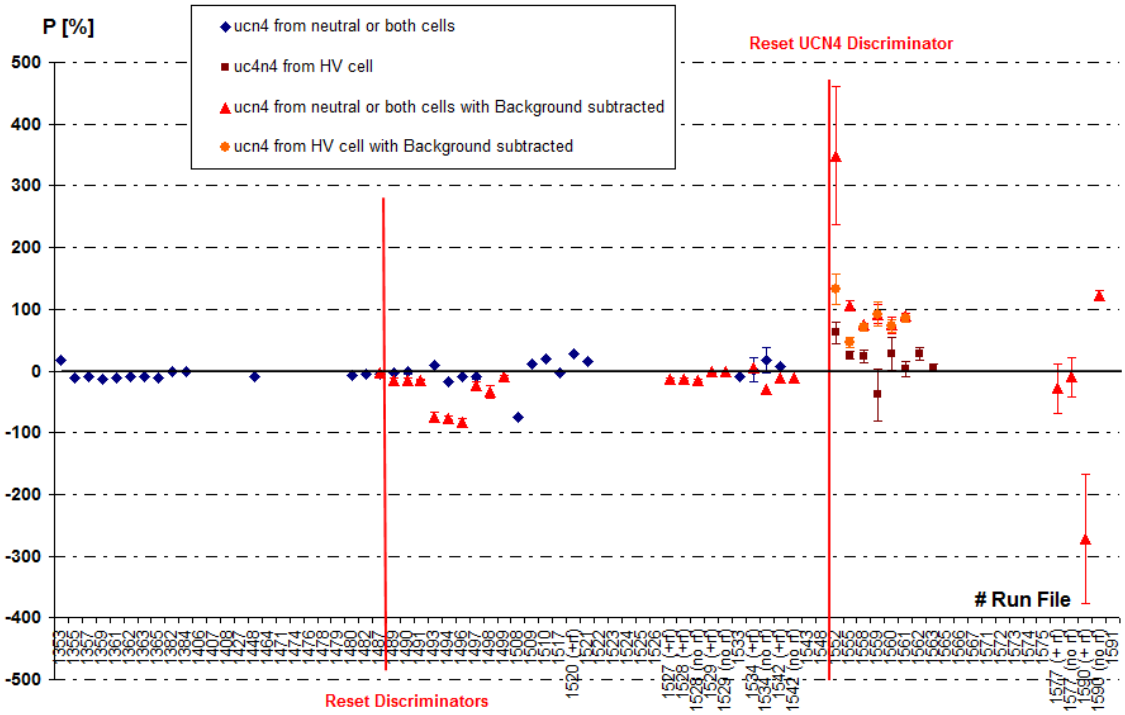

Figure 6.46: Polarisation from the UCN4 detector for neutrons from the cells with and without background subtraction from the MCA spectra. Figure 6.47 is a magnified version of this Figure.

check the performance of the detectors and their amplifiers as it is more likely a problem to occur to one of the detectors rather then all at the same time.

Monitor and store information related to electronics/electrical devices settings and performance. This includes:

1. The discriminator settings at the DataView header. This information was only available on the electronic logbook but tracing back to it is not very helpful when someone needs information for a certain individual file.

2. The performance state of the timer box channels (if one is broken and then functional) and also the position of each element in separate tables which will be available on demand. It is quite illustrative to have the overall picture if it is needed.

3. The output (0 to 5 Volts) of the 8 pin chips (for all 3 chips) in the timer box with time within a single run. Any possible discrepancies on the valves' functionality -that also have to be visually inspected on the MCS spectra- and/or the MCS/MCA ratio can be attributed to timer box malfunction.

4. The holding field coils current.

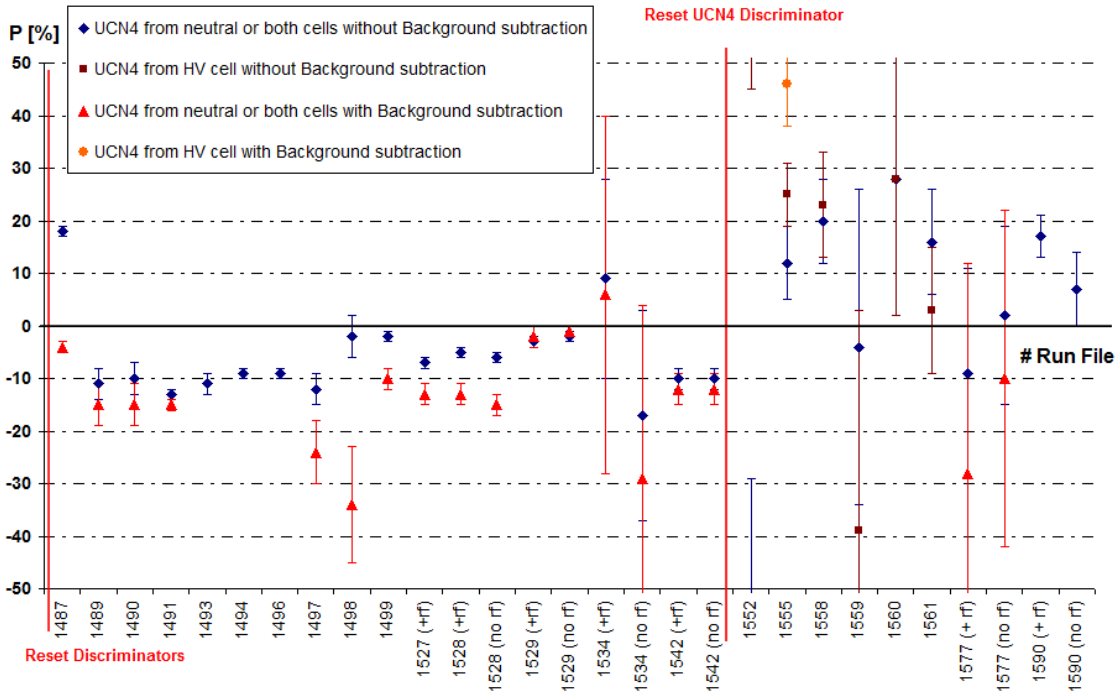

Figure 6.47: A magnified section of Figure 6.46 (Polarisation from the UCN4 detector for neutrons from the cells with and without background subtraction from the MCA spectra).

Do's and Don'ts before and during a run:

1. The amplification should be set such as both alpha and triton peaks are clearly visible and away from any background/noise in the MCA spectra.

2. The holding field should be set at temperature well above the transition temperature of all the SC parts close to the guides and remain unchanged. Ideally, the SC parts should be removed.

3. No more than one parameter should change from one run to another. Changing the holding field and the aperture diameter at the entrance of the Source Volume for example at the same time, can both alter the polarisation of neutrons.

4. Have a back-up power supply for the two solenoid end compensation coils and the carbon fibre former coils. An unexpected power shut down happened at ILL during the #160 run and in principle can happen again. Turning these coils off would not alter the magnetic field configuration in an infinitely long superconducting cylinder but this is clearly not the case with the SC shield and solenoid for which L/D $\approx$4.

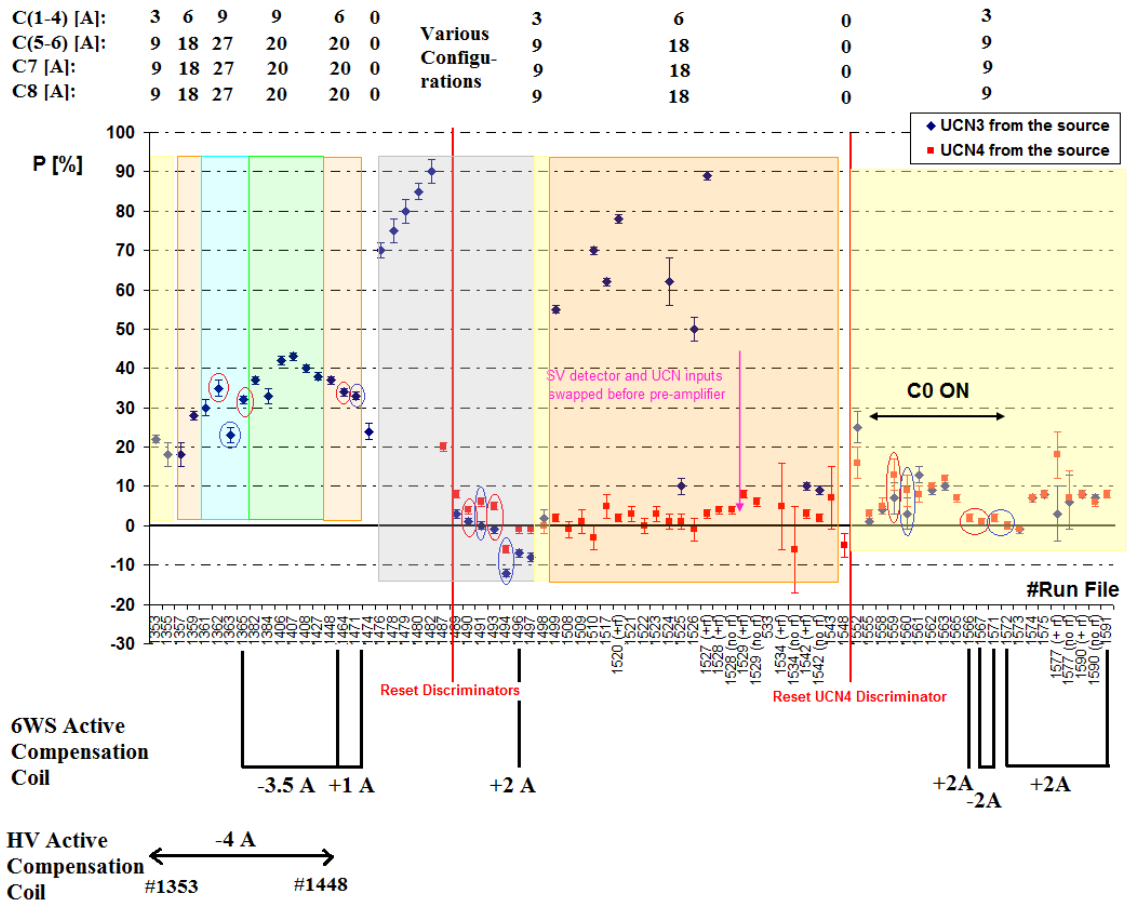

Figure 6.48: Raw polarisation data with the holding field configuration information added. Each different colour corresponds to a particular set of currents in the holding field coils, C1 to C8, with the currents shown above the plot. The two active compensation coils were energised only over the regions indicated at the bottom of the plot. The SQUIDs compensation coil was activated only for the runs for which the data point is circled. Red circles indicate positive and blue ones negative polarity in this coil. For all coils, positive current produces a B-field in the downstream direction.

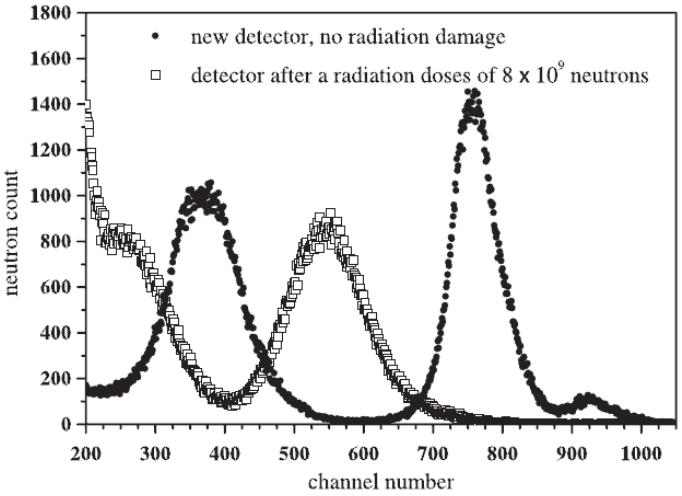

Figure 6.49: Pulse height spectra from a new and a degraded ORTEC silicon detector. For the detector which has suffered a strong radiation dose, the two peaks are no longer resolved and a "background"appears at low energies (channel number).

Chapter 7

Conclusions

This thesis is concerned with various magnetic aspects of the Cryo-nEDM experiment. It has involved experimental development, magnetostatic simulations, analytical calculations and finally data analysis.

The experimental part revolved around the improvement of the Cryogenic Dynamic Magnetic Shielding Factor (DMSF). By building a $1/12.5^{th}$ scale model of the apparatus, we reproduced previously taken data and showed that by placing a 1 m long superconducting cylindrical shield within the solenoid, we can restore the shielding factor to about the required level. The accuracy of these results could be improved by using more sensitive instruments to record to magnetic field changes. As a continuation of the work presented here, a SQUID magnetometer should be used to repeat the experiments.

We then concentrated on aspects of the polarisation holding field and the resonance fields. For the of these OPERA was used to simulate a full model of the apparatus. Having this as a basis, other parts can be added in the future if needed. We estimated the effect of the mu-metal shields and the SQUIDs around the neutron guides on the holding field and and used the model to propose currents configurations to smooth the axial gradient with the existing set of coils outside the horizontal shields. Superconducting items were simulated in QuickField (QF). Further analytical calculations are in a good agreement with the results of QF.

A full magnetic scan at low temperature of the interior of the vessel that accommodates the neutron cells was carried out and the actual response of the compensation coils measured. Using this information, a systematic method to improve the homogeneity of the resonance magnetic field has been developed. This method was used to determine a specific set of currents for the 19 correction coils. According to Monte Carlo simulations this should allow an increase in the T_2 relaxation time from about 2 sec to more than

20 sec. The optimisation method proposed is not restricted by the specific profile of the existing field and can be used in the future for different vessels as long as the magnetic field configuration in their interior is known.

Finally, the polarisation data analysis carried out in this thesis can be considered as a useful guide for future use. This is now being used as the basis to develop an automated, real-time analysis package. The analysis has also revealed a number of hardware problems, particularly with the timer box and the amplifier stability. The problems revealed by the analysis will lead to significant changes to both the hardware and the software systems used in the Cryo-nEDM experiment.

References

[1] Pendlebury J M. Dynamic shielding of the b-field in the cryo-nedm experiment. A Report to the Oversight Committee, Internal paper, May 2006. xiii, 71

[2] Golub R and Pendlebury J M. *Phys. Lett. A*, 62, 337, 1975. xvii, 30, 31

[3] Grozier J R. *The Cryogenic Neutron Electric Dipole Moment Experiment: Magnetic Challenges and Solutions.* PhD thesis, University of Sussex, 2007. xviii, 20, 40, 41, 43, 44, 54, 55, 122

[4] Collaboration meeting april 2005, 0504ill3 – performance update – effect of cooling procedures on field homogeneity. xviii, xxiii, 47, 105

[5] Baker C.A. et al. Development of solid-state silicon devices as ultra cold neutron detectors. *Nucl. Instr. Meth. Phys. Research A*, 487:511–520, 2002. xviii, 47, 48, 187

[6] Dynamic shielding of the b-field in the cryo-nedm experiment – a report to the oversight committee. Technical report, May 2006. page 3. xviii, 55

[7] Goldhaber M, Grodzins L, and Sunyar A W. *Phys. Rev.*, 109:1015, 1958. 5

[8] Lee T D and Yang C N. *Phys. Rev.*, 104:254, 1956. 5

[9] Wu C S, Ambler E, Haywood R W, Hoppes D D, and Hudson R P. *Phys. Rev.*, 105:1413, 1957. 5

[10] Garwin R L, Lederman L M, and Weinrich M. *Phys. Rev.*, 105, 1957. 6

[11] Landau L D. *Zh. Eksp. Teor. Fiz.*, 32:405, 1957. 6

[12] Landau L D. *Nucl. Phys.*, 3:137, 1957. 6

[13] Christenson J H, Cronin J W, Fitch V L, and Turlay R. *Phys. Rev. Lett.*, 13:138, 1964. 6

[14] Burkhardt H et al. *Phys. Lett.*, B206:169, 1988. 6

[15] Abe K. et al. *[BELLE Collaboration], Phys. Rev.*, D 61:074024, 2000. 6

[16] Brau B. *Nucl. Phys. B (Proc. Suppl.)*, 115:67, 2003. 6

[17] Lüders G. *Kgl. Danske Vid. Sek. Mat-fys. Medd,.*, 28, No5, 1954. 6

[18] Lüders G and Zumino B. *Phys. Rev.*, 106:385, 1957. 6

[19] Pauli W. *Niels Bohr and the Development Physics.* Oxford:Pegamon, 1955. 6

[20] Sakharov A D. *JETP Lett.*, 5, 24, 1967. 6

[21] Esterman I and Stern O. *Phys. Rev.*, 45:76, 1934. 7

[22] Tamm I E and Altschuler S A. *C. R. Acad. Sci. URSS*, 1934. 7

[23] Frisch O R, Halban Jr H V, and Kock J. *Nature*, 140:360, 1937. 7

[24] Cabibbo N. *Phys. Rev. Lett.*, 10:531, 1963. 10

[25] T Maskawa M, Kobayashi. *Prog. Theor. Phys.*, 49:652, 1973. 10

[26] Ellis J. Theory of the neutron electric dipole moment. *Nuclear Instruments and Methods in Physics Research A284*, pages 33–39, 1989. 10

[27] Ellis J and Fogh G L. *Phys. Lett.*, B213, 1988. 10

[28] Albajar C et al. Ua1 collaboration. *Z. Phys.*, C37, 1988. 10

[29] Hooft G. *Phys. Rept.*, 142(35), 1986. 11

[30] Baluni V. *Phys. Rev.*, D19:2227, 1979. 11

[31] Crewther R J, Vecchia P Di, Veneziano G, and Witten E. *Phys. Lett.*, 88B:123, 1979. 11

[32] He X G, McKellar B H J, and Pakvasa S. *University of Hawaii UH-511-666-89*, 1989. 11

[33] Baker C A et al. Improved experimental limit on the electric dipole moment of the neutron. *Phys. Rev. Lett.*, 97(13): 131801, 2006. 11

[34] Ellis J and Gaillard M K. *Nucl. Phys.*, B150, 141, 1979. 11

[35] Lebedev O, Olive K, Pospelov M, and Ritz A. *hep-ph/0402023*, 2004. 12

[36] Barr S M. *Phys. Rev.*, D56:1475, 1997. 12

[37] Peccei R D and Quinn H R. *Phys. Rev. Lett.*, 38(1440); Phys. Rev. D16 (1977) 1791, 1977. 12

[38] Nilles H P. *Phys. Rep.*, 110C, 1984. 13, 14

[39] Gerard J M, Grimus W, Masiero A, Nanopoulos D V, and Raychaud A. *Nucl. Phys.*, B253, 1985. 13, 14

[40] Weinberg S. *Phys. Rev. Lett.*, 37, 1976. 13

[41] Khatsimovsku V M, Khriplovich I B, and Zhitnitskii A R. *Z. Phys.*, C36, 1987. 13

[42] Pain J and Salam A. *Phys. Rev.*, D10, 1974. 13

[43] He X-G, McKellar B H J, and Pakvasa S. *Phys. Rev. Lett.*, 61:1267, 1988. 13

[44] Schlicter C P. *Principles of Magnetic Resonance (3rd edition)*. Springer, 1989. 19

[45] Ramsey N F. Experiments with separated oscillatory fields and hydrogen masers. *Rev. Mod. Phys.*, 62:541553, 1990. 19

[46] Ramsey N F. Resonance transitions induced by perturbations at two or more different frequencies. *Phys. Rev.*, 100:1191–1194, 1955. 19

[47] Golub R, Richardson D, and Lamoreaux S K. *Ultra Cold Neutrons*. Adam Hilger, 1997. 20, 33, 94

[48] Doyle D D. *Systematic effects in the neutron EDM experiment and its constraints in physics beyond the standard model*. PhD thesis, University of Sussex, 2005. 20

[49] Karamath J R. *He-II under high electric field conditions for the cryogenic neutron electric dipole moment experiment*. PhD thesis, University of Sussex, 2007. 20

[50] Pendlebury J M et al. Geometric phase induced false electric dipole moment signals for particles in traps. *Physical Review A*, 70:032102, 2004. 22

[51] Aldrich L T and Nier A O. The occurrence of helium-3 in natural source of helium. *Phys. Rev.*, 74(11):1590–4, 1948. 25

[52] Yoshiki H, Nakai H, and Gutsmiedl E. A new superleak to remove helium-3 for ucn experiments. *Elsevier (Cryogenics)*, 45:399–403, 2005. 25

[53] Davidson A J. *PhD Thesis, Chapter 4*. PhD thesis. 26

[54] Golub R and Pendlebury J M. Super-thermal sources of ultra-cold neutrons. *Physics Letters A*, 53(2):133 – 135, 1975. 30, 36

[55] Cohen M and Feynman R P. *Phys. Rev.*, 107:13, 1957. 30

[56] Landau J. *Phys U.S.S.R.*, 5:71, 1941. 30

[57] Landau J. *Phys U.S.S.R.*, 11:91, 1947. 30

[58] Feynman R P. *Phy. Rev.*, 91:1291, 1954. 30

[59] Fermi E and Marshall L. *Phys. Rev.*, 71:666–77, 1974. 33

[60] Peskin M and Ringo G R. *Am. J. Phys.*, 39:324–7, 1971. 33

[61] Fermi E. *Ricerca Scientifica*, 7:13–52, 1936. 33

[62] Spin echo IN15 spectrometer. http://www.ill.eu/?id=789. 51

[63] Claycomb J. *Applied Electromagnetics Using QuickField and Matlab*. Engineering Series, 2009. 57

[64] Thomas Gameson and Sons Limited. http://www.gameson.co.uk/. 61

[65] QuickField-Tera Analysis Ltd. http://www.quickfield.com/. 83

[66] Jackson J D. *Classical Electrodynamics*. New York: John Wiley and Sons, 1975. 87

[67] OPERA Vector Fields Ltd. http://www.vector-fields-opera/. 93

[68] Pendlebury J M. Holding field gradients and ucn spin relaxation. Internal paper, 2005. 95, 99

[69] Harris P G. Monte carlo simulations routine stored at cryo-nedm repository. 2002. 101

[70] M Barnett-Raso. *due to,September 2012*. PhD thesis. 101

[71] Clarke C. More on squids and coils. August 2010, internal pages. 112

[72] Harris P G. Neutron numbers and edm sensitivity. Internal paper, 2011. 121

[73] Golub R and Pendlebury J M. Ultra cold neutrons. *Rep. Prog. Phys.*, 42:441–501, 1979. 121

[74] Pendlebury J M. Bo field properties: Presentation to cryo-edm collaboration meeting. September 2004. Internal paper. 122

[75] Harris P G, Katsika A, and M J Raso-Barnett. Optimisation of the magnetic field. June 25th 2010, cryo-nEDM internal papers. 134

[76] Halpern O and Holstein T. On the depolarization of neutron beams by magnetic fields. *Phys. Rev.*, 59:960, 1941. 161

Appendix A

OPERA Full Model

```
////////////////////////////////////////
//x=y=z=0 represents the centre of 6 way section (6WS)
//axis of symmetry is z
////////////////////////////////////////

////////////////////////
//Design the 12 SQUIDs Cryoperms along z axis (15-24 cm from zero wich is taken at 6WS centre)
////////////////////////

/SQUID1
CYLINDER Name='SQUID 1out Cryoperm' X0=0 Y0=5.5 Z0=15 X1=0 Y1=5.5 Z1=24 MAJORRADIUS=0.68 MINORRADIUS=0.68 TOPRADIUS=0.68
CYLINDER Name='SQUID 1in Cryoperm' X0=0 Y0=5.5 Z0=15.1 X1=0 Y1=5.5 Z1=23.9 MAJORRADIUS=0.58 MINORRADIUS=0.58 TOPRADIUS=0.58
PICK OPTION=ADD, | PICK PROPERTY=Name LABEL='SQUID 1out Cryoperm'
PICK OPTION=ADD, | PICK PROPERTY=Name LABEL='SQUID 1in Cryoperm'
COMBINE OPERATION=SUBTRACT +REGULAR

/SQUID2
CYLINDER Name='SQUID 2out Cryoperm' X0=-1.6 Y0=6.5 Z0=15 X1=-1.6 Y1=6.5 Z1=24 MAJORRADIUS=0.68 MINORRADIUS=0.68 TOPRADIUS=0.68
CYLINDER Name='SQUID 2in Cryoperm' X0=-1.6 Y0=6.5 Z0=15.1 X1=-1.6 Y1=6.5 Z1=23.9 MAJORRADIUS=0.58 MINORRADIUS=0.58 TOPRADIUS=0.58
PICK OPTION=ADD, | PICK PROPERTY=Name LABEL='SQUID 2out Cryoperm'
PICK OPTION=ADD, | PICK PROPERTY=Name LABEL='SQUID 2in Cryoperm'
COMBINE OPERATION=SUBTRACT +REGULAR

/SQUID3
CYLINDER Name='SQUID 3out Cryoperm' X0=1.6 Y0=6.5 Z0=15 X1=1.6 Y1=6.5 Z1=24 MAJORRADIUS=0.68 MINORRADIUS=0.68 TOPRADIUS=0.68
CYLINDER Name='SQUID 3in Cryoperm' X0=1.6 Y0=6.5 Z0=15.1 X1=1.6 Y1=6.5 Z1=23.9 MAJORRADIUS=0.58 MINORRADIUS=0.58 TOPRADIUS=0.58
PICK OPTION=ADD, | PICK PROPERTY=Name LABEL='SQUID 3out Cryoperm'
PICK OPTION=ADD, | PICK PROPERTY=Name LABEL='SQUID 3in Cryoperm'
COMBINE OPERATION=SUBTRACT +REGULAR


/SQUID4
CYLINDER Name='SQUID 4out Cryoperm' X0=4.9 Y0=0 Z0=15 X1=4.9 Y1=0 Z1=24 MAJORRADIUS=0.68 MINORRADIUS=0.68 TOPRADIUS=0.68
CYLINDER Name='SQUID 4in Cryoperm' X0=4.9 Y0=0 Z0=15.1 X1=4.9 Y1=0 Z1=23.9 MAJORRADIUS=0.58 MINORRADIUS=0.58 TOPRADIUS=0.58
PICK OPTION=ADD, | PICK PROPERTY=Name LABEL='SQUID 4out Cryoperm'
PICK OPTION=ADD, | PICK PROPERTY=Name LABEL='SQUID 4in Cryoperm'
COMBINE OPERATION=SUBTRACT +REGULAR


/SQUID5
CYLINDER Name='SQUID 5out Cryoperm' X0=5.9 Y0=1.6 Z0=15 X1=5.9 Y1=1.6 Z1=24 MAJORRADIUS=0.68 MINORRADIUS=0.68 TOPRADIUS=0.68
CYLINDER Name='SQUID 5in Cryoperm' X0=5.9 Y0=1.6 Z0=15.1 X1=5.9 Y1=1.6 Z1=23.9 MAJORRADIUS=0.58 MINORRADIUS=0.58 TOPRADIUS=0.58
PICK OPTION=ADD, | PICK PROPERTY=Name LABEL='SQUID 5out Cryoperm'
PICK OPTION=ADD, | PICK PROPERTY=Name LABEL='SQUID 5in Cryoperm'
COMBINE OPERATION=SUBTRACT +REGULAR
```

```
/SQUID6
CYLINDER Name='SQUID 6out Cryoperm' X0=5.9 Y0=-1.6 Z0=15 X1=5.9 Y1=-1.6 Z1=24 MAJORRADIUS=0.68 MINORRADIUS=0.68 TOPRADIUS=0.68
CYLINDER Name='SQUID 6in Cryoperm' X0=5.9 Y0=-1.6 Z0=15.1 X1=5.9 Y1=-1.6 Z1=23.9 MAJORRADIUS=0.58 MINORRADIUS=0.58 TOPRADIUS=0.58
PICK OPTION=ADD, | PICK PROPERTY=Name LABEL='SQUID 6out Cryoperm'
PICK OPTION=ADD, | PICK PROPERTY=Name LABEL='SQUID 6in Cryoperm'
COMBINE OPERATION=SUBTRACT +REGULAR

/SQUID7
CYLINDER Name='SQUID 7out Cryoperm' X0=0 Y0=-5.5 Z0=15 X1=0 Y1=-5.5 Z1=24 MAJORRADIUS=0.68 MINORRADIUS=0.68 TOPRADIUS=0.68
CYLINDER Name='SQUID 7in Cryoperm' X0=0 Y0=-5.5 Z0=15.1 X1=0 Y1=-5.5 Z1=23.9 MAJORRADIUS=0.58 MINORRADIUS=0.58 TOPRADIUS=0.58
PICK OPTION=ADD, | PICK PROPERTY=Name LABEL='SQUID 7out Cryoperm'
PICK OPTION=ADD, | PICK PROPERTY=Name LABEL='SQUID 7in Cryoperm'
COMBINE OPERATION=SUBTRACT +REGULAR

/SQUID8
CYLINDER Name='SQUID 8out Cryoperm' X0=-1.6 Y0=-6.5 Z0=15 X1=-1.6 Y1=-6.5 Z1=24 MAJORRADIUS=0.68 MINORRADIUS=0.68 TOPRADIUS=0.68
CYLINDER Name='SQUID 8in Cryoperm' X0=-1.6 Y0=-6.5 Z0=15.1 X1=-1.6 Y1=-6.5 Z1=23.9 MAJORRADIUS=0.58 MINORRADIUS=0.58 TOPRADIUS=0.58
PICK OPTION=ADD, | PICK PROPERTY=Name LABEL='SQUID 8out Cryoperm'
PICK OPTION=ADD, | PICK PROPERTY=Name LABEL='SQUID 8in Cryoperm'
COMBINE OPERATION=SUBTRACT +REGULAR

/SQUID9
CYLINDER Name='SQUID 9out Cryoperm' X0=1.6 Y0=-6.5 Z0=15 X1=1.6 Y1=-6.5 Z1=24 MAJORRADIUS=0.68 MINORRADIUS=0.68 TOPRADIUS=0.68
CYLINDER Name='SQUID 9in Cryoperm' X0=1.6 Y0=-6.5 Z0=15.1 X1=1.6 Y1=-6.5 Z1=23.9 MAJORRADIUS=0.58 MINORRADIUS=0.58 TOPRADIUS=0.58
PICK OPTION=ADD, | PICK PROPERTY=Name LABEL='SQUID 9out Cryoperm'
PICK OPTION=ADD, | PICK PROPERTY=Name LABEL='SQUID 9in Cryoperm'
COMBINE OPERATION=SUBTRACT +REGULAR


/SQUID10
CYLINDER Name='SQUID 10out Cryoperm' X0=-4.9 Y0=0 Z0=15 X1=-4.9 Y1=0 Z1=24 MAJORRADIUS=0.68 MINORRADIUS=0.68 TOPRADIUS=0.68
CYLINDER Name='SQUID 10in Cryoperm' X0=-4.9 Y0=0 Z0=15.1 X1=-4.9 Y1=0 Z1=23.9 MAJORRADIUS=0.58 MINORRADIUS=0.58 TOPRADIUS=0.58
PICK OPTION=ADD, | PICK PROPERTY=Name LABEL='SQUID 10out Cryoperm'
PICK OPTION=ADD, | PICK PROPERTY=Name LABEL='SQUID 10in Cryoperm'
COMBINE OPERATION=SUBTRACT +REGULAR


/SQUID11
CYLINDER Name='SQUID 11out Cryoperm' X0=-5.9 Y0=1.6 Z0=15 X1=-5.9 Y1=1.6 Z1=24 MAJORRADIUS=0.68 MINORRADIUS=0.68 TOPRADIUS=0.68
CYLINDER Name='SQUID 11in Cryoperm' X0=-5.9 Y0=1.6 Z0=15.1 X1=-5.9 Y1=1.6 Z1=23.9 MAJORRADIUS=0.58 MINORRADIUS=0.58 TOPRADIUS=0.58
PICK OPTION=ADD, | PICK PROPERTY=Name LABEL='SQUID 11out Cryoperm'
PICK OPTION=ADD, | PICK PROPERTY=Name LABEL='SQUID 11in Cryoperm'
COMBINE OPERATION=SUBTRACT +REGULAR


/SQUID12
CYLINDER Name='SQUID 12out Cryoperm' X0=-5.9 Y0=-1.6 Z0=15 X1=-5.9 Y1=-1.6 Z1=24 MAJORRADIUS=0.68 MINORRADIUS=0.68 TOPRADIUS=0.68
CYLINDER Name='SQUID 12in Cryoperm' X0=-5.9 Y0=-1.6 Z0=15.1 X1=-5.9 Y1=-1.6 Z1=23.9 MAJORRADIUS=0.58 MINORRADIUS=0.58 TOPRADIUS=0.58
PICK OPTION=ADD, | PICK PROPERTY=Name LABEL='SQUID 12out Cryoperm'
PICK OPTION=ADD, | PICK PROPERTY=Name LABEL='SQUID 12in Cryoperm'
COMBINE OPERATION=SUBTRACT +REGULAR




////////////////////////
//Set SQUIDs Magnetic Properties (mu=10000) + Data Storage Level=50 + Potential (Total) + meshing size=2
////////////////////////


FILTER COMMAND=PICK
FILTER TYPE=CELL
PICK OPTION=TOGGLE TYPE=CELL N=1
PICK OPTION=TOGGLE TYPE=CELL N=2
PICK OPTION=TOGGLE TYPE=CELL N=3
```

```
PICK OPTION=TOGGLE TYPE=CELL N=10
PICK OPTION=TOGGLE TYPE=CELL N=11
PICK OPTION=TOGGLE TYPE=CELL N=12
PICK OPTION=TOGGLE TYPE=CELL N=7
PICK OPTION=TOGGLE TYPE=CELL N=8
PICK OPTION=TOGGLE TYPE=CELL N=9
PICK OPTION=TOGGLE TYPE=CELL N=4
PICK OPTION=TOGGLE TYPE=CELL N=5
PICK OPTION=TOGGLE TYPE=CELL N=6
CELLDATA OPTION=MODIFY MATERIALLABEL='12 SQUIDs' POTENTIAL=Total ELEMENTTYPE=Linear LEVEL=50 SIZE=2
MATERIAL UNPICK
MATERIAL PICK '12 SQUIDs'
MATERIAL OPTION=CGS MULINEARITY=LINEAR MUANISOTROPY=ISOTROPIC MU=10000 EPSANISOTROPY=ISOTROPIC SIGANISOTROPY=ISOTROPIC KAPANISOTROPY=ISOTROPIC
MATERIAL OPTION=MODIFY MULINEARITY=LINEAR MUANISOTROPY=ISOTROPIC MU=10000 EPSANISOTROPY=ISOTROPIC SIGANISOTROPY=ISOTROPIC KAPANISOTROPY=ISOTROPIC
MATERIAL OPTION=MODIFY MULINEARITY=LINEAR MUANISOTROPY=ISOTROPIC MU=10000 EPSANISOTROPY=ISOTROPIC SIGANISOTROPY=ISOTROPIC KAPANISOTROPY=ISOTROPIC




////////////////////////////////
//Make 3 cuts at each SQUID
////////////////////////////////

BLOCK Name=cut X0=-30 Y0=-30 Z0=18 X1=30 Y1=30 Z1=18
FILTER COMMAND=PICK
FILTER TYPE=BODY
PICK OPTION=TOGGLE TYPE=BODY N=13
TRANSFORM OPTION=COPY TYPE=DISPLACE COUNT=2 DU=0 DV=0 DW=2
FILTER COMMAND=PICK
PICK OPTION=ADD, | PICK PROPERTY=Name LABEL='SQUID 1out Cryoperm'
PICK OPTION=ADD, | PICK PROPERTY=Name LABEL='cut'
COMBINE OPERATION=SUBTRACT +REGULAR

BLOCK Name=cut X0=-30 Y0=-30 Z0=18 X1=30 Y1=30 Z1=18
PICK OPTION=TOGGLE TYPE=BODY N=13
TRANSFORM OPTION=COPY TYPE=DISPLACE COUNT=2 DU=0 DV=0 DW=2
FILTER COMMAND=PICK
FILTER COMMAND=PICK
PICK OPTION=ADD, | PICK PROPERTY=Name LABEL='SQUID 2out Cryoperm'
PICK OPTION=ADD, | PICK PROPERTY=Name LABEL='cut'
COMBINE OPERATION=SUBTRACT +REGULAR

BLOCK Name=cut X0=-30 Y0=-30 Z0=18 X1=30 Y1=30 Z1=18
PICK OPTION=TOGGLE TYPE=BODY N=13
TRANSFORM OPTION=COPY TYPE=DISPLACE COUNT=2 DU=0 DV=0 DW=2
FILTER COMMAND=PICK
PICK OPTION=ADD, | PICK PROPERTY=Name LABEL='SQUID 3out Cryoperm'
PICK OPTION=ADD, | PICK PROPERTY=Name LABEL='cut'
COMBINE OPERATION=SUBTRACT +REGULAR

BLOCK Name=cut X0=-30 Y0=-30 Z0=18 X1=30 Y1=30 Z1=18
PICK OPTION=TOGGLE TYPE=BODY N=13
TRANSFORM OPTION=COPY TYPE=DISPLACE COUNT=2 DU=0 DV=0 DW=2
FILTER COMMAND=PICK
PICK OPTION=ADD, | PICK PROPERTY=Name LABEL='SQUID 4out Cryoperm'
PICK OPTION=ADD, | PICK PROPERTY=Name LABEL='cut'
COMBINE OPERATION=SUBTRACT +REGULAR

BLOCK Name=cut X0=-30 Y0=-30 Z0=18 X1=30 Y1=30 Z1=18
PICK OPTION=TOGGLE TYPE=BODY N=13
TRANSFORM OPTION=COPY TYPE=DISPLACE COUNT=2 DU=0 DV=0 DW=2
FILTER COMMAND=PICK
PICK OPTION=ADD, | PICK PROPERTY=Name LABEL='SQUID 5out Cryoperm'
PICK OPTION=ADD, | PICK PROPERTY=Name LABEL='cut'
COMBINE OPERATION=SUBTRACT +REGULAR
```

```
BLOCK Name=cut X0=-30 Y0=-30 Z0=18 X1=30 Y1=30 Z1=18
PICK OPTION=TOGGLE TYPE=BODY N=13
TRANSFORM OPTION=COPY TYPE=DISPLACE COUNT=2 DU=0 DV=0 DW=2
FILTER COMMAND=PICK
PICK OPTION=ADD, | PICK PROPERTY=Name LABEL='SQUID 6out Cryoperm'
PICK OPTION=ADD, | PICK PROPERTY=Name LABEL='cut'
COMBINE OPERATION=SUBTRACT +REGULAR

BLOCK Name=cut X0=-30 Y0=-30 Z0=18 X1=30 Y1=30 Z1=18
PICK OPTION=TOGGLE TYPE=BODY N=13
TRANSFORM OPTION=COPY TYPE=DISPLACE COUNT=2 DU=0 DV=0 DW=2
FILTER COMMAND=PICK
FILTER COMMAND=PICK
PICK OPTION=ADD, | PICK PROPERTY=Name LABEL='SQUID 7out Cryoperm'
PICK OPTION=ADD, | PICK PROPERTY=Name LABEL='cut'
COMBINE OPERATION=SUBTRACT +REGULAR

BLOCK Name=cut X0=-30 Y0=-30 Z0=18 X1=30 Y1=30 Z1=18
PICK OPTION=TOGGLE TYPE=BODY N=13
TRANSFORM OPTION=COPY TYPE=DISPLACE COUNT=2 DU=0 DV=0 DW=2
FILTER COMMAND=PICK
PICK OPTION=ADD, | PICK PROPERTY=Name LABEL='SQUID 8out Cryoperm'
PICK OPTION=ADD, | PICK PROPERTY=Name LABEL='cut'
COMBINE OPERATION=SUBTRACT +REGULAR

BLOCK Name=cut X0=-30 Y0=-30 Z0=18 X1=30 Y1=30 Z1=18
PICK OPTION=TOGGLE TYPE=BODY N=13
TRANSFORM OPTION=COPY TYPE=DISPLACE COUNT=2 DU=0 DV=0 DW=2
FILTER COMMAND=PICK
PICK OPTION=ADD, | PICK PROPERTY=Name LABEL='SQUID 9out Cryoperm'
PICK OPTION=ADD, | PICK PROPERTY=Name LABEL='cut'
COMBINE OPERATION=SUBTRACT +REGULAR

BLOCK Name=cut X0=-30 Y0=-30 Z0=18 X1=30 Y1=30 Z1=18
PICK OPTION=TOGGLE TYPE=BODY N=13
TRANSFORM OPTION=COPY TYPE=DISPLACE COUNT=2 DU=0 DV=0 DW=2
FILTER COMMAND=PICK
PICK OPTION=ADD, | PICK PROPERTY=Name LABEL='SQUID 10out Cryoperm'
PICK OPTION=ADD, | PICK PROPERTY=Name LABEL='cut'
COMBINE OPERATION=SUBTRACT +REGULAR

BLOCK Name=cut X0=-30 Y0=-30 Z0=18 X1=30 Y1=30 Z1=18
PICK OPTION=TOGGLE TYPE=BODY N=13
TRANSFORM OPTION=COPY TYPE=DISPLACE COUNT=2 DU=0 DV=0 DW=2
FILTER COMMAND=PICK
PICK OPTION=ADD, | PICK PROPERTY=Name LABEL='SQUID 11out Cryoperm'
PICK OPTION=ADD, | PICK PROPERTY=Name LABEL='cut'
COMBINE OPERATION=SUBTRACT +REGULAR

BLOCK Name=cut X0=-30 Y0=-30 Z0=18 X1=30 Y1=30 Z1=18
PICK OPTION=TOGGLE TYPE=BODY N=13
TRANSFORM OPTION=COPY TYPE=DISPLACE COUNT=2 DU=0 DV=0 DW=2
FILTER COMMAND=PICK
PICK OPTION=ADD, | PICK PROPERTY=Name LABEL='SQUID 12out Cryoperm'
PICK OPTION=ADD, | PICK PROPERTY=Name LABEL='cut'
COMBINE OPERATION=SUBTRACT +REGULAR

////////////////////////////////////////



////////////////////////////////
//guide tube (Desing)
////////////////////////////////
```

```
BLOCK Name='guide tube' X0=-3.1 Y0=-3.7 Z0=-110 X1=3.1 Y1=3.7 Z1=280


////////////////////////
//guide tube (Set properties) (Data Storage Level=50, mesh size=2, Potential=Total)
////////////////////////


FILTER COMMAND=PICK
FILTER TYPE=CELL
PICK OPTION=TOGGLE TYPE=CELL N=49
CELLDATA OPTION=MODIFY MATERIALLABEL='guide tube' POTENTIAL=Total ELEMENTTYPE=Linear LEVEL=50 SIZE=2
MATERIAL UNPICK
MATERIAL PICK 'guide tube'
MATERIAL OPTION=CGS MULINEARITY=LINEAR MUANISOTROPY=ISOTROPIC MU=1 EPSANISOTROPY=ISOTROPIC SIGANISOTROPY=ISOTROPIC KAPANISOTROPY=ISOTROPIC
MATERIAL OPTION=MODIFY MULINEARITY=LINEAR MUANISOTROPY=ISOTROPIC MU=1 EPSANISOTROPY=ISOTROPIC SIGANISOTROPY=ISOTROPIC KAPANISOTROPY=ISOTROPIC
MATERIAL OPTION=MODIFY MULINEARITY=LINEAR MUANISOTROPY=ISOTROPIC MU=1 EPSANISOTROPY=ISOTROPIC SIGANISOTROPY=ISOTROPIC KAPANISOTROPY=ISOTROPIC


////////////////////////////////////////////////
//Make 12 cuts on guide tube (starting here at z=-80cm and copyed 11 times every 30 cm along z axis)
////////////////////////////////////////////////

BLOCK Name=cut X0=-10 Y0=-10 Z0=-80 X1=10 Y1=10 Z1=-80
FILTER COMMAND=PICK
FILTER TYPE=BODY
PICK OPTION=TOGGLE TYPE=BODY N=14
TRANSFORM OPTION=COPY TYPE=DISPLACE COUNT=11 DU=0 DV=0 DW=30
FILTER COMMAND=PICK
PICK OPTION=ADD, | PICK PROPERTY=Name LABEL='guide tube'
PICK OPTION=ADD, | PICK PROPERTY=Name LABEL='cut'
COMBINE OPERATION=SUBTRACT +REGULAR
////////////////////////////////////////




///////////////////////////////////
///mu metal nose 6WS end (12.1 mm thick)
///////////////////////////////////

CYLINDER Name='mu metal nose 6WS end' X0=0 Y0=0 Z0=39.8 X1=0 Y1=0 Z1=67 MAJORRADIUS=59.21 MINORRADIUS=59.21 TOPRADIUS=59.21
CYLINDER Name=cylinder1a X0=0 Y0=0 Z0=59.95 X1=0 Y1=0 Z1=67 MAJORRADIUS=58 MINORRADIUS=58 TOPRADIUS=58
CYLINDER Name=cylinder1b X0=0 Y0=0 Z0=39.8 X1=0 Y1=0 Z1=59.95 MAJORRADIUS=18 MINORRADIUS=18 TOPRADIUS=18
FILTER COMMAND=PICK
PICK OPTION=ADD, | PICK PROPERTY=Name LABEL='mu metal nose 6WS end'
PICK OPTION=ADD, | PICK PROPERTY=Name LABEL='cylinder1a'
PICK OPTION=ADD, | PICK PROPERTY=Name LABEL='cylinder1b'
COMBINE OPERATION=SUBTRACT +REGULAR
CYLINDER Name=cylinder2 X0=0 Y0=0 Z0=39.8 X1=0 Y1=0 Z1=59.8 MAJORRADIUS=59.21 MINORRADIUS=59.21 TOPRADIUS=59.21
CYLINDER Name=cylinder2a X0=0 Y0=0 Z0=39.8 X1=0 Y1=0 Z1=59.8 MAJORRADIUS=19.21 MINORRADIUS=19.21 TOPRADIUS=19.21
FILTER COMMAND=PICK
PICK OPTION=ADD, | PICK PROPERTY=Name LABEL='cylinder2'
PICK OPTION=ADD, | PICK PROPERTY=Name LABEL='cylinder2a'
COMBINE OPERATION=SUBTRACT +REGULAR
PICK OPTION=ADD, | PICK PROPERTY=Name LABEL='mu metal nose 6WS end'
PICK OPTION=ADD, | PICK PROPERTY=Name LABEL='cylinder2'
COMBINE OPERATION=SUBTRACT +REGULAR


////////////////////////////////////
///Set "mu metal nose 6WS end" properties (mu = 50000, Total Potential, Data Storage Level=50, mesh size=2)
///////////////////////////////////

PICK OPTION=ADD, | PICK PROPERTY=Name LABEL='mu metal nose 6WS end'
PICK OPTION=CHANGE TYPE=CELL
```

```
CELLDATA OPTION=MODIFY MATERIALLABEL='mu metal nose 6WS end' POTENTIAL=Total ELEMENTTYPE=Linear LEVEL=50 SIZE=2
MATERIAL UNPICK

MATERIAL PICK 'mu metal nose 6WS end'
MATERIAL OPTION=MODIFY MULINEARITY=LINEAR MUANISOTROPY=ISOTROPIC MU=50000 EPSANISOTROPY=ISOTROPIC SIGANISOTROPY=ISOTROPIC KAPANISOTROPY=ISOTROPIC
MATERIAL OPTION=MODIFY MULINEARITY=LINEAR MUANISOTROPY=ISOTROPIC MU=50000 EPSANISOTROPY=ISOTROPIC SIGANISOTROPY=ISOTROPIC KAPANISOTROPY=ISOTROPIC

////////////////////////////////////




////////////////////////////////
///mu metal nose HV end (1.5 mm thick)
////////////////////////////////

CYLINDER Name='mu metal nose HV end' X0=0 Y0=0 Z0=373 X1=0 Y1=0 Z1=400.1 MAJORRADIUS=59.21 MINORRADIUS=59.21 TOPRADIUS=59.21
CYLINDER Name='cylinder 1a' X0=0 Y0=0 Z0=373 X1=0 Y1=0 Z1=379.95 MAJORRADIUS=59.06 MINORRADIUS=59.06 TOPRADIUS=59.06
CYLINDER Name='cylinder 1b' X0=0 Y0=0 Z0=379.95 X1=0 Y1=0 Z1=400.1 MAJORRADIUS=18 MINORRADIUS=18 TOPRADIUS=18
FILTER COMMAND=PICK
PICK OPTION=ADD, | PICK PROPERTY=Name LABEL='mu metal nose HV end'
PICK OPTION=ADD, | PICK PROPERTY=Name LABEL='cylinder 1a'
PICK OPTION=ADD, | PICK PROPERTY=Name LABEL='cylinder 1b'
COMBINE OPERATION=SUBTRACT +REGULAR
CYLINDER Name='cylinder 2' X0=0 Y0=0 Z0=380.1 X1=0 Y1=0 Z1=400.1 MAJORRADIUS=59.21 MINORRADIUS=59.21 TOPRADIUS=59.21
CYLINDER Name='cylinder 2a' X0=0 Y0=0 Z0=380.1 X1=0 Y1=0 Z1=400.1 MAJORRADIUS=18.15 MINORRADIUS=18.15 TOPRADIUS=18.15
PICK OPTION=ADD, | PICK PROPERTY=Name LABEL='cylinder 2'
PICK OPTION=ADD, | PICK PROPERTY=Name LABEL='cylinder 2a'
COMBINE OPERATION=SUBTRACT +REGULAR
PICK OPTION=ADD, | PICK PROPERTY=Name LABEL='mu metal nose HV end'
PICK OPTION=ADD, | PICK PROPERTY=Name LABEL='cylinder 2'
COMBINE OPERATION=SUBTRACT +REGULAR

////////////////////////////////////
///Set "mu metal nose HV end" properties (mu = 50000, Total Potential, Data Storage Level=50, mesh size=2)
////////////////////////////////

PICK OPTION=ADD, | PICK PROPERTY=Name LABEL='mu metal nose HV end'
PICK OPTION=CHANGE TYPE=CELL
CELLDATA OPTION=MODIFY MATERIALLABEL='mu metal nose HV end' POTENTIAL=Total ELEMENTTYPE=Linear LEVEL=50 SIZE=2
MATERIAL UNPICK

MATERIAL PICK 'mu metal nose HV end'
MATERIAL OPTION=MODIFY MULINEARITY=LINEAR MUANISOTROPY=ISOTROPIC MU=50000 EPSANISOTROPY=ISOTROPIC SIGANISOTROPY=ISOTROPIC KAPANISOTROPY=ISOTROPIC
MATERIAL OPTION=MODIFY MULINEARITY=LINEAR MUANISOTROPY=ISOTROPIC MU=50000 EPSANISOTROPY=ISOTROPIC SIGANISOTROPY=ISOTROPIC KAPANISOTROPY=ISOTROPIC
////////////////////////////////////




////////////////////////////////
///3 mu metal layers (Rin=50.9cm, 54.9cm, 58.9cm, thickness t=t1=t2=t3=0.16x3=0.48cm --> real t=0.16cm)
////////////////////////////////

///mu 1
CYLINDER Name=mu1 X0=0 Y0=0 Z0=59.95 X1=0 Y1=0 Z1=379.95 MAJORRADIUS=51.38 MINORRADIUS=51.38 TOPRADIUS=51.38
CYLINDER Name=mu1in X0=0 Y0=0 Z0=59.95 X1=0 Y1=0 Z1=379.95 MAJORRADIUS=50.9 MINORRADIUS=50.9 TOPRADIUS=50.9
FILTER COMMAND=PICK
PICK OPTION=ADD, | PICK PROPERTY=Name LABEL='mu1'
PICK OPTION=ADD, | PICK PROPERTY=Name LABEL='mu1in'
COMBINE OPERATION=SUBTRACT +REGULAR


///mu 2
CYLINDER Name=mu2 X0=0 Y0=0 Z0=59.95 X1=0 Y1=0 Z1=379.95 MAJORRADIUS=55.38 MINORRADIUS=55.38 TOPRADIUS=55.38
CYLINDER Name=mu2in X0=0 Y0=0 Z0=59.95 X1=0 Y1=0 Z1=379.95 MAJORRADIUS=54.9 MINORRADIUS=54.9 TOPRADIUS=54.9
FILTER COMMAND=PICK
```

```
PICK OPTION=ADD, | PICK PROPERTY=Name LABEL='mu2'
PICK OPTION=ADD, | PICK PROPERTY=Name LABEL='mu2in'
COMBINE OPERATION=SUBTRACT +REGULAR


///mu 3
CYLINDER Name=mu3 X0=0 Y0=0 Z0=59.95 X1=0 Y1=0 Z1=379.95 MAJORRADIUS=59.38 MINORRADIUS=59.38 TOPRADIUS=59.38
CYLINDER Name=mu3in X0=0 Y0=0 Z0=59.95 X1=0 Y1=0 Z1=379.95 MAJORRADIUS=58.9 MINORRADIUS=58.9 TOPRADIUS=58.9
FILTER COMMAND=PICK
PICK OPTION=ADD, | PICK PROPERTY=Name LABEL='mu3'
PICK OPTION=ADD, | PICK PROPERTY=Name LABEL='mu3in'
COMBINE OPERATION=SUBTRACT +REGULAR
////////////////////////////////




//////////////////////////////////
///Set magnetic properties of 3 mu metal layers (Potential=Total,mesh size=1,Data Storage Level=45, mu=50000)
//////////////////////////////////

PICK OPTION=ADD, | PICK PROPERTY=Name LABEL='mu1'
PICK OPTION=CHANGE TYPE=CELL
CELLDATA OPTION=MODIFY MATERIALLABEL='mu 1' POTENTIAL=Total ELEMENTTYPE=Linear LEVEL=45 SIZE=1

PICK OPTION=ADD, | PICK PROPERTY=Name LABEL='mu2'
PICK OPTION=CHANGE TYPE=CELL
CELLDATA OPTION=MODIFY MATERIALLABEL='mu 2' POTENTIAL=Total ELEMENTTYPE=Linear LEVEL=45 SIZE=1

PICK OPTION=ADD, | PICK PROPERTY=Name LABEL='mu3'
PICK OPTION=CHANGE TYPE=CELL
CELLDATA OPTION=MODIFY MATERIALLABEL='mu 3' POTENTIAL=Total ELEMENTTYPE=Linear LEVEL=45 SIZE=1
MATERIAL UNPICK

MATERIAL PICK 'mu 1'
MATERIAL OPTION=MODIFY MULINEARITY=LINEAR MUANISOTROPY=ISOTROPIC MU=50000 EPSANISOTROPY=ISOTROPIC SIGANISOTROPY=ISOTROPIC KAPANISOTROPY=ISOTROPIC

MATERIAL UNPICK 'mu 1' | MATERIAL PICK 'mu 2'
MATERIAL OPTION=MODIFY MULINEARITY=LINEAR MUANISOTROPY=ISOTROPIC MU=50000 EPSANISOTROPY=ISOTROPIC SIGANISOTROPY=ISOTROPIC KAPANISOTROPY=ISOTROPIC

MATERIAL UNPICK 'mu 2' | MATERIAL PICK 'mu 3'
MATERIAL OPTION=MODIFY MULINEARITY=LINEAR MUANISOTROPY=ISOTROPIC MU=50000 EPSANISOTROPY=ISOTROPIC SIGANISOTROPY=ISOTROPIC KAPANISOTROPY=ISOTROPIC

MATERIAL OPTION=MODIFY MULINEARITY=LINEAR MUANISOTROPY=ISOTROPIC MU=50000 EPSANISOTROPY=ISOTROPIC SIGANISOTROPY=ISOTROPIC KAPANISOTROPY=ISOTROPIC
//////////////////////////////////




//////////////////////////////////
/// make 7 cuts at each mu layer (1st at 100cm + 6 copies every 40 cm) so totally 8 parts//
//////////////////////////////////

//mu 1//
BLOCK Name=cut X0=-600 Y0=-600 Z0=100 X1=600 Y1=600 Z1=100
PICK OPTION=ADD, | PICK PROPERTY=Name LABEL='cut'
TRANSFORM OPTION=COPY TYPE=DISPLACE COUNT=6 DU=0 DV=0 DW=40
PICK OPTION=ADD, | PICK PROPERTY=Name LABEL='mu1'
PICK OPTION=ADD, | PICK PROPERTY=Name LABEL='cut'
COMBINE OPERATION=SUBTRACT +REGULAR

//mu 2//
BLOCK Name=cut X0=-600 Y0=-600 Z0=100 X1=600 Y1=600 Z1=100
PICK OPTION=ADD, | PICK PROPERTY=Name LABEL='cut'
TRANSFORM OPTION=COPY TYPE=DISPLACE COUNT=6 DU=0 DV=0 DW=40
PICK OPTION=ADD, | PICK PROPERTY=Name LABEL='mu2'
PICK OPTION=ADD, | PICK PROPERTY=Name LABEL='cut'
```

```
COMBINE OPERATION=SUBTRACT +REGULAR

//mu 3//
BLOCK Name=cut X0=-600 Y0=-600 Z0=100 X1=600 Y1=600 Z1=100
PICK OPTION=ADD, | PICK PROPERTY=Name LABEL='cut'
TRANSFORM OPTION=COPY TYPE=DISPLACE COUNT=6 DU=0 DV=0 DW=40
PICK OPTION=ADD, | PICK PROPERTY=Name LABEL='mu3'
PICK OPTION=ADD, | PICK PROPERTY=Name LABEL='cut'
COMBINE OPERATION=SUBTRACT +REGULAR
////////////////////////////////




////////////////////////////////
//3 mu metal layers volume
////////////////////////////////

CYLINDER Name='3 mu cylinder' X0=0 Y0=0 Z0=59.95 X1=0 Y1=0 Z1=379.95 MAJORRADIUS=61 MINORRADIUS=61 TOPRADIUS=61
CYLINDER Name='cylinder in' X0=0 Y0=0 Z0=59.95 X1=0 Y1=0 Z1=379.95 MAJORRADIUS=49 MINORRADIUS=49 TOPRADIUS=49
FILTER COMMAND=PICK
PICK OPTION=ADD, | PICK PROPERTY=Name LABEL='3 mu cylinder'
PICK OPTION=ADD, | PICK PROPERTY=Name LABEL='cylinder in'
COMBINE OPERATION=SUBTRACT +REGULAR


//// set magnetic properties for "3 mu cylinder"//
FILTER TYPE=CELL
PICK OPTION=ADD, | PICK PROPERTY=Name LABEL='3 mu cylinder'
PICK OPTION=CHANGE TYPE=CELL
CELLDATA OPTION=MODIFY MATERIALLABEL='3 mu culinder' POTENTIAL=Total ELEMENTTYPE=Linear LEVEL=15 SIZE=3
MATERIAL UNPICK

MATERIAL PICK '3 mu culinder'
MATERIAL OPTION=CGS MULINEARITY=LINEAR MUANISOTROPY=ISOTROPIC EPSANISOTROPY=ISOTROPIC SIGANISOTROPY=ISOTROPIC KAPANISOTROPY=ISOTROPIC
MATERIAL OPTION=MODIFY MULINEARITY=LINEAR MUANISOTROPY=ISOTROPIC MU=1 EPSANISOTROPY=ISOTROPIC SIGANISOTROPY=ISOTROPIC KAPANISOTROPY=ISOTROPIC
MATERIAL OPTION=MODIFY MULINEARITY=LINEAR MUANISOTROPY=ISOTROPIC MU=1 EPSANISOTROPY=ISOTROPIC SIGANISOTROPY=ISOTROPIC KAPANISOTROPY=ISOTROPIC
////////////////////////////////




////make cuts in 3 mu cylinder (initially a cut is created at +100 and copied 6 times avery 40cm) along Z axis ///

BLOCK Name=cut X0=-600 Y0=-600 Z0=100 X1=600 Y1=600 Z1=100
PICK OPTION=ADD, | PICK PROPERTY=Name LABEL='cut'
TRANSFORM OPTION=COPY TYPE=DISPLACE COUNT=6 DU=0 DV=0 DW=40
PICK OPTION=ADD, | PICK PROPERTY=Name LABEL='3 mu cylinder'
PICK OPTION=ADD, | PICK PROPERTY=Name LABEL='cut'
COMBINE OPERATION=SUBTRACT +REGULAR


////make cuts in 3 mu cylinder (at +/- 10,20,30,40 55) along X axis ///
BLOCK Name=cut X0=-600 Y0=-600 Z0=0 X1=600 Y1=600 Z1=0

//that is at XY plane. Rotate it at YZ plane (Rotation of 90 deg around Y axis)//
PICK OPTION=ADD, | PICK PROPERTY=Name LABEL='cut'
TRANSFORM OPTION=APPLY TYPE=ROTATE ROTU=0 ROTV=1 ROTW=0 ANGLE=90

PICK OPTION=ADD, | PICK PROPERTY=Name LABEL='cut'


// copy it at +10, +20,+30 and +40 cm //
TRANSFORM OPTION=COPY KEEP=YES TYPE=DISPLACE COUNT=4 DU=10 DV=0 DW=0

// copy it at +55 cm //
```

```
TRANSFORM OPTION=COPY KEEP=YES TYPE=DISPLACE COUNT=1 DU=55 DV=0 DW=0

// copy it at -10,-20,-30 and -40 cm //
TRANSFORM OPTION=COPY KEEP=YES TYPE=DISPLACE COUNT=4 DU=-10 DV=0 DW=0

// copy it at -55 cm //
TRANSFORM OPTION=COPY TYPE=DISPLACE COUNT=1 DU=-55 DV=0 DW=0

///Subtraction with regularisation //
PICK OPTION=ADD, | PICK PROPERTY=Name LABEL='3 mu cylinder'
PICK OPTION=ADD, | PICK PROPERTY=Name LABEL='cut'
COMBINE OPERATION=SUBTRACT +REGULAR
////////////////////////////////



////////////////////////////////
//COILS
////////////////////////////////

////////////////////////////////
//C8 (CURD=130 gives 7 Gauss @ the coils' position)
////////////////////////////////

RACETRACK OPTION=LOAD
RACETRACK OPTION=NEW -KEEP XP1=46 YP1=45 A=2 B=2 H1=0 R1=46 INCIRCUIT=NO CIRCUITELEMENT= CURD=61.1 TOLERANCE=1000 DRIVELABEL=ONE
LCNAME='Global coordinate //system' XCEN2=0 YCEN2=0 ZCEN2=0 THETA2=90 PHI2=180 PSI2=-90 RXY=0 RYZ=0 RZX=0 SYMMETRY=0
////////////////////////////////////



////////////////////////////////
//////// 1 Rectangular Coil along z axis - Design (with I=1.5x8.8 mA) (CURD=12.44 for 8.8 mA)
////////////////////////////////

//RACETRACK OPTION=LOAD
//RACETRACK OPTION=NEW -KEEP XP1=3.9 YP1=-24.8 A=0.054 B=10 H1=3.3 R1=0.01 INCIRCUIT=NO CIRCUITELEMENT= CURD=0 TOLERANCE=1000
//DRIVELABEL=ONE LCNAME='Global coordinate system' XCEN2=0 YCEN2=0 ZCEN2=0 THETA2=90 PHI2=180 PSI2=-90 RXY=0 RYZ=0 RZX=0
////////////////////////////////////



////////////////////////////////
//Dave's Coil (6WS end) (CURD=18 gives 1 Gauss on axis and at coil's plane)
////////////////////////////////

//RACETRACK OPTION=LOAD
//RACETRACK OPTION=NEW -KEEP XP1=100 YP1=-93.1 A=3 B=3 H1=0 R1=100 INCIRCUIT=NO CIRCUITELEMENT= CURD=0 TOLERANCE=1000 //DRIVELABEL=ONE
//LCNAME='Global coordinate system' XCEN2=0 YCEN2=0 ZCEN2=0 THETA2=90 PHI2=180 PSI2=-90 RXY=0 RYZ=0 RZX=0 SYMMETRY=0
////////////////////////////////////



////////////////////////////////
//Dave's Coil (HV end) (CURD=18 gives 1 Gauss on axis and at coil's plane)
////////////////////////////////

//RACETRACK OPTION=LOAD
//RACETRACK OPTION=NEW -KEEP XP1=100 YP1=-340 A=3 B=3 H1=0 R1=100 INCIRCUIT=NO CIRCUITELEMENT= CURD=0 TOLERANCE=1000 //DRIVELABEL=ONE
//LCNAME='Global coordinate system' XCEN2=0 YCEN2=0 ZCEN2=0 THETA2=90 PHI2=180 PSI2=-90 RXY=0 RYZ=0 RZX=0 SYMMETRY=0
////////////////////////////////////



////////////////////////////////////
//Solenoid//
//RACETRACK OPTION=LOAD
//RACETRACK OPTION=NEW -KEEP XP1=34.2 YP1=-351.3 A=0.077 B=262.7 H1=0 R1=34.2 INCIRCUIT=NO CIRCUITELEMENT= CURD=0.531 TOLERANCE=1000
DRIVELABEL=ONE LCNAME='Global coordinate system' XCEN2=0 YCEN2=0 ZCEN2=0 THETA2=90 PHI2=180 PSI2=-90 RXY=0 RYZ=0 RZX=0
```

```
////////////////////////////////////////

//6WS TC//
//RACETRACK OPTION=LOAD
//RACETRACK OPTION=NEW -KEEP XP1=30.5 YP1=-77.45 A=0.75 B=0.75 H1=0 R1=30.5 INCIRCUIT=NO CIRCUITELEMENT= CURD=5.1 TOLERANCE=1000
DRIVELABEL=ONE LCNAME='Global coordinate system' XCEN2=0 YCEN2=0 ZCEN2=0 THETA2=90 PHI2=180 PSI2=-90 RXY=0 RYZ=0 RZX=0,
//SYMMETRY=0
////////////////////////////////////


////////////////////////////
//background (QUARTER)
////////////////////////////

BLOCK Name=background X0=0 Y0=0 Z0=-150 X1=200 Y1=200 Z1=550


////////////////////////////
//make cuts on background
//
//15 totally:
//
//11 on z axis (every 100 cm (x2 every -100cm and x5 every +100cm))
//1 on x axis (z=0 rotated and copied to y=0)
//and 3 on y axis (z=0 rotated and copied to x=0)
////////////////////////////

//along z axis: first at +50 and then 10 copies avery 50cm//

BLOCK Name=cut X0=-1000 Y0=-1000 Z0=0 X1=1000 Y1=1000 Z1=0

//copy it 10 times//
PICK OPTION=ADD, | PICK PROPERTY=Name LABEL='cut'
TRANSFORM OPTION=COPY KEEP=YES TYPE=DISPLACE COUNT=2 DU=0 DV=0 DW=-50
TRANSFORM OPTION=COPY TYPE=DISPLACE COUNT=10 DU=0 DV=0 DW=50

PICK OPTION=ADD, | PICK PROPERTY=Name LABEL='background'
PICK OPTION=ADD, | PICK PROPERTY=Name LABEL='cut'
COMBINE OPERATION=SUBTRACT +REGULAR


//along x axis: rotate the inital block at x=0 and then copy it at +100//
BLOCK Name=cut X0=-1000 Y0=-1000 Z0=0 X1=1000 Y1=1000 Z1=0

//rotate it at x=0
PICK OPTION=ADD, | PICK PROPERTY=Name LABEL='cut'
TRANSFORM OPTION=APPLY TYPE=ROTATE ROTU=0 ROTV=1 ROTW=0 ANGLE=90

//copy it at +100cm
PICK OPTION=ADD, | PICK PROPERTY=Name LABEL='cut'
TRANSFORM OPTION=COPY TYPE=DISPLACE COUNT=1 DU=100 DV=0 DW=0

PICK OPTION=ADD, | PICK PROPERTY=Name LABEL='background'
PICK OPTION=ADD, | PICK PROPERTY=Name LABEL='cut'
COMBINE OPERATION=SUBTRACT +REGULAR

//along Y axis: rotate the inital block at x=0 and then copy it at +100//
BLOCK Name=cut X0=-1000 Y0=-1000 Z0=0 X1=1000 Y1=1000 Z1=0

//rotate it at y=0
PICK OPTION=ADD, | PICK PROPERTY=Name LABEL='cut'
TRANSFORM OPTION=APPLY TYPE=ROTATE ROTU=1 ROTV=0 ROTW=0 ANGLE=90

//copy it at
PICK OPTION=ADD, | PICK PROPERTY=Name LABEL='cut'
TRANSFORM OPTION=COPY KEEP=YES TYPE=DISPLACE COUNT=1 DU=0 DV=35 DW=0
```

```
TRANSFORM OPTION=COPY KEEP=YES TYPE=DISPLACE COUNT=1 DU=0 DV=65 DW=0
TRANSFORM OPTION=COPY KEEP=YES TYPE=DISPLACE COUNT=1 DU=0 DV=100 DW=0
TRANSFORM OPTION=COPY TYPE=DISPLACE COUNT=1 DU=0 DV=150 DW=0

PICK OPTION=ADD, | PICK PROPERTY=Name LABEL='background'
PICK OPTION=ADD, | PICK PROPERTY=Name LABEL='cut'
COMBINE OPERATION=SUBTRACT +REGULAR
////////////////////////////////////////



////////////////////////////////////////
//Create Model Body
////////////////////////////////////////

//MODEL CREATE
////////////////////////////////////////


////////////////////////////////////////
//Surface mesh size
////////////////////////////////////////

//MESH SIZE=7 NORMALTOL=30 SURFACETOL=0 TOLERANCE=1.0E-06
////////////////////////////////////////
```

Appendix B

SQUIDs effect on the B-field when placed inside the SCV

B.1 Placing the SQUID magnetometers inside the SCV

The SQUID magnetometers are very sensitive devices to e/m noise such that above a certain level prevents them from functionality. In our experiment, it has been proven impossible by now to protect them against it. One of the proposed solutions was to bring them inside the metallic SCV to reduce the RF noise that they pick-up. This idea though has a handicap; the SQUIDs sensor is encompassed by SC (Nb) parts that interact independently with the static field and the external magnetic fluctuations, effecting the homogeneity of the field seen by the neutrons within the RCs.

There were two questions that had to be answered before we proceed to this solution; a) how many SQUIDs can we have inside the SCV and b) what is the closest possible distance from the RCs that can be mounted, without distorting the **B** field more than the established by now limitations.

I approached the problem doing both Quick Field simulations and analytical calculations considering both of the possible cases where Nb parts go SC before and after a magnetic field is applied. The answers seem to be in a good agreement.

The actual mechanical design and the design that I used in my simulations are given in the following pictures.

B.1.1 5 μT Field Cooling

We first establish the holding field of 5 μT and then the Nb parts go SC. In this case the B flux is excluded from the bulk of the material that goes SC. In order to calculate this effect

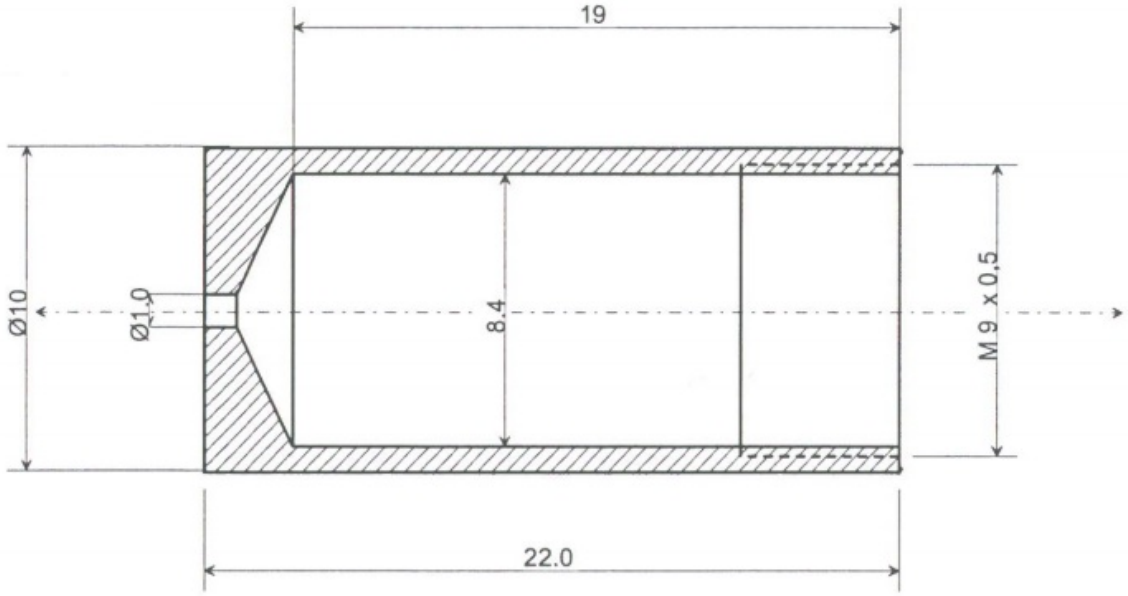

Figure B.1: The actual design of the SC Nb parts (cap and cylinder) of Supracon SQUID.

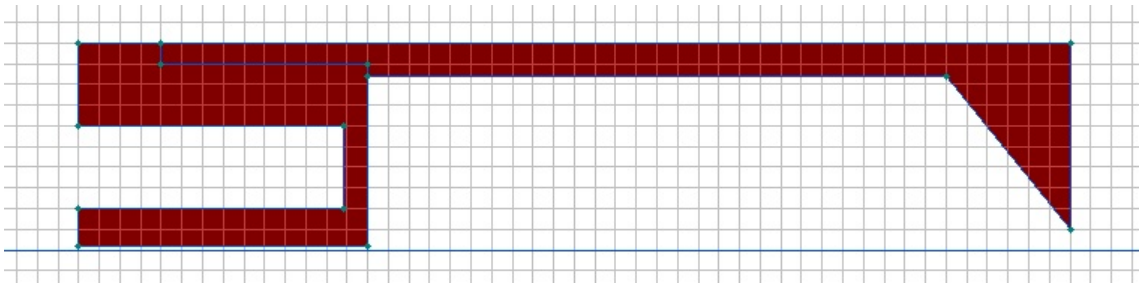

Figure B.2: The closest possible geometry to Nb parts of Supracon SQUID was introduced in Quick Filed program to find its effect to B field homogeneity within the RCs region. The above picture represents only the half part of the total volume of the SC item as Quick Field "reads" it with axis symmetry (w.r.t. the blue thin line at the bottom).

analytically, the volume of the Nb parts was roughly estimated and then "concentrated" to one solid cylinder of the same length (l=24mm).

Nb cap volume:

$$V_{cap} \simeq 446mm^3$$

Nb cylinder volume:

$$V_{cyl} \simeq 620mm^3$$

Total volume:

$$V = V_{cap} + V_{cyl} \simeq 1066mm^3$$

So the radius R of the imaginary solid cylinder is:

$$R = \sqrt{\frac{V}{\pi l}} \Rightarrow R = 3.8mm$$

and the cross section area of it is:

$$A = \pi R^2 = 4.5 \cdot 10^{-5} m^2$$

The flux passing through that area for B=5μT is:

$$\Phi = \vec{B_o} \times \vec{A} = 2.2 \cdot 10^{-10}\, Wb$$

In order to simulate the effect of the screening currents of the SC cap+cylinder of the SQUID to the magnetic field inside the RCs, we calculate the value of Ampere· turns of a solenoid which has the same length (l=24mm) and produces equal and opposite magnetic flux to that penetrating the solenoid at z=-l/2=-0.012m.

The axial field of a finite solenoid is given by:

$$B_z = \frac{\mu_o (N \cdot I)\alpha}{4\pi l} \int_0^{2\pi} \frac{\alpha - r\cos\theta}{\alpha^2 + r^2 - 2\alpha r \cos\theta} \cdot$$

$$\cdot \left(\frac{z + l/2}{\sqrt{\alpha^2 + r^2 - 2\alpha r\cos\theta + (z + l/2)^2}} - \frac{z - l/2}{\sqrt{\alpha^2 + r^2 - 2\alpha r\cos\theta + (z - l/2)^2}} \right) d\theta$$

where:

$$\frac{\mu_o (N \cdot I)\alpha}{4\pi l} = 1.6 \cdot 10^{-8} (N \cdot I)$$

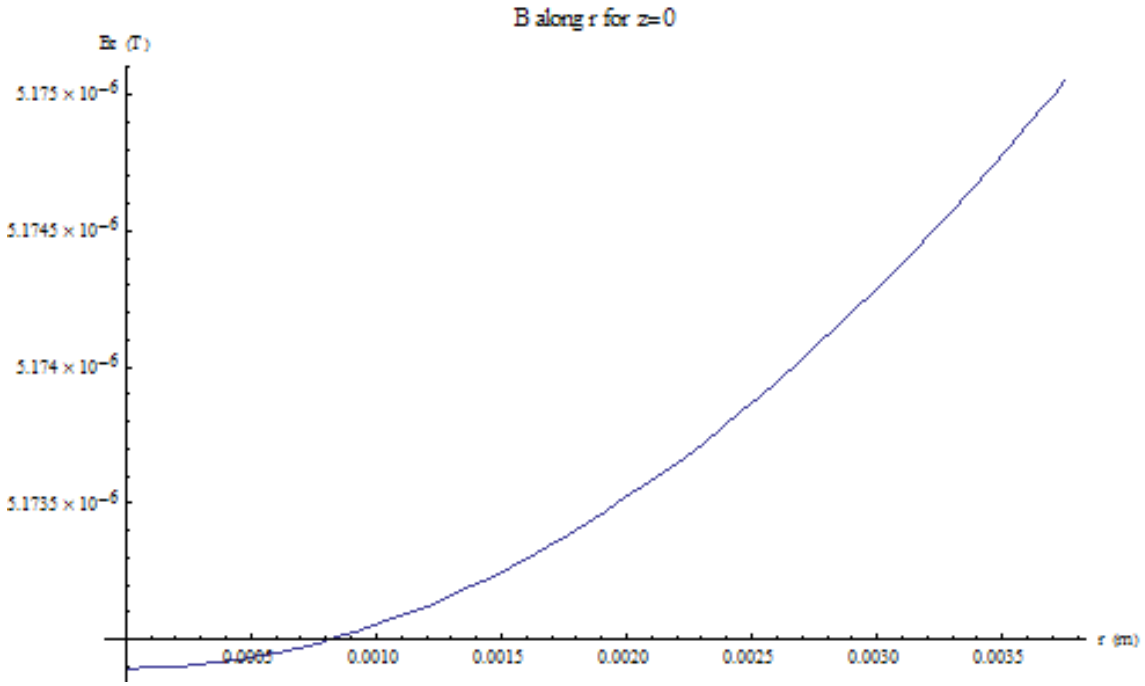

Figure B.3: Solenoid Bz field along r for z at the end of the solenoid (z=-l/2) for the case of 5μT field cooling.

The Bz = f(r) at z=-0.012 is given at Figure 4.13 and the integral of this function over all the cross section area gives us the total flux produced by the solenoid at its end.

The flux is given by:

$$\Phi_{sol} = \int_{r=0}^{3.8\cdot10^{-3}} Bz \cdot (2\pi r)\, dr$$

For:

$$\Phi_{sol} = -\Phi_{ext}$$

we get: $N \cdot I = 0.105A \cdot turns$ and for N = 5 dipoles (at distance 24mm/4=6mm):

$$m = I \cdot A = 9.3 \cdot 10^{-7} Am^2 \text{ for each dipole.}$$

The magnetic field produced by a magnetic moment is given by:

$$B(\vec{r}) = \frac{\mu_o}{4\pi} \cdot \frac{3\vec{r}(\vec{m}\vec{r}) - \vec{m}r^2}{r^5}$$

In our case we consider $\vec{m}$ along z, so:

$$B_z(x,y,z) = \frac{\mu_o}{4\pi} 3m \frac{(z^2 - \frac{x^2+y^2+z^2}{3})}{(x^2+y^2+z^2)^{5/2}}$$

With z being the distance from the plane of the 1st dipole:

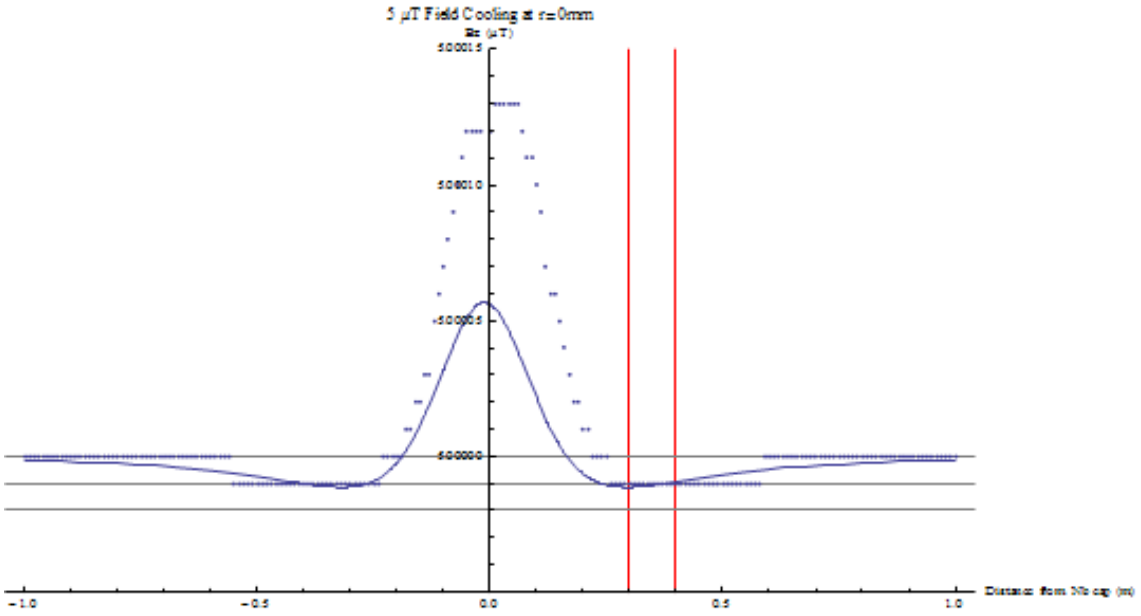

Figure B.4: Bz field on axis (r=0) caused by Nb parts of SQUID magnetometer when it is placed 250 mm away from central axis, at 5 μT field cooling. According to QF (dots)+analytical solution (solid line): dBz/dz=0.02nT/m within RCs volume (red lines).

$$Bz(total) = \sum_{i=1}^{5} Bz_i$$

where:

$$Bz_i = \frac{\mu_o}{4\pi} 3m \frac{[z+(n-i)6\cdot10^{-3}]^2 - \frac{[x^2+y^2+(z+(n-i)6\cdot10^{-3})]^2}{3}}{[x^2+y^2+(z+(n-i)6\cdot10^{-3})]^{5/2}} \text{ for i=1,2..5.}$$

The results of the analytical calculations and from Quick Field are shown to the following plots. When one single SQUID is placed at the further possible distance from RCs (250mm from central axis and 300mm from RCs along z axis) the distortion of B homogeneity seems to be negligible along the central axis, but reaches our limitations at the boundaries of the storage cells.

If one SQUID is placed 90mm closer to the central axis (at r=160mm but still 300mm away from RCs along z axis) then the distortion according to Quick Field just exceeds our restrictions.

B.1.2 Zero Field Cooling and 1 nT magnetic fluctuation

In this case the Nb parts are SC before a fluctuation of 1 nT occurs. The diameter of Nb cap + cylinder is ϕ= 5·10^{-3}m so the cross section area is A = πR^2= 7.85 10^{-5}m^2 and the flux penetrating it is:

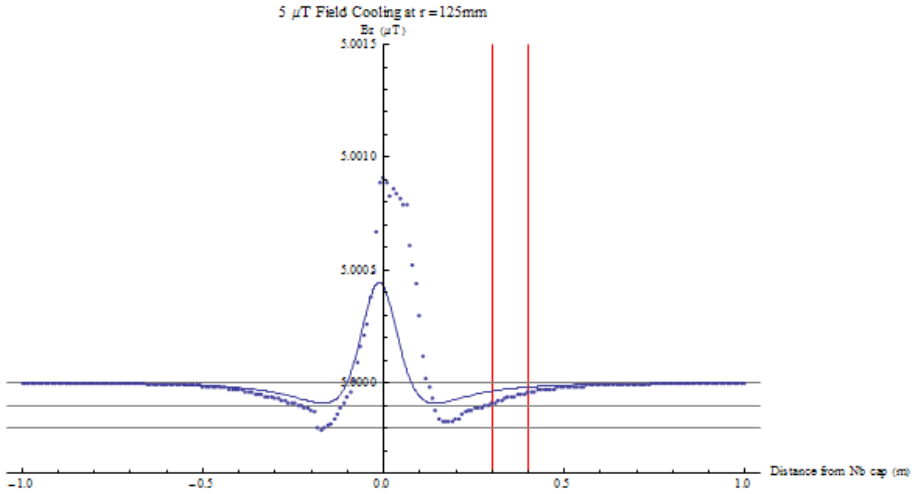

Figure B.5: Bz field at r=125mm off axis caused by Nb parts of SQUID magnetometer when it is placed 250 mm away from central axis, at 5 μT field cooling. According to QF (dots) dBz/dz=1nT/m while the analytical solution (solid line) gives gradient of dBz/dz=0.5nT/m within RCs volume (red lines).

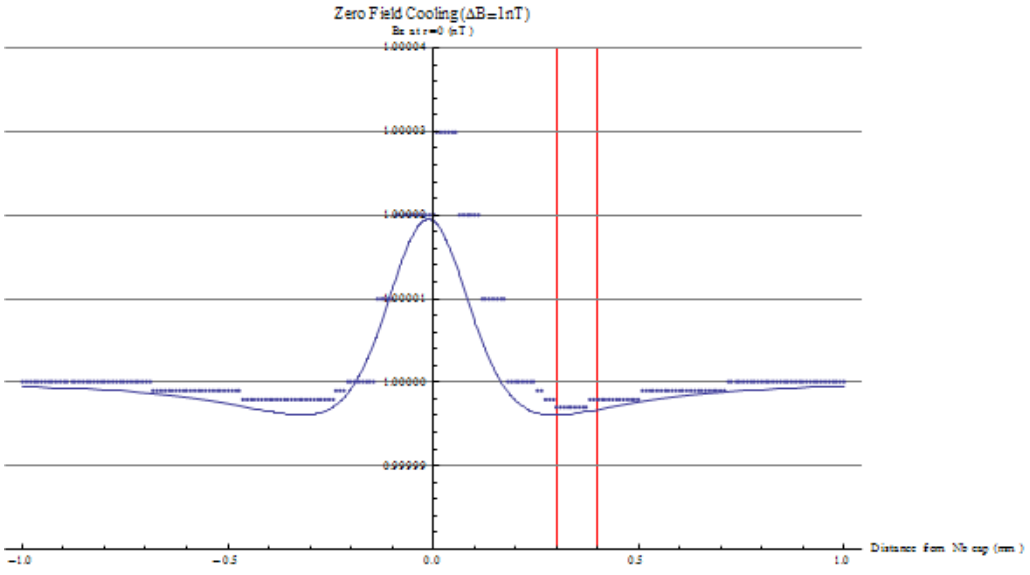

Figure B.6: Bz field at r=125mm off axis caused by Nb parts of SQUID magnetometer when it is placed 160 mm away from central axis, at 5 μT field cooling. According to QF (dots) dBz/dz=1.1nT/m while the analytical solution (solid line) gives gradient of dBz/dz=0.5nT/m within RCs volume (red lines).

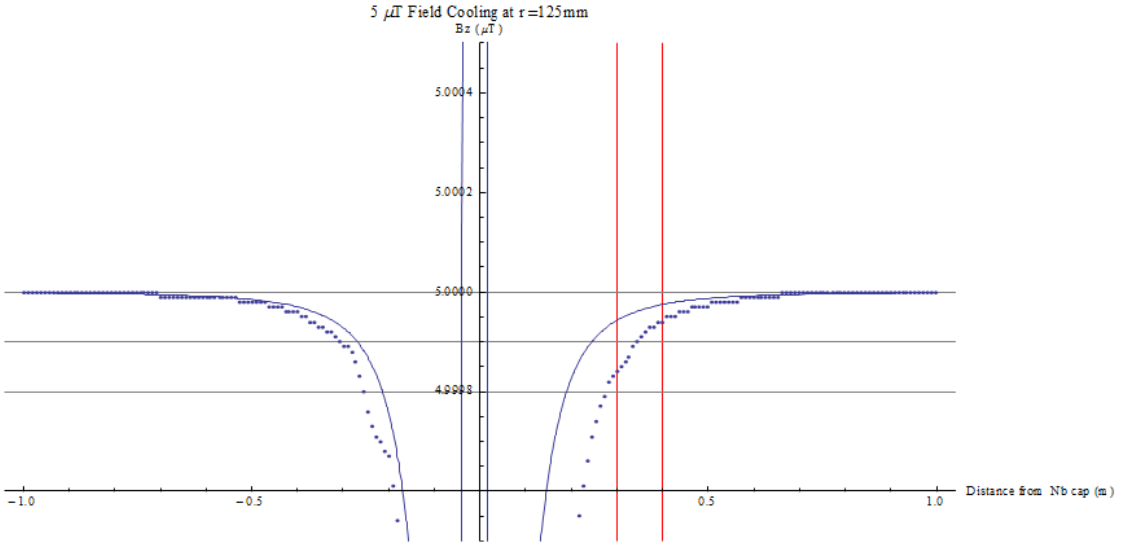

Figure B.7: Solenoid Bz field along r for z at the end of the solenoid (z=-l/2) for the case of zero field cooling.

$$\Phi = \vec{B_o} \times \vec{A} = 7.85 \cdot 10^{-14}\, Wb$$

Following the same procedure as for the 5 μT field cooling case, we simulate the effect of the screening currents of the SC cap+cylinder of the SQUID to the magnetic field inside the RCs, by calculating first the value of Ampere·turns of a solenoid which has the same length (l=24mm) and produces equal and opposite magnetic flux to that penetrating the solenoid at z=-l/2=-0.012m.

Here we have:

$$\frac{\mu_o (N \cdot I)\alpha}{4\pi l} = 2.08 \cdot 10^{-8} (N \cdot I)$$

The flux is given again by:

$$\Phi_{sol} = \int_{r=0}^{5 \cdot 10^{-3}} Bz \cdot (2\pi r)\, dr$$

And for:

$$\Phi_{sol} = -\Phi_{ext}$$

we get: $N \cdot I = 3.9 \cdot 10^{-5} A \cdot turns$ and for N = 5 dipoles (at distance 24mm/4=6mm):

$$m = I \cdot A = 6.13 \cdot 10^{-10} Am^2 \text{ of each dipole.}$$

Finally we get the total B by adding the contribution of all the 5 dipoles:

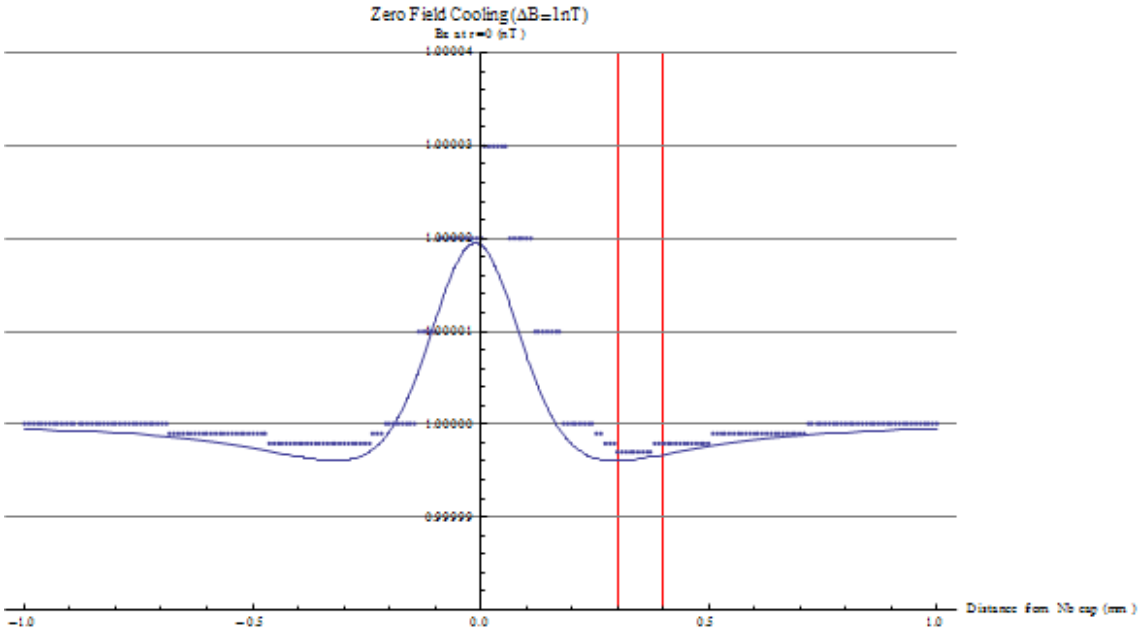

Figure B.8: Bz field on axis (r=0) caused by Nb parts of SQUID magnetometer when it is placed 250 mm away from central axis, at zero field cooling and when 1nT external magnetic fluctuation occurs. According to QF (dots)+analytical solution (solid line): dBz/dz=0.01nT/m within RCs volume (red lines).

$$Bz(total) = \sum_{i=1}^{5} Bz_i$$

The results of these calculations compared with that of Quick Field is given in Plot 9. The gradient of the axial component within the RCs seems to be well below our limitations.

Conclusively, we can say that we could try to place one single SQUID magnetometer inside the SCV at the furthest possible position from RCs (at r=250mm and z=300mm) without distorting the field homogeneity above to what is allowed.

Appendix C

SQUIDs mounts drawing

SQUIDs mounts drawing: Doc # 579

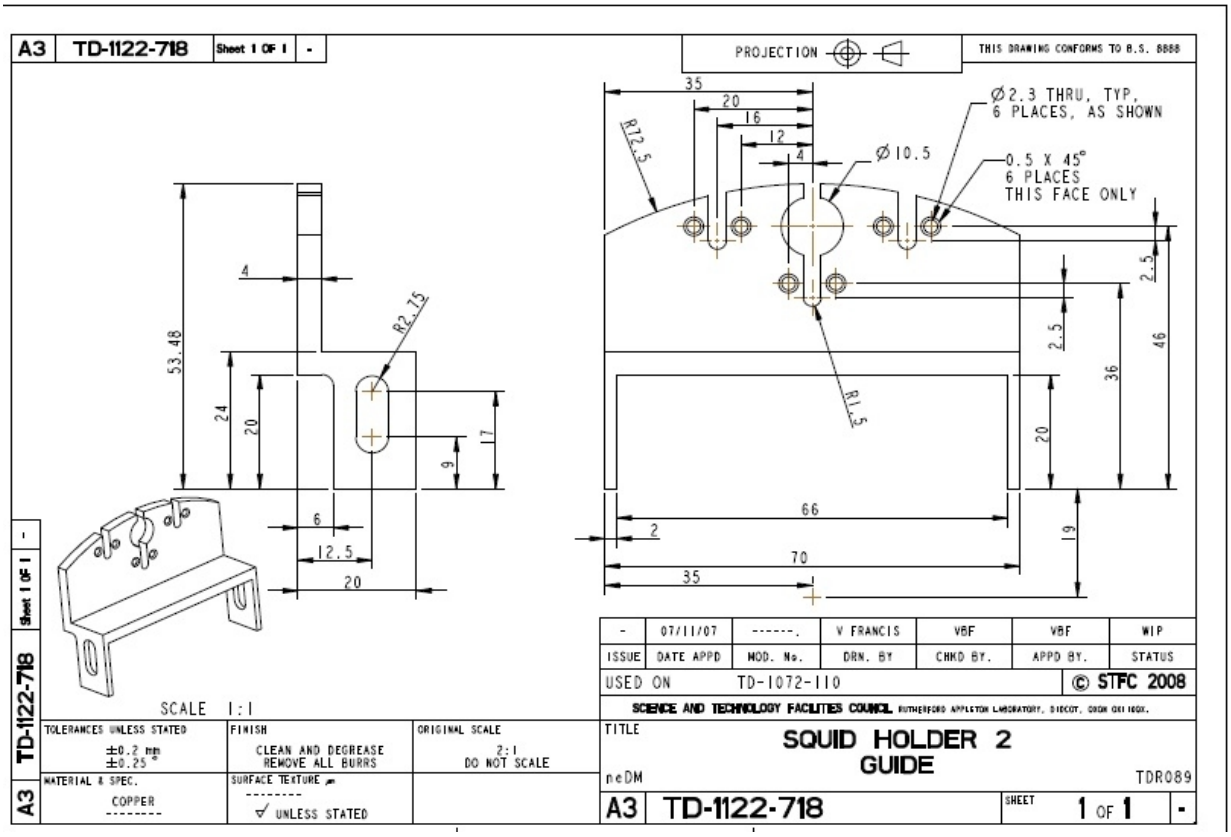

Figure C.1: SQUIDs mounts drawing

Appendix D

Drawings of the $1/12^{th}$ scale model components

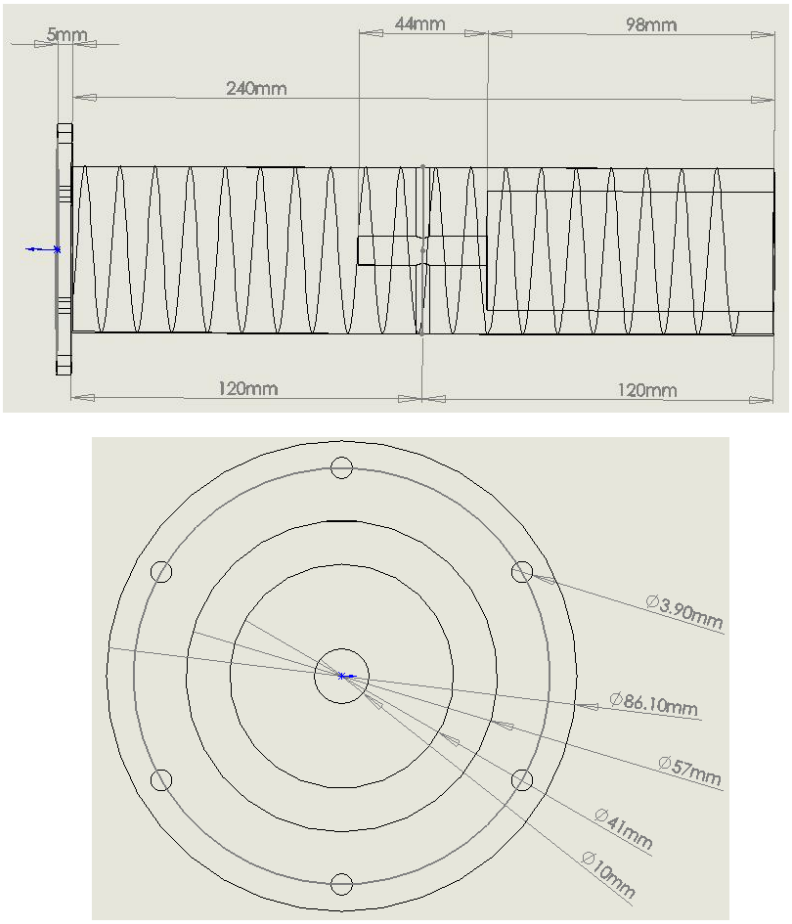

Figure D.1: The dural former which accommodated the outer Pb shield/solenoid of the $1/12^{th}$ scale model.

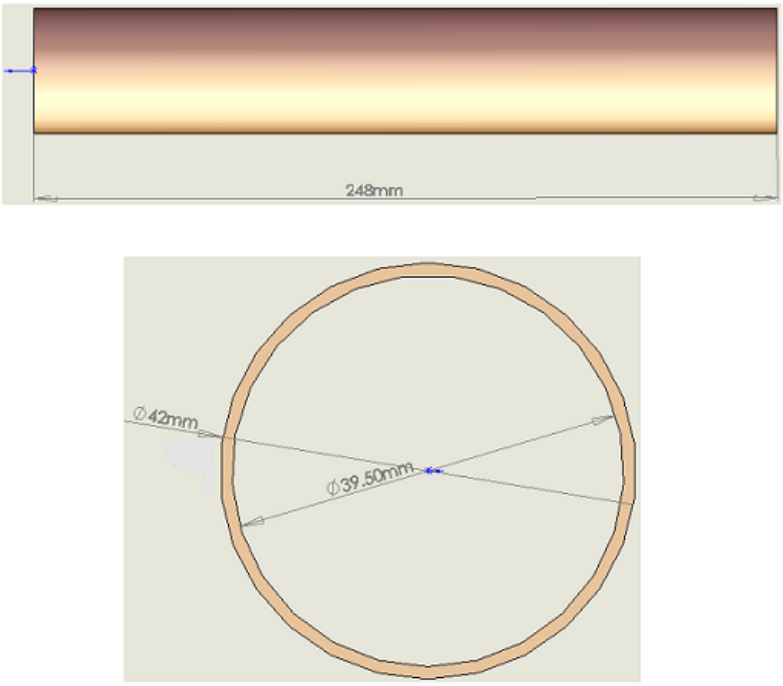

Figure D.2: The Copper Tube used as a base for the ISS of the scale model.

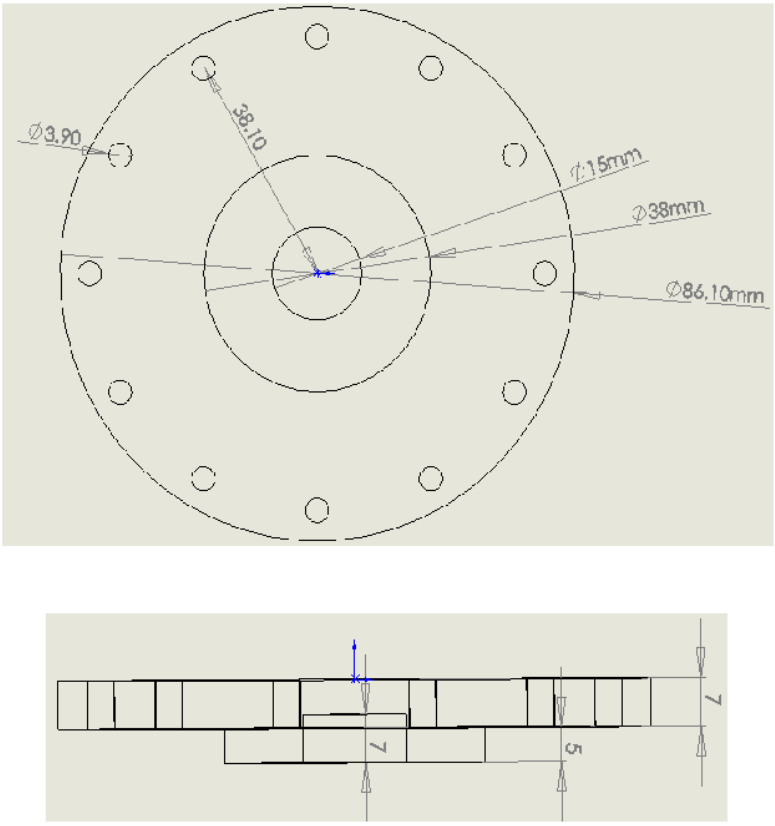

Figure D.3: The mounting flange brazed on the Copper tube.

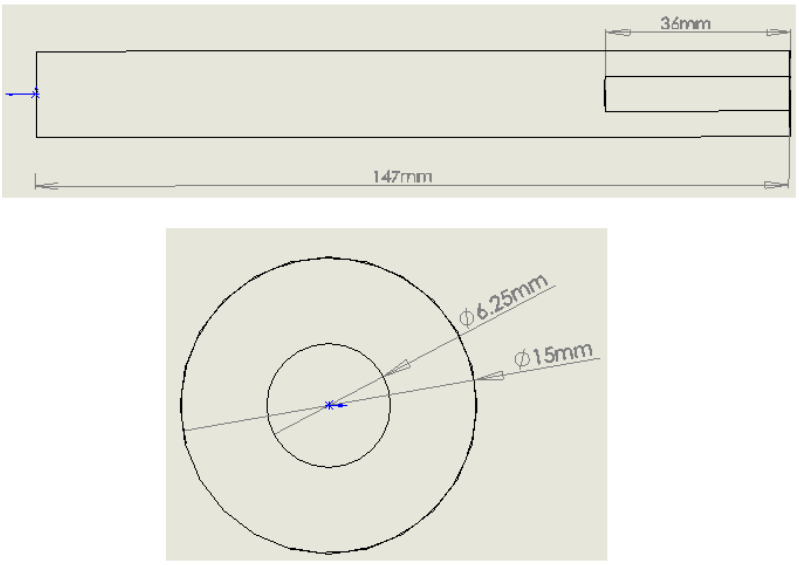

Figure D.4: The Aluminium rod that the fluxgate sensor was inserted to.

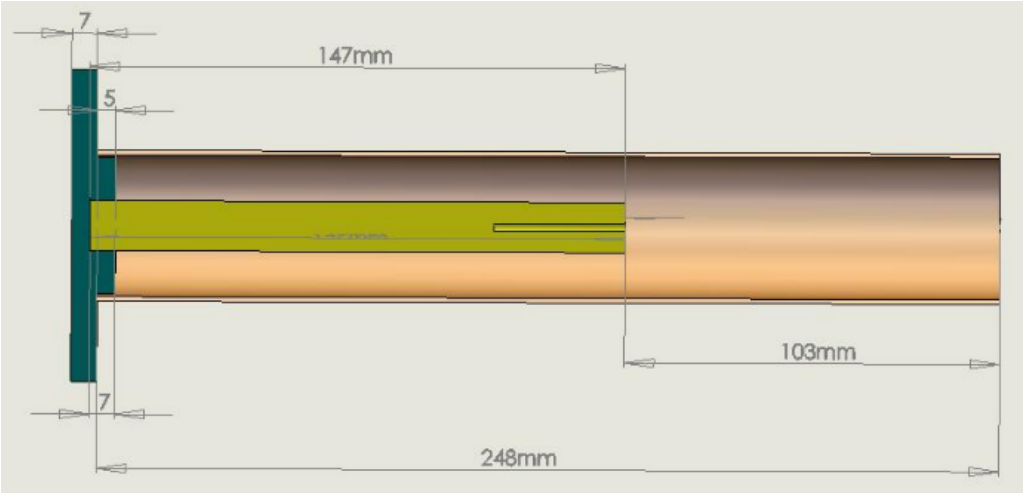

Figure D.5: The assembly of the Copper tube with the mounting flange on the top and the fluxgate accommodation rod in the middle.

Appendix E

Mathematica Code for SCV B-field mapping

```
(*  Structure
  A. Import Data
  B. Select data for 3 fg's in the form (r,θ,z,Bz)
  Γ. θ correction (+20deg/-55deg)
  Δ. 2D Plots -  θ / z slices (Data Selection - Plots/Exports)
  E. 3D Plots -  rθ / zθ/ rz slices (Data Selection - Plots/Exports)
*)
```

```
(*
   A. Import Data:
       At first (as a check),
give the first few and the last line of the DataFile -
 including the headings.
       Then import ALL the rows in "DataFile".
*)
```

```
Import["nEDM\\Data\\Mag Scans\\SCV_Below_Tc\\SCV_Below_Tc.xls", {"Data", 1,
   {7, 8, 9, 10, 11, 659}, {34, 36, 12, 24, 16, 20, 44, 109, 110, 111}}] // Grid
```

Theta Manual [degrees]	z Manual [cm]	FG_Z0_R0_Blue [uT]	FG_Z0_R75_Red [uT]	FG_Z0_R150_Yellow [uT]	FG_G10_Black [uT]	External_FG_Y [uT]	Rblue	Rred	Ryellow
-180.	0.	-0.131048	-0.158295	-0.316264	-0.111812	-6.5551	0.	0.075	0.15
-165.	0.	-0.131186	-0.119698	-0.337813	-0.113036	-6.55152	0.	0.075	0.15
-150.	0.	-0.131377	-0.110593	-0.282769	-0.113035	-6.54935	0.	0.075	0.15
-135.	0.	-0.131983	-0.129729	-0.261345	-0.113134	-6.55405	0.	0.075	0.15
-180.	50.	0.0407658	0.0453242	0.0868619	-0.111998	-6.5403	0.	0.075	0.15

```
DataFile = Import["nEDM\\Data\\Mag Scans\\8 July
     2010\\magscan_dat_20100708152944_Optimasation_3.xls",
   {"Data", 1, Range[7, 286], {34, 36, 12, 24, 16, 20, 44, 109, 110, 111}}];
```

```
(*
   B. Select the row data of all the 5
 fluxgates seperately in the form of (r,θ,z,Bz)
*)
```

```
BlueFG = DataFile[[All, {8, 1, 2, 3}]]; RedFG = DataFile[[All, {9, 1, 2, 4}]];
YellowFG = DataFile[[All, {10, 1, 2, 5}]];
BlackFG = DataFile[[All, {1, 2, 6}]]; ExtYFG = DataFile[[All, {1, 2, 7}]];
```

```
(*
  Γβ. θ correction (-50 deg)
*)
```

```
(* Isolate only θ=0 for 20<z<40 and introduce theta correction *)
```

```
T0θ20z40 = Table[{_, 0., z, _}, {z, 20., 40., 2.}];
B0θ20z40row = Table[Cases[BlueFG, T0θ20z40[[w]]], {w, 1, 11}];
R0θ20z40row = Table[Cases[RedFG, T0θ20z40[[w]]], {w, 1, 11}];
Y0θ20z40row = Table[Cases[YellowFG, T0θ20z40[[w]]], {w, 1, 11}];
```

```
Bm50θ20z40 =
 Table[B0θ20z40row[[j]] + Table[{0, -50 * 1^k, 0, 0}, {k, 1, 1}], {j, 1, 11}];
Rm50θ20z40 = Table[R0θ20z40row[[j]] + Table[{0, -50 * 1^k, 0, 0}, {k, 1, 1}],
  {j, 1, 11}]; Ym50θ20z40 =
 Table[Y0θ20z40row[[j]] + Table[{0, -50 * 1^k, 0, 0}, {k, 1, 1}], {j, 1, 11}];
```

```
(*Isolate each θ seperately for all z
 It is (R O W values): θ1=-180, θ2=-165, θ3=-150, θ4=-135,
θ5=-120, θ6=-105, θ7=-90, θ8=-75, θ9=-60, θ10=-45, θ11=-30, θ12=-15
                                                    θ13=0,
    θ14=15, θ15=30, θ16=45, θ17=60, θ18=75, θ19=90,
θ20=105, θ21=120, θ22=135, θ23=150 θ24=165 θ25=180 θ24=165 θ25=180
 *)
```

```
Tθ = Table[{_, θ, _, _}, {θ, -180., 180., 15.}];
Tθb = Table[{θ, _, _}, {θ, -180., 180., 15.}];
Bθrow = Table[Cases[BlueFG, Tθ[[w]]], {w, 1, 25}];
Rθrow = Table[Cases[RedFG, Tθ[[w]]], {w, 1, 25}];
Yθrow = Table[Cases[YellowFG, Tθ[[w]]], {w, 1, 25}];
Blackθrow = Table[Cases[BlackFG, Tθb[[w]]], {w, 1, 25}];
ExtYθrow = Table[Cases[ExtYFG, Tθb[[w]]], {w, 1, 25}];
```

```
Sizeθs = Table[Length[Bθrow[[w]]], {w, 1, 25}];
```

```
Bθm50 = Join[Table[Bθrow[[j]] +
      Table[{0, -50 * 1^k + 360, 0, 0}, {k, 1, Sizeθs[[j]]}], {j, 1, 4}], Table[
    Bθrow[[m]] + Table[{0, -50 * 1^l, 0, 0}, {l, 1, Sizeθs[[m]]}], {m, 5, 25}]];
Rθm50 = Join[Table[Rθrow[[j]] + Table[{0, -50 * 1^k + 360, 0, 0},
     {k, 1, Sizeθs[[j]]}], {j, 1, 4}],
  Table[Rθrow[[m]] + Table[{0, -50 * 1^l, 0, 0}, {l, 1, Sizeθs[[m]]}], {m, 5, 25}]];
Yθm50 = Join[Table[Yθrow[[j]] +
     Table[{0, -50 * 1^k + 360, 0, 0}, {k, 1, Sizeθs[[j]]}], {j, 1, 4}], Table[
   Yθrow[[m]] + Table[{0, -50 * 1^l, 0, 0}, {l, 1, Sizeθs[[m]]}], {m, 5, 25}]];
Blackθm50 = Join[Table[Blackθrow[[j]] +
      Table[{-50 * 1^k + 360, 0, 0}, {k, 1, Sizeθs[[j]]}], {j, 1, 4}], Table[
    Blackθrow[[m]] + Table[{-50 * 1^l, 0, 0}, {l, 1, Sizeθs[[m]]}], {m, 5, 25}]];
ExtYθm50 = Join[Table[ExtYθrow[[j]] + Table[{-50 * 1^k + 360, 0, 0},
       {k, 1, Sizeθs[[j]]}], {j, 1, 4}], Table[
    ExtYθrow[[m]] + Table[{-50 * 1^l, 0, 0}, {l, 1, Sizeθs[[m]]}], {m, 5, 25}]];
```

Δ. 2 D Plots

θ slices

```
(* The 25 θ slices (fixed θ along z) are Bθ20,
Rθ20 and Yθ20. Remember we have taken +180 and -180 seperately,
that's why we have 25 and not 24 angles.. *)
```

```
(* I select from {r,θ,z,Bz} only the {z,Bz} for given θ and for each fluxgate
 in order to produce the 2D Plots of θ slices (along z for fixed θ) *)
```

```
Bθm50;
```

```
BθzBz = Table[Bθm50[[j, All, {3, 4}]], {j, 1, 25}];
RθzBz = Table[Rθm50[[j, All, {3, 4}]], {j, 1, 25}];
YθzBz = Table[Yθm50[[j, All, {3, 4}]], {j, 1, 25}];
```

```
(* +20 deg θ correction table *)
```

```
θm50a = Table[q "deg", {q, 130, 175, 15}];
θm50b = Table[w "deg", {w, -170, 130, 15}]; θm50 = Join[θm50a, θm50b];
```

```
(* Table with all theta slices for the 3 fluxgates *)
```

```
<< PlotLegends`
```

```
Plotθm50 = Table[ListPlot[{BθzBz[[q]], RθzBz[[q]], YθzBz[[q]]},
    PlotLabel → "SCV B Field Below 9 K" Evaluate[θm50[[q]]],
    AxesLabel → {"z[cm]", "Bz[μT]"}, PlotRange → {-5.09, -4.95},
    PlotStyle → {{Blue, PointSize[0.007]},
      {Red, PointSize[0.007]}, {Darker[Yellow], PointSize[0.007]}},
    GridLines → {{{24, Dashed}, {36, Dashed}}, None},
    PlotLegend → {"r = 0 m", "r = 0.075 m", "r = 0.15 m"},
    LegendSize → 0.3, LegendPosition → {0.8, 0.3}, LegendShadow → None,
    LegendBorder → None, LegendTextSpace → 7.3], {q, 1, 25}]
```

```
Export["nEDM\\Data\\Mathematica_Plots\\2D_axial\\θ=-180-50 deg.pdf", Plotθm50[[1]]];
Export["nEDM\\Data\\Mathematica_Plots\\2D_axial\\θ=-165-50 deg.pdf", Plotθm50[[2]]];
Export["nEDM\\Data\\Mathematica_Plots\\2D_axial\\θ=-150-50 deg.pdf", Plotθm50[[3]]];
Export["nEDM\\Data\\Mathematica_Plots\\2D_axial\\θ=-135-50 deg.pdf", Plotθm50[[4]]];
Export["nEDM\\Data\\Mathematica_Plots\\2D_axial\\θ=-120-50 deg.pdf", Plotθm50[[5]]];
Export["nEDM\\Data\\Mathematica_Plots\\2D_axial\\θ=-105-50 deg.pdf", Plotθm50[[6]]];
Export["nEDM\\Data\\Mathematica_Plots\\2D_axial\\θ=-90-50 deg.pdf", Plotθm50[[7]]];
Export["nEDM\\Data\\Mathematica_Plots\\2D_axial\\θ=-75-50 deg.pdf", Plotθm50[[8]]];
Export["nEDM\\Data\\Mathematica_Plots\\2D_axial\\θ=-60-50 deg.pdf", Plotθm50[[9]]];
Export["nEDM\\Data\\Mathematica_Plots\\2D_axial\\θ=-45-50 deg.pdf", Plotθm50[[10]]];
Export["nEDM\\Data\\Mathematica_Plots\\2D_axial\\θ=-30-50 deg.pdf", Plotθm50[[11]]];
Export["nEDM\\Data\\Mathematica_Plots\\2D_axial\\θ=-15-50 deg.pdf", Plotθm50[[12]]];
Export["nEDM\\Data\\Mathematica_Plots\\2D_axial\\θ=0-50 deg for all z.pdf", Plotθm50[[13]]];
Export["nEDM\\Data\\Mathematica_Plots\\2D_axial\\θ=15-50 deg.pdf", Plotθm50[[14]]];
Export["nEDM\\Data\\Mathematica_Plots\\2D_axial\\θ=30-50 deg.pdf", Plotθm50[[15]]];
Export["nEDM\\Data\\Mathematica_Plots\\2D_axial\\θ=45-50 deg.pdf", Plotθm50[[16]]];
Export["nEDM\\Data\\Mathematica_Plots\\2D_axial\\θ=60-50 deg.pdf", Plotθm50[[17]]];
Export["nEDM\\Data\\Mathematica_Plots\\2D_axial\\θ=75-50 deg.pdf", Plotθm50[[18]]];
Export["nEDM\\Data\\Mathematica_Plots\\2D_axial\\θ=90-50 deg.pdf", Plotθm50[[19]]];
Export["nEDM\\Data\\Mathematica_Plots\\2D_axial\\θ=105-50 deg.pdf", Plotθm50[[20]]];
Export["nEDM\\Data\\Mathematica_Plots\\2D_axial\\θ=120-50 deg.pdf", Plotθm50[[21]]];
Export["nEDM\\Data\\Mathematica_Plots\\2D_axial\\θ=135-50 deg.pdf", Plotθm50[[22]]];
Export["nEDM\\Data\\Mathematica_Plots\\2D_axial\\θ=150-50 deg.pdf", Plotθm50[[23]]];
Export["nEDM\\Data\\Mathematica_Plots\\2D_axial\\θ=165-50 deg.pdf", Plotθm50[[24]]];
Export["nEDM\\Data\\Mathematica_Plots\\2D_axial\\θ=180-50 deg.pdf", Plotθm50[[25]]];
```

```
(* ROW θ=0 for 20<z<40 only *)
```

```
Plot0θm50 = ListPlot[{Bm50θ20z40[[All, 1]][[All, {3, 4}]],
     Rm50θ20z40[[All, 1]][[All, {3, 4}]], Ym50θ20z40[[All, 1]][[All, {3, 4}]]},
    AxesLabel → {"z[cm]", "Bz[μT"}, PlotLabel → "SCV B Field Below 9 K",
    PlotRange → {-5.09, -4.95}, PlotStyle → {{Blue, PointSize[0.007]},
      {Red, PointSize[0.007]}, {Darker[Yellow], PointSize[0.007]}},
    GridLines → {{{24, Dashed}, {36, Dashed}}, None},
    PlotLegend → {"r = 0 m", "r = 0.075 m", "r = 0.15 m"},
    LegendSize → 0.3, LegendPosition → {0.8, 0.3},
    LegendShadow → None, LegendBorder → None, LegendTextSpace → 7.3];
```

```
Export["nEDM\\Data\\Mathematica_Plots\\2D_axial\\θ=0+50 deg.pdf", Plot0θm50];
```

z slices

```
Tz = Table[{_, _, z, _}, {z, 0., 50., 2.}];
Tzb = Table[{_, z, _}, {z, 0., 50., 2.}];
```

```
(* Make the z slices *)

Bz = Table[Table[Cases[Bθm50[[k, All]], Tz[[q]]], {k, 1, 25}], {q, 1, 26}];
Rz = Table[Table[Cases[Rθm50[[k, All]], Tz[[q]]], {k, 1, 25}], {q, 1, 26}];
Yz = Table[Table[Cases[Yθm50[[k, All]], Tz[[q]]], {k, 1, 25}], {q, 1, 26}];
Blackz =
  Table[Table[Cases[Blackθm50[[k, All]], Tzb[[q]]], {k, 1, 25}], {q, 1, 26}];
ExtYz = Table[Table[Cases[ExtYθm50[[k, All]], Tzb[[q]]], {k, 1, 25}],
   {q, 1, 26}];

(* Select (θ,Bz) for fixed z -for all the 5 fluxgates *)

BzθBzt = Table[Bz[[q]][[All, 1]][[All, {2, 4}]], {q, 1, 26}];
RzθBzt = Table[Rz[[q]][[All, 1]][[All, {2, 4}]], {q, 1, 26}];
YzθBzt = Table[Yz[[q]][[All, 1]][[All, {2, 4}]], {q, 1, 26}];
BlackBzt = Table[Blackz[[q]][[All, 1]][[All, {1, 3}]], {q, 1, 26}];
ExtYBzt = Table[ExtYz[[q]][[All, 1]][[All, {1, 3}]], {q, 1, 26}];

Tza = Table[q "cm", {q, 0, 50, 2}];

(* Table with all z slices for the 3 fluxgates *)

Plotz = Table[ListPlot[{BzθBzt[[q]], RzθBzt[[q]], YzθBzt[[q]]},
    PlotLabel → "SCV B Field Below 9 K" Evaluate[Tza[[q]]],
    AxesLabel → {"θ [deg]", "Bz[μT]"}, PlotRange → {-5.09, -4.95},
    PlotStyle → {{Blue, PointSize[0.007]},
      {Red, PointSize[0.007]}, {Darker[Yellow], PointSize[0.007]}},
    PlotLegend → {"r = 0 m", "r = 0.075 m", "r = 0.15 m"},
    LegendSize → 0.3, LegendPosition → {0.8, 0.3}, LegendShadow → None,
    LegendBorder → None, LegendTextSpace → 7.3], {q, 1, 26}];

(*Export[
 "nEDM\\Mag scans May-July 2010\\Data_Mag Scans\\pdf_files\\2D_angular\\z=0.pdf",Plotz[[1]]];
Export["nEDM\\Mag scans May-July 2010\\Data_Mag Scans\\pdf_files\\2D_angular\\z=2cm.pdf",
 Plotz[[2]]];
Export["nEDM\\Mag scans May-July 2010\\Data_Mag Scans\\pdf_files\\2D_angular\\z=4cm.pdf",
 Plotz[[3]]];
Export["nEDM\\Mag scans May-July 2010\\Data_Mag Scans\\pdf_files\\2D_angular\\z=6cm.pdf",
 Plotz[[4]]];
Export["nEDM\\Mag scans May-July 2010\\Data_Mag Scans\\pdf_files\\2D_angular\\z=8cm.pdf",
 Plotz[[5]]];
Export["nEDM\\Mag scans May-July 2010\\Data_Mag Scans\\pdf_files\\2D_angular\\z=10cm.pdf",
 Plotz[[6]]];
Export["nEDM\\Mag scans May-July 2010\\Data_Mag Scans\\pdf_files\\2D_angular\\z=12cm.pdf",
 Plotz[[7]]];
Export["nEDM\\Mag scans May-July 2010\\Data_Mag Scans\\pdf_files\\2D_angular\\z=14cm.pdf",
 Plotz[[8]]];
Export["nEDM\\Mag scans May-July 2010\\Data_Mag Scans\\pdf_files\\2D_angular\\z=16cm.pdf",
 Plotz[[9]]];
Export["nEDM\\Mag scans May-July 2010\\Data_Mag Scans\\pdf_files\\2D_angular\\z=18cm.pdf",
 Plotz[[10]]];*)
```

```
Export["nEDM\\Data\\Mathematica_Plots\\2D_angular\\z=20cm.pdf", Plotz[[11]]];
Export["nEDM\\Data\\Mathematica_Plots\\2D_angular\\z=22cm.pdf", Plotz[[12]]];
Export["nEDM\\Data\\Mathematica_Plots\\2D_angular\\z=24cm.pdf", Plotz[[13]]];
Export["nEDM\\Data\\Mathematica_Plots\\2D_angular\\z=26cm.pdf", Plotz[[14]]];
Export["nEDM\\Data\\Mathematica_Plots\\2D_angular\\z=28cm.pdf", Plotz[[15]]];
Export["nEDM\\Data\\Mathematica_Plots\\2D_angular\\z=30cm.pdf", Plotz[[16]]];
Export["nEDM\\Data\\Mathematica_Plots\\2D_angular\\z=32cm.pdf", Plotz[[17]]];
Export["nEDM\\Data\\Mathematica_Plots\\2D_angular\\z=34cm.pdf", Plotz[[18]]];
Export["nEDM\\Data\\Mathematica_Plots\\2D_angular\\z=36cm.pdf", Plotz[[19]]];
Export["nEDM\\Data\\Mathematica_Plots\\2D_angular\\z=38cm.pdf", Plotz[[20]]];
Export["nEDM\\Data\\Mathematica_Plots\\2D_angular\\z=40cm.pdf", Plotz[[21]]];

(*Export["nEDM\\Mag scans May-July 2010\\Data_Mag
   Scans\\pdf_files\\2D_angular\\z=42cm.pdf",Plotz[[22]]];
Export["nEDM\\Mag scans May-July 2010\\Data_Mag
   Scans\\pdf_files\\2D_angular\\z=44cm.pdf",Plotz[[23]]];
Export["nEDM\\Mag scans May-July 2010\\Data_Mag
   Scans\\pdf_files\\2D_angular\\z=46cm.pdf",Plotz[[24]]];
Export["nEDM\\Mag scans May-July 2010\\Data_Mag
   Scans\\pdf_files\\2D_angular\\z=48cm.pdf",Plotz[[25]]];
Export["nEDM\\Mag scans May-July 2010\\Data_Mag
   Scans\\pdf_files\\2D_angular\\z=50cm.pdf",Plotz[[26]]];*)

(* Subtract time variation (== Blue variation for different thetas) *)

MeanBlueAllz = Table[Mean[BzⵔBzt[[q]][[All, 2]]], {q, 1, 26}];

MeanBlueRC = Table[Mean[BzⵔBzt[[q]][[All, 2]]], {q, 11, 21}];
MeanRedRC = Table[Mean[RzⵔBzt[[q]][[All, 2]]], {q, 11, 21}];
MeanYellowRC = Table[Mean[YzⵔBzt[[q]][[All, 2]]], {q, 11, 21}];

Table[{(w + 10) * 2 - 2, MeanBlueRC[[w]],
    MeanRedRC[[w]], MeanYellowRC[[w]]}, {w, 1, 11}] // Grid;

      (* Table of {0,Blue Mean Value} *)

TBlueMean = Table[Table[{0, MeanBlueAllz[[q]] * 1^w}, {w, 1, 25}], {q, 1, 26}];

VariationBz =
  Table[BzⵔBzt[[q]][[All, 2]] - TBlueMean[[q]][[All, 2]], {q, 1, 26}];

TimeVar = Table[Table[{0, VariationBz[[q, k]]}, {k, 1, 25}], {q, 1, 26}];

BzⵔBz = TBlueMean;
RzⵔBz = RzⵔBzt - TimeVar;
YzⵔBz = YzⵔBzt - TimeVar;

ListPlot[{BzⵔBz[[11]], RzⵔBz[[11]]}]

Table[ListPlot[{BzⵔBz[[q]], RzⵔBz[[q]], YzⵔBz[[q]]}], {q, 1, 26}];

ListPlot[YzⵔBz[[11]]]
```

E. 3 D Plots

z slices (r,θ,Bz)

```
Brθt = Table[Bz[[q]][[All, 1]][[All, {1, 2, 4}]], {q, 1, 26}];
Rrθt = Table[Rz[[q]][[All, 1]][[All, {1, 2, 4}]], {q, 1, 26}];
Yrθt = Table[Yz[[q]][[All, 1]][[All, {1, 2, 4}]], {q, 1, 26}];
```

```
Brθ = Table[Join[Brθt[[q]], Rrθt[[q]], Yrθt[[q]]], {q, 1, 26}];
```

```
Plotz3d = Table[ListPlot3D[Brθ[[q]],
    PlotLabel → "SCV B Field Below 9 K" Evaluate[Tza[[q]]],
    AxesLabel → {"r [m]", "θ [deg]", "Bz[μT]"}, Mesh → 3,
    ColorFunction → "BrightBands", Ticks → {{0, 0.075, 0.15},
      {-180, -135, -90, -45, 0, 45, 90, 135, 180}, {-5.05, -5.0, -4.95}},
    PlotRange → {-5.09, -4.95}, ViewPoint → {1.5, -1.8, 1}], {q, 11, 21}];
```

```
Export["nEDM\\Data\\Mathematica_Plots\\3D_z slices\\z=20cm.pdf", Plotz3d[[1]]];
Export["nEDM\\Data\\Mathematica_Plots\\3D_z slices\\z=22cm.pdf", Plotz3d[[2]]];
Export["nEDM\\Data\\Mathematica_Plots\\3D_z slices\\z=24cm.pdf", Plotz3d[[3]]];
Export["nEDM\\Data\\Mathematica_Plots\\3D_z slices\\z=26cm.pdf", Plotz3d[[4]]];
Export["nEDM\\Data\\Mathematica_Plots\\3D_z slices\\z=28cm.pdf", Plotz3d[[5]]];
Export["nEDM\\Data\\Mathematica_Plots\\3D_z slices\\z=30cm.pdf", Plotz3d[[6]]];
Export["nEDM\\Data\\Mathematica_Plots\\3D_z slices\\z=32cm.pdf", Plotz3d[[7]]];
Export["nEDM\\Data\\Mathematica_Plots\\3D_z slices\\z=34cm.pdf", Plotz3d[[8]]];
Export["nEDM\\Data\\Mathematica_Plots\\3D_z slices\\z=36cm.pdf", Plotz3d[[9]]];
Export["nEDM\\Data\\Mathematica_Plots\\3D_z slices\\z=38cm.pdf", Plotz3d[[10]]];
Export["nEDM\\Data\\Mathematica_Plots\\3D_z slices\\z=40cm.pdf", Plotz3d[[11]]];
```

θ slices (r,z,Bz)

```
Brzt = Table[Bθm50[[j, All, {1, 3, 4}]], {j, 1, 25}];
Rrzt = Table[Rθm50[[j, All, {1, 3, 4}]], {j, 1, 25}];
Yrzt = Table[Yθm50[[j, All, {1, 3, 4}]], {j, 1, 25}];
```

```
Brz = Table[Join[Brzt[[q]], Rrzt[[q]], Yrzt[[q]]], {q, 1, 25}];
```

```
Plotθ3d = Table[ListPlot3D[Brz[[q]],
    PlotLabel → "SCV B Field Below 9 K" Evaluate[θm50[[q]]],
    AxesLabel → {"r [m]", "z [cm]", "Bz[μT]"},
    Mesh → 3, ColorFunction → "BrightBands", Ticks →
     {{0, 0.075, 0.15}, {20, 25, 30, 35, 40, 45, 50}, {-5.05, -5.0, -4.95}},
    PlotRange → {-5.09, -4.95}, ViewPoint → {1.5, -1.8, 1}], {q, 1, 25}];
```

```
Export["nEDM\\Data\\Mathematica_Plots\\3D_theta slices\\θ=-180-50 deg.pdf", Plotθ3d[[1]]];
Export["nEDM\\Data\\Mathematica_Plots\\3D_theta slices\\θ=-165-50 deg.pdf", Plotθ3d[[2]]];
Export["nEDM\\Data\\Mathematica_Plots\\3D_theta slices\\θ=-150-50 deg.pdf", Plotθ3d[[3]]];
Export["nEDM\\Data\\Mathematica_Plots\\3D_theta slices\\θ=-135-50 deg.pdf", Plotθ3d[[4]]];
Export["nEDM\\Data\\Mathematica_Plots\\3D_theta slices\\θ=-120-50 deg.pdf", Plotθ3d[[5]]];
Export["nEDM\\Data\\Mathematica_Plots\\3D_theta slices\\θ=-105-50 deg.pdf", Plotθ3d[[6]]];
Export["nEDM\\Data\\Mathematica_Plots\\3D_theta slices\\θ=-90-50 deg.pdf", Plotθ3d[[7]]];
Export["nEDM\\Data\\Mathematica_Plots\\3D_theta slices\\θ=-75-50 deg.pdf", Plotθ3d[[8]]];
Export["nEDM\\Data\\Mathematica_Plots\\3D_theta slices\\θ=-60-50 deg.pdf", Plotθ3d[[9]]];
Export["nEDM\\Data\\Mathematica_Plots\\3D_theta slices\\θ=-45-50 deg.pdf", Plotθ3d[[10]]];
Export["nEDM\\Data\\Mathematica_Plots\\3D_theta slices\\θ=-30-50 deg.pdf", Plotθ3d[[11]]];
Export["nEDM\\Data\\Mathematica_Plots\\3D_theta slices\\θ=-15-50 deg.pdf", Plotθ3d[[12]]];
Export["nEDM\\Data\\Mathematica_Plots\\3D_theta slices\\θ=0-50 deg for all z.pdf", Plotθ3d[[13]]];
Export["nEDM\\Data\\Mathematica_Plots\\3D_theta slices\\θ=15-50 deg.pdf", Plotθ3d[[14]]];
Export["nEDM\\Data\\Mathematica_Plots\\3D_theta slices\\θ=30-50 deg.pdf", Plotθ3d[[15]]];
Export["nEDM\\Data\\Mathematica_Plots\\3D_theta slices\\θ=45-50 deg.pdf", Plotθ3d[[16]]];
Export["nEDM\\Data\\Mathematica_Plots\\3D_theta slices\\θ=60-50 deg.pdf", Plotθ3d[[17]]];
Export["nEDM\\Data\\Mathematica_Plots\\3D_theta slices\\θ=75-50 deg.pdf", Plotθ3d[[18]]];
Export["nEDM\\Data\\Mathematica_Plots\\3D_theta slices\\θ=90-50 deg.pdf", Plotθ3d[[19]]];
Export["nEDM\\Data\\Mathematica_Plots\\3D_theta slices\\θ=105-50 deg.pdf", Plotθ3d[[20]]];
Export["nEDM\\Data\\Mathematica_Plots\\3D_theta slices\\θ=120-50 deg.pdf", Plotθ3d[[21]]];
Export["nEDM\\Data\\Mathematica_Plots\\3D_theta slices\\θ=135-50 deg.pdf", Plotθ3d[[22]]];
Export["nEDM\\Data\\Mathematica_Plots\\3D_theta slices\\θ=150-50 deg.pdf", Plotθ3d[[23]]];
Export["nEDM\\Data\\Mathematica_Plots\\3D_theta slices\\θ=165-50 deg.pdf", Plotθ3d[[24]]];
Export["nEDM\\Data\\Mathematica_Plots\\3D_theta slices\\θ=180-50 deg.pdf", Plotθ3d[[25]]];
```

```
(* ROW θ=0 for 20<z<40 only *)
```

```
------------------------------------------------------
```

Appendix F

Tables

F1. Axial Gradients of the SS SCV as measured during the scans at Room Temperature and at T=10 K (Summer 2010 Run)

	Room Temperature magnetic scan			T=10K magnetic scan		
Theta	Axial Gradient (nT/cm)			Axial Gradient (nT/cm)		
degrees	R=0 (Blue)	R=0.075 m (Red)	R=0.15 m (Yellow)	R=0 (Blue)	R=0.075 m (Red)	R=0.15 m (Yellow)
-175	3.529	4.071	3.52	2.667	3.256	3.118
-160	3.558	4.331	4.625	2.709	3.425	3.778
-145	3.143	4.307	6.45	2.666	3.658	5.387
-130	3.279	4.518	8.736	2.67	3.795	7.892
-115	3.648	4.499	7.948	2.713	3.689	8.865
-100	3.246	4.158	6.354	2.687	3.483	6.963
-85	3.588	3.775	3.879	2.701	3.023	3.827
-70	3.531	3.329	3.193	2.714	2.56	2.3
-55	3.323	2.624	1.572	2.722	2.202	1.715
-40	3.455	2.431	0.9009	2.755	1.935	1.003
-25	3.523	2.438	0.7129	2.775	1.663	0.4241
-10	3.425	2.037	0.1306	2.771	1.473	0.19
5	3.427	2.183	0.2279	2.735	1.431	-0.05624
20	3.699	2.512	1.046	2.731	1.445	0.02802
35	3.209	2.171	1.027	2.719	1.533	0.3272
50	3.3	2.369	1.56	2.713	1.857	1.023
65	3.482	2.862	2.385	2.702	2.228	1.949
80	3.078	2.839	3.172	2.696	2.559	2.901
95	2.565	2.675	4.097	2.699	2.948	4.213
110	3.461	3.72	6.02	2.692	3.17	5.623
125	3.008	3.433	5.762	2.648	3.231	6.257
140	3.198	3.602	4.644	2.622	3.179	4.741

F2. Detection Settings for Oct-Nov 2010 Run

#Run	MCS1	MCS2	MCS3	MCS4	MCA1	MCA2	MCA3	MCA4
1353	SV	T1	Fe3	Open2	Open1	Open2	Fe3	Fe4
1355	SV	T1	Fe3	Open2	Open1	Open2	Fe3	Fe4
1357	SV	T1	Fe3	Open2	Open1	Open2	Fe3	Fe4
1359	SV	T1	Fe3	Open2	Open1	Open2	Fe3	Fe4
1361	SV	T1	Fe3	Open2	Open1	Open2	Fe3	Fe4
1362	SV	T1	Fe3	Open2	Open1	Open2	Fe3	Fe4
1363	SV	T1	Fe3	Open2	Open1	Open2	Fe3	Fe4
1365	Open1	Fe4	Fe3	Open2	Open1	Open2	Fe3	Fe4
1382	SV	T1	Fe3	Open1	Open1	Open2	Fe3	Fe4
1384	SV	T1	Fe3	Open1	Open1	Open2	Fe3	Fe4
1406	T1 (not starting)	SV	Fe3	Open1	Open1	Open2 (not good spectrum)	Fe3	Fe4
1407	T1 (not starting)	SV	Fe3	Open1	Open1	Open2 (not good spectrum)	Fe3	Fe4
1408	T1 (not starting)	SV	Fe3	Open1	Open1	Open2 (not good spectrum)	Fe3	Fe4
1427	T1 (not starting)	SV	Fe3	Open1	Open1	Open2	Fe3	Fe4
1448	T1 (not starting)	SV	Fe3	Open1	Open1	Open2	Fe3	Fe4
1464	SV (not starting)	T1	Fe3	Open1	Open1	Open2 (not good spectrum)	Fe3	Fe4

1471	SV (not starting)	T1	Fe3	Open1	Open1	Open2 (not good spectrum)	Fe3	Fe4
1474	SV (not starting)	T1	Fe3	Open1	Open1	Open2 (not good spectrum)	Fe3	Fe4
1476	SV (not starting)	T1	Fe3	Open1	Open1	Open2 (not good spectrum)	Fe3	Fe4
1478	SV (not starting)	T1	Fe3	Open1	Open1	Open2 (not good spectrum)	Fe3	Fe4
1479	SV (not starting)	T1	Fe3	Open1	Open1	Open2 (not good spectrum)	Fe3	Fe4
1480	SV (not starting)	T1	Fe3	Open1	Open1	Open2 (not good spectrum)	Fe3	Fe4
1482	SV (not starting)	T1	Fe3	Open1	Open1	Open2	Fe3	Fe4
1487	SV (not starting)	T1	Fe4	Open1	Open1	Open2	Fe3	Fe4
1489	SV (not starting)	Fe4	Fe3	Open1	Open1	Open2 (not good spectrum)	Fe3	Fe4
1490	SV (not starting)	Fe4	Fe3	Open1	Open1	Open2 (not good spectrum)	Fe3	Fe4
1491	SV (not starting)	Fe4	Fe3	Open1	Open1	Open2 (not good spectrum)	Fe3	Fe4

1493	SV (not starting)	Fe4	Fe3	Open1	Open1	Open2 (not good spectrum)	Fe3	Fe4
1494	SV (not starting)	Fe4	Fe3	Open1	Open1	Open2 (not good spectrum)	Fe3	Fe4
1496	SV (not starting)	Fe4	Fe3	Open1	Open1	Open2 (not good spectrum)	Fe3	Fe4
1497	SV (not starting)	Fe4	Fe3	Open1	Open1	Open2 (not good spectrum)	Fe3	Fe4
1498	SV (not starting)	Fe4	Fe3	Open1	Open1	Open2 (not good spectrum)	Fe3	Fe4
1499	SV (not starting)	Fe4	Fe3	Open1	Open1	Open2 (not good spectrum)	Fe3	Fe4
1508	SV (not starting)	Fe4	Fe3	Open1	Open1	Open2 (not good spectrum)	Fe3	Fe4
1509	SV (not starting)	Fe4	Fe3	Open1	Open1	Open2 (not good spectrum)	Fe3	Fe4
1510	SV (not starting)	Fe4	Fe3	Open1	Open1	Open2 (not good spectrum)	Fe3	Fe4
1517	SV (not starting)	Fe4	Fe3	Open1	Open1	Open2 (not good spectrum)	Fe3	Fe4

1520 (+rf)	SV (not starting)	Fe4	Fe3	Open1	Open1	Open2 (not good spectrum)	Fe3	Fe4
1521	SV (not starting)	Fe4	Fe3	Open1	Open1	Open2 (not good spectrum)	Fe3	Fe4
1522	SV (not starting)	Fe4	Fe3	Open1	Open1	Open2 (not good spectrum)	Fe3	Fe4
1523	SV (not starting)	Fe4	Fe3	Open1	Open1	Open2 (not good spectrum)	Fe3	Fe4
1524	SV (not starting)	Fe4	Fe3	Open1	Open1	Open2 (not good spectrum)	Fe3	Fe4
1525	SV (not starting)	Fe4	Fe3	Open1	Open1	Open2 (not good spectrum)	Fe3	Fe4
1526	SV (not starting)	Fe4	Fe3	Open1	Open1	Open2 (not good spectrum)	Fe3	Fe4
SV detector and UCN2 inputs swapped before pre-amplifier to check if the electronics are at the origin of the UCN3 fluctuations (so it meant to be swapped with UCN3)								
1527 (+rf)	SV (not starting)	Fe4	Fe3	Open1	Open1	-	Fe3	Fe4
1528 (+rf)	SV (not starting)	Fe4	-	Open1	Open1	Fe3	Open2 (not good spectrum)	Fe4
1528 (no rf)	SV (not starting)	Fe4	-	Open1	Open1	Fe3	Open2 (not good	Fe4

							spectrum)	
1529 (+rf)	SV (not starting)	Fe4	-	Open1	Open1	Fe3	Open2 (not good spectrum)	Fe4
1529 (no rf)	SV (not starting)	Fe4	-	Open1	Open1	Fe3	Open2 (not good spectrum)	Fe4
1533	Fe3 (not starting)	T1	Fe4	Open1	Open1	Open2 (not good spectrum)	Fe3	Fe4
1534 (+rf)	SV (not starting)	Fe3	Fe4	Open1	Open1	Fe3	-	Fe4
1534 (no rf)	SV (not starting)	Fe3	Fe4	Open1	Open1	Fe3	-	Fe4
1542 (+rf)	SV (not starting)	Fe3	Fe4	Open1	Open1	Fe3	Open2 (not good spectrum)	Fe4
1542 (no rf)	SV (not starting)	Fe3	Fe4	Open1	Open1	Fe3	Open2 (not good spectrum)	Fe4
1543	SV (not starting)	T1	Fe4	Open1	Open1	Fe3	Open2 (not good spectrum)	Fe4
1548	SV (not starting)	T1	Fe4	Open1	Open1	Fe3	Open2 (not good spectrum)	Fe4
1552	SV (not starting)	Fe3	Fe4	Open1	Open1	Fe3	Open2 (not good spectrum)	Fe4

1555	SV (not starting)	Fe3	Fe4	Open1	Open1	Fe3	Open2 (not good spectrum)	Fe4
1558	SV (not starting)	Fe3	Fe4	Open1	Open1	Fe3	Open2 (not good spectrum)	Fe4
1559	SV (not starting)	Fe3	Fe4	Open1	Open1	Fe3	Open2 (not good spectrum)	Fe4
1560	SV (not starting)	Fe3	Fe4	Open1	Open1	Fe3	Open2 (not good spectrum)	Fe4
1561	SV (not starting)	Fe3	Fe4	Open1	Open1	Fe3	Open2 (not good spectrum)	Fe4
1562	SV (not starting)	Fe3	Fe4	Open1	Open1	Fe3	Open2 (not good spectrum)	Fe4
1563	SV (not starting)	Fe3	Fe4	Open1	Open1	Fe3	Open2 (not good spectrum)	Fe4
1565	SV (not starting)	T1	Fe4	Open1	Open1	Fe3	Open2 (not good spectrum)	Fe4
1566	SV (not starting)	T1	Fe4	Open1	Open1	Fe3	Open2 (not good spectrum)	Fe4
1567	SV (not starting)	T1	Fe4	Open1	Open1	Fe3	Open2 (not good spectrum)	Fe4

1571	SV (not starting)	T1	Fe4	Open1	Open1	Fe3	Open2 (not good spectrum)	Fe4
1572	SV (not starting)	T1	Fe4	Open1	Open1	Fe3	Open2 (not good spectrum)	Fe4
1573	SV (not starting)	Fe3	Fe4	Open1	Open1	Fe3	Open2 (not good spectrum)	Fe4
1574	SV (not starting)	Fe3	Fe4	Open1	Open1	Fe3	Open2 (not good spectrum)	Fe4
1575	SV (not starting)	Fe3	Fe4	Open1	Open1	Fe3	Open2 (not good spectrum)	Fe4
1577	SV (not starting)	Fe3	Fe4	Open1	Open1	Fe3	Open2 (not good spectrum)	Fe4
1586	SV (not starting)	Fe3	Fe4	Open1	Open1	Fe3	Open2 (not good spectrum)	Fe4
1590	SV (not starting)	Fe3	Fe4	Open1	Open1	Fe3	Open2 (not good spectrum)	Fe4
1591	SV (not starting)	T1	Fe4	Open1	Open1	Fe3	Open2 (not good spectrum)	Fe4

F3. Timer Box Settings

#Run File	MCA Opening Time 1	MCA Closing Time 1	MCA Opening Time 2	MCA Closing Time 2
1353 1355 1357 1359	SV opens 50.2 s (N/A)	SV closes + end of run 158.2 s (N/A)	N/A (N/A)	N/A (N/A)
1361	SV opens 50.2 s (0 s)	SV closes + end of run 158.2 s (51.2 s)	N/A (N/A)	N/A (N/A)
1362 1363 1365	MCA closes 51.2 s (0 s)	SV closes + end of run 158.2 s (51.2 s)	N/A (N/A)	N/A (N/A)
1382 1384	Start of run 0s (62.2 s)	MCA opens 61.2 s (93.2 s)	Arbitrary time 78.2 s (N/A)	MCA closes + end of run 93.2 s (N/A)
1427	SV opens 40.2 s (151.2 s)	End of run 191.2 s (191.2 s)	N/A (N/A)	N/A (N/A)
1448	N/A (330 s)	N/A (371.2 s)	N/A (N/A)	N/A (N/A)
1464	SV opens 144 s (185 s)	MCA opens 185 s (220 s)	N/A (N/A)	N/A (N/A)
1471 1474	Start of run 0s (105 s)	MCA opens 105 s (125 s)	N/A (N/A)	N/A (N/A)
1487 1489 1490 1491	Start of run 0s (47 s)	SV closes 44 s (68 s)	MCA closes 68 s (N/A)	End of run 90 s (N/A)
1493 1494 1496 1497 1498	SV opens 14 s (37 s)	SV closes 34 s (58 s)	N/A (N/A)	N/A (N/A)
1499 (SV unplugged)	Start of run 0s (37 s)	SV closes 34 s (58 s)	N/A (N/A)	N/A (N/A)
1520	Start of run 0s (47 s)	SV closes 44 s (73 s)	MCA closes 73 s (N/A)	End of run 94 s (N/A)
1527	SV opens + MCA opens 24 s (24 s)	Arbitrary time 26 s (83 s)	MCA closes 83 s (N/A)	End of run 105 s (N/A)
1528 1529	SV closes 30 s (10 s)	MCA closes 56 s (56 s)	SV closes 118.6 s (98.4 s)	End of run 167 s (144.6)
1534	SV opens + MCA opens 10 s (10 s)	MCA 2nd closing time 144.6 s (56 s)	N/A (98.6 s)	N/A (144.6 s)

1542	SV opens + MCA opens 10 s (10 s)	MCA 2nd closing time 144.4 s (56 s)	N/A (98.4 s)	N/A (144.4 s)
1548	MCA closes 1 s (0 s)	End of run 130 s (1 s)	N/A (N/A)	N/A (N/A)
1552 1555 (SV unplugged)	Start of run 0s (132 s)	MCA opens 132 s (172 s)	N/A (N/A)	N/A (N/A)
1558 (SV unplugged)	Start of run 0 s (132 s)	MCA opens 132 s (212 s)	N/A (N/A)	N/A (N/A)
1559 1560 1561 (SV unplugged)	N/A (132 s)	N/A (192 s)	N/A (N/A)	N/A (N/A)
1562 (SV unplugged)	Start of run 0s (132 s)	MCA opens 132 s (252 s)	N/A (N/A)	N/A (N/A)
1563 (SV unplugged)	Start of run 0s (132 s)	MCA opens 132 s (152 s)	N/A (N/A)	N/A (N/A)
1565 1566 1567 1571 1572 1573 1574 1575 (SV unplugged)	Start of run 0s (51 s)	MCA/SV close + end of run 151 s (151 s)	N/A (N/A)	N/A (N/A)
1577 (SV unplugged)	Start of run 0s (21 s)	End of run 178 s (67 s)	N/A (109.6 s)	N/A (155.6 s)
1590 (SV unplugged)	Start of run 0s (73.6 s)	End of run 268 s (133.6 s)	N/A (207.2 s)	N/A (267.2 s)
1591 (SV unplugged)	Start of run 0s (51 s)	End of run 151 s (101 s)	N/A (N/A)	N/A (N/A)

Table F3: Timer box settings for the MCA gate time window as were set and recorded on the DataView header (red figures) and as it estimated finally to be (information in black).

F4. MCA and MCS Background Count Rates

	MCA Background Count Rates				MCS Background Count Rate		
#Run	Open	Fe3	Fe4		Open	Fe3	Fe4
1353	3,6	0,0	0,7				
1355	7,2	0,0	0,0				
1357	0,2	0,0	0,0				
1359	39,8	0,4	0,3				
1361	7,8	0,0	0,0				
1362	0,0	0,0	0,0				
1363	1,3	0,0	0,0				
1365	20,4	0,5	0,9				
1382	113,6	6,4	6,2				
1384	20,8	1,2	1,1				
1406	312,6	12,9	14,1		85,7	0,0	0,0
1407	37,6	2,2	2,6				
1408	219,7	12,4	14,4				
1427	27,4	2,1	1,9				
1448							
1464	170,6	12,4	9,8		54,2	0,0	0,0
1471	148,8	9,5	9,5		72,0	0,0	0,0
1474	21,1	1,1	1,3				
1476	96,5	0,0	7,3				
1478	23,4	0,0	1,9				
1479	653,5	0,0	39,3				
1480	180,1	0,0	11,6				
1482	38,3	0,0	0,0				
1487	235,7	0,0	15,8				
1489	36,4	8,1	13,9				
1490	38,2	6,8	13,1				
1491	131,6	35,8	54,0		88,9	22,2	22,2
1493	127,6	28,7	33,3		11,1	0,0	0,0

	MCA Background Count Rates				MCS Background Count Rate		
#Run	Open	Fe3	Fe4		Open	Fe3	Fe4
1494	485,9	110,2	110,1		122.2	44.4	44.4
1496	509,4	105,6	122,3		122,2	33,3	44,4
1497	59,9	14,4	22,3				
1498	41,9	4,2	12,4				
1499	242,4	0,0	78,1				
1508							
1509							
1510							
1517							
1520 (+rf)	173,2	0,0	49,4				
1521							
1522							
1523							
1524							
1525							
1526							
1527 (+rf)	201,3	0,0	72,3				
1528 (+/no rf)	190,6	0,0	59,2				
1529 (+/no rf)	160,4	0,0	71,1				
1533							
1534 (+/no rf)	1,1	0,4	0,4				
1542 (+/no rf)	124,8	39,5	51,6		162,8	29,1	58,1
1543							
1548	5,5	1,5	2,3				
1552	3,0	1,1	0,0				
1555	67,0	16,6	9,4				
1558	48,6	13,4	7,3				
1559	4,1	1,1	0,6				

	MCA Background Count Rates				MCS Background Count Rate		
#Run	Open	Fe3	Fe4		Open	Fe3	Fe4
1560	4,1	1,0	0,6				
1561	25,8	6,4	3,6				
1562	72,7	17,9	10,2				
1563	56,5	13,9	7,7				
1565	19,5	9,4	3,6				
1566	3,9	2,2	0,7				
1567	23,7	4,7	2,8				
1571	42,0	7,9	4,3				
1572	8,9	2,4	1,1				
1573	70,5	17,9	9,0				
1574	9,7	1,5	1,2				
1575	9,0	2,3	1,6				
1577	1,1	0,3	0,3				
1586	0,1	0,0	0,0				
1590	40,6	16,7	6,1				
1591	189,3	57,2	30,2				

Table F4: Background Count Rates as calculated from the MCA and MCS spectra for all the useful run files.

F5. Guide Field Coils Configuration

Run #	Coils Setup								
	C0 [A]	C1-4 [A]	C5-6 [A]	C7 [A]	C8 [A]	C9 [A]	SQUIDs Coil [mA]	Feedback Coil 6WS [A]	Feedback Coil HV [A]
1353	-	3	9	9	9	-	-	-	-4
1355	-	3	9	9	9	-	-	-	-4
1357	-	6	18	18	18	-	-	-	-4
1359	-	6	18	18	18	-	-	-	-4
1361	-	9	27	27	27	-	-	-	-4
1362	-	9	27	27	27	-	30	-	-4
1363	-	9	27	27	27	-	-30	-	-4
1365	-	9	27	27	27	-	30	-3,5	-4
1382 to 1427	-	9	20	20	20	-	-	-3,5	-4
1448	-	6	20	20	20	-	-	-3,5	-4
1464	-	6	20	20	20	-	30	1	-
1465	-	6	20	20	20	-	30	1	-
1477	-	6	20	20	20	-	30 opp polar	1	-
1474	-	-	-	-	-	-	-	-	-
1476	-	6,2	-	-	-	-	-	-	-
1478	-	6,2	20,2	-	-	-	-	-	-
1479	-	6,2	20,2	20,2	-	-	-	-	-
1480	-	-6,2	-20,2	20,2	-	-	-	-	-
1482	-	-6,2	-20,2	20,2	3	-	-	-	-
1487	-	-6,2	-20,2	20,2	3	-	-	-	-
1489	-	-6,2	-20,2	20,2	6	-	-	-	-
1490	-	-6,2	-20,2	20,2	6	-	20 (T3+)	-	-
1491	-	-6,2	-20,2	20,2	6	-	20 (T3-)	-	-
1493	-	-6,2	-20,2	20,2	3	-	20 (T3+)	-	-
1494	-	6,2	20,2	20,2	3	-	20 (T3-)	-	-
1496	-	6,05	20,2	20,2	20,2	10	-	2	-
1498	-	3	9	9	9	-	-	-	-
1499 to 1542	-	6	18	18	18	-	-	-	-

Run #	C0 [A]	C1-4 [A]	C5-6 [A]	C7 [A]	C8 [A]	C9 [A]	SQUIDs Coil [mA]	Feedback Coil 6WS [A]	Feedback Coil HV [A]
1552	-	3	9	9	9	-	-	-	-
1555	0.38	3	9	9	9	-	-	-	-
1559	0.17	3	9	9	9	-	30 Pos	-	-
1560	0.17	3	9	9	9	-	30 Neg	-	-
1561 to 1565	0.17	3	9	9	9	-	-	-	-
1566	0.17	3	9	9	9	-	26.4 Pos	2	-
1567	0.17	3	9	9	9	-	26.4 Pos	-2	-
1571	0.17	3	9	9	9	-	-26,4	-2	-
1572	0.17	3	9	9	9	-	-26,4	2	-
1573 to 1591	-	3	9	9	9	-	-	2	-

Table F5: The current values of the coils between the exit of the polariser up to the entrance of the horizontal shields for all the useful run files.